Title
Numerical Study of Freestream Waves Receptivity and Nonlinear Breakdown in Hypersonic Boundary Layer

Permalink
https://escholarship.org/uc/item/4sp9w1tk

Author
Lei, Jia

Publication Date
2013

UNIVERSITY OF CALIFORNIA

Los Angeles

Numerical Study of Freestream Waves Receptivity and Nonlinear Breakdown in Hypersonic Boundary Layer

A dissertation submitted in partial satisfaction of the
requirements for the degree Doctor of Philosophy
in Aerospace Engineering

by

Jia Lei

2013

ABSTRACT OF DISSERTATION

Numerical Study of Freestream Waves Receptivity and Nonlinear Breakdown in Hypersonic Boundary Layer

by

Jia Lei
Doctor of Philosophy in Aerospace Engineering
University of California, Los Angeles, 2013
Professor Xiaolin Zhong, Chair

Laminar-turbulent transition prediction in hypersonic boundary layer remains one of the most challenging topics in the design of hypervelocity vehicle. It requires thorough understanding of the physical mechanisms underlay freestream wave receptivity and nonlinear breakdown process. Freestream wave receptivity concerns the evolution of freestream disturbance passing through the shock and exciting the boundary layer normal modes that eventually become unstable. Nonlinear breakdown focuses on the study of the relevant mechanisms in the secondary instability region that leads to laminar-turbulent transition. These two topics have been extensively studied separately for decades. Significant progress has been made in terms of understanding how the instability waves form and develop in the early region as well as what are the viable paths from breakdown to turbulent. However, the linkage between receptivity and breakdown is still not well understood. The nature transition process commonly observed in hypersonic boundary layer consists of the following ingredients: freestream wave receptivity, linear growth, secondary instability and breakdown to turbulent. The transition location highly depends on the freestream wave disturbance profile. In order to attain a better understanding of the natural transition process, it is necessary to conduct a complete simulation from freestream wave receptivity all the way to nonlinear breakdown. This kind of simulation is considered beyond the capability of current computer power. The objective of current research is to devise a new three-step approach to simulate the flow from receptivity process to breakdown. In order to achieve the goal, direct numerical simulations (DNS) are performed over various freestream conditions and cone geometries to investigate the hypersonic boundary layer stability, freestream wave receptivity and nonlinear breakdown. In the study of nose bluntness effect on hypersonic boundary layer stability, three cone models with different nose radii are investigated by linear stability theory (LST). It is found that, if only considering the second-mode instabilities, the onset of instability is always delayed as the nose bluntness increases. In the effort to simulate the entire process from freestream wave receptivity to nonlinear breakdown, a new approach is applied to break the simulation into three steps: meanflow calculation, linear receptivity simulation and nonlinear breakdown simulation. Extensive case studies demonstrate that it is feasible to simulate the flow from receptivity to breakdown using our new simulation approach. From the breakdown simulations, it is found that the breakdown is the result of fundamental resonance that occurs between the two-dimensional second-mode wave and their three-dimensional modes. In the secondary instability growth region, the two-dimensional and three-dimensional modes need to attain the same amplitude level for the breakdown to take place.

The dissertation of Jia Lei is approved.

Oddvar Bendiksen

John Kim

Marcus Roper

Xiaolin Zhong, Committee Chair

University of California, Los Angeles

2013

CONTENTS

LIST OF FIGURES

ACKNOWLEDGEMENTS

I wish to express my sincere appreciation to my advisor and committee chair, Professor Xiaolin Zhong, for his insightful advice, numerous encouragement, and unconditioned support during the completion of this dissertation. I also wish to thank Professor John Kim, Professor Oddvar Bendiksen, and Professor Marcus Roper for the time and patience to serve on my committee.

In addition, I would like to thank my colleagues, Dr. Xiaowen Wang, Dr. Pradeep Rawat, Dr. Akshay Prakash, Dr. Le Duan, Yuet Huang, Danny Fong, and Clifton Mortensen for the help, support and friendship through all these tough years.

This work was partially sponsored by AFOSR/NASA National Center of Hypersonic Research in Laminar-Turbulent transition and by the Air Force Office of Scientific Research under the grant No.FA9550-07-1-0414, monitored by Dr. John Schmisseur. The computational resources are provided by Extreme Science and Engineering Discovery Environment (XSEDE) under project No.ASC090076 and DoD Supercomputing Resource Center (DSRC) under project WPTAFOSR33272DNS.

VITA

2005 - 2007	B.S. in Aerospace Engineering - *summa cum laude,* UCLA, Los Angeles, California
2007 - 2009	M.S in Aerospace Engineering, UCLA, Los Angeles, California
2007 - 2013	Graduate Student Researcher, MAE department, UCLA, Los Angeles, California

PUBLICATIONS

- J. Lei and X. Zhong, "Linear Stability Analysis of Nose Bluntness Effects on Hypersonic Boundary Layer Transition," Journal of Spacecraft and Rockets, vol. 49, no. 1, pp. 24-37, 2012.
- J. Lei and X. Zhong, "Numerical Simulation of Freestream Waves Receptivity and Breakdown in Mach 6 Flow over Cone", AIAA paper 2013-2741, June 2013.
- J. Lei and X. Zhong, "Numerical Study of Freestream Waves Induced Breakdown in Hypersonic Boundary Layer Transition", AIAA paper 2012-2692, June 2012.

- J. Lei, and X. Zhong, “Non-linear Breakdown in Hypersonic Boundary Layer Transition Induced by Freestream Disturbances”, AIAA paper 2011-3563, 2011.
- X. Zhong and J. Lei, “Numerical Simulation of Nose Bluntness Effects on Hypersonic Boundary Layer Receptivity to Freestream Disturbances,” AIAA paper 2011-3079, June 2011.
- J. Lei, and X. Zhong, “Linear Stability Analysis of Nose Bluntness Effects on Hypersonic Boundary Layer Transition”, AIAA paper 2010-0898, 2010.
- J. Lei and X. Zhong, “Linear Stability Study of Hypersonic Boundary Layer Transition on Blunt Circular Cones,” AIAA paper 2009-939, January 2009.

1. Introduction

1.1. Historical Background

A reliable prediction of laminar-turbulent transition of hypersonic boundary layers is critically important to the development of hypersonic vehicles that are to be used for rapid global access[1]. Boundary layer transition has first-order impact to aerodynamic heating, drag and control of hypersonic vehicles. Extreme heat transfer from flow to body structure is arguably the prime constraint in the design of hypersonic aircraft. Great success has been achieved in predicting heating rates in laminar and fully turbulent flow region, but accurate prediction in a transitional region remains elusive. Uncertainty in heat transfer rate requires large factors of safety to be used in current vehicle designs. Improved computational accuracy could lead to significant improvements in hypersonic vehicle performance by allowing the removal of unnecessary weight in the thermal protection system.

The success of transition and related heating prediction relies on the good understanding of the relevant physical mechanisms leading to transition. In spite of considerable efforts in experimental, theoretical, and numerical studies, many critical physical mechanisms underlying hypersonic boundary-layer transition are still poorly understood. Engineering design of hypersonic vehicles has mainly been based on transition criteria obtained by empirical correlations of experimental data. The e^n method, which predicts boundary layer transition based solely on linear stability theory, is by far the most successful physics-based prediction method for transition prediction. Nevertheless, the e^n method suffers from a major drawback that it does not consider the effects of receptivity of the boundary layer to freestream disturbances, surface roughness, or other perturbation sources. In reality, the transition location is very sensitive to the level of forcing disturbances [2].

Receptivity of low-speed incompressible boundary layer flows has been extensively studied in the last three decades[2]. However, there have been only a limited number of theoretical [3-9], experimental[10-12], and computational [13-24] studies on the receptivity of compressible boundary layers. The different paths from receptivity to transition of boundary layer flow are shown in Fig. 1. Path A is considered the most common path to transition; and it is the path that we consider in the current study. This path consists of receptivity of linear freestream wave disturbance, unstable normal-mode growth and secondary instability, and nonlinear breakdown to transition. Fedorov et al. [3-6, 25, 26] showed that the receptivity mechanisms of supersonic and hypersonic boundary-layer flows are essentially different from those of subsonic and relatively low supersonic flows. Specifically, they found that two boundary-layer wave modes, which were termed mode F (mode 1) and mode S (mode 2), can be synchronized with the fast and slow acoustic waves in the leading edge region, respectively. Note that the mode F and mode S were adopted in more recent year to standardize the terminology. Mode 1 and Mode 2 were used in Ma's original paper. Secondly, Mode F can be synchronized with external entropy/vorticity waves with a phase speed equal to free-stream velocity. Third, there is a synchronization point between Mode F and S near the Branch I of the second-mode neutral stability point.

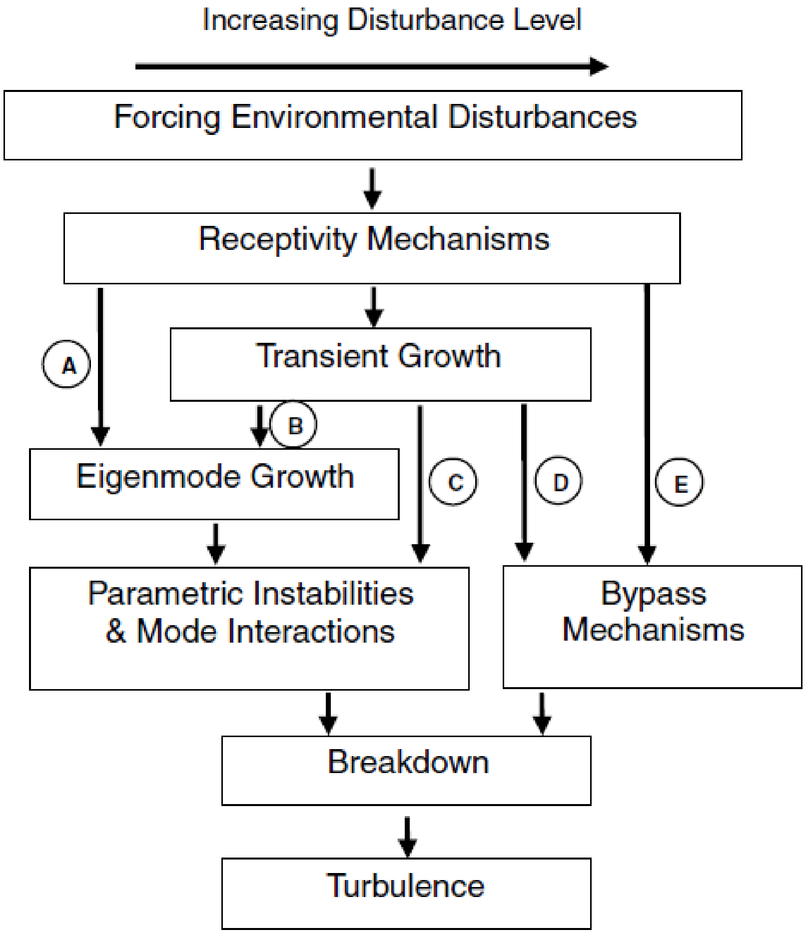

Fig. 1. Paths to boundary layer transition in terms of freestream wave disturbance amplitude [27].

The main features of the supersonic boundary-layer normal modes analyzed by Fedorov et al. were in qualitative agreement with Zhong's numerical simulation [13, 14, 16]. It was shown that both Mode F and the first Mack mode can convert to the unstable second Mack mode in numerical simulations. It was also shown that the receptivity leads to the excitation of both Mack modes and a family of stable modes, i.e., mode I, mode II, etc. The forcing fast acoustic waves do not interact directly with the unstable second Mack mode. Instead, the stable mode I waves interact with both the fast acoustic waves near the leading edge and the unstable Mack-mode waves downstream. Through this two-step interaction process, the stable mode I waves transfer wave energy from the forcing fast acoustic waves to the second Mack-mode waves inside the boundary layer. These receptivity studies have led to a better understanding of the hypersonic boundary receptivity mechanisms for instability modes. The receptivity results can be coupled with a nonlinear breakdown in the DNS of hypersonic boundary layer transition.

Since 1990s, significant progress has been made by several research groups in DNS studies of fundamental mechanisms leading to nonlinear breakdown and transition in supersonic and hypersonic boundary layers [28-32]. In DNS studies, the full 3-D Navier-Stokes equations are applied to simulate the development and nonlinear interaction of the disturbances waves. A number of transition related mechanisms have been identified and studied. In some cases, flow field was simulated up to the beginning of turbulence. Detailed information on the formation and evolution of transitional flow structures, as well as average heating rates and skin friction, could be obtained by the simulation. It was found that the transition mechanisms for supersonic boundary layers include secondary instability of either sub-harmonic or fundamental resonances [33]. By using DNS, Thumm [34] and Fasel et al. [35] discovered a new breakdown mechanism for a boundary layer at Mach 1.6, which they termed oblique breakdown. This breakdown to turbulence is initiated by the nonlinear wave interaction of two oblique instability waves with equal but opposite wave angles. The mechanisms have also been confirmed by many researchers, including Chang and Malik [36]. For supersonic flows, it was shown that oblique breakdown leads to a more rapid transition than other secondary instability mechanisms. It also requires much lower threshold disturbance amplitudes for the nonlinear development [37]. For these reasons, oblique breakdown has been suggested to be of practical importance for supersonic transition in low-disturbance environments [38, 39].

Husmeier and Fasel [40] did DNS studies of secondary instability mechanisms of hypersonic boundary layers over cones with a circular cross section. The computational domain is a cut-out section of the whole flow field (Fig.2). Though hypersonic boundary layer is most unstable to second-mode two-dimensional waves, their investigations indicated that secondary instability mechanisms involving two-dimensional waves appear to be of lesser importance in the nonlinear stages of breakdown. Instead, second-mode oblique waves at small wave angles, which are almost as amplified as second-mode two-dimensional waves, were found to dominate the nonlinear behavior. It seems that further studies are necessary in order to confirm this conclusions because extensive experimental results have pointed to the dominant of 2-D second mode before transition in hypersonic boundary layers [41, 42].

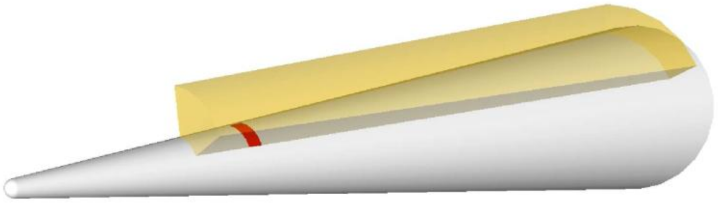

Fig.2. Computational domain used in Husmeier and Fasel's DNS simulation [40].

For hypersonic boundary layer transition, Pruett and his colleges did spatial DNS of hypersonic boundary layers of Mach 8 flow over a cone of eight-degree half angle [28, 29, 43]. The transitional state was triggered by a symmetric pair of oblique second-mode disturbances whose nonlinear interactions generate strong streamwise vorticity, which leads severe spanwise variations in the flow and eventual laminar breakdown. In their simulations, the PSE method was used to compute the weakly and moderately nonlinear initial stages of the transition process and, thereby, to derive a harmonically rich inflow condition for the DNS. The strongly nonlinear and laminar-breakdown stages of transition were subsequently computed by well-resolved DNS.

1.2. Current Challenges in Hypersonic Transition Simulation

Because of the difficulties in conducting hypersonic experiments and the complexity of hypersonic flows, fundamental hypersonic studies have been increasingly relied on the use of direct numerical simulations (DNS). In order for a DNS technique to perform reliable “numerical experiments”, it is necessary to develop and validate high-order accurate numerical algorithms suitable for highly accurate simulation of transient high-speed flows. So far, Zhong’s hypersonic CFD group at UCLA have developed and validated a high order DNS method and computer code for the DNS studies of hypersonic boundary layer stability and receptivity over various body geometries [44-47]. They have done many successful studies on the receptivity and stability for a number of 2-D and 3-D hypersonic flows over blunt bodies and flat plates [13-21]. These numerical simulations have led to a better understanding of hypersonic boundary layer receptivity and stability physics.

As mentioned in section 1.1, most of the previous hypersonic boundary layer transition simulation studies were not linked to practical disturbance environment. Only theoretical or artificial forcing waves were used primarily by means of blowing and suction hole to study the transition mechanisms. To date, with the exception of Rai and Moin [48], almost all other numerical experiments have simulated controlled rather than natural occurring instability processes. In a controlled experiment, instability waves of a particular wavelength or frequency are excited by imposed forcing. In contrast, in natural transition, the input contains a continued frequency and wave number spectra, and the flow selects the preferred instability modes. A few of the cited simulations are hybrid in the sense that the primary instability wave is imposed, whereas secondary instability is triggered by low-level noise [49, 50].

Due to the enormous requirements on computation resources, full scale DNS studies of boundary layer transition from the leading edge receptivity process to the breakdown in transition are impossible to accomplish. All the current DNS works have been limited to idealized cases of boundary layer response to artificial imposed forcing waves. So far, the complete process of laminar-turbulent transition from leading edge to the beginning of transition has not been computed by direct numerical simulation. Such a task has been commonly regarded as beyond the capability of currently available computer powers. On the other hand, if possible, such simulation can make a significant impact on the state on current transition research because the effects of freestream disturbance on transition can be analyzed. It is realized that an innovative approach is required to tackle this challenge.

Therefore, the purpose of current research is to develop, demonstrate, and validate a new approach to numerically simulate the complete process of hypersonic boundary layer transition. Such simulation tool can be valuable in the prediction of surface heat transfer rates in transitional hypersonic boundary layers.

1.3. Research Objectives and Plan

Since the transition in hypersonic boundary layer flow highly depends on the freestream wave disturbance profile in both the amplitude level and spectrum, it is necessary to link the freestream wave receptivity to breakdown study so that the complete transition picture can be better understood. Therefore, the objective of current research is to devise a new three-step approach to simulate hypersonic boundary layer flow from freestream wave receptivity process to nonlinear breakdown and use this simulation framework to study the hypersonic boundary layer transition. It is expected that the success of this kind of simulation will help us in understanding the flow physics and breakdown mechanisms during the hypersonic boundary layer transition process. Once this framework is established successfully, it can be applied to more general transition studies.

During the framework development of current research, several research topics are emphasized. Nose bluntness effects play important roles in the transition of hypersonic boundary layer. But the physics behind it is not well understood. Hence, the nose bluntness effects on the flow stability over cone configurations will be studied using the numerical and theoretical tools. The purpose is to understand how the nose bluntness of cone changes the stability characteristic of boundary layer flow. Subsequently, the linear receptivity to freestream wave will be studied by numerical simulations to understand the receptivity process in the nose region and how the instability modes excite and develop within the hypersonic boundary layer. Lastly, the linear receptivity response library will be used to construct the inflow conditions for the final nonlinear breakdown simulations so that the relevant breakdown mechanisms can be investigated. The ultimate goal is to establish a framework to simulate the hypersonic boundary layer transition by directly linking the freestream receptivity process to the nonlinear breakdown.

2. Governing Equations and Numerical Methods

In this chapter, the numerical tools that are utilized for the current study are presented in detail. Both the two-dimensional freestream wave receptivity and three-dimensional nonlinear breakdown are investigated by numerical simulations. The steady flow solution is computed using the same program and setup as the two-dimensional receptivity case with the freestream wave disturbance level set to zero. Grid convergence studies are performed to ensure the accuracy of the steady base flow. The linear stability analysis numerical tool is developed based on the classical linear stability theory (LST). The LST analysis uses the steady flow result as base flow solution. The LST decomposes the boundary layer perturbation into normal modes so that the stability characteristics of boundary layer flow can be identified. It provides theoretical solution to predict the behavior of the disturbance within boundary layer and can be use to validate the numerical simulation where the development of disturbance are calculated using full governing equations. The unsteady flows are simulated numerically using the high-order shock-fitting method coupled with high-order finite difference upwind scheme to attain a uniformly high-order and high accurate flow solutions. The numerical program has the capability to conduct both two-dimensional and three-dimensional flow filed simulation. The current numerical program is also capable of performing parallel computation on any super computer that has message passing interface (MPI) architecture.

2.1. Governing Equations

The governing equations are the compressible three-dimensional Navier-Stokes equations, which can be written in the following conservative variables form:

$$\frac{\partial U*}{\partial t*}+\frac{\partial F_j*}{\partial x_j*}+\frac{\partial F_{vj}*}{\partial x_j*}=0 \qquad (1)$$

where $U*=(\rho^*,\rho^* u_1^*,\rho^* u_2^*,\rho^* u_3^*,e^*)$, and superscript * represents dimensional variables. Cartesian coordinates are denoted by (x_1^*,x_2^*,x_3^*) in tensor notation. For the current simulation study of axisymmetric flow over circular cones, x_1^* is the coordinate along the centerline of the cone pointing toward the downstream direction. x_2^* and x_3^* are the coordinates perpendicular to each other are along the radius directions of circular cross-section of cone point outward. The origin of coordinate is co-located with the center of spherical nose. In later simulation result coordinates (x,y,z) will be used in place of (x_1^*,x_2^*,x_3^*) for convenience. The F^* s are inviscid and viscous flux terms that can be expanded as

$$F^{*}{}_{j} = \begin{Bmatrix} \rho u_{j} \\ \rho u_{j1} u_{j} + p\delta_{1j} \\ \rho u_{j2} u_{j} + p\delta_{1j} \\ \rho u_{j3} u_{j} + p\delta_{1j} \\ (e+p)u_{j} \end{Bmatrix} \quad \text{and} \quad F^{*}{}_{vj} = \begin{Bmatrix} 0 \\ \tau_{1j} \\ \tau_{2j} \\ \tau_{3j} \\ \tau_{jk} u_{k} - K\dfrac{\partial T}{x_{j}} \end{Bmatrix}. \tag{2}$$

In eq. (2), δ is Kronecker delta and only δ_{ii} equals to 1. K is the heat conductivity coefficient and τ_{ij} is the viscous stress tensor that can be expanded as

$$\tau_{ij} = \mu\left(\frac{\partial u_i}{\partial x_j} + \frac{\partial u_j}{\partial x_i}\right) - \frac{2}{3}\mu\frac{\partial u_n}{\partial x_n}\delta_{ij}, \tag{3}$$

where μ is the viscosity coefficient. Where both K and μ can be calculated by empirical Sutherland's Law as:

$$\mu = \mu_r \left(\frac{T}{T_r}\right)^{3/2} \frac{T_r + T_s}{T + T_s} \tag{4}$$

$$K = \frac{\mu c_p}{\mathrm{Pr}} \tag{5}$$

K is related to μ by eq. (5) with an assumed constant Prandtl number, Pr, of 0.72; and c_p is the specific heat at constant pressure. In eq. (2) the e is the specific total energy that can be written as

$$e = \rho c_v T + \frac{\rho}{2}(u_1^2 + u_2^2 + u_3^2) \tag{6}$$

where c_v is the specific heat at constant volume.

In current study, even the freestream flow Mach numbers of study cases are around 6, the freestream temperature and pressure are relatively low. Even the temperature of the flow the shock jumps substantial but is still well below 1000K. Therefore, the thermal and chemical effects are not very significant. To simplify the gas model and place our focus only on the receptivity and transition mechanisms, we assume the air gas is thermally and calorically perfect such that the following ideal gas model in eq. (7) can be applied.

$$p = \rho R T \tag{7}$$

To make the problem well-posed, the appropriated boundary conditions are needed. At the cone body and flow interface, the non-slip conditions are enforced for velocity. Either isothermal or adiabatic wall condition is used for temperature at the cone surface. At the shock, since the shock-fitting method used for current simulation study, the shock boundary conditions are determined by Rakine-Hugoniot relation and characteristic compatibility relation. The detail on how the flow variables attain will be explain in section 2.3. The inflow conditions for flow over cone can be the same as shock boundary conditions or specified by the flow conditions at the exit of the preceding computational domain. For the outflow, a high-order extrapolation is deployed to attain the flow variables at the last grid points across the exit of computational domain.

2.2. Coordinate Transformation

For the circular cone geometry in the test cases use for current study, the curvilinear body fitted grids are used. The curvilinear coordinate system is denoted by (ξ, η, ζ). ξ is the coordinate along the cone surface in the streamwise direction. η is the coordinate in the wall-normal direction pointing away from boundary layer. ζ is the coordinate in the spanwise direction of the cone. The Cartesian coordinates and curvilinear coordinates are illustrated in Fig. 3 using two-dimensional grid over a blunt cone as example.

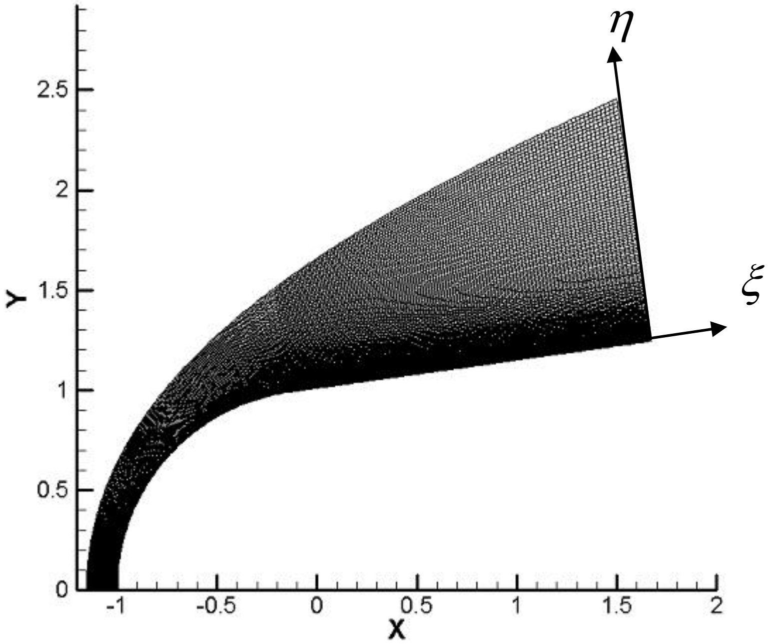

Fig. 3. Schematic of 2D grid near the leading edge of a blunt circular cone.

In order to make the numerical method formulations independent of grid, a coordinate transformation is needed to connect the Cartesian coordinates and curvilinear coordinates. To completely distinguish these two coordinate systems in formulations, a temporal coordination is also included denoted by τ . The coordinate transformation relations can be expressed as the following:

$$\begin{cases} \xi = \xi(x,y,z) \\ \eta = \eta(x,y,z,t) \\ \zeta = \zeta(x,y,z) \\ \tau = t \end{cases} \Leftrightarrow \begin{cases} x = x(\xi,\eta,\zeta,\tau) \\ y = y(\xi,\eta,\zeta,\tau) \\ z = z(\xi,\eta,\zeta,\tau) \\ t = \tau \end{cases} \tag{8}$$

Due to the nature of shock fitting method, the girds in η coordinate is adjusted in each time based on the shock height, therefore, η is a time dependent function. With the transformation relation established, their derivatives can be worked out using the chain rule of derivative.

$$\begin{bmatrix} \frac{\partial}{\partial x} \\ \frac{\partial}{\partial y} \\ \frac{\partial}{\partial z} \\ \frac{\partial}{\partial t} \end{bmatrix} = \underbrace{\begin{bmatrix} \xi_x & \eta_x & \varsigma_x & 0 \\ \xi_y & \eta_y & \varsigma_y & 0 \\ \xi_z & \eta_z & \varsigma_z & 0 \\ \xi_t & \eta_t & \varsigma_t & 1 \end{bmatrix}}_{A} \begin{bmatrix} \frac{\partial}{\partial \xi} \\ \frac{\partial}{\partial \eta} \\ \frac{\partial}{\partial \varsigma} \\ \frac{\partial}{\partial \tau} \end{bmatrix} \Leftrightarrow \begin{bmatrix} \frac{\partial}{\partial \xi} \\ \frac{\partial}{\partial \eta} \\ \frac{\partial}{\partial \varsigma} \\ \frac{\partial}{\partial \tau} \end{bmatrix} = \underbrace{\begin{bmatrix} x_\xi & y_\xi & z_\xi & 0 \\ x_\eta & y_\eta & z_\eta & 0 \\ x_\varsigma & y_\varsigma & z_\varsigma & 0 \\ x_\tau & y_\tau & z_\tau & 1 \end{bmatrix}}_{B} \begin{bmatrix} \frac{\partial}{\partial x} \\ \frac{\partial}{\partial y} \\ \frac{\partial}{\partial z} \\ \frac{\partial}{\partial t} \end{bmatrix} \tag{9}$$

For convenience, we further define the Jacobian of the transformation metrics as

$$\frac{1}{J} = \|B\| = x_\xi\left(y_\eta z_\varsigma - y_\varsigma z_\eta\right) - x_\eta\left(y_\xi z_\varsigma - y_\varsigma z_\xi\right) + x_\varsigma\left(y_\xi z_\eta - y_\eta z_\xi\right). \tag{10}$$

With the coordinate transformation in place, the governing equations can be rewritten in $(\xi,\eta,\varsigma,\tau)$ coordinate system into the following format:

$$\frac{1}{J}\frac{\partial U}{\partial \tau}+\frac{\partial \hat{F}_1}{\partial \xi}+\frac{\partial \hat{F}_2}{\partial \eta}+\frac{\partial \hat{F}_3}{\partial \varsigma}+U\frac{\partial\left(\frac{1}{J}\right)}{\partial \tau}=0. \tag{11}$$

And, the flux terms, $\hat{F}$, are related to the flux terms in Cartesian system, F , by

$$\hat{F}_i=\frac{1}{J}\frac{\partial \xi_i}{\partial x_j}F_j+\frac{1}{J}\frac{\partial \xi_i}{\partial t}U\,, \tag{12}$$

where the $\frac{\partial \xi_i}{\partial x_j}$ terms are calculated using the Jacobian in the following equations.

$$\begin{cases}\xi_x=J\left(y_\eta z_\varsigma-y_\varsigma z_\eta\right)\\ \xi_y=J\left(x_\varsigma z_\eta-x_\eta z_\varsigma\right)\\ \xi_z=J\left(x_\eta y_\varsigma-x_\varsigma y_\eta\right)\end{cases}\quad \begin{cases}\eta_x=J\left(y_\varsigma z_\xi-y_\xi z_\varsigma\right)\\ \eta_y=J\left(z_\varsigma x_\xi-z_\xi x_\varsigma\right)\\ \eta_z=J\left(x_\varsigma y_\xi-x_\xi y_\varsigma\right)\end{cases}\quad \begin{cases}\varsigma_x=J\left(y_\xi z_\eta-y_\eta z_\xi\right)\\ \varsigma_y=J\left(z_\xi x_\eta-z_\eta x_\xi\right)\\ \varsigma_z=J\left(x_\xi y_\eta-x_\eta y_\xi\right)\end{cases} \tag{13}$$

The $\frac{\partial \xi_i}{\partial t}$ terms are all zero except for η_t, which changes as the shock moves.

$$\eta_t=-J\left[x_\tau\left(\frac{\eta_x}{J}\right)+y_\tau\left(\frac{\eta_y}{J}\right)+z_\tau\left(\frac{\eta_z}{J}\right)\right] \tag{14}$$

These coordinate transformation formulas are generally applicable to any computations using shock-fitting method. It can be easily adapted to any flow geometry like flat plate, wedge or airplane wing. The advantage is to reduce the complexity to modify the numerical scheme formulations for a specific grid setup. With the coordinate transformations, we can apply non-uniform grids to increase the resolution in the area where the flow physics is critical to current research without a whole lot of efforts in code modification.

2.3. Shock-fitting Method

The high-order shock-fitting scheme is modified from the one originally developed by Zhong [45] to accommodate a newly developed fresstream pulse model used for the receptivity simulation of freestream wave disturbance in current study. The advantage of this method as compared to traditional shock capturing method is that, it can achieve uniform high-order, so that the shock location can be accurately located. The shock-fitting method treats the shock as the boundary of numerical simulation domain so that the discontinuity across the shock is avoided. The shock variables, namely shock height and shock speed, coupled with flow variables behind the shock are solved by Rakine-Hugoniot relation and the characteristic compatibility relation.

The Rakine-Hugoniot relation in the direction normal to the shock boundary can be written as:

$$\left(\vec{F}_s-\vec{F}_\infty\right)\cdot\vec{l}_s+\left(U_s-U_\infty\right)l_t=0 \quad \text{where}\begin{cases}\vec{l}_s=\dfrac{\left(\eta_x,\eta_y,\eta_z\right)}{J}\\ l_t=\dfrac{\eta_t}{J}\end{cases} \tag{15}$$

s denotes the quantity behind shock and ∞ denotes the quantity in front of shock. F is the flux vector along the η grid line. The jump conditions across the shock can be computed by the following equations:

$$p_s=p_\infty\left[1+\frac{2\gamma}{\gamma+1}\left(M_{n\infty}^2-1\right)\right], \tag{16}$$

$$\rho_s = \rho_\infty \left[\frac{(\gamma+1)M_{n\infty}^2}{(\gamma-1)M_{n\infty}^2 + 2} \right], \tag{17}$$

$$u_{ns} = v_n + \frac{\rho_\infty}{\rho_s}(u_{n\infty} - v_n), \tag{18}$$

$$\vec{u}_s = \vec{u}_\infty + (u_{ns} - u_{n\infty})\vec{n}, \tag{19}$$

$$\vec{u}_{ts} = \vec{u}_\infty - u_{n\infty}\vec{n}. \tag{20}$$

In the above equations, if the shock speed, v_n, is given, the other flow variables behind the shock can be computed. The shock normal velocity, v_n, can be obtained from the characteristic compatibility relation behind the shock. Apply compatibility relation to eq. (11), we get

$$\vec{L} \cdot \frac{\partial U}{\partial \tau} = -\vec{L} \cdot \left(\frac{\partial \hat{F}_1}{\partial \xi} + \frac{\partial \hat{F}_2}{\partial \eta} + \frac{\partial \hat{F}_3}{\partial \varsigma} + U \frac{\partial\left(\frac{1}{J}\right)}{\partial \tau} \right) J, \tag{21}$$

where $\vec{L}$ is the left eigenvector for the corresponding eigenvalue $\lambda = u_n - \mathrm{v}_{\mathrm{gn}} + c$ of Jacobian matrix $B = \partial\vec{F} / \partial\vec{U}$ right behind the shock.

$$\vec{L} = \frac{1}{c^2} \begin{bmatrix} \frac{\gamma-1}{2}\vec{u}\cdot\vec{u} - cu_n \\ -\left(\frac{1}{2}cn_x - \frac{\gamma-1}{2}u\right) \\ -\left(\frac{1}{2}cn_y - \frac{\gamma-1}{2}v\right) \\ -\left(\frac{1}{2}cn_z - \frac{\gamma-1}{2}w\right) \\ \frac{\gamma-1}{2} \end{bmatrix}_s . \tag{18}$$

By taking the derivative of Rakine-Hugoniot relation and apply the compatibility relation, the equation becomes:

$$\left[-\vec{L}\cdot(U_s-U_\infty)\right]\frac{\partial l_t}{\partial\tau}=\left[\frac{\|\nabla\eta\|}{J}(u_n-\mathrm{v}_{\mathrm{gn}}+c)\vec{L}\left(\frac{\partial U_s}{\partial\tau}\right)\right]+\vec{L}\cdot\left[\vec{F}_s-\vec{F}_\infty\right]\cdot\frac{\partial\vec{l}_s}{\partial\tau}-\vec{L}\cdot A'_\infty\left(\frac{\partial U_\infty}{\partial\tau}\right), \qquad (22)$$

Where A'_{s} can be expanded into

$$A'_{\mathrm{s}}=\left[\left(\frac{\partial F_1}{\partial U}\right)\left(\frac{\eta_x}{J}\right)+\left(\frac{\partial F_2}{\partial U}\right)\left(\frac{\eta_y}{J}\right)+\left(\frac{\partial F_3}{\partial U}\right)\left(\frac{\eta_z}{J}\right)+I\left(\frac{\eta_t}{J}\right)\right]. \qquad (23)$$

In eq. (22), v_{gn} is the velocity for the grid point at the shock in the shock normal direction. $\frac{\partial l_t}{\partial\tau}$ can be related to the shock acceleration, $H_{\tau\tau}$, by $\frac{\partial l_t}{\partial\tau}=aH_{\tau\tau}+b$, where *a* and *b* can be computed from grid metrics. And, $\frac{\partial U_s}{\partial\tau}$ can be calculated from eq. (11) in section 2.2. Finally, at the shock boundary point, the following system of ODEs is solved simultaneously at each simulation time step.

$$\left\{\begin{array}{l} \dfrac{\partial U_s}{\partial\tau}=-J\left[\dfrac{\partial F_1}{\partial\xi}+\dfrac{\partial F_2}{\partial\eta}+\dfrac{\partial F_3}{\partial\varsigma}+U\dfrac{\partial\left(\frac{1}{J}\right)}{\partial\tau}\right] \\ \dfrac{\partial H_\tau}{\partial\tau}=H_{\tau\tau}=f\left(U_s,U_\infty\dfrac{\partial U_s}{\partial\tau},H,H_\xi,H_\varsigma,H_\tau\right) \\ \dfrac{\partial H}{\partial\tau}=H_\tau \end{array}\right. \qquad (24)$$

In eq. (24), the *H* is the shock height measured normal to the cone surface. The first equation in the system of ODEs is the symbolic representation of another system of equations that are used to solve for the flow variables in the interior grid points.

2.4. High-order Finite Difference Method

In order to achieve high accuracy results in steady base flow solution and receptivity simulation, low dissipation numerical scheme is required. Especially for the receptivity simulation, the wave perturbation is usually very small. Low-order finite difference scheme is so dissipative that the perturbation could be damped out numerical. Therefore, in solving the governing equations, the spatial derivative terms are treated using high-order finite difference scheme with the exception in the spanwise direction. The derivatives in spanwise direction of the cone are calculated using Fourier spectral method due to its periodic nature. In our program, we use fifth-order upwind scheme on the inviscid flux terms and sixth-order central difference scheme on the viscous flux terms.

To calculate the spatial derivatives of inviscid flux, $\frac{\partial \hat{F}_i}{\partial \xi_j}$ in the governing equations, the Lax-Friedrichs flux splitting scheme is utilized. This flux split scheme splits the flux term into two terms corresponding to its positive and negative eigenvalues. Hence, the inviscid flux can be written into

$$\vec{F} = \vec{F}_+ + \vec{F}_- . \tag{25}$$

For simplicity, the eigenvalue is chosen so that it is always equal or greater than its local maximum eigenvalue of $\vec{F}$ as shown below:

$$\lambda = \frac{\left|\nabla \eta\right|}{J}\left(\sqrt{\left(\varepsilon c\right)^2 + u^2} + c\right) \tag{26}$$

The parameter ε is inserted to ensure the smoothness of the flux splitting. c is the speed of sound at the grid point; and u can be computed using the following equation:

$$u = \frac{\eta_x u + \eta_y v + \eta_z w + \eta_t}{\left| \nabla \eta \right|}. \tag{27}$$

Once the λ is determined, the inviscid flux can be split as

$$\vec{F}_+ = \frac{1}{2}\left(\vec{F} + \lambda \vec{U} \right) \tag{28}$$

$$\vec{F}_+ = \frac{1}{2}\left(\vec{F} - \lambda \vec{U} \right) \tag{29}$$

So that the $\vec{F}_+$ flux vector only contains positive eigenvalue and $\vec{F}_-$ term only contain negative eigenvalue. After the flux is split, the derivative is taken on each term individually. The $\frac{\partial \hat{F}_{+i}}{\partial \xi_j}$ is approximated using 7 points upwind stencil finite difference formula and similarly, the $\frac{\partial \hat{F}_{-i}}{\partial \xi_j}$ is approximated using 7 points downwind stencil finite difference formula. The explicit equation is provided as following:

$$\frac{\partial q}{\partial \xi}_i = \frac{1}{hb_i} \sum_{j=-3}^{3} a_{i+j} q_{i+j} + \text{H.O.T}, \tag{30}$$

Where the coefficients for finite difference scheme are provided as:

$$\begin{cases} a_{i\pm 3} = \pm 1 + \frac{1}{12}\beta \\ a_{i\pm 2} = \mp 9 - \frac{1}{2}\beta \\ a_{i\pm 1} = \pm 45 + \frac{5}{4}\beta \\ a_i = -\frac{5}{3}\beta \\ b_i = 60 \end{cases} . \tag{31}$$

h is the spatial grid size, which is always 1 in transformed coordinate. H.O.T is the acronym for higher order terms, which is ignored without affecting the order of accuracy of numerical scheme. β is a free parameter used to control the weight of the upwind scheme. The optimal value of β is determined experimentally so that the solution is less dissipative but at the same time numerically stable enough. β needs to be a negative number to make eq. (30) a upwind scheme.

The viscous flux terms contain second order derivative and the following six-order central difference scheme is deployed:

$$\frac{\partial^2 q}{\partial \xi^2}_i = \frac{1}{ch^2}\sum_{j=-3}^{3} b_{i+j} q_{i+j} + \mathrm{H.O.T}, \tag{32}$$

Where

$$\begin{cases} b_{i\pm 3} = 1 \\ b_{i\pm 2} = -\frac{17}{2} \\ b_{i\pm 1} = 135 \\ b_i = -245 \\ c = 90 \end{cases} . \tag{33}$$

With this high-order finite difference scheme for all the interior grid points and the high-order shock-fitting scheme for the points along the shock boundary, a unified high-order numerical simulation code is set up.

The time advancement is calculated by Runge-Kutta method. Both RK-1 and RK-3 are implemented in current program. Further investigation reveals minimal accuracy improvement using RK-3 over RK-1 mainly because the flow stability requirement overwhelms the numerical stability requirement for time step. Therefore, only RK-1 is used for all the simulations. This high-order simulation program serves as the cornerstone for a series of receptivity and stability simulation studies over variety of test cases with different geometries and flow conditions; and has been proven successfully and accurately on those studies [13, 14, 16, 17, 19, 20, 51-57].

2.5. Linear Stability Theory

The linear stability theory (LST) is used to perform theoretical study of the instability modes in the boundary layer of hypersonic flow over blunt cones in this paper. The linear stability equations used to solve for the theoretical stability mode solutions are derived from the full Navier-stoke equations as presented in eq. (1). Further, we represented the flow solutions by their mean value and perturbations as shown below:

$$q = \bar{q}(x,y,z) + \tilde{q}(x,y,z,t). \tag{34}$$

Where $q = \langle u,v,w,p,T,\rho,\mu,K \rangle$. $\bar{q}$ is the steady base flow value of flow filed and $\tilde{q}$ is the linear perturbation of flow variable which is time dependent. If eq. (34) is substituted into eq. (1), the mean flow solution can be cancelled out. The remaining terms in the equations can be linearized by dropping the higher order perturbation terms and written into:

$$\begin{aligned}(\frac{\partial\tilde{u}}{\partial t}+U\frac{\partial\tilde{u}}{\partial x}+\tilde{v}\frac{dU}{dy}+W\frac{\partial\tilde{u}}{\partial z})/T=-\frac{\partial\tilde{p}}{\partial x}+\frac{\mu}{\mathrm{Re}}\Bigg[&l_2\frac{\partial^2\tilde{u}}{\partial x^2}+l_1\left(\frac{\partial^2\tilde{v}}{\partial x\partial y}+\frac{\partial^2\tilde{w}}{\partial x\partial z}\right)\\&+\frac{\partial^2\tilde{u}}{\partial y^2}+\frac{\partial^2\tilde{u}}{\partial z^2}+\frac{1}{\mu}\frac{d\mu}{dT}\frac{dT}{dy}\left(\frac{\partial\tilde{u}}{\partial y}+\frac{\partial\tilde{v}}{\partial x}\right)\\&+\frac{1}{\mu}\frac{d\mu}{dT}\left(\frac{\partial^2U}{\partial y^2}\tilde{T}+\frac{dU}{dy}\frac{\partial\tilde{T}}{\partial y}\right)+\frac{1}{\mu}\frac{d^2\mu}{dT^2}\frac{dT}{dy}\frac{dU}{dy}\tilde{T}\Bigg]\end{aligned}\tag{35}$$

$$\begin{aligned}(\frac{\partial\tilde{v}}{\partial t}+U\frac{\partial\tilde{v}}{\partial x}+W\frac{\partial\tilde{v}}{\partial z})/T=-\frac{\partial\tilde{p}}{\partial y}+\frac{\mu}{\mathrm{Re}}\Bigg[&\frac{\partial^2\tilde{v}}{\partial x^2}+l_1\left(\frac{\partial^2\tilde{u}}{\partial x\partial y}+\frac{\partial^2\tilde{w}}{\partial x\partial z}\right)\\&+l_2\frac{\partial^2\tilde{v}}{\partial y^2}+\frac{\partial^2\tilde{v}}{\partial z^2}+\frac{1}{\mu}\frac{d\mu}{dT}\left(\frac{\partial\tilde{T}}{\partial x}\frac{\partial U}{\partial y}+\frac{\partial\tilde{T}}{\partial z}\frac{\partial W}{\partial y}\right)\\&+\frac{1}{\mu}\frac{d\mu}{dT}\frac{dT}{dy}\left\{l_0\left(\frac{\partial\tilde{u}}{\partial x}+\frac{\partial\tilde{w}}{\partial z}\right)+l_2\frac{\partial\tilde{v}}{\partial y}\right\}\Bigg]\end{aligned}\tag{36}$$

$$\begin{aligned}(\frac{\partial\tilde{w}}{\partial t}+U\frac{\partial\tilde{w}}{\partial x}+\tilde{v}\frac{dW}{dy}+W\frac{\partial\tilde{w}}{\partial z})/T=-\frac{\partial\tilde{p}}{\partial z}+\frac{\mu}{\mathrm{Re}}\Bigg[&\frac{\partial^2\tilde{w}}{\partial x^2}+l_1\left(\frac{\partial^2\tilde{u}}{\partial x\partial z}+\frac{\partial^2\tilde{v}}{\partial y\partial z}\right)\\&+\frac{\partial^2\tilde{w}}{\partial y^2}+l_2\frac{\partial^2\tilde{w}}{\partial z^2}+\frac{1}{\mu}\frac{d\mu}{dT}\frac{dT}{dy}\left(\frac{\partial\tilde{v}}{\partial z}+\frac{\partial\tilde{u}}{\partial y}\right)\\&+\frac{1}{\mu}\frac{d\mu}{dT}\left(\frac{\partial^2W}{\partial y^2}\tilde{T}+\frac{dW}{dy}\frac{\partial\tilde{T}}{\partial y}\right)+\frac{1}{\mu}\frac{d^2\mu}{dT^2}\frac{dT}{dy}\frac{dW}{dy}\tilde{T}\Bigg]\end{aligned}\tag{37}$$

$$\begin{aligned}\frac{\gamma M^2}{T}\frac{\partial\tilde{p}}{\partial t}-\frac{1}{T^2}\frac{\partial\tilde{T}}{\partial t}+\frac{1}{T}\frac{\partial\tilde{u}}{\partial x}+U\left(\frac{\gamma M^2}{T}\frac{\partial\tilde{p}}{\partial x}-\frac{1}{T^2}\frac{\partial\tilde{T}}{\partial x}\right)&\\+\frac{1}{T}\frac{\partial\tilde{u}}{\partial y}-\frac{1}{T^2}\frac{\partial\tilde{T}}{\partial y}\tilde{v}+\frac{1}{T}\frac{\partial\tilde{w}}{\partial z}+W\left(\frac{\gamma M^2}{T}\frac{\partial\tilde{p}}{\partial z}-\frac{1}{T^2}\frac{\partial\tilde{T}}{\partial z}\right)&=0\end{aligned}\tag{38}$$

$$\begin{aligned}\left(\frac{\partial \tilde{T}}{\partial t}+U\frac{\partial \tilde{T}}{\partial x}+\tilde{v}\frac{\partial \tilde{T}}{\partial y}+W\frac{\partial \tilde{T}}{\partial z}\right)/T &= (\gamma-1)M^{2}\left[\frac{\partial \tilde{p}}{\partial t}+U\frac{\partial \tilde{p}}{\partial x}+W\frac{\partial \tilde{p}}{\partial z}\right]\\ &+\frac{\mu}{\mathrm{Re}\,\sigma}\left[\frac{\partial^{2}\tilde{T}}{\partial x^{2}}+\frac{\partial^{2}\tilde{T}}{\partial y^{2}}+\frac{\partial^{2}\tilde{T}}{\partial z^{2}}+\frac{2}{k}\frac{dk}{dT}\frac{dT}{dy}\frac{\partial \tilde{T}}{\partial y}\ldots\right.\\ &\left.\ldots+\left(\frac{1}{k}\frac{dk}{dt}\frac{d^{2}T}{dy^{2}}+\frac{1}{k}\frac{d^{2}k}{dT}\left(\frac{dT}{dy}\right)^{2}\right)\tilde{T}\right]\\ &+(\gamma-1)M^{2}\frac{\mu}{\mathrm{Re}}\left[2\frac{dU}{dy}\left(\frac{\partial \tilde{u}}{\partial y}+\frac{\partial \tilde{v}}{\partial x}\right)\ldots\right.\\ &\left.\ldots+2\frac{dW}{dy}\left(\frac{\partial \tilde{w}}{\partial y}+\frac{\partial \tilde{v}}{\partial z}\right)+\frac{1}{\mu}\frac{d\mu}{dT}\left(\left(\frac{dU}{dy}\right)^{2}+\left(\frac{dW}{dy}\right)^{2}\right)\right]\end{aligned} \qquad (39)$$

Where $l_i = i - \lambda/\mu$. To apply the LST, the perturbation amplitudes are assumed to be small so that they do not interact non-linearly with each other. The normal mode of a disturbance is assumed to have the following form:

$$\tilde{q} = \hat{q}(y_n)e^{i(-\omega t+\alpha s)} \qquad (40)$$

where $\tilde{q}$ can be any dimensionless flow variable such as velocities, temperature, density and pressure, all of which are normalized by the freestream quantities. $\hat{q}$ is the mode structure representing the complex amplitude of the disturbance. The eigenfunction is considered a function of y only because for the boundary layer flow, the wavelength in streamwise direction is much shorter that in wall-normal direction so that the variations in streamwise direction is ignored. In the spatial stability theory, ω , the dimensionless angular frequency of a normal disturbance mode, is set to be a real number. $\alpha = \alpha_r + i\alpha_i$ is the stream-wise complex wave number non-dimensionalized by L^* . The imaginary part of wave number represents the spatial growth rate of a specific disturbance mode. When α_i is negative, the disturbance becomes unstable. The real part of wave number α_r is the spatial wave number. By substituting eq. (40) into eq. (35)-(39), the system of equations can be reduced into a matrix form:

$$(AD^2 + BD + C)\Phi = 0 \tag{41}$$

And $\Phi = [\hat{u}, \hat{v}, \hat{p}, \hat{T}, \hat{w}]$. Also, in the matrix notation D=d/dy. A, B and C are matrices that turn the system of equations into an eigenvalue problem. In our LST code, we use a multi-domain spectral method that was originally derived by Malik [58] to solve for the eigenvalue and its corresponding eigenvector.

An important quantity that can be extracted from α_r is the non-dimensional phase velocity, which is defined as

$$a = \frac{\omega}{\alpha_r} = \frac{FR}{\alpha_r} \tag{42}$$

In the above equation, the dimensionless phase velocity, a, is normalized by the free-stream velocity. F is the dimensionless frequency that is related to the dimensional angular frequency by,

$$F = \frac{\omega^* \upsilon_\infty^*}{u_\infty^{*2}} \tag{43}$$

R is local Reynolds number based on the length scale of boundary layer thickness and s^* is the curvilinear coordinate along the cone surface as measured from the nose.

$$R = \frac{\rho_\infty^* u_\infty^* L^*}{\mu_\infty^*} \tag{44}$$

$$L^* = \sqrt{\frac{\mu_\infty^* s^*}{\rho_\infty^* U_\infty^*}} \tag{45}$$

One of the most common applications of LST analysis in predicting the laminar-turbulent transition is to calculate the N factor based on a semi-empirical method called the e^N method. According to the theory, when the amplification of the disturbances reaches certain levels, transition will occur. The ratio of the amplitude of disturbance waves with a fixed frequency can be calculated as they travel downstream. Since the growth rate varies from location to location, the amplitude ratio between two locations can be expressed as the following integral:

$$e^N = \frac{A}{A_0} = \exp\int_{s_0^*}^{s^*} \frac{1}{A}\frac{dA}{ds} ds^* \tag{46}$$

or, just for the N factor,

$$N = \int_{s_0^*}^{s^*} -\alpha_i^* ds^* \tag{47}$$

In eq. (46), s_0^* corresponds to the location that the disturbance just becomes neutrally stable (also called branch I instability point). By computing this integral, we know how much the amplitude for a specific disturbance changes as it moves downstream. On the other hand, the N factor leading to transition is correlated to the experimental measurement. The N factor is not unique for all the cases: it depends on the flow conditions, object geometry, amplitude of freestream disturbance and other unknown parameters.

Even in one single case, the N factor differs when different unstable modes are considered. Here, the different unstable modes refer to the first mode and the second mode introduced by Mack [59]. In general, the N factor for the first mode is smaller than the one for the second mode. It should be noted the main focus of the paper is on the stability and N-factor calculations of the two-dimensional (axisymmetric) second mode for the current test case. Even though the three-dimensional first-mode instability is responsible for the transition at a lower Mach number flow, extensive theoretical analysis, numerical simulations and experiments have shown that, for higher Mach number flows ($M > 4$), the axisymmetric second-mode instability is the most dominant unstable mechanism in the hypersonic boundary layer [23, 60]. The current paper only focuses on the second-mode instability, which is most amplified when the disturbance is axisymmetric [59, 61].

2.6. New Three-Step Approach to Link Receptivity and Breakdown Simulations

Currently, a complete direct numerical simulation that computes hypersonic boundary layer flow from freestream wave receptivity all the way to transition is considered impossible due to the limitation on computation power. We propose to tackle this problem by using an innovative approach that separates the linear receptivity simulation from the nonlinear breakdown simulation. By this way, we are able to make the computational cost manageable through breaking the whole simulation study into three steps. The schematic of the simulation procedure is presented in Fig. 4 shown below.

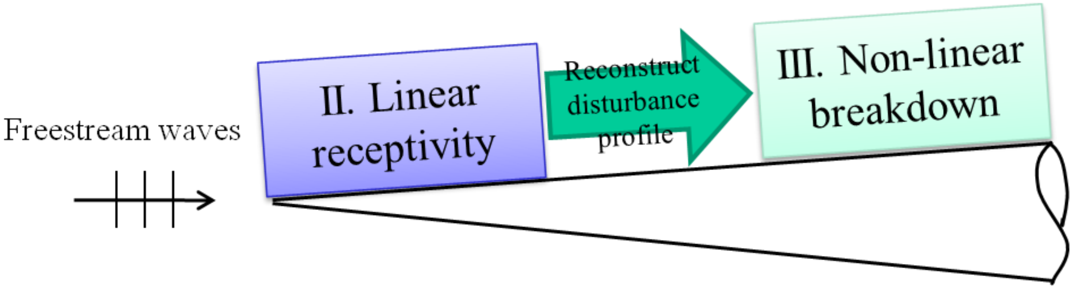

Fig. 4. Schematic of proposed simulation procedures to non-linear breakdown.

- **Step I: Meanflow Calculation**. The high accuracy mean flow solution without any freestream disturbance is obtained using our high-order shock-fitting code. This is done with multiple zone approach that partitions the whole computational domain into many subzones along the cone surface into shorter subzones and marching the solution downstream as long as we needed. Once the meanflow solution is obtained, we can apply linear stability theory to study the stability property of flow and determine the relevant frequency range of the unstable modes that need to be captured in the subsequent linear receptivity simulations.

- **Step II: Linear Receptivity Simulation.** In step two, the linear receptivity simulations are carried out using different types of freestream disturbances: fast acoustic wave, slow acoustic wave, entropy wave, or vorticity wave. The disturbance waves are imposed into the freestream flow in front of the shock. In the receptivity simulation of each type of freestream wave disturbance, multiple frequencies are imposed to cover the complete freestream wave disturbance spectrum. Depending on what model is used, the disturbance spectrum can be either discrete or continued. More detail will be provided when the freestream wave models are introduced in next chapter. Because different type of freestream wave behaves differently during the receptivity process. It is recommended to just use one type of disturbance in each receptivity simulation. Since the imposed wave is linear, the receptivity results can always be superimposed later to represent the aggregated response of all types of disturbance waves imposed simultaneously.

The receptivity simulation will be carried all the way to the end of the linear growth region, where substantial second-mode instability can be observed. This flow unstable location can be estimated by LST analysis or by investigation of simulation result. From the linear theory, it has been proven that the most dominant unstable second modes are two-dimensional wave in nature. That means the unstable modes potentially responsible for flow transition can be captured using 2-D receptivity simulation. Ideally, the 3-D receptivity simulation should be more appropriated. But the 2-D linear receptivity simulation is computationally much less expensive than the full scale 3-D linear simulation due to the fact that disturbance wave in the simulation is axis-symmetric. So, a 2-D simulation with significant less number of grid points is sufficient. At the exit of receptivity simulation, the receptivity response is collected. This information will be used as inflow conditions for the nonlinear breakdown simulation in step III.

- **Step III: Nonlinear Breakdown Simulation**. The goal of nonlinear breakdown simulation is to understand how the real freestream disturbance wave leads to the breakdown in transition. Therefore, upon completion of the receptivity simulation, the inflow disturbance for the 3-D nonlinear simulation is re-constructed based on the receptivity response library obtained from the linear simulation to represent the actual freestream disturbance spectrum. The inflow boundary condition is obtained from the preceding linear receptivity simulations. Fourier decomposition is applied to decompose the disturbance waves into frequency spectrum. The inflow disturbance can be from freestream fast/slow acoustic wave, entropy waves or combination of all. The detail formulations are presented here to illustrate how this inflow profile reconstruction is performed on a 2-D receptivity simulation. The formulations can be easily extended to 3-D case as well.

  At the exit of receptivity simulation, the flow quantity time histories are recorded at N uniformly spaced sampling times at the last grid points in the streamwise direction. At each grid point, any flow quantity can be represented by

$$q(x_{exit,} y_{exit}, t) = q_k(t) . \tag{48}$$

Discrete time Fourier decomposition is applied to transform the time signal into frequency domain. The transform frequency spectrum can be represented by

$$Q(\omega_n) = \Delta \sum_{k=0}^{N-1} q_k e^{i\omega_n t_k} \quad . \tag{49}$$

In the above equation, Δ is the time step and ω_n is the angular frequency of the disturbance wave. The amplitude and phase angle of each ω_n can be obtained:

$$|Q_n| = abs(Q(\omega_n)) = \sqrt{\mathrm{Re}(Q(\omega_n))^2 + \mathrm{Im}(Q(\omega_n))^2} \tag{50}$$

$$\angle Q(\omega_n) = \phi_n = \tan^{-1}\left(\frac{\mathrm{Im}(Q(\omega_n))}{\mathrm{Re}(Q(\omega_n))}\right) \tag{51}$$

The inflow profile can be reconstructed using the $Q(\omega_n)$ information from the exit of previous computation domain. If the desired spectrum is given as $Q_D(\omega_n)$ and the actual spectrum is given as $Q_a(\omega_n)$, define

$$\alpha_n = \frac{|Q_D(\omega_n)|}{|Q_a(\omega_n)|} \text{ and } \beta_n = \angle Q_D(\omega_n) - \angle Q_a(\omega_n) \tag{52}$$

for n=0, N/2. So that,

$$q(t) = \frac{\sigma}{N} \sum_{n=0}^{N/2} \left\{ \alpha_n |Q_n| \left[\cos(\omega_n t + \beta_n) \right] \right\}, \quad \sigma = \begin{cases} 0.5, n = 0 \\ 1, \ others \end{cases} . \tag{53}$$

Using these formulations, a more realistic disturbance profile can be constructed to represent those from typical experiments. Since the Fourier transform in time can be applied to decompose the receptivity response in linear region into frequency components, we can re-scale the magnitude of wave disturbance for each frequency to match the freestream wave disturbance spectrum in a typical experiment. Therefore, the complete transition process due to different freestream disturbance profiles can be simulated by using single receptivity simulation results. Therefore, we just need to do the receptivity simulation in step II once for different freestream spectra and different disturbance amplitudes. As a result, for various freestream disturbance profiles, step III is repeated to investigate the effects of freestream disturbance levels on the location of boundary layer transition.

3. Computation Cases and Setup

In this chapter, the detail of flow conditions used in present study and the computation implementations for each research topics are provided. As the first simulation case, the flow conditions from Stetson's Mach 5.5 transition experiment conducted in 1967 is utilized. In this experiment, the transition locations were measured on a series of cone models with a wide range of nose bluntness, which make this case a good candidate for nose bluntness effects study. Cone models with 3 different nose radii are computed. However, this experiment lacked of detail stability measurement therefore it is hard to correlate with the current numerical results. Because of this shortfall, we decide to adopt flow conditions from more recent experiments that are actively studied by other research groups. The TAMU Mach 6 quiet tunnel experiment is the best fit because many numerical and theoretical studies have been performed based on these flow conditions and test models. Two cone models are computed with two different nose radii and cone shapes.

For the receptivity and breakdown simulation studies, two different freestream wave models are deployed. The first one is a discrete-frequency model that superimposes the simple harmonic waves from freestream at selected wave frequencies. This model is very effective in the receptivity and stability study, but fails to provide the continued frequency response information that is needed for subsequent breakdown study. Therefore, a Gaussian pulse model is devised to account for the need to capture the continued frequency response during the freestream receptivity process. Due to difference in the two freestream wave models, the computation setups for both receptivity and breakdown simulation are adjusted accordingly to complete the numerical studies. The implementations are entailed in subsequent sections.

3.1. Flow Conditions of Stetson's Mach 5.5 Case

In this paper, we use the flow conditions from Stetson's Mach 5.5 experiment [62] to study the nose bluntness effects on hypersonic boundary layer transition. LST analysis has been performed on circular blunt cones of three different nose radii [63]. The specific flow conditions are:

- $M_\infty = 5.468$
- $P_\infty^* = 7756.56\,Pa$, $T_\infty^* = 174.46K$
- Wall temperature: $T_w = 296K$
- $\gamma = 1.4$, $\mathrm{Pr} = 0.72$, $R^* = 286.94Nm/kgK$
- Freestream unit Reynolds number: $\mathrm{Re}_\infty^* = 18.95 \times 10^6 m^{-1}$
- Blunt cone half angle: $\theta = 8^\circ$, the freestream flow has a zero angle of attack
- Parameters in Sutherland's viscosity law: $T_r^* = 288K$, $T_s^* = 110.33K$,

$$\mu_r^* = 0.17894 \times 10^{-4} kg/ms$$

In this paper, we simulate both the steady meanflow and the receptivity due to freestream wave on cone models with nose radii of 0.156, 0.5 and 1.5 inches. We also use the cone with nose radius of 0.156 inch for code testing purpose on the 3-D nonlinear breakdown simulation.

3.2. Flow Conditions of TAMU Mach 6 Case

In the effort to collaborate with National Center of Hypersonic Laminar-turbulent Transition Research at Texas A&M university, we continue our numerical studies using the flow conditions and cone models that the experimental team at TAMU used to develop their Mach 6 quiet tunnel, such that the experiment and simulation can assist each other on their way to attain a better understanding of the hypersonic boundary layer transition. Fig. 5 shows the drawing of the flared cone model used by TAMU team on its Mach 6 quiet tunnel. The nominal flow conditions are listed below:

- $M_\infty = 5.91$
- $P_\infty^* = 622.84 Pa$, $T_\infty^* = 56.35K$
- Wall temperature: $T_w =$ adibatic wall
- $\gamma = 1.4$, $\Pr = 0.72$, $R^* = 286.94 Nm/kgK$
- Freestream unit Reynolds number: $\mathrm{Re}_\infty^* = 9.25 \times 10^6 m^{-1}$
- Blunt cone half angle: $\theta = 5^\circ$, the freestream flow has a zero angle of attack

- Parameters in Sutherland's viscosity law: $T_r^* = 288K$, $T_s^* = 110.33K$,

$$\mu_r^* = 0.17894 \times 10^{-4} kg / ms \ .$$

Using the cone geometry provided by TAMU quiet tunnel experiment team, we perform the meanflow calculations on both a flared cone with 0.125 inch nose radius and a straight cone with 0.1mm nose radius. The Flared cone case has the exact geometry as in Fig. 5. The straight cone case has a much small nose radius compared to straight cone; and the cone is straight all the way to the end of cone model.

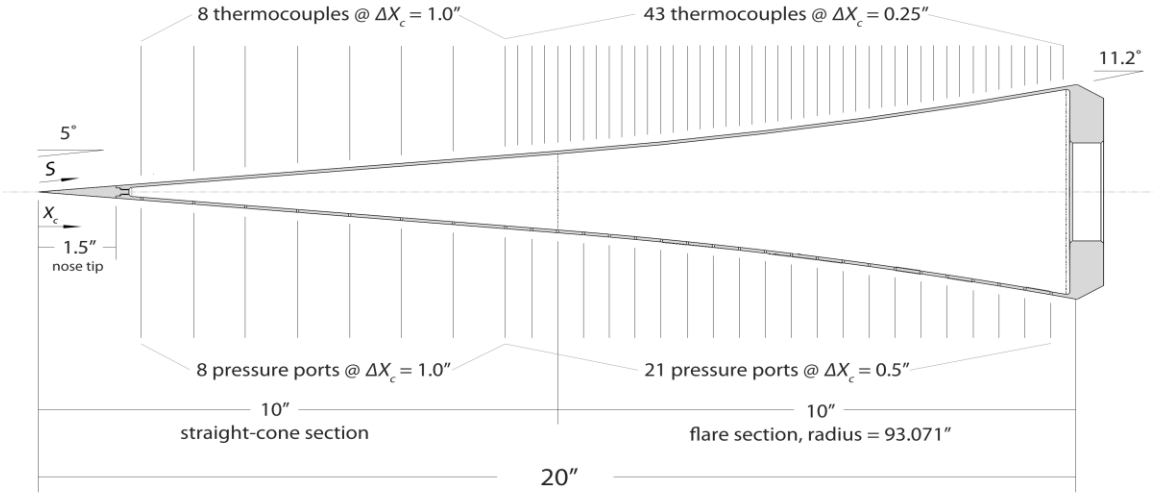

Fig. 5. Schematic of flared cone model for TAMU Mach 6 quiet tunnel.

3.3. Freestream Discrete Frequency Model

For the Stetson's Mach 5.5 case, a discrete frequency freestream disturbance model was used. In this model, it assumes that a planner wave comes from far away that contains finite number of frequency components. The disturbance can be fast acoustic, slow acoustic, entropy or vorticity wave in nature. In current receptivity simulation, the fast acoustic wave was used mainly because it is more efficient in exciting the boundary layer instability from previous study.

$$q(x,t) = \sum_{n=1}^{N} |q'|_n e^{i(k_n x - \omega_n t + \phi_n)}, \quad \text{where } q = \langle \rho, u, v, w, p \rangle \tag{54}$$

1) <u>Fast acoustic wave:</u> $c_\infty = u_\infty + a$

$$|s'| = |v'| = |w'| = 0 \quad \text{and} \quad |\rho'| = \frac{|p'|}{\gamma} = |u'| M_\infty = \varepsilon M_\infty$$

2) <u>Slow acoustic wave:</u> $c_\infty = u_\infty - a$

$$|s'| = |v'| = |w'| = 0 \quad \text{and} \quad |\rho'| = \frac{|p'|}{\gamma} = -|u'| M_\infty = \varepsilon M_\infty$$

3) <u>Entropy wave:</u> $c_\infty = u_\infty$

$$|u'| = |v'| = |w'| = |p'| = 0 \quad \text{and} \quad |\rho'| = -|s'| = \varepsilon M_\infty$$

4) <u>Vorticity wave:</u> $c_\infty = u_\infty$

$$|u'| = |w'| = |p'| = |s'| = 0 \quad \text{and} \quad |v'| M_\infty = \varepsilon M_\infty$$

In the streamwise direction, wave number and frequency can be related by $\omega_n = c_\infty k_n$, where c_∞ depends on the type of disturbance. For fast acoustic disturbance, $c_\infty = u_\infty + a$; for slow acoustic , $c_\infty = u_\infty - a$; and for entropy/vorticity disturbance, $c_\infty = u_\infty$.

This model is very easy to implement and can be changed to any desired type of disturbance wave. However, it is not realistic when there is a need to build a receptivity response library that ideally should contain all disturbance frequencies in a freestream. This drawback spurs us to develop a new and better freestream wave model for current research effort.

3.4. Freestream Gaussian Pulse Model

In the numerical study of hypersonic boundary layer transition from freestream receptivity to breakdown, we want to exam the linear receptivity response of freestream waves for a wide range of frequencies, so that a data base can be built to capture the freestream wave response for entire frequency spectrum. In order to do so, we introduce a Gaussian pulse that contains a continued frequency spectrum. Depending on the type of disturbance, The Gaussian pulse can be applied to acoustic wave, entropy wave and vorticity wave as well. The formula of the pulse is the following:

$$q(x,t) = |q'| \exp\left(-\frac{\left(X_0 + x - c_\infty t\right)^2}{\sigma^2} \right), \quad \text{where } q = \langle \rho, u, v, w, p \rangle \tag{55}$$

5) <u>Fast acoustic wave:</u> $c_\infty = u_\infty + a$

$$|s'| = |v'| = |w'| = 0 \quad \text{and} \quad |\rho'| = \frac{|p'|}{\gamma} = |u'| M_\infty = \varepsilon M_\infty$$

6) Slow acoustic wave: $c_\infty = u_\infty - a$

$$|s'| = |v'| = |w'| = 0 \quad \text{and} \quad |\rho'| = \frac{|p'|}{\gamma} = -|u'| M_\infty = \varepsilon M_\infty$$

7) Entropy wave: $c_\infty = u_\infty$

$$|u'| = |v'| = |w'| = |p'| = 0 \quad \text{and} \quad |\rho'| = -|s'| = \varepsilon M_\infty$$

8) Vorticity wave: $c_\infty = u_\infty$

$$|u'| = |w'| = |p'| = |s'| = 0 \quad \text{and} \quad |v'| M_\infty = \varepsilon M_\infty$$

In the streamwise direction, wave number and frequency can be related by $\omega_n = c_\infty k_n$. In eq.(55), σ is the parameter that uses to control the band width of the Gaussian pulse. c_∞ is the pulse transport velocity which varies to the type of disturbance. In the case of fast acoustic wave pulse, c_∞ equals to $(u_\infty + a)$. The advantage of using the Gaussian sharp pulse model is that the analytical solution exists; so that the freestream wave frequency band width can be decided easily. With all the freestream parameters given, the freestream wave spectrum can be represented by

$$Q(f_n) = \frac{|q'|\sqrt{\pi\sigma}}{\sqrt{c_\infty}} e^{\frac{-(\sigma\pi f_n)^2}{c_\infty^2}} \tag{56}$$

Fig. 6 shows the pulse as function of time for $\sigma = 0.0005$ and its frequency spectrum assuming unity wave amplitude. This is exactly the same pulse that is used in our TAMU Mach 6 case freestream receptivity simulation.

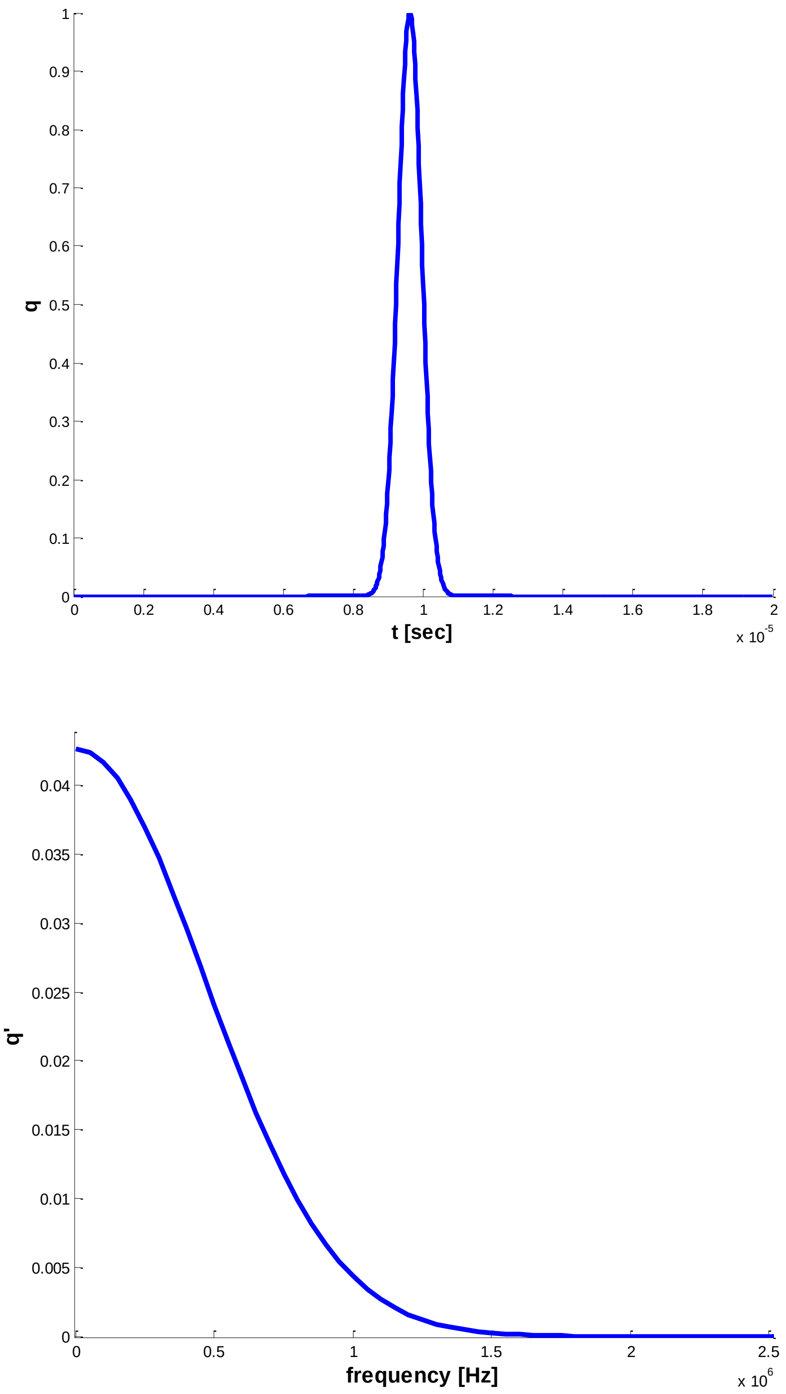

Fig. 6. Gaussian pulse function used for freestream fast acoustic wave and its frequency spectrum.

3.5. Computation Implementation of Receptivity Simulations

Due to the fact that two different freestream models are applied to current receptivity study, the numerical implementations are slight different. For receptivity simulations in general, the multiple zones matching technique is utilized to partition the entire computational domain into subzones, so that the computational cost is more manageable. However, for this approach, the wave disturbance data need to be collected completely and accurately in order to be applied in the next subzones. Different numerical treatments are needed to achieve that.

For the receptivity simulation utilizing the freestream discrete-frequency model, the simulation is run based off the forcing period. The forcing period is determined by the lowest frequency imposed in the freestream. Multiple forcing periods will be run to ensure the flow reaches to steady state. Once the steady state reaches, the last forcing period will be recorded at the interface between current subzone and next subzone. At the inflow of next subzone, the disturbance time signal is re-created using Fourier series.

For the freestream pulse receptivity simulation, only single wave pulse is applied to the freestream. Therefore, the flow field is in transient state. In order to capture the pulse response, the windowing technique is engaged. As the pulse propagates in the downstream direction, the window moves with the pulse with shifted time stamp. The window is kept long enough to capture the pulse including its trailing ripple caused by excitation of boundary layer modes. The same Fourier series expansion as the discrete-frequency model case is applied to re-create the inflow conditions for the next sub zone.

3.6. Computation Implementation of Nonlinear Breakdown simulations

The implementation of nonlinear breakdown simulation required some modification of the computer program used for receptivity simulation. The original program is capable to conduct both 2-D and 3-D simulation. But the 3-D simulation only limits to use one quarter of the cone, one half of the cone or the whole cone. This is due to the fact that the program is implemented in Cartesian coordinate system. However, for the breakdown simulation conducted in present study, it is too expensive computationally to use even one quarter of cone as computational domain because it required lot of grid points in spanwise direction to resolve the breakdown. In order to be able to compute any arbitrary arc angle in spanwise direction, an ad-hoc solution is devised.

The key issue with arbitrary arc angle computational domain is how to treat the periodic boundary conditions in the spanwise direction. This problem can be easily resolved by transferring the flow variables from Cartesian coordinates to polar coordinates. The flow variables involved in the transforms are the velocities and fluxes in Y and Z directions. Hence, the following formulas are applied at each time iteration step to convert these flow variables into polar coordinates before the spatial derivatives are calculated.

$$\begin{cases} q_T = q_y \cos\theta + q_z \sin\theta \\ q_N = q_z \cos\theta - q_y \sin\theta \end{cases}, \tag{57}$$

where $q = \langle u_i, F \rangle$. θ is the angle at each grid point in polar system. After the spatial derivative operations completes, the derivatives of the flow variables need to convert back to Cartesian coordinates in order to correctly calculate the flux to time advancement. And the derivatives can be reverted to original Cartesian coordinates by

$$\begin{cases} \dfrac{\partial q_y}{\partial Z} = \left(\dfrac{\partial q_T}{\partial Z}\right)\cos\theta + q_T \sin\theta - \left(\dfrac{\partial q_N}{\partial Z}\right)\sin\theta - q_N \cos\theta \\ \dfrac{\partial q_z}{\partial Z} = \left(\dfrac{\partial q_T}{\partial Z}\right)\sin\theta + q_T \cos\theta + \left(\dfrac{\partial q_N}{\partial Z}\right)\cos\theta + q_N \sin\theta \end{cases} . \tag{58}$$

By using this ad-hoc solution, we are able to change the arc angle of the computational domain to any degree and substantially reduce the computational cost of breakdown simulation. Furthermore, this modification allows us to perform parametric study in the computational domain arc angle effect to the simulation results.

3.7. Sponge Layer at the Exit of Nonlinear Breakdown Simulation

For the nonlinear portion of the unsteady simulation, a sponge layer needs to be added to the outflow to avoid spurious reflection and blowing up. The sponge layer implementation is modified from the formula by Bodony [64] so that it can be applied to current simulation. In the sponge layer, an additional term is used to force the solution toward target values as shown in eq. (59). U is the place holder for any conservative variable. $A(\xi)$ is a weight function smoothly increases from 0 to 1. The steady flow values are used as the reference values in the equation, so that the flow will be forced back to laminar state. Fig. 7 shows the test case which the sponge layer is added at the exit of computational domain. It clearly demonstrates that the sponge layer damps out the disturbance wave smoothly without any numerical reflection.

$$\frac{dU}{dt}_{adj} = \frac{dU}{dt} - \sigma A(\xi)\left[U - U_{ref}\right] \tag{59}$$

$$A(\xi) = \frac{1}{t_{ref}} e^{-\xi^4/10} (1-\xi^{50})^4 \tag{60}$$

$$t_{ref} = \frac{u_\infty}{L_{buf}} \tag{61}$$

$$\xi = \frac{x_L - x}{L_{buf}} \quad (1 \geq \xi \geq 0) \tag{62}$$

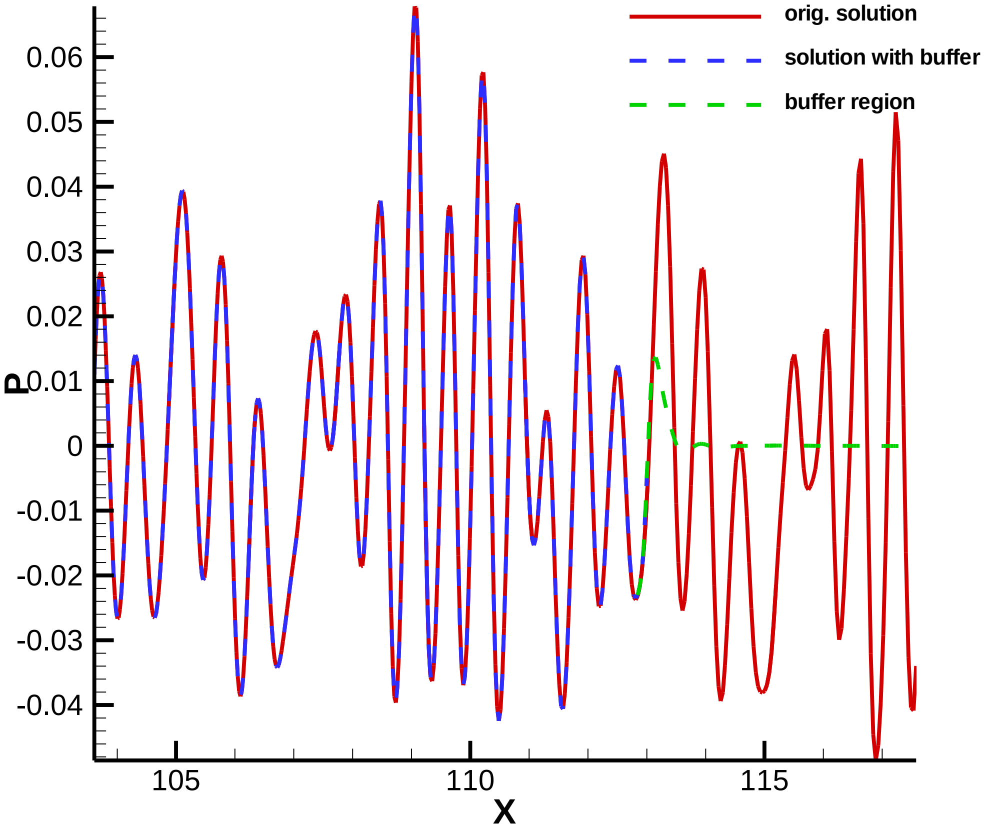

Fig. 7. Comparison of solutions before and after the buffer is applied.

4. Nose Bluntness Effects on Stability over Cones

For hypersonic flow over blunt cones, it has been experimentally observed [65] and theoretically explained [61] that the location of laminar-turbulent transition moves downstream when the nose radii increase within the small bluntness region. This trend is reversed when the nose radii are larger than some certain critical values based on experimental observations [62, 66]. This phenomenon is known as the transition reversal due to nose bluntness. In other words, increasing the nose radius beyond the critical value leads to an upstream movement of the location of transition. The downstream movement of transition location at small radii can be explained by the reduction of local Reynolds numbers owing to the entropy layer created by the nose bluntness. However, there is still no satisfactory explanation for the cause of the transition reversal at large nose bluntness.

Most of the previous studies of bluntness effects on transition were based on linear stability analysis, performed on Stetson's stability experiments of an axisymmetric blunt cone in a Mach 7.99 flow [42]. In these experiments, detailed fluctuation spectra were documented for disturbance waves developing along the body surface. The freestream unit Reynolds number per foot was 2.68×10^{6}. The experimental results showed the disturbances in the boundary layer were dominated by the second-mode instability. Significant super harmonic components of the second mode were also observed after the second mode became dominant. The cone models used in the experiments were not long enough for transition to occur in the boundary layer. As a result, transition reversal phenomenon was not observed in these experiments. Compared with hypersonic flow over a sharp cone, second-mode instability of the blunt cones appeared at much further downstream locations, indicating a stabilization of the boundary layer by small nose bluntness.

Linear stability characteristics of the boundary layer flow over the same blunt cone used in Stetson's Mach 7.99 experiments have been studied by a number of researchers [61, 67-70]. Malik et al. [61] computed the neutral stability curve and compared the growth rates obtained from linear stability theory (LST) with the experimental results. The steady base flow solution was computed using the parabolized Navier-Stokes equations. The results showed that the nose blunting effect stabilizes the boundary layer. The linear stability analyses predicted a slightly lower frequency for the dominant second mode, but much higher amplification rates than the experimental results. Rosenboom et al. [70] did a further linear stability study on the effect of nose bluntness on hypersonic boundary-layer stability. In their calculations, the cone geometry and flow conditions were the same as those used in the Stetson's Mach 7.99 experiments. Three cases of blunt cones with different nose radii covering both "small" and "large" bluntness were considered. The purpose was to investigate the transition reversal phenomenon at "large" bluntness. By a linear stability analysis, Rosenboom et al. confirmed a monotonic downstream movement of the second-mode critical Reynolds number as the nose radius increases. Their LST results did not show the transition reversal phenomenon observed in experiments at "large" bluntness.

Extensive experimental data on transition and transition reversal were reported by Stetson for Mach 5.5 flow over sharp and blunt cones [62]. Blunt cones, with nose radii ranging from $\frac{1}{32}$ to $1\frac{1}{2}$ in., were tested; and the transition locations were measured. Transition data obtained in these test models is re-plotted in Fig. 8, which shows the transitional Reynolds numbers vs. free stream Reynolds numbers based on nose radii, Re_n. The figure shows a clear transition reversal as Re_n increases, with 2×10^5 as the dividing line between "large" and "small" nose radii for Re_n. These results have a very similar trend to the transition reversal results of Softley [66] collected from Mach 10–12 flows over a set of "small" and "large" blunt cones as shown in Fig. 8. These surprisingly consistent results from two separate experiments motivate us investigate the reversal mechanisms behind it.

Stetson's Mach 5.5 case [62] is the primary case of investigation on this topic. This case is especially interesting because it was one of a few experiments that revealed a phenomenon called transition reversal, which referred to the observation that when the nose bluntness reaches a critical value the downward movement of transition location reverses abruptly. Cones with three nose radii of 0.156 inch, 0.5 inch and 1.5 inch are considered in the current study. The result in this chapter has also been published in Journal of Spacecraft and Rockets in 2011 [63] .

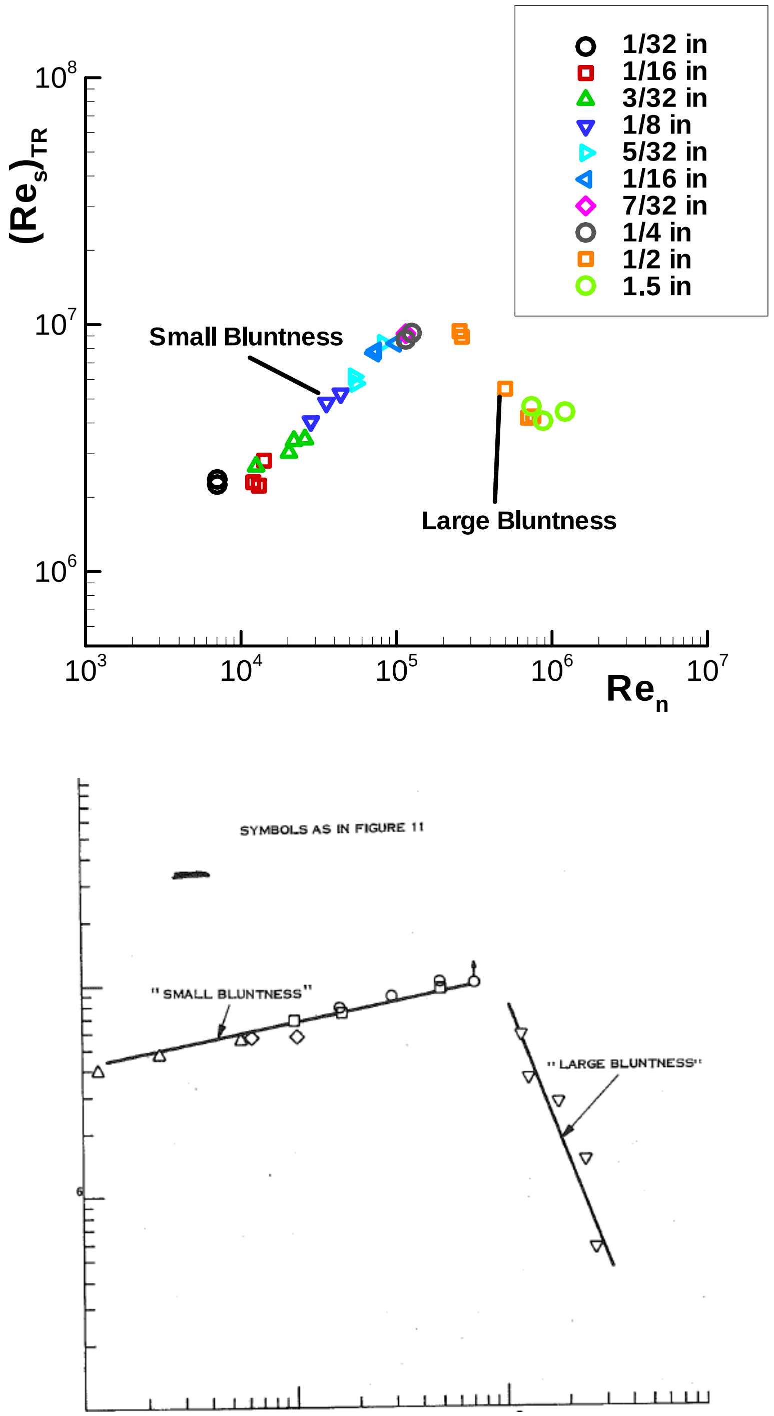

Fig. 8. Transition Reynolds number vs. Reynolds number based on nose radius reported by Stetson (top) re-plotted from [62] and Softley (bottom).

4.1. Meanflow Calculations

The steady base flows are computed using a fifth-order shock-fitting scheme with a multiple zones approach. In the computational domain, the wall normal direction is resolved using 240 grid points with stretching toward the cone surface to ensure that there is approximately 100 grid points within the boundary layer. The simulations are carried out up to 0.8m, 1.8m and 3.2 m along the cone surfaces for the cases with nose radii of 0.156, 0.5 and 1.5 inch respectively.

In Fig. 9, the Mach number contours for blunt cones with different nose radii are shown. As the nose radius increases, the shock layer becomes thicker and a stronger entropy layer effect can be observed in the region near the leading nose for the blunter cases. The entropy layer gradually merges into the boundary layer further downstream and is eventually “swallowed” by the boundary layer. The appearance of an entropy layer is one of the characteristics of hypersonic flow over blunt cone. Some studies hypothesized that the entropy layer effect would introduce new instability mechanism into boundary layer transition [71]. However, this new instability mechanism cannot be identified based on current LST study in this region.

The contours of local unit Reynolds number for the three cases are shown in Fig. 10. As the nose becomes blunter, the local Reynolds number within the boundary layer is substantially reduced. As found in many previous studies, this unique pattern causes a delay in the onset of second-mode instabilities and hence moves the transition location further downstream. This theory has been verified experimentally on small bluntness cones

[65]. However, it cannot be used to explain the transition reversal for cones with large nose bluntness.

The pressure along the cone surfaces are presented in Fig. 11 for cones with different nose radii. The pressure distributions show that all three cones reach very high pressure at the nose tip. As moving away from the nose tip, the pressure on cone with the smallest nose drop most rapidly due to the expansion effect near the nose and frustum interface. Once the pressure reaches the lowest point, it quickly recovers and gradually approaches a relatively constant level. This pressure recovery is the signature of blunt cone, because for the ideal sharp cone, there is no pressure recovery and the pressure reaches frustum pressure immediately. As observed on the blunter nose cone models, as the nose radius increases, the pressure recovery takes longer disturbance. For the nose with 1.5 inch nose, the pressure never recovers to the sharp cone level up to the end of simulation domain. This slow pressure recovery somewhat delays the growth of instability as argued by some researchers.

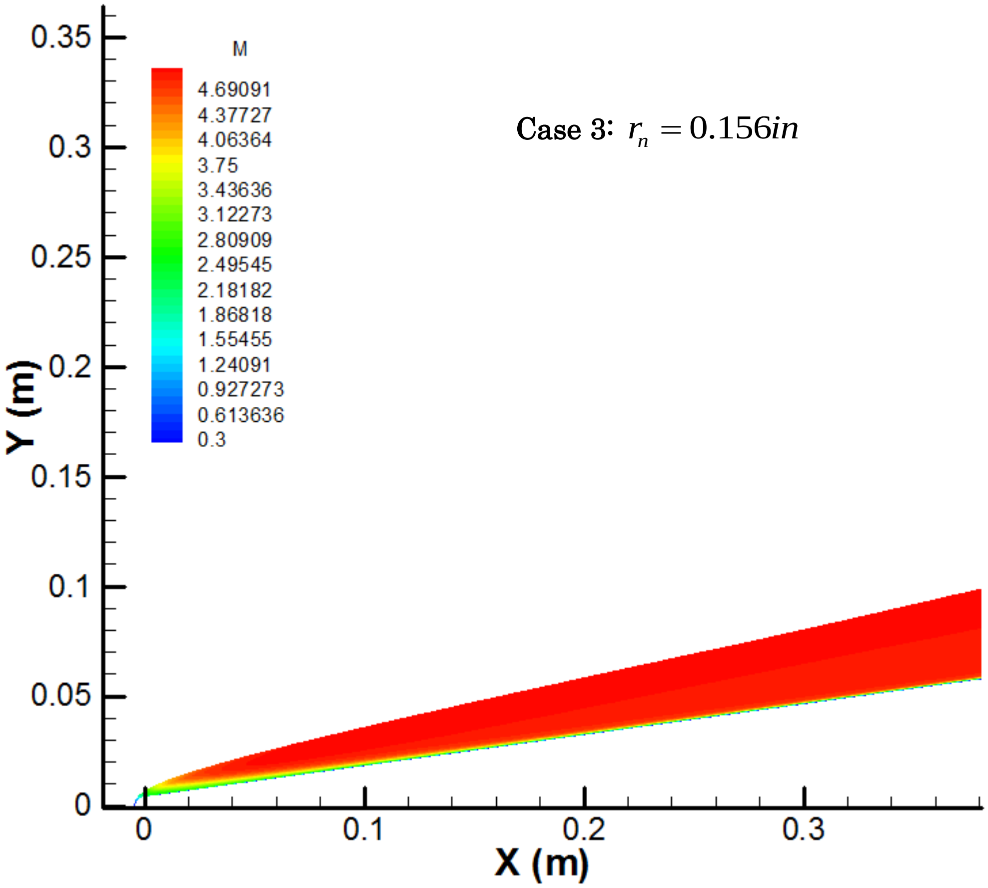
M
4.69091
4.37727
4.06364
3.75
3.43636
3.12273
2.80909
2.49545
2.18182
1.86818
1.55455
1.24091
0.927273
0.613636
0.3
Case 3: $r_n = 0.156 in$
Y (m)
0.35
0.3
0.25
0.2
0.15
0.1
0.05
0
X (m)
0
0.1
0.2
0.3

(a)

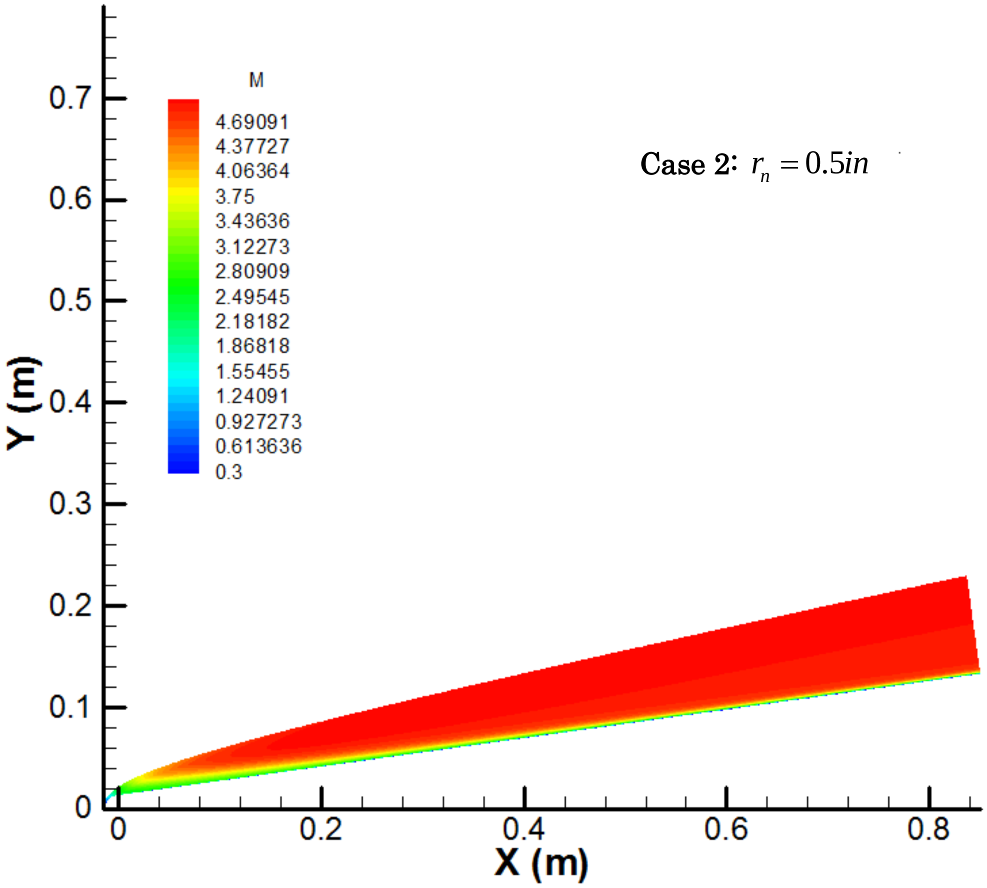
M
4.69091
4.37727
4.06364
3.75
3.43636
3.12273
2.80909
2.49545
2.18182
1.86818
1.55455
1.24091
0.927273
0.613636
0.3
Case 2: $r_n = 0.5in$
Y (m)
0.7
0.6
0.5
0.4
0.3
0.2
0.1
0
0
0.2
0.4
0.6
0.8
X (m)

(b)

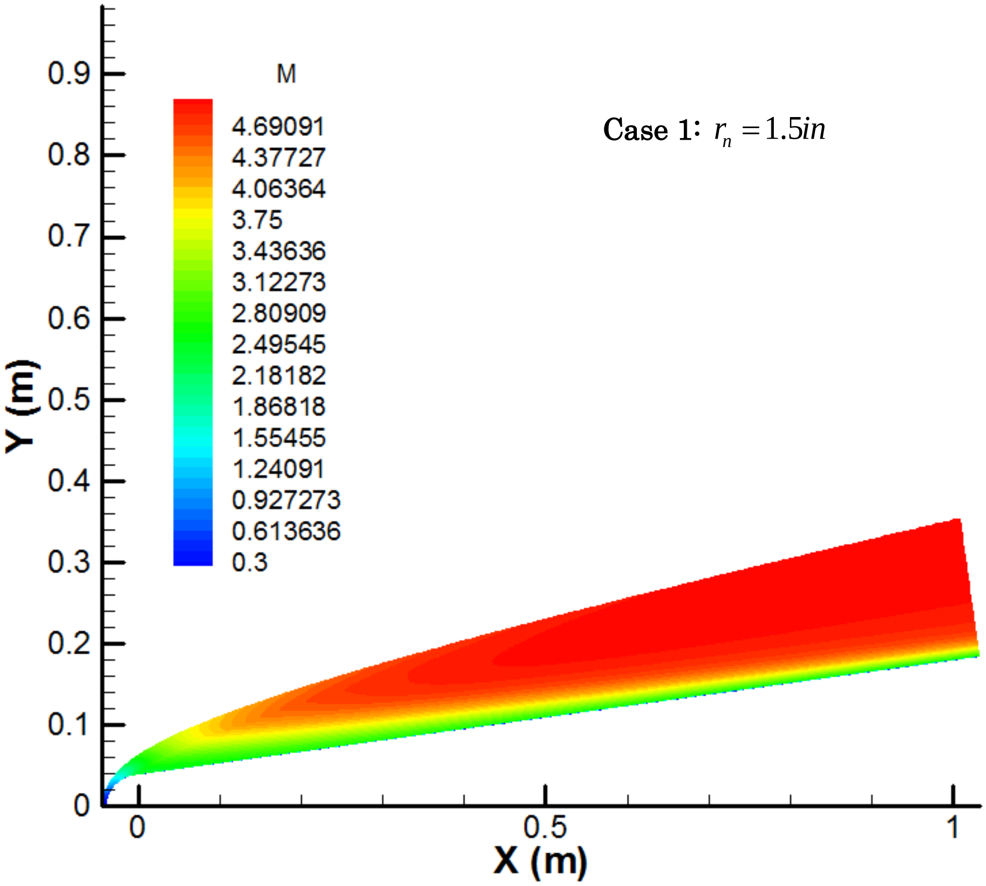

(c)

Fig. 9. Mach number contours of the three test cases of different nose radii.

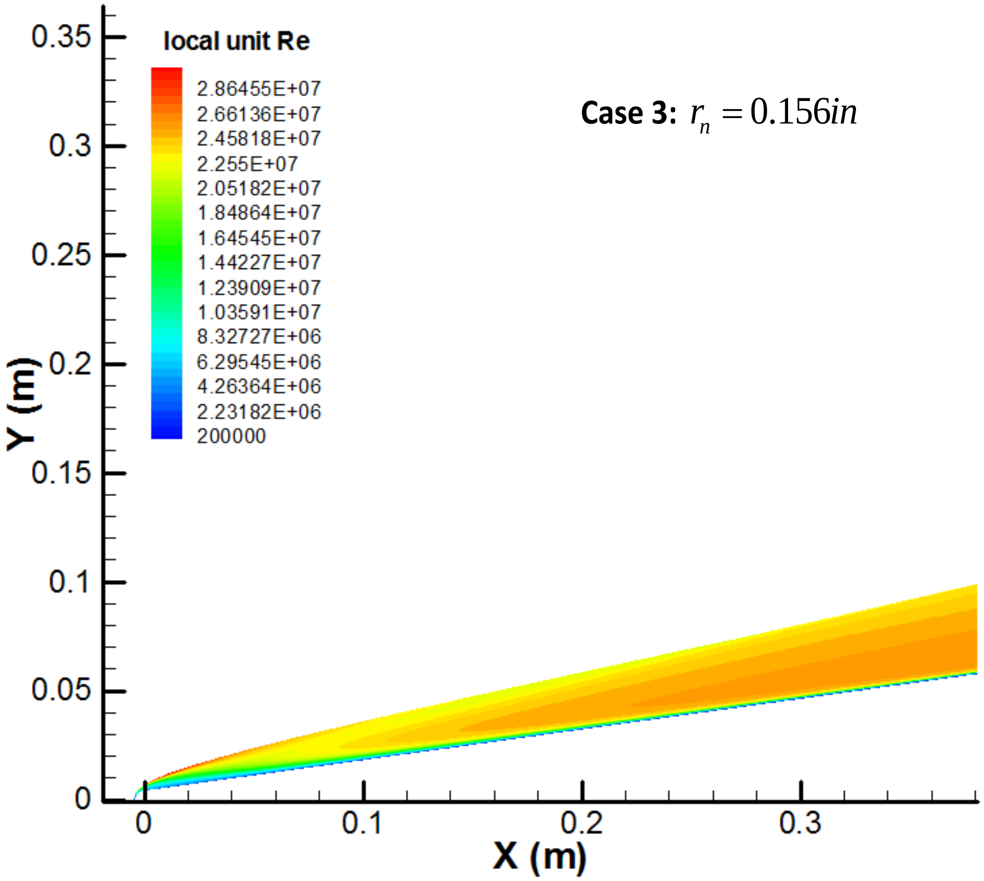
local unit Re
2.86455E+07
2.66136E+07
2.45818E+07
2.255E+07
2.05182E+07
1.84864E+07
1.64545E+07
1.44227E+07
1.23909E+07
1.03591E+07
8.32727E+06
6.29545E+06
4.26364E+06
2.23182E+06
200000
Case 3: $r_n = 0.156in$
0.35
0.3
0.25
0.2
0.15
0.1
0.05
0
Y (m)
0
0.1
0.2
0.3
X (m)

(a)

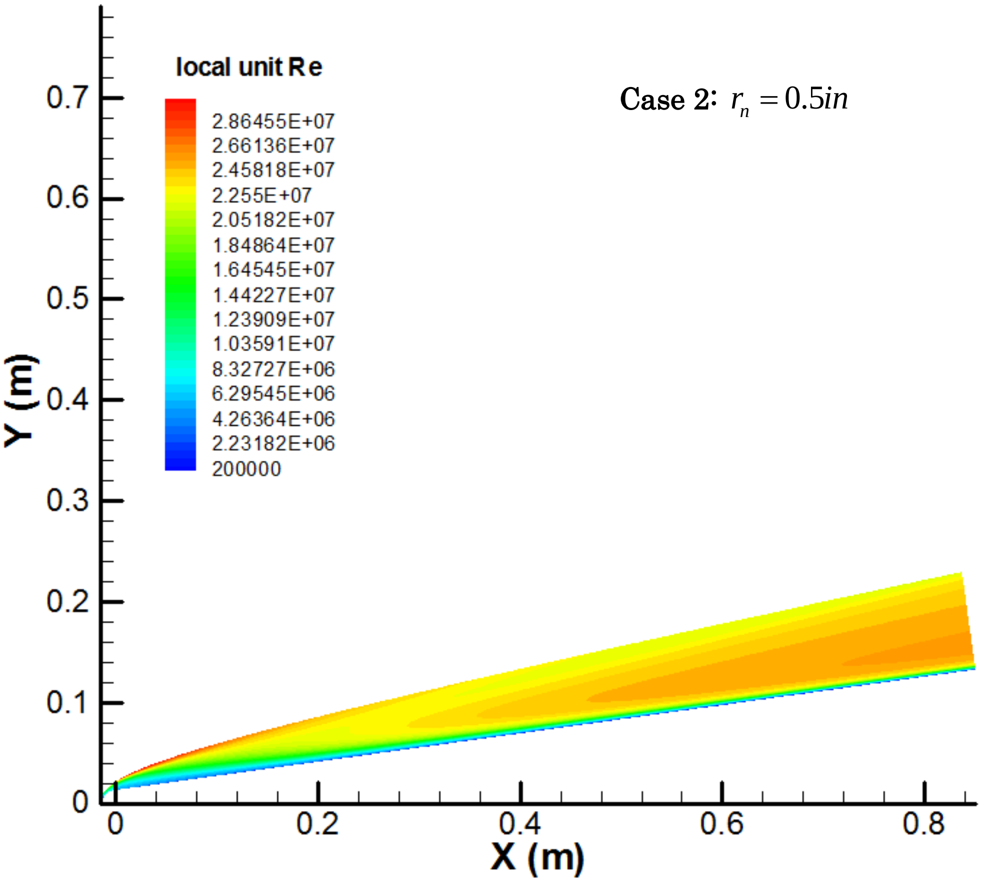
local unit Re
2.86455E+07
2.66136E+07
2.45818E+07
2.255E+07
2.05182E+07
1.84864E+07
1.64545E+07
1.44227E+07
1.23909E+07
1.03591E+07
8.32727E+06
6.29545E+06
4.26364E+06
2.23182E+06
200000
Case 2: $r_n = 0.5in$
Y (m)
0.7
0.6
0.5
0.4
0.3
0.2
0.1
0
X (m)
0
0.2
0.4
0.6
0.8

(b)

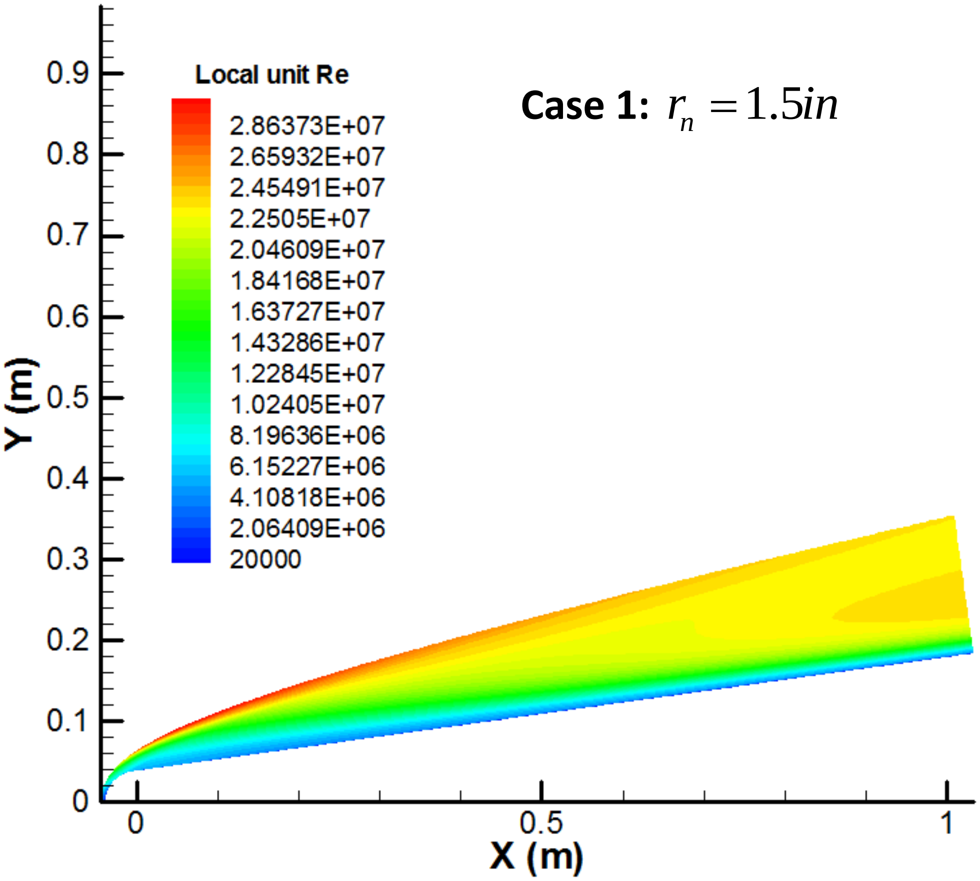

(c)

Fig. 10. Contours of the local unit Reynolds numbers for the base flows with different nose radii.

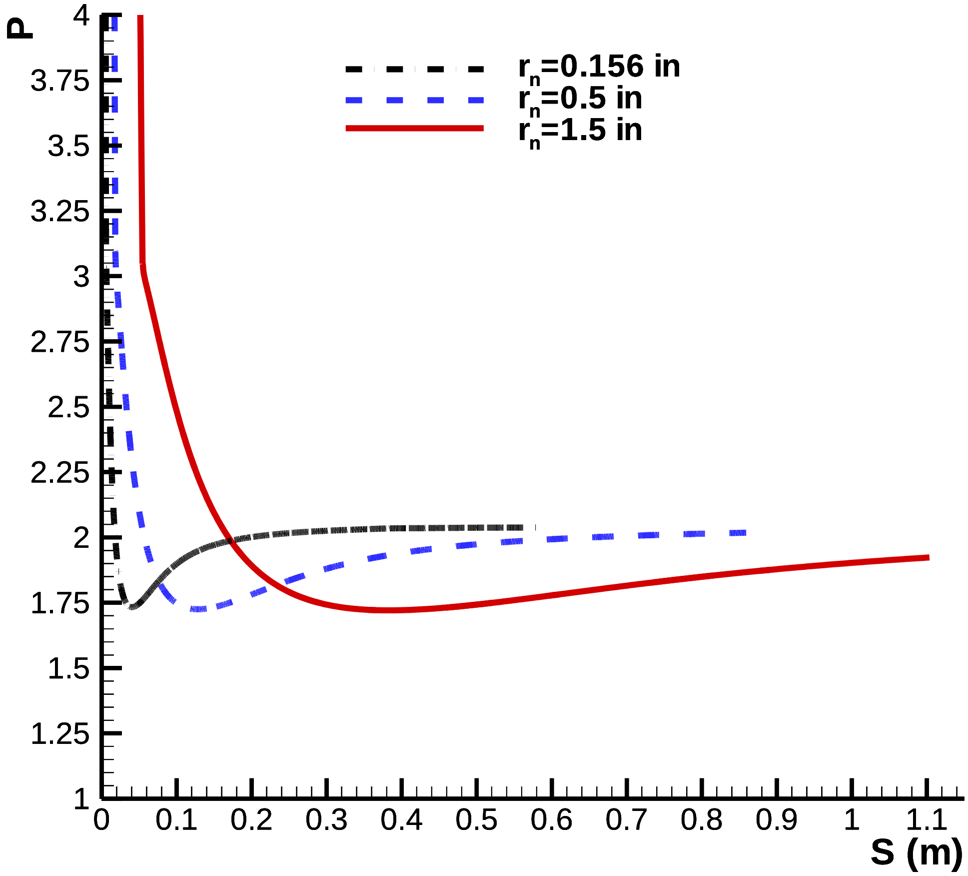

Fig. 11. Pressure distributions along the cone surfaces for the three sets steady base flows of different nose bluntness.

4.2. Linear Stability Analysis

From the mean flow data obtained by the numerical simulation, the instability waves for all three cones are calculated using LST. For the base flows calculations, the cone surface temperature is set at constant room temperature creating a cooling effect to the flow at the cone surface. According to the theoretical study [59], the wall cooling effect stabilizes the first mode instability and destabilizes the second mode. In the current study, no first mode instability is found for axisymmetric waves in all three test cases. Therefore, only the second-mode instability is calculated. The LST results presented are calculated by re-stretching the base flow profile with 121 points in the wall normal direction. The current LST code applies multi-domain approach so that we can cluster more grid points to the location where the flow variables' gradients are high. This approach substantially reduces the number of grid points needed in the LST calculation. To check the numerical accuracy of the LST results, a comparison is made on the growth rates at a fixed frequency of 656.8 kHz in case 3 for two sets of grid points in Fig. 12. The comparison shows that the growth rates from the current grid and the refined grid are completely identical, which implies the current grid is adequate to obtain credible LST results.

Fig. 13 shows the second-mode neutral stability curves on each case. The neutral curve of 1.5 inch case looks less smooth compared to the other two cases. This is due to the fact that less data points (frequencies) are taken for this particular case. However, the general shape will not change with more points added. In this figure, it is observed that the unstable second-mode spectrum falls into very different frequency ranges for cones of different nose bluntness. Also, as the nose bluntness increases, the onset of second-mode instabilities moves downstream accordingly. In the actual experiments, the locations of the onset of instability were not reported; therefore it is hard to confirm if the transition is triggered by the same instability mechanism as predicted by the LST. But as shown in the figure, no reversal is found on the onset of instability locations. In the authors' opinion, in order to have a reversal in transition, a similar pattern in the onset of instability should be observed.

To validate the current LST results, unsteady simulations are carried out by imposing a wall blowing and suction perturbation at the surface of the cone with the LST predicted unstable frequencies. This method has been used by many researchers to generate a vorticity disturbance without introducing extra mass flux into the flow [51, 72]. The surface blowing and suction is applied by specifying the perturbations to the wall normal velocities in the following form

$$v_{n,wall}(x,t) = \varepsilon \sin\left[\alpha_w (x - x_0)\right] \sum_{n=1}^{N} A_n \cos(\omega_n t + \phi_n) \qquad (x_0 < x < x_1) \tag{63}$$

In order to make comparisons with the linear stability results, the disturbance amplitude is set small enough to ensure the growth of instabilities is within the linear regime. For the current simulation, ε is set to 1×10^{-5}. The blowing and suction simulation is performed on the case of 0.156 inch nose radius cone. Instead of using a single unstable frequency, 15 equally distributed frequencies ranging from 52.55 kHz to 797.05 kHz are imposed encompassing the unstable second-mode frequencies predicted by LST calculation. Since the perturbation amplitude is linear, multiple frequencies can be easily separated by Fourier decomposition. The blowing and suction slot is placed at s= 0.33 m. The disturbance waves are introduced into the steady mean flow downstream of the blowing and suction slot. Fig. 14 presents the contours of the tangential velocity disturbance wave at 744.5 kHz after the Fourier decomposition. A clear periodic wave pattern can be observed in these contours as the wave propagates downstream.

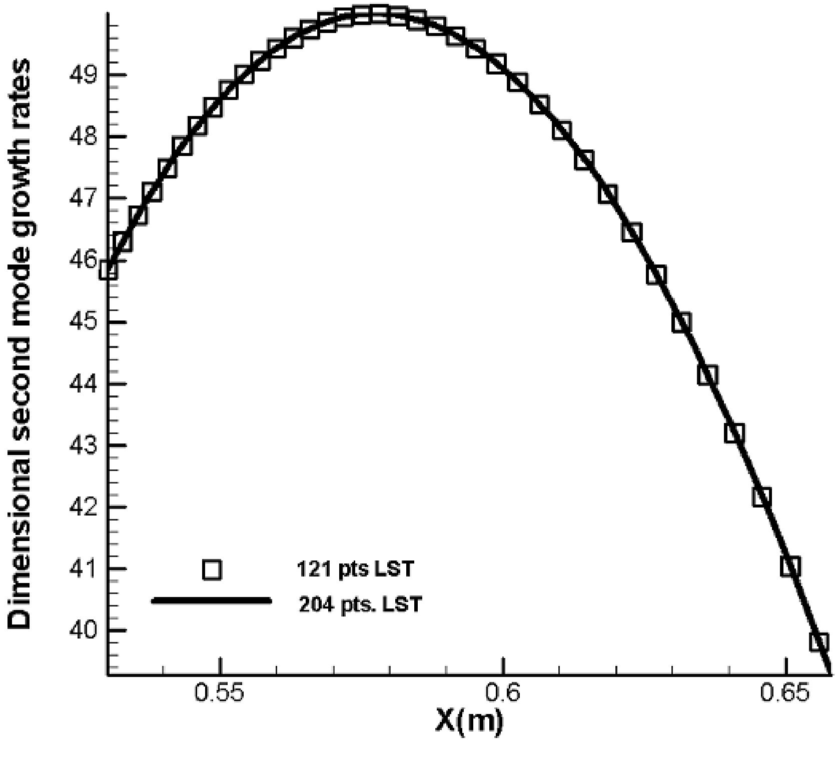

Fig. 12. Dimensional growth rates at F= 656.8 kHz calculated with different numbers of grid points.

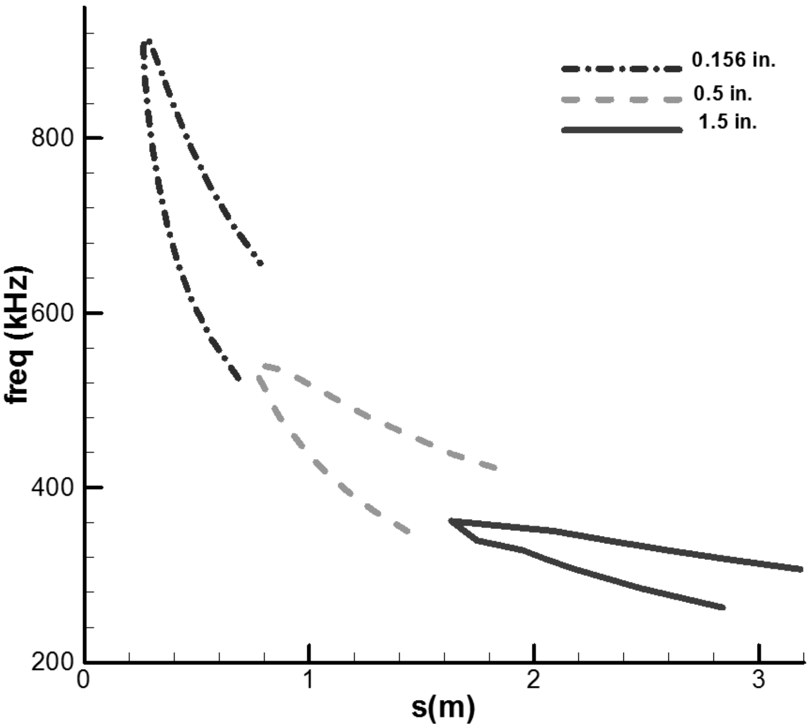

Fig. 13. Second-mode neutral stability curve for cones with three different nose radii.

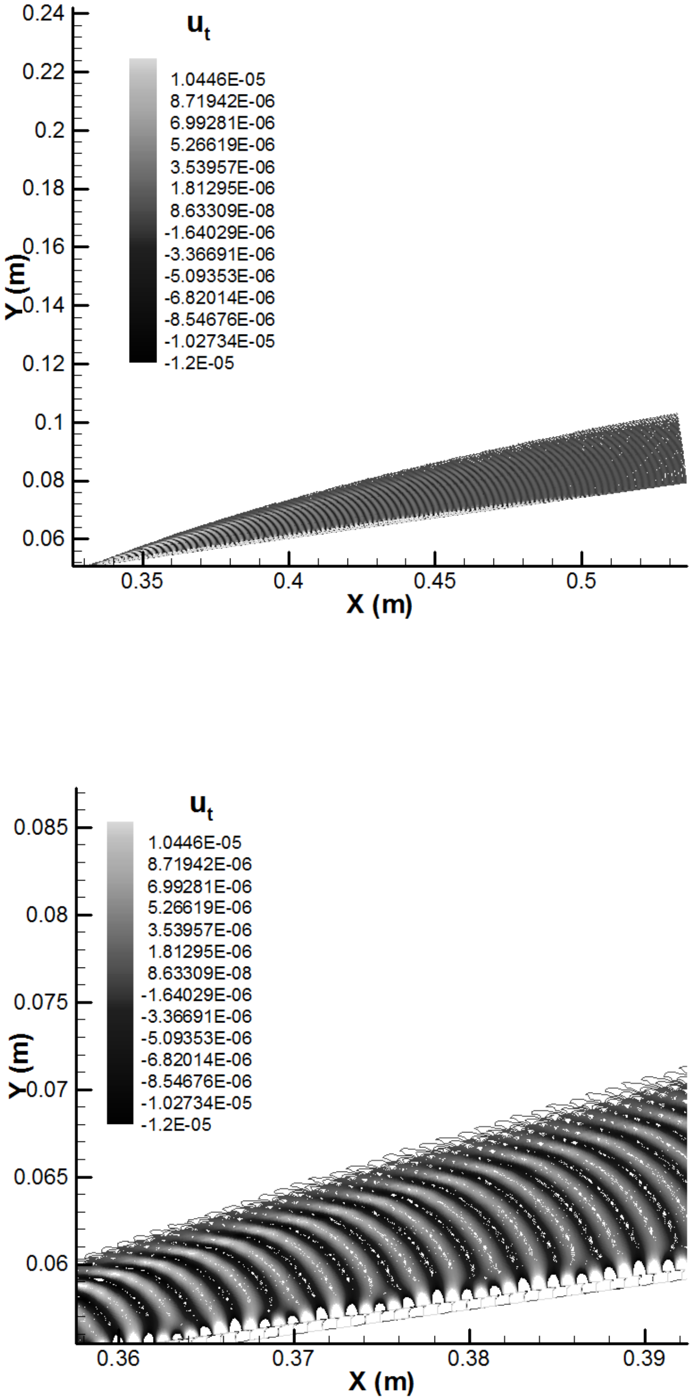

Fig. 14. Contours of tangential velocity disturbance in the unsteady simulation with frequency of 744.5 kHz for the case R_n = 0.156 in.

From the flow field decomposed by temporal Fourier analysis, each fixed-frequency disturbance can be represented by eq. (64) where q' is the placeholder of any flow disturbance quantity; ω is the angular frequency of the disturbance; and ϕ is the phase angle of the disturbance. Also, the disturbance growth rate and wave number can be derived from eq. (65) and (66) respectively. In the results presented later on, the disturbance growth rate and wave number are calculated based on the pressure disturbance along the cone surface. The non-dimensional phase speed is obtained using eq. (42) while the wave number was also obtained from the pressure disturbance along the cone surface.

$$q'(x,y,t) = \mathrm{Re}\left\{ \left| q'(x,y) \right| \exp(i[-\omega t + \phi(x,y)]) \right\} \tag{64}$$

$$\alpha_i = -\frac{1}{|q'|}\frac{d|q'|}{ds} \tag{65}$$

$$\alpha_r = \frac{d\phi}{ds} \tag{66}$$

If the flow perturbations of the simulation results in a local region of the boundary layer are dominated by a single wave mode, the growth rate (α_i), the wave number (α_r), and wave speed (a) computed by eq. (65), (66), and (42) are smooth functions of *s*. On the other hand, if the simulation results contain simultaneously multiple wave modes in a local region of the boundary layer, the results do not represent the wave number, growth rate, and wave speed of a single wave mode. Instead, these parameters represent a modulation of two or more wave modes. As a result, the wave number, growth rate, and wave speed along the surface direction will be oscillatory. In this case, further decomposition of different wave components is required in order to obtain the growth rates and wave numbers of the individual wave modes.

In Fig. 15, the non-dimensional wave speed along the cone surface obtained from both the unsteady numerical simulation and the mode F from LST analysis at the same frequency of 774.5 kHz are shown. The early portion of the wave speed curve matches up with the LST prediction very well. However, the oscillation started around s = 0.45 m indicates that this mode has not become dominant and subsequently jumps to another mode further downstream. At s = 0.55 m, a new mode becomes dominant with a substantially higher wave speed. This mode is also identified by Zhong et al. [52] in their LST analysis of a different test case. They named this the mode II, which is another stable mode excited inside the boundary layer in the later region. In addition, this figure implies that the partially excited mode in the early region is the fast mode (or mode F). Even though the LST predicts that, at this particular frequency, the unstable second mode should appear at this location, the excited wave mode appears to be stable due to the strong influence of the forcing blowing-suction mechanism and the existence of multiple stable modes that have not been damped out [73]. Details on mode analysis will be discussed in the next section. Here, the comparison is sorely to demonstrate how the LST result can be correlated to the unsteady numerical simulation.

The mode structures from the simulation and LST are also compared to verify that the LST predicted mode is captured by the numerical simulation. Fig. 16 shows the excited mode in the blowing-suction simulation in comparison with the normal modes, both fast and slow, from the LST analysis at the location $s = 0.44$ m. The excited mode in simulation agrees well with the mode F from LST. It also further-justifies the statement made earlier that the dominant mode excited inside the boundary layer is mode F.

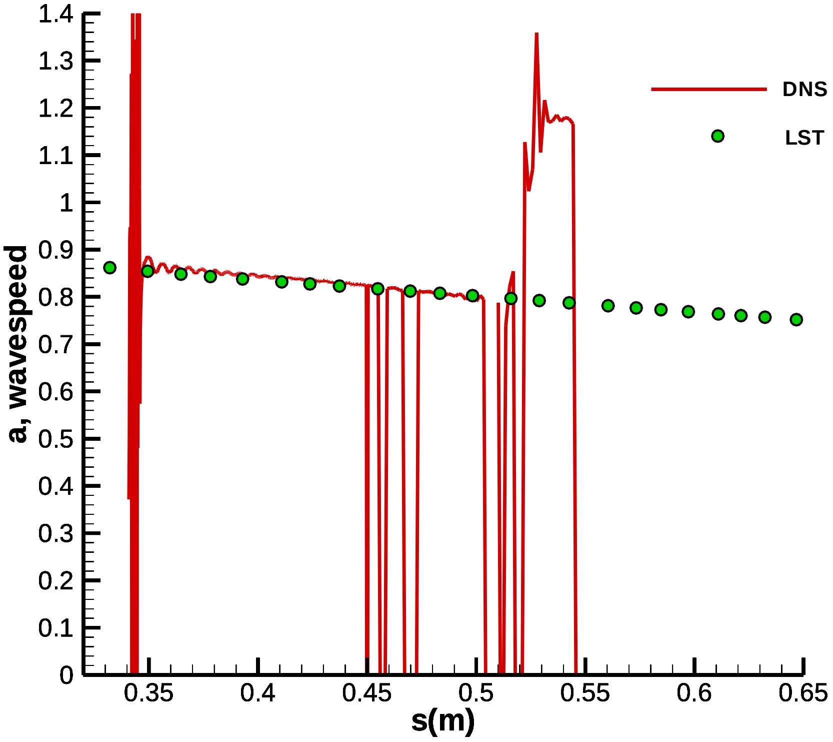

Fig. 15. Comparison of non-dimensional wave numbers from DNS and LST with the disturbance frequency of 744.5 kHz for the case R_n = 0.156 in.

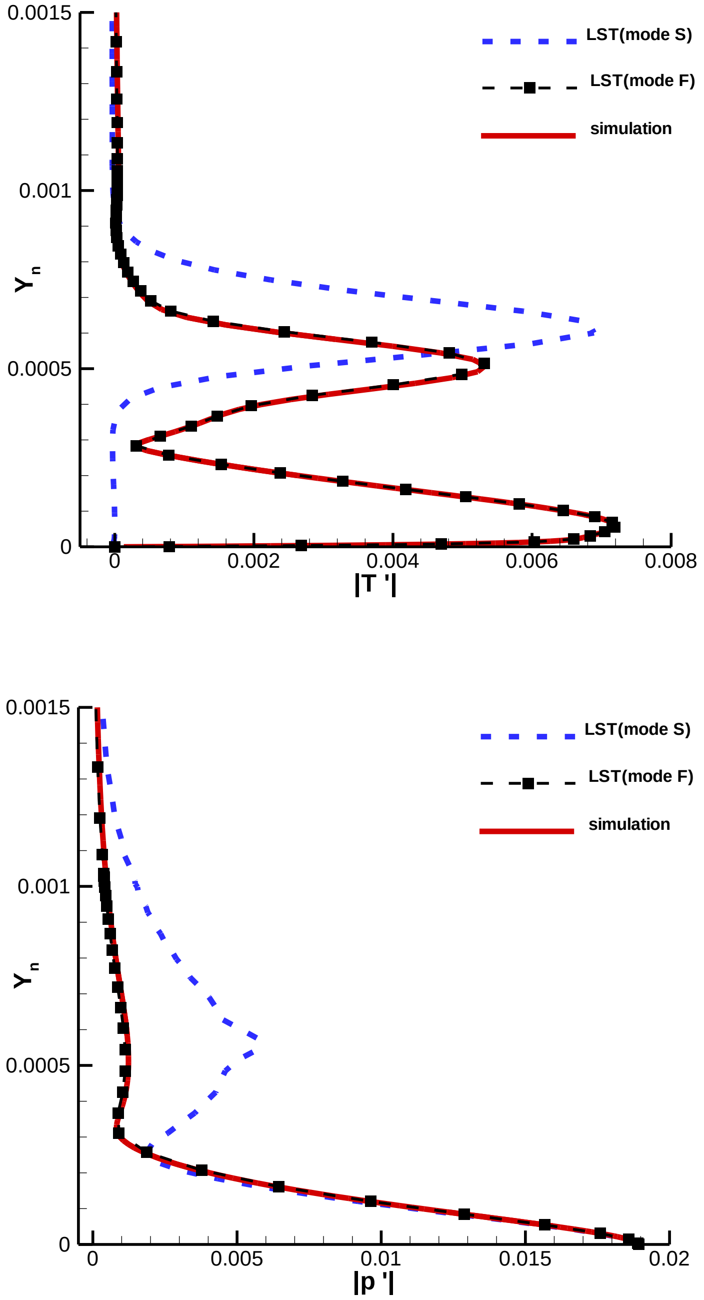

Fig. 16. Comparison of mode structures between DNS and LST at the disturbance frequency of 744.5 kHz for the case R_n = 0.156 inch at s = 0.44 m.

To further verify how well the LST calculations predict the unstable second mode inside the boundary layer, another blowing and suction simulation is conducted further downstream to avoid the strong influence from the blowing and suction slot. In the blowing and suction simulation further downstream with a slightly different set of frequencies, substantial growths of disturbance waves at certain frequencies are clearly observed. Fig. 17 shows the growths of amplitude of the pressure disturbances along the cone surface, which are set to 1×10^{-5} in the magnitude initially, for the highest five frequencies imposed in the simulation. It can be seen that the disturbance wave at 656.8 kHz is growing exponentially at this location. A similar behavior is found for the disturbance wave at 606.4 kHz. For other frequencies, the wave amplitudes either grow slowly or decay rapidly. For the other 10 waves at lower frequency, the disturbance amplitudes are all decaying.

Fig. 18 shows the wave structure of a single wave frequency from the simulation in comparison to the mode S and mode F structures from LST calculation at the location s = 0.57 m. The mode shapes of mode F and mode S look very similar in the location close to the surface, but gradually deviate from each other as they move toward the edge of boundary layer. In the figure, the edge of the boundary layer locates around Y_n = 0.006. Similar to the previous discussion, the excited mode in the simulation is consistent with the mode F wave structure from the LST. The only difference here is that, at the specific frequency presented, the mode F is actually the unstable second mode. The magnitude of mode S is scaled up for comparison purposes. In the simulation, the magnitude of mode S is several orders smaller than the one of mode F and continues to decrease as it propagates downstream.

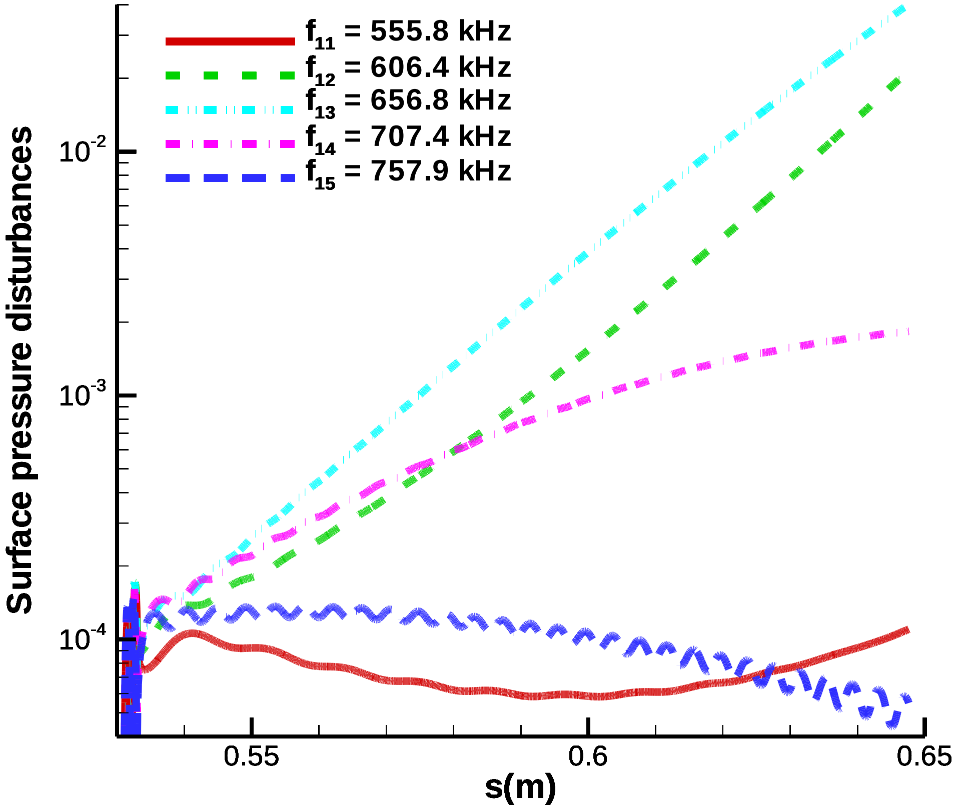

Fig. 17. Pressure disturbance amplitudes (in log-scale) along the surface for five selected frequencies.

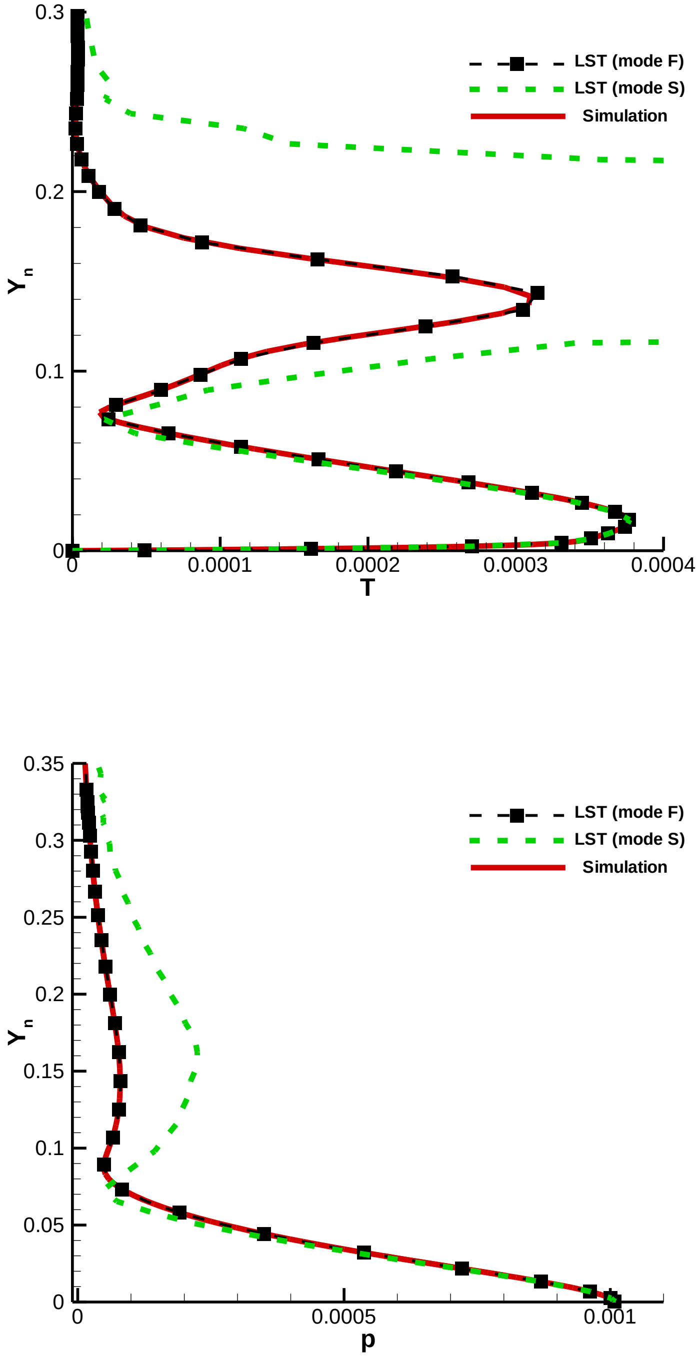

Fig. 18. Comparison of mode structures between DNS and LST at the disturbance frequency of 656.8 kHz for the case R_n = 0.156 inch at s = 0.57 m.

Fig. 19 shows that, for the disturbance wave at the frequency of 656.8 kHz, the wave speed from simulation and LST agree very well. However, the LST predicted growth rate is about 10% lower than as observed from simulation. In most cases, it is hard to match the result of simulation and the LST exactly because the simulation result contains multiple excited modes. The only condition for which those two results can be well compared is when the instability completely dominates other stable modes. This condition typically occurs at the location where the instability is sufficiently far away from the forcing waves. In such cases, the stable modes will more likely decay to negligible levels compared to unstable mode. In addition, the discrepancy in growth rates can probably be attributed to the non-parallel effect of the flow within the boundary layer which is not accounted for in the current LST model [74]. Overall, the LST analysis is proven to be a reliable tool in the calculation of small amplitude instabilities in the hypersonic boundary layers. Also, the LST analysis and blowing-suction simulation show consistent results in predicting the unstable second-mode behavior.

The second-mode dimensional growth rates versus the distance along the surface of the blunt cone are presented in Fig. 20 for the three cases with different nose radii. Some common characteristics are observed in all these cases. First, the disturbances at higher frequencies become unstable at locations closer to the nose. Second, as the frequency decreases, the maximum second-mode growth rate becomes higher. Some trends are also found among these three cases. As the nose bluntness increases, the onset of the second-mode instability moves downstream. The range of unstable mode frequency keeps shifting to the lower end and becomes narrower as the nose becomes blunter. The frequency ranges shifting to lower value can be explained by the increase of boundary layer thickness due to blunting the nose, which causes the wave lengths of unstable modes to become longer. The growth rates for the blunter cone are substantially lower than those of the sharper cone. Also, for the blunter case, the instability of a fixed frequency tends to grow for a longer distance to compensate the lower growth rate it has.

With the second-mode growth rates calculated, the N factors can be obtained by integrating the dimensional growth rates along the cone surface. In Fig. 21, the second-mode N factors for the three cases of different nose bluntness are presented. The N factors calculations show that the shaper cone actually has much higher N factors than the blunter cones. In the current study, the N factors of the 0.156 inch blunt cone reach 16 at $s = 0.8$ m, while, to the other end, the 1.5 inch blunt cone only has a N factor about 3 at $s = 3.2$ m.

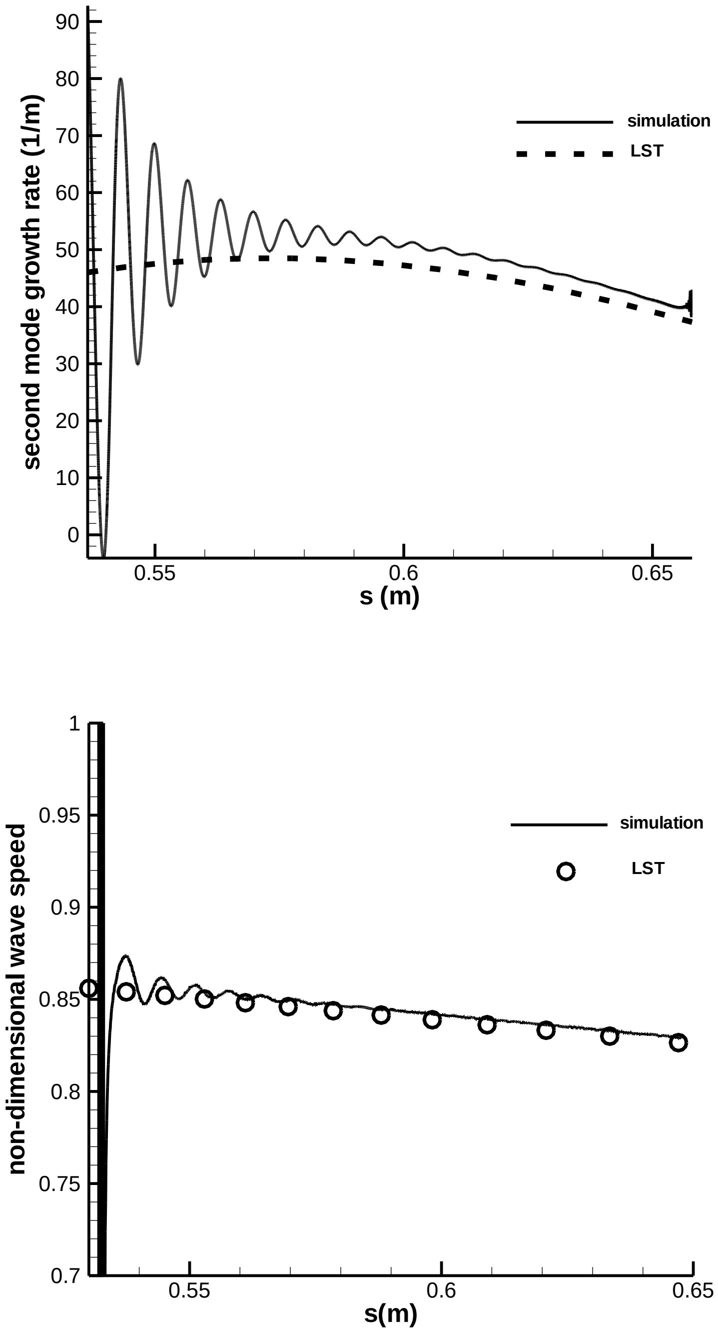

Fig. 19. Comparison of second-mode growth rate and wave speed at *F* = 656.8 kHz.

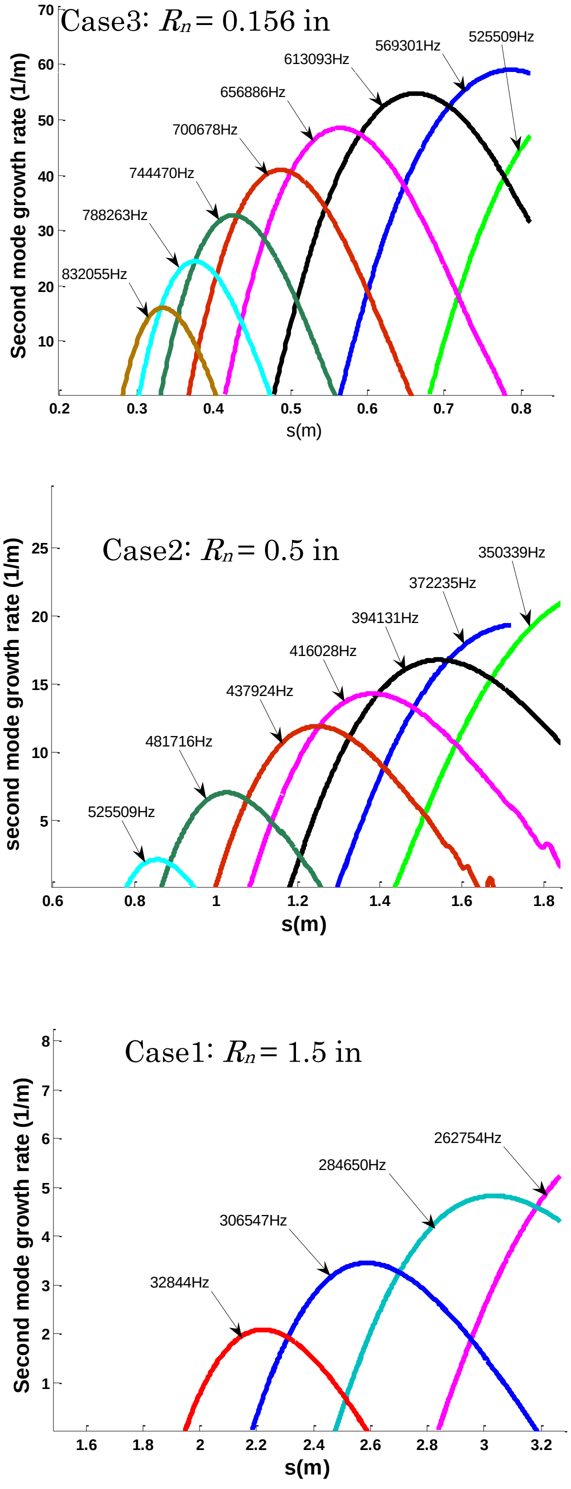

Fig. 20. Second-mode dimensional growth rates for the three cases with different nose radii.

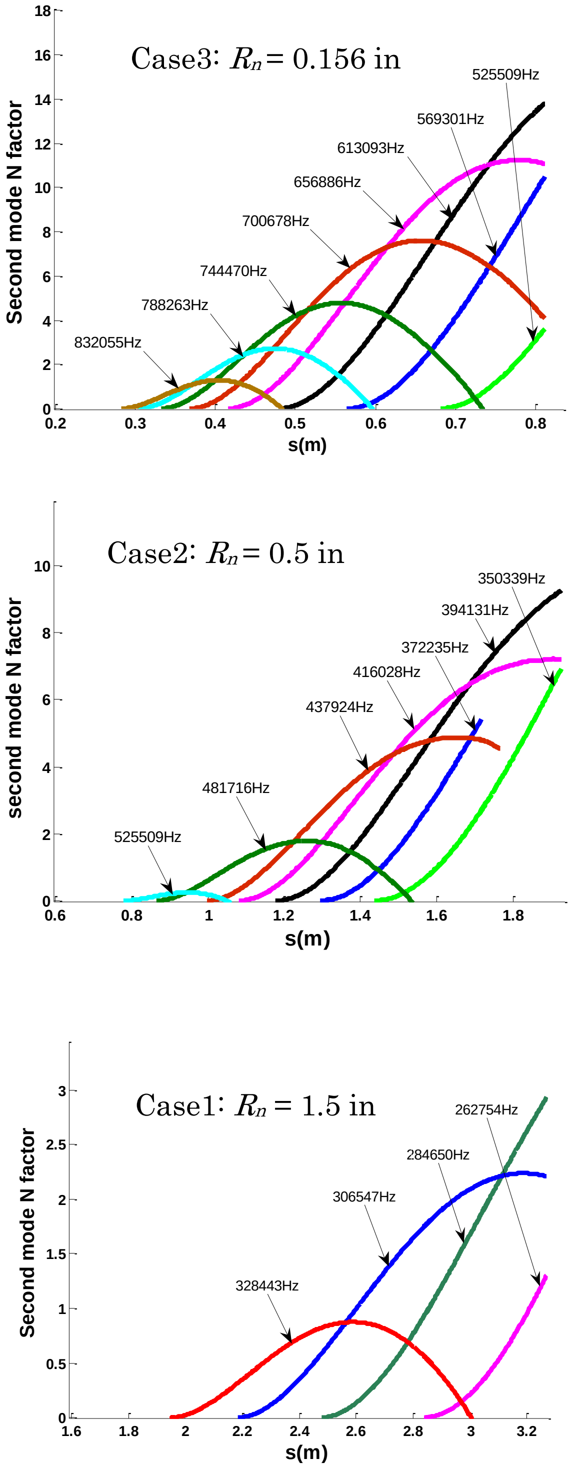

Fig. 21. Second-mode N factors for the three cases with different nose radii.

By comparing the current LST results to the experimental transition data reported by Stetson, disagreements are found between LST predicted transition locations and experimentally observed transition locations. For the two cases of 0.5 inch and 1.5 inch nose radius, the experiment showed transitions occurred at 0.421m and 0.243m, while no second-mode instabilities were found at these locations according to the LST analysis. Traditionally, the N factor for transition is between 5 and 10. If taking N factor equals to 10 as the transition prediction criteria, LST predicts that the transitions occur at 0.7 m and 1.9 m for case 3 and case 2 respectively. For case 1, the N factors calculation does not show a substantially large growth up to 3.2 m from the nose, which is not likely to become transition unless the initial disturbance level is very high. In Table 1, the experimental measurements and LST results are summarized.

Table 1. Comparison of LST and experimental results.

Nose radius	Freestream *Re* based on nose radius	Experimental transition location	N factor based on transition data	Instability onset location based on LST
0.156 in	75,213	0.406 m	2.3	0.3 m
0.5 in	240,665	0.421 m	N/A	0.8 m
1.5 in	721,995	0.243 m	N/A	1.7 m

Stetson's Mach 5.5 experiment conducted in 1967, in which the actual reversals in transition were reported, is investigated using LST technique and the results are verified by unsteady blowing and suction simulations. The ranges of second-mode instability frequency for blunt cones with nose radii of 0.156, 0.5 and 1.5 inch are identified by LST. Due to the "cool wall" temperature condition being used to simulate the steady mean flows, the mode F becomes the unstable second mode in the current study which is different from some previous studies. The growth rates and N factors are computed for each case on selected unstable frequencies. According to the LST calculations, no reversal in the onset of the second-mode instability is observed. Because the onset locations of instability waves were not measured in the experiment, no comparisons can be made to verify the reversal in experiments were caused by the second-mode instability waves. Since the experiments were conducted in a noisy tunnel environment, there is likelihood that the reversal is caused by some uncontrollable noises with the amplitude large enough that the growths of disturbances bypass the linear region and force the transition to occur earlier. However, this hypothesis cannot be justified based on the LST analysis. Hence, it is necessary to further study the nonlinear effect (finite disturbance amplitude effect) on transition to gain a more complete understanding of transition reversal.

5. Freestream Wave Linear Receptivity

The linear receptivity simulations are conducted to study the receptivity and stability characteristic of hypersonic boundary layer to the freestream wave disturbance over cone configurations. The simulation results are also used to build up the receptivity response library for subsequent nonlinear breakdown simulations. Two different freestream models are implemented on the receptivity simulations. The discrete freestream model is applied to the Stetson's Mach 5.5 case. And the newly developed Gaussian pulse model is used on the TAMU Mach 6 case.

5.1. Linear Receptivity Simulation of Stetson Mach 5.5 Case

The meanflow calculations of Stetson Mach 5.5 Case have been presented in section 4.1. From the LST calculations of Stetson's Mach 5.5 cases presented in section 4.2, only the case with 0.156 inch nose radius has substantial second-mode growth to possibly reach transition. For the other two cases, even the second-mode instabilities are found, the N factor are too weak to lead to transition. Therefore, the receptivity simulation is only performed on the cone with 0.156 inch nose radius. The result of receptivity simulation is presented in this section. Only fast acoustic type of freestream wave disturbance is considered for the current study. The discrete-frequency fast acoustic wave model that contains only 15 frequency components is introduced into the freestream of receptivity simulation.

The evolutions of surface pressure perturbations in the streamwise direction along the cone surface are shown in Fig. 22. Each line represents the amplitude of pressure disturbance along the cone surface for one of the 15 frequencies ranging from 52.5 kHz for n=1 to 788.3 kHz for n=15 imposed in the freestream. Dimensional surface location in curved-linear coordinate s^* is used in the plots so that the results can be correlated with the LST calculations. This figure shows that the freestream wave receptivity process leads to complex wave responses inside the boundary layer. At a location that the given frequency is not dominantly unstable, the amplitude response represents a combination of all stable and unstable mode as well as forcing wave that penetrates through shock and enters into boundary layer. Strong wave modulation is found when the boundary layer unstable mode develops but not yet reaches very high amplitude. When the second-mode instability grows to dominant level, it overwhelms the others stable modes and forcing. Therefore, the moderation gradually diminishes. A clean exponential growth in pressure disturbance amplitude is observed. For perturbation wave at a fixed frequency, the wave structures change dramatically as it enters the second-mode region. It also clearly show that, the waves at frequency between n=10 to n=15 are growing in the later region of simulation domain. However, a shift of pattern is visible for disturbance waves at frequencies n=12 to n=14. Strong modulations are found on these waves during unstable growth region. Further investigation reveals that these modulations are due to presences of higher harmonic wave at twice the frequency. Higher harmonic wave is an indication that the flow disturbance becomes nonlinear so that wave interaction leads to growth of wave at higher frequency. General speaking, these results show good agreements with the LST predictions especially in the linear growth region of simulation domain as the unstable second modes become dominant.

In summary, the linear receptivity responses due to freestream fast acoustic wave at discrete number of frequencies are capture by simulation. And the results are validated by comparing with LST analysis. Good agreement is attained in the region where second modes become overly dominant. However, some drawbacks are also realized during framework development using the discrete-frequency freestream wave model. First of all, the finite number of freestream wave frequencies cannot fully represent the freestream disturbance environment which embraces a much boarder frequency spectrum. The discrete frequency approach is very effective in studying the linear receptivity process but may not be realistic when it reaches the breakdown stage. In addition, The Stetson's Mach 5.5 experiment, which was conducted more than 30 years ago, does not have stability measurements. This makes it difficult when trying to correlate simulation results with transition mechanisms. However, this simulation results provide the ingredients sufficient for code development purpose.

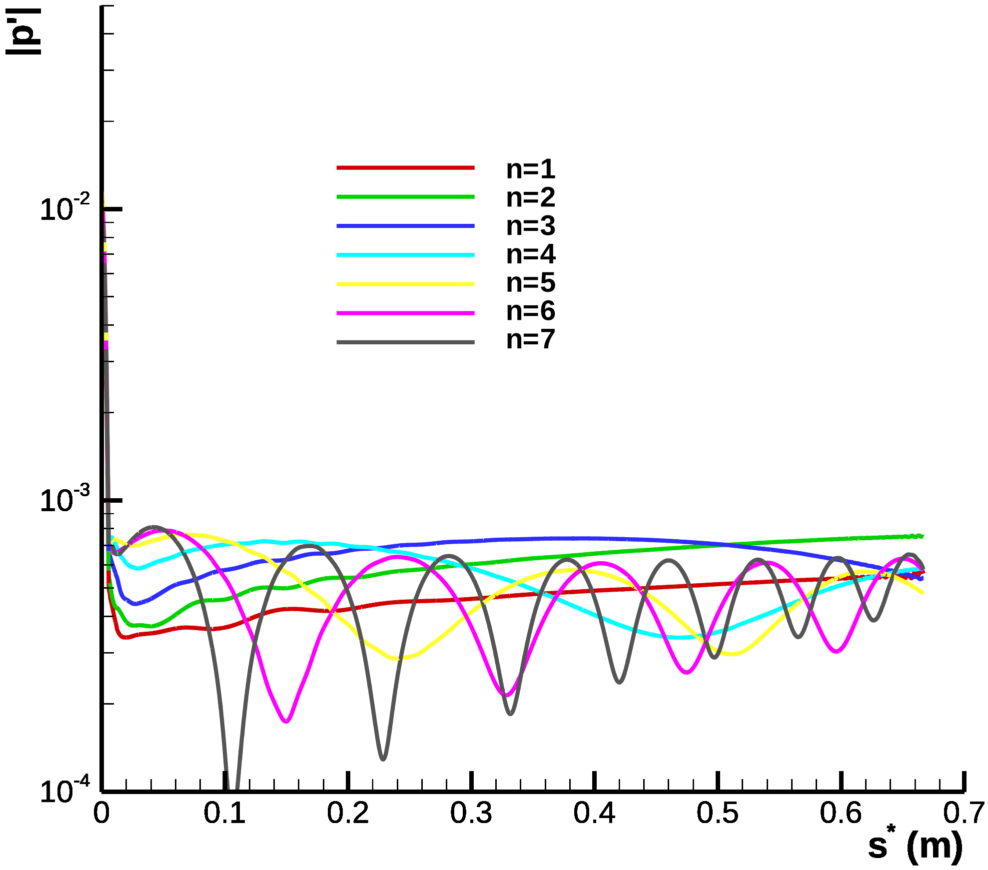

(a)

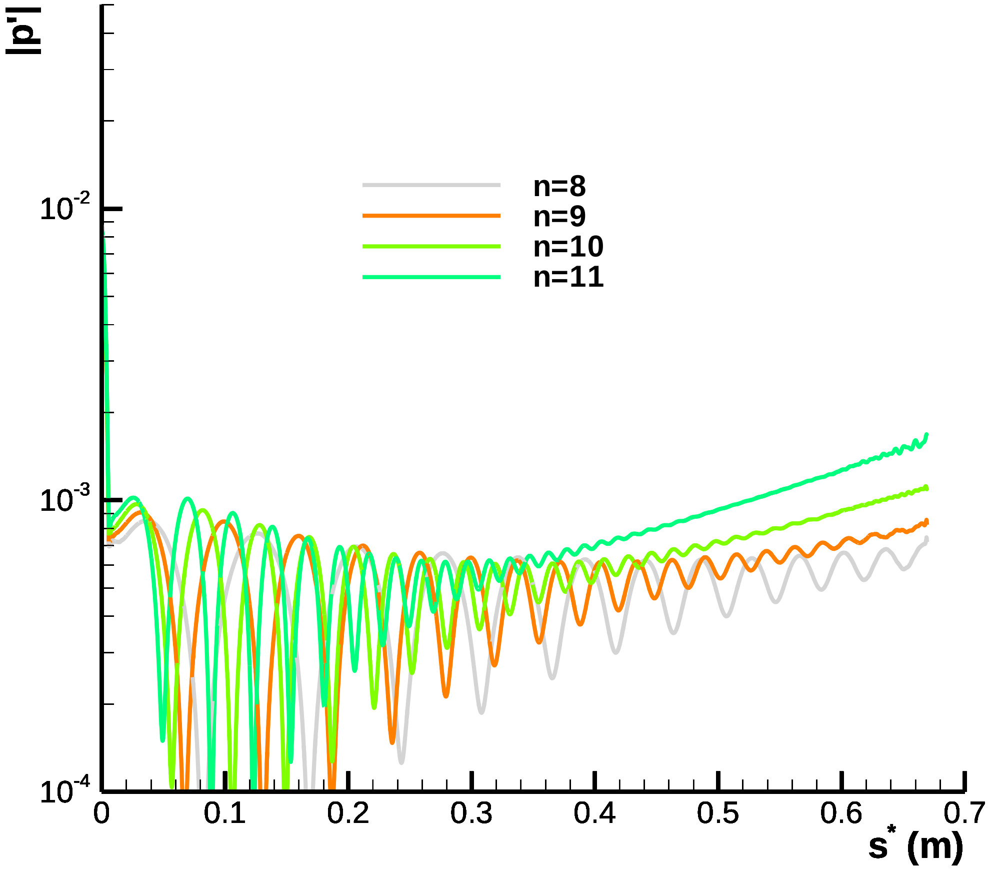

(b)

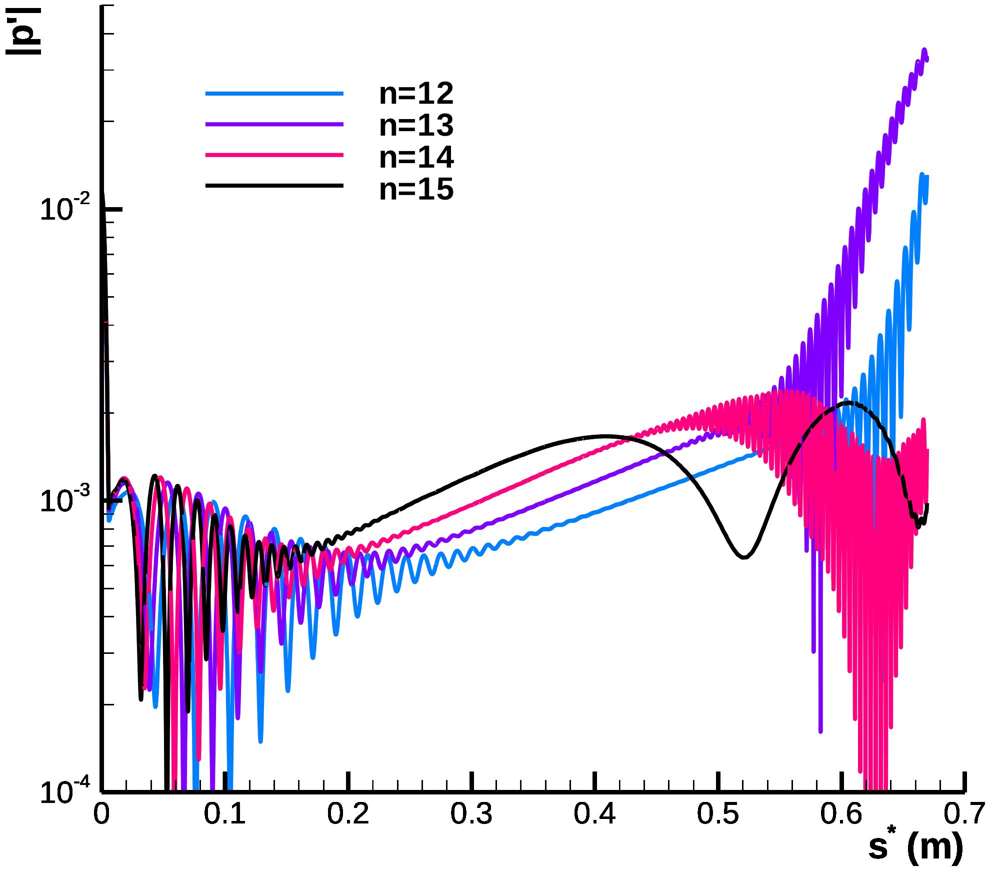

(c)

Fig. 22. Amplitude profiles of surface pressure perturbations along the cone surface.

5.2. Freestream Receptivity of TAMU Mach 6 Case

The TAMU Mach 6 quiet tunnel flow conditions are utilized for further study in current research effort. In addition to the ongoing experiments at TAMU, this flow conditions with various cone models has been numerically and theoretical studied by many other research groups, so it is easier to compare the simulation results with. Due to the drawback on discrete-frequency freestream wave model discussed in previous section, a new freestream Gaussian pulse model is developed to introduce freestream wave containing a continued frequency spectrum into the flow field. With this newly developed pulse model, it is possible to replicate any freestream disturbance wave profile from experimental data so that the simulation and experiment can better correlate.

5.2.1. Meanflow Calculations

The meanflows are computed for two different cone models with the same freestream conditions. The first cone model has nose radius of 0.125 inch. The first half of cone is straight from the nose up to x=0.254 m with 5 degree half angle and flared for the second half as shown in Fig. 5. This design is adapted purposely to expedite the transition process as the adverse pressure gradient facilitates the growth of instability. The second cone model is a modified version of the first cone model with a much smaller nose radius. The first half of the cone is exactly the same as previous cone with the exception that the radius of nose is 0.1 mm. On the second half of the cone, instead of using a flared geometry, we keep the cone body straight all the way till the end of computational domain. These two different cone models are chosen with the purpose to study both the nose bluntness effects on the freestream wave receptivity and flared cone compression effects on the flow stability.

The meanflow of flared cone is computed from nose tip all the way to X=0.6 m. it has the grid resolution of 4800 × 240 in streamwise and wall-normal directions respectively. The grid in streamwise direction is uniformly distributed; and the grid in wall-normal direction is highly stretched toward the cone surface so that the boundary layer profile can be well resolved. The meanflow of straight cone model has grid resolution of 5760 × 240 in streamwise and wall-normal directions. The meanflow calculation is carried out up to X=0.75 m. The grid stretching is similar to the flared cone case.

For the flared cone model, a clear compression effect in the flared section of cone is observed from the computed pressure contour in Fig. 23. Comparing the surface pressures of these two cone models as shown in Fig. 25, a strong pressure recovery effect is found in the blunt cone near the nose region. On the other hand, no pressure recovery is observed in the sharp nose cone model. And the surface pressure gradually decreases in the downstream direction.

As shown in Fig. 24, the straight cone has constantly thickening shock layer as well as boundary layer; and the surface pressure keeps decreasing along the downstream direction. In addition, because of the nose bluntness difference, the flare cone with blunter nose shows strong entropy layer swallowing near the nose region in the Mach number contour.

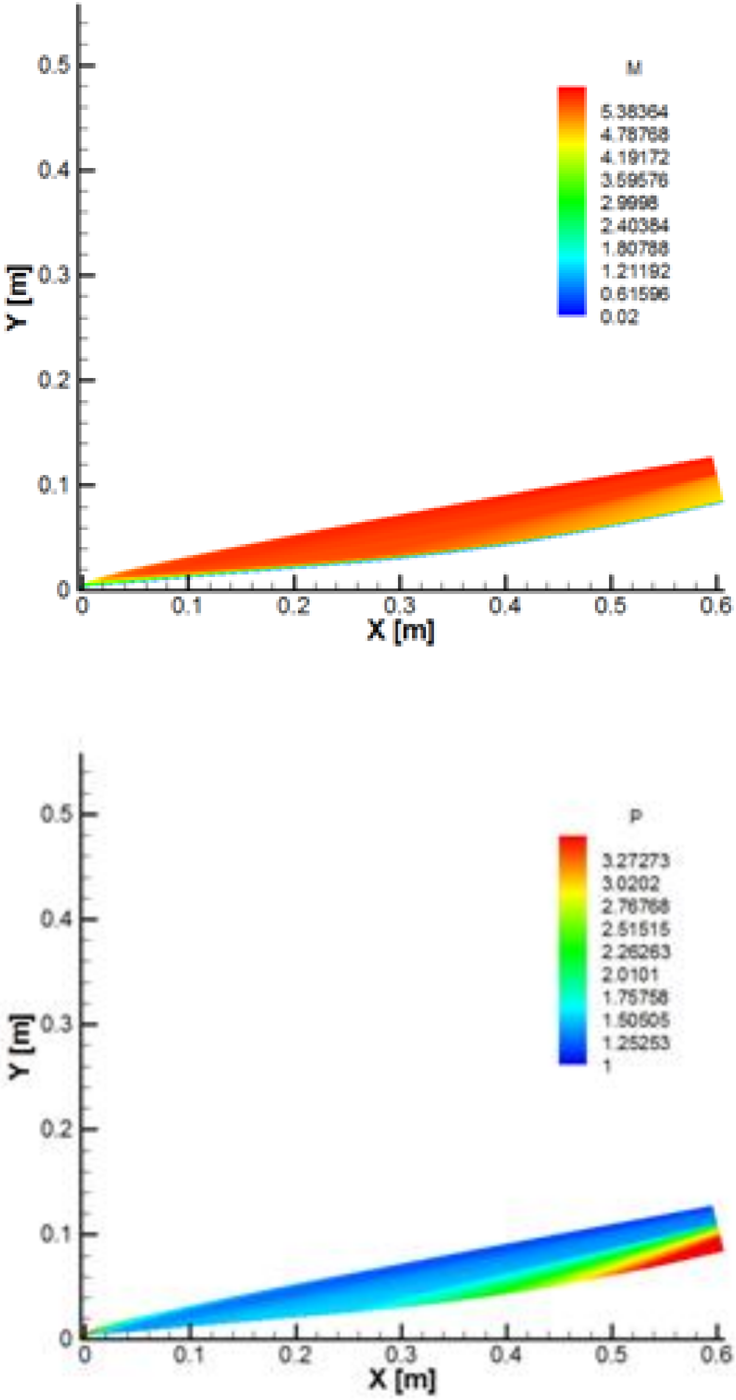

Fig. 23. Mach number contour and pressure contour for flare cone with 0.125 inch nose bluntness.

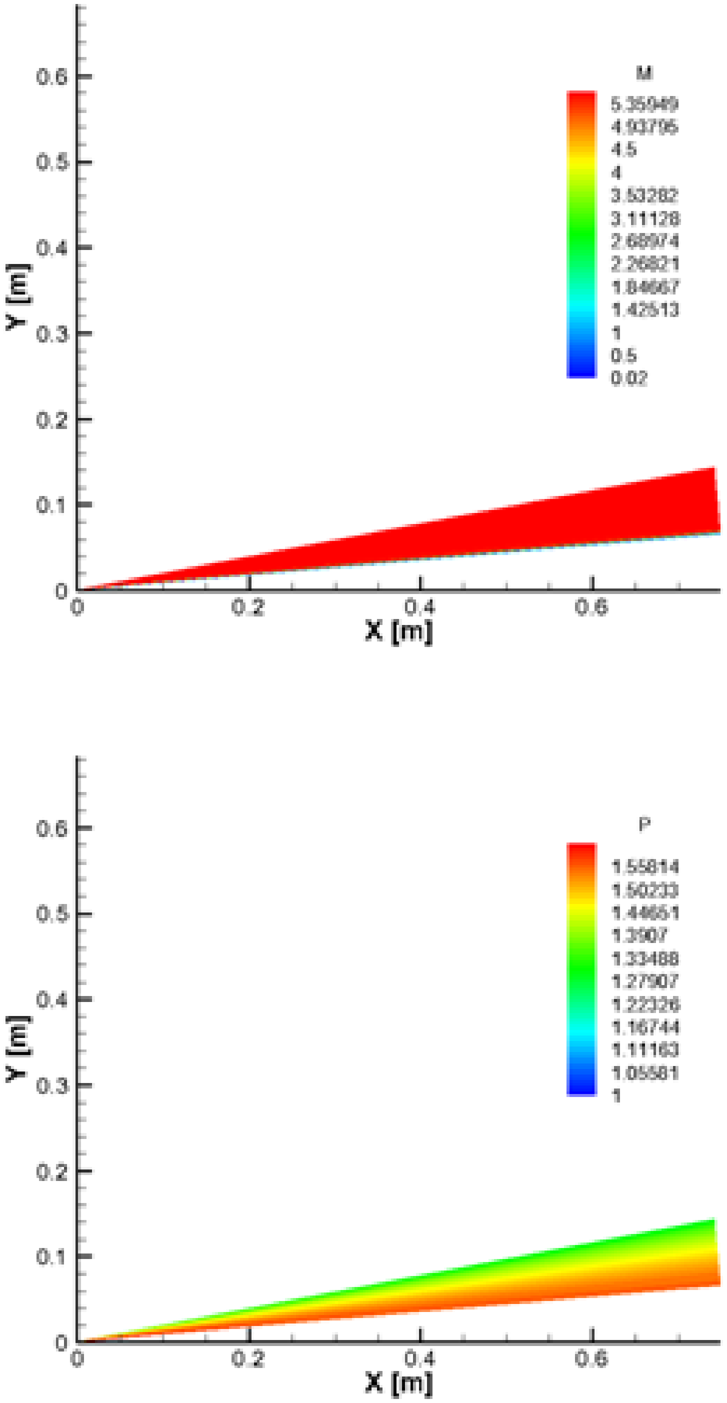

Fig. 24. Mach number contour and pressure contour for straight cone with 0.1 mm nose bluntness.

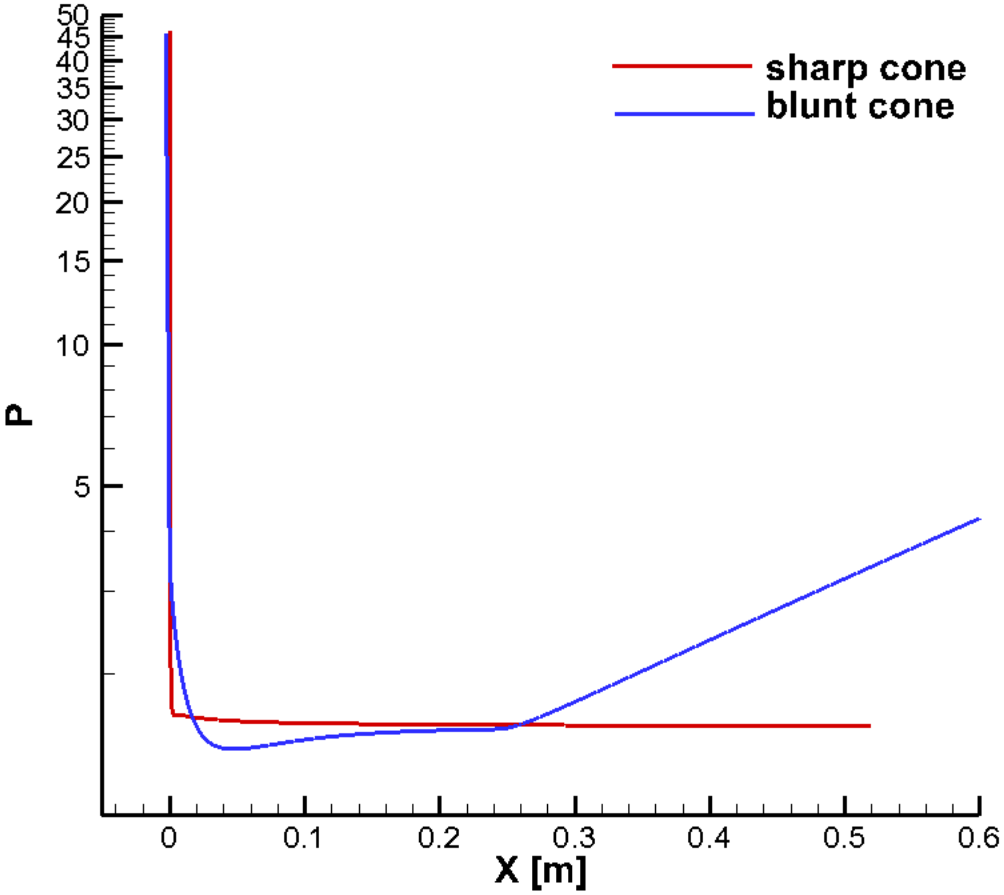

Fig. 25. Pressure along the cone surface normalized by freestream pressure for two different cone models.

5.2.2. Linear Stability Analysis

The LST calculations are performed using the meanflow simulation results from section 5.2.1 as the base flow solutions. The N factors are calculated to compare the linear stability characteristics of flow fields over two different cone models. Fig. 26 shows the N factor calculations of both cones for selected unstable frequencies. Due to the nose bluntness effect, the second-mode instability of the flared cone case is substantially delayed. The instability appears only on the flared portion of the cone thanks to the compression effect. The instability of the “shape” straight cone appears much earlier. In addition, a very interesting trend is observed on the flared cone model. For the “blunter” flared cone, the higher frequency wave becomes unstable at location further downstream, while the trend is opposite for the straight cone. This phenomenon can be explained by the compression effect on the flared cone that causes reduction of boundary layer thickness at further downstream location. And it is known that the unstable frequency is proportional to the boundary layer thickness. In other words, thicker the boundary layer is, the lower the unstable frequency will be.

Based on the LST calculations, the sharp straight cone has a slight higher overall N factor than the blunt flare cone; and the instability appears earlier in the flow field. In addition, the unstable frequency range for the “sharp” straight cone model is also slight toward the lower end compared to the flared cone. This observation is also consistent with the fact that the boundary layer of straight cone is constantly thickening in downstream direction.

In addition, the non-dimensional wave speeds of selected frequencies are presented in Fig. 27. The wave speeds are non-dimensionalized by the freestream quantity so that, the wave speed of 1 means the wave is traveling as the same speed as freestream flow. From the plots, all the wave speeds are below 1. From LST, that means all the unstable modes are from Mode S, the slow mode. The slow mode comes from the slow acoustic wave that travels with the speed low than flow speed. Also, the wave speeds of unstable modes are decreasing in the downstream direction for the flared cone model versus increasing for the straight cone model. This might be due to adverse pressure gradient that slowing down the traveling wave in the flared cone case.

Furthermore, the wave numbers of unstable modes are plotted in Fig. 28 for selected frequencies. These plots show that the wave number is generally higher for higher frequency. Unlike in the non-dimensional wave speed plots, the values of wave numbers remain quiet constant even the normal modes change from stable to unstable.

The LST analysis provides us the overall stability properties of flows over two different cone models. Moreover, it also assists in determining which case to focus on in the subsequent receptivity and breakdown simulations. Once the receptivity simulation is conducted, it can be also used to validate the simulation results in the linear growth region.

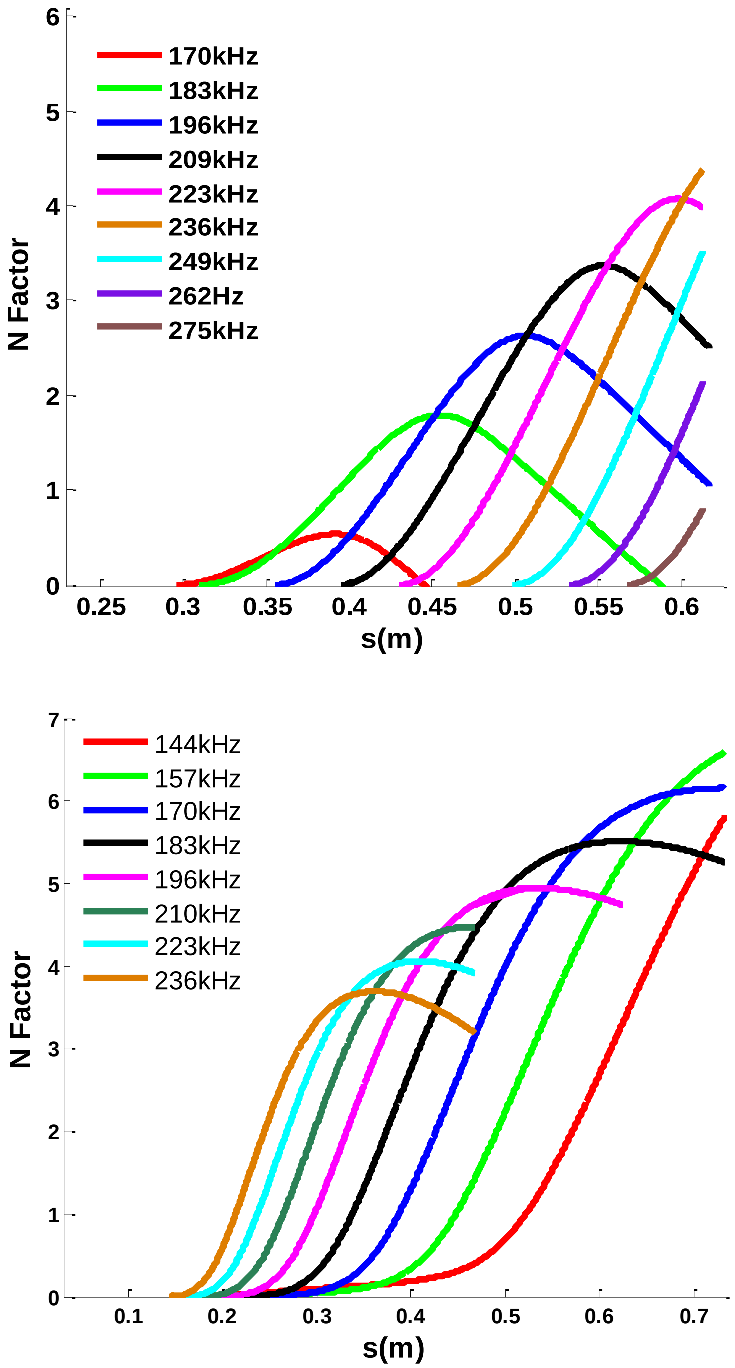

Fig. 26. *N* Factor for selected frequencies: (top) 0.125 inch flare cone, (bottom) 0.1 mm straight cone.

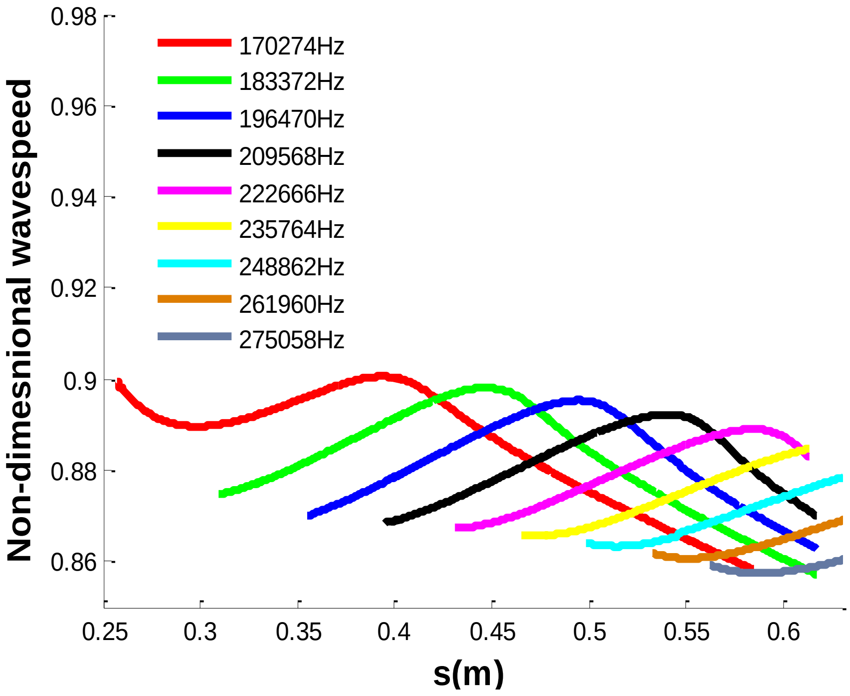

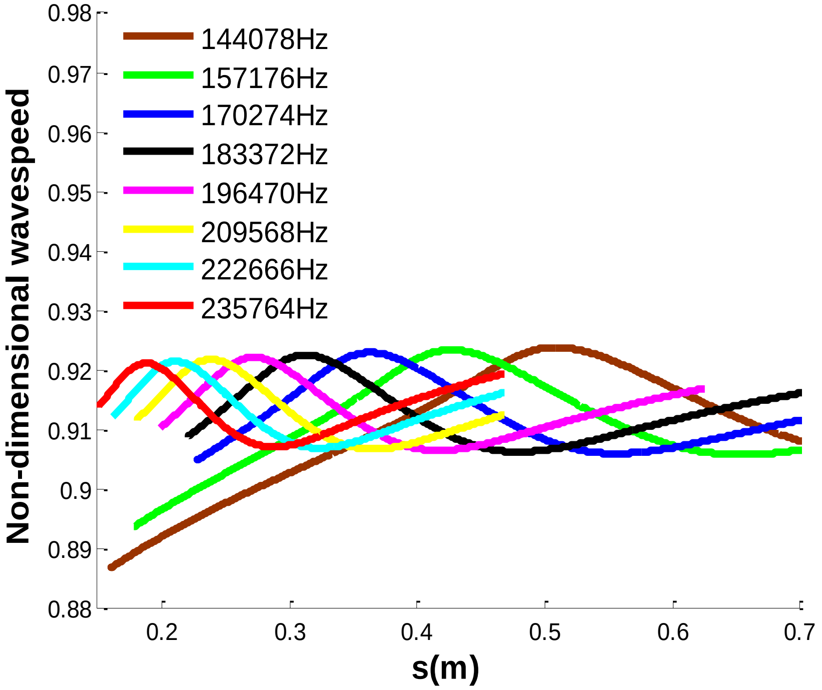

Fig. 27. Non-dimensional wave speed for selected frequencies: (top) 0.125 inch flare cone, (bottom) 0.1 mm straight cone.

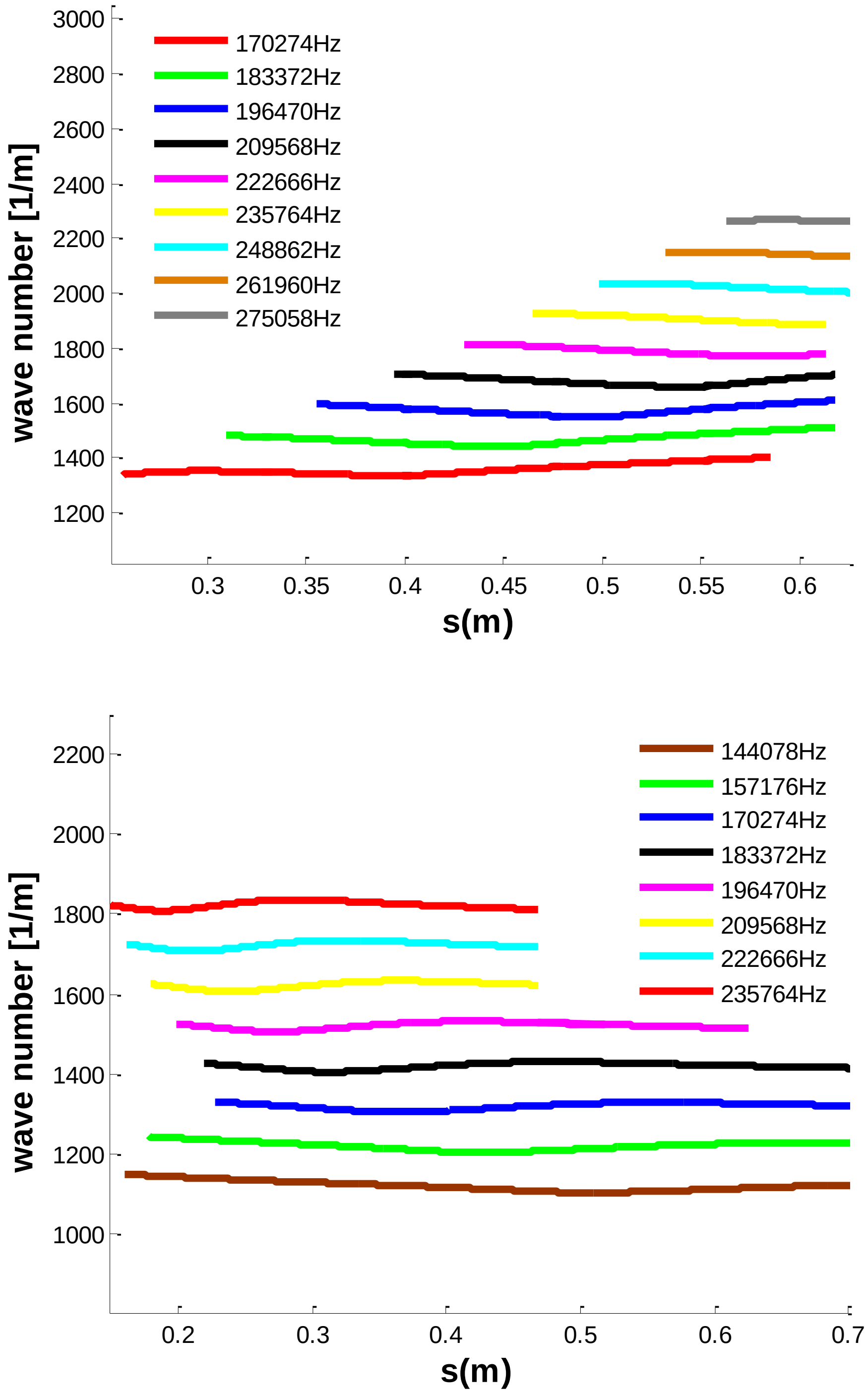

Fig. 28. Wave number for selected frequencies: (top) 0.125 inch flare cone, (bottom) 0.1 mm straight cone.

5.2.3. Linear Receptivity Simulation

As shown in Fig. 4, the second step of current numerical study is to conduct the linear receptivity simulation that captures the mechanism of freestream disturbance entering the bow shock and interacting with boundary layer. In the current study case, the newly developed Gaussian pulse model is utilized, so that the freestream disturbance that contains a wide range of continued frequency spectrum can be studied. By comparing the LST calculations of the two cones we used for this study, it is found that the sharp cone case has a higher overall N factor. So, it will make the simulation easier to reach the breakdown stage. Hence, for the receptivity simulation, we focus primarily on the sharp straight cone case. Since we have the meanflow for both cases, we decide to also use this opportunity to study the nose bluntness effects to the freestream receptivity. Therefore, the receptivity simulations in the nose region are conducted for both blunt and sharp nose cases. We consider using only one type of disturbance in this simulation to make the analysis easier. While, in reality, a combination of acoustic, entropy, and vorticity disturbance exists in the freestream.

In current receptivity simulation, only the fast acoustic freestream wave is considered. Fig. 30 shows the snapshots of pressure contour of the receptivity simulation at the nose region of the 0.125 inch nose radius. At the nose region, the freestream acoustic pulse passed the bow shock and hit the cone surface then bounces off. As the wave reflected back from shock and hit the cone surface again later at further downstream, the wave amplitude drops quickly and significantly during the wave reflection. During this entire process, the boundary layer modes are not yet excited within the nose region.

Nose region receptivity simulations are performed on both the cases with blunt (0.125 inch) and sharp (0.1 mm) nose radii. Fig. 31 shows the pressure disturbance amplitude spectrum at the nose tip. The pressure disturbance is normalized by the freestream wave spectrum. Therefore, the line in each plot represents the amplification ratios of pressure disturbance of the entire frequency range after the freestream wave passing the bow shock. The peak ratio of the blunt cone case is about 0.035 compared to the shape cone that has a max ratio about 0.085. It manifests that the freestream wave decays more on the blunter nose compared to sharper nose. This comparison also demonstrates the importance of freestream wave receptivity. Although the freestream amplitude is the same, the actual wave amplitude inside the boundary layer can be different depending on the nose radius of the cone leading edge.

More interestingly, two different responses are observed for the cones with different nose radii. For the 0.125 inch case, there are two peaks in the frequency spectrum at 190 kHz and 590 kHz respectively, while the sharp cone response shows no peak in the range of frequency showed. These peaks shown in the blunt nose case is believed to be caused by the resonance effect due to the bow shock stand-off distances. The resonance occurs when the forward traveling wave and the reflected wave bouncing back from stagnation point happen to be in phase. The resonance peak at 195 kHz matches with a simple calculation provided by Professor Hans Hornung from Caltech in our private communications. In his argument, along the stagnation line, the weak shock catching up with the strong shock is reflected as expansion wave. The frequency of which this could happen can be estimated by

$$f_s = \frac{1}{2\tau}, \tag{67}$$

Where f_s is resonance frequency and τ is the transverse time of acoustic wave from shock to body and back; and the transverse time can be estimated by

$$\tau = \int_0^{\Delta} \frac{ds}{u + c_0} + \int_{\Delta}^{0} \frac{ds}{u - c_0}. \tag{68}$$

In eq. (68), Δ denotes the shock stand-off distance. u and c_0 are assumed constant and linearly decreased from shock to body respectively. These assumptions are very consistent with the actual simulation results as demonstrated in Fig. 29.

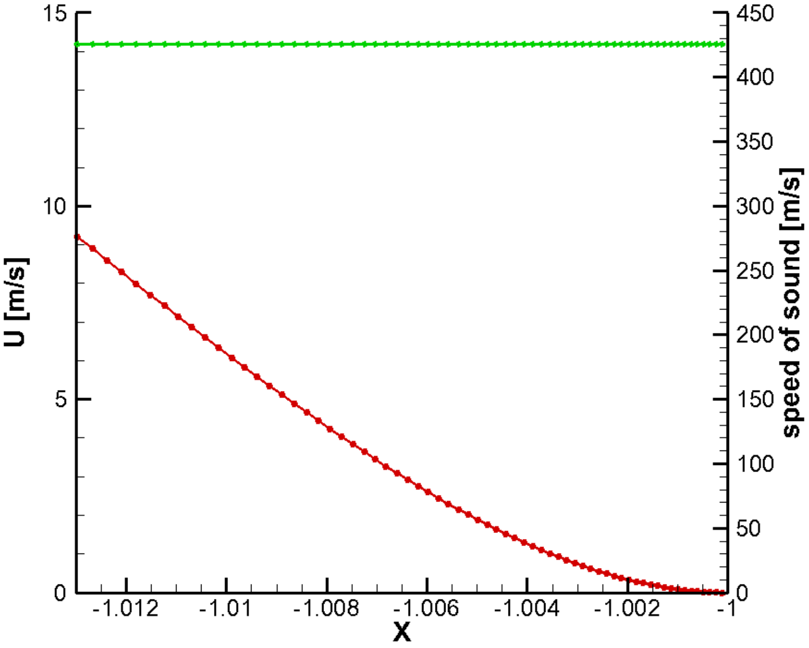

Fig. 29. Sonic speed (green) and flow velocity (red) along stagnation line of nose on TAMU 0.156 inch case.

Using these simplified models, the transverse time for current conditions can be estimated to be $\tau = \frac{2.1\Delta}{c_0}$. Plugging this back into eq. (67), we get

$$f_s = \frac{c_0}{4.2\Delta} = \frac{430}{4.2 \cdot 0.000495} \simeq 200 \text{ kHz} \tag{69}$$

This result is in good agreement with what we observed in the simulation. It suggests that, the resonance could occur in nose region that alters the wave disturbance response significantly.

Now, we know that the resonance frequency is sensitive to the shock stand-off distance. Looking at Fig. 32 , the shock stand-off distance of the 0.125 inch nose radius case is about 0.5 mm, but it is only about 0.02 mm for the 0.1 mm nose radius cone case. Therefore, for the blunter nose, there is a resonance in the frequency range of interest. For the sharp cone, the resonance only occurs at frequency 25 times higher which is about 5 MHz according to previous estimation. That is totally out of the frequency range we imposed in this freestream wave model. It explains why the resonance can only be observed on relatively sharp nose.

As the wave keeps propagating down into the straight cone portion, the boundary layer modes start to emerge as shown in Fig. 33. However, the amplitude of boundary layer modes sustains in the same order of magnitude as it moves further downstream indicating these modes are still stable. When the disturbances reach the unstable region as predicted by LST calculation, they quickly amplify. Fig. 34 shows the development of second mode instabilities in terms of time signals along the cone surface in more downstream locations.

From frequency spectrum, we can better track the evolution of wave disturbance as it propagates downstream along the cone surface. The disturbance wave amplitudes decay quickly in the nose region after passing through the bow shock. At the region after the nose, the wave spectrum keeps oscillating while remained at comparable level. In the surface locations between x=0.115 m and x=0.252 m, there is a weak growing first mode region at frequency below 200 kHz. The unstable frequencies quickly shift toward the lower end as they move downstream. The growth of first mode is very moderate. At further downstream location, as predicted by LST calculation, the second mode instability emerged. As shown in Fig. 35, starting from location X=0.185 m, a spike is observed around 300 kHz. The second-mode instability grows exponentially as it propagates in the downstream direction. Fig. 36 shows how the phase angles look across different frequencies before and after the instability wave becomes dominated. At the early region along the cone surface, an organized repeating pattern is observed across all frequencies indicated that the freestream forcing wave is the most dominant wave inside boundary layer at that location. However, in the lower figure, there is clearly a narrower pattern in the spectrum that distinguishes itself from other frequencies. This pattern falls into the second mode instability range.

The freestream wave receptivity simulation is carried up to x=0.57 m, where the most amplified wave reach an N factor about 6 according to the LST calculation. Fig. 37 shows the growths of disturbance waves for selected frequencies in the second mode frequency range. The general trends are qualitatively consistent to the LST calculations shown in Fig. 26.

To further validate current linear receptivity simulation, the simulation result is compared with the LST calculations of the sharp straight cone. Fig. 38 shows the DNS and

LST comparison of both growth rate and streamwise wave number of the disturbance wave at 150 kHz. Both mode F and mode S are calculation for this particular frequency. Since the disturbance wave is fast acoustic wave in nature, the mode F should be excited in the early stage of simulation where forcing wave is still dominant. According to LST prediction, the mode S becomes unstable second mode after the synchronization process that occur at around X=0.58 m. The simulation shows strong wave modulation before the synchronization point. However, once the unstable second mode appears, the modulation quickly diminishes; and the DNS result gradually converges to LST mode S result. Good agreement is obtained in the wave speed comparison between DNS and LST in the second mode region. However, the growth rate comparison is a bit difficult because the instability wave is modulated with the relatively strong freestream forcing waves that pass through the shock. As the instability wave becomes more and more dominated further downstream, the DNS growth rate tends to converge with the LST calculation. In addition, from the LST and DNS comparison, it is found that even the forcing wave is fast acoustic wave; the excited second mode instability is mode S which is from slow acoustic continued spectrum originally.

In summary, the freestream wave pulse model is successfully integrated into the receptivity simulation. The receptivity response of continued frequency spectrum is captured with the second-mode instability identified. The simulation result can be used to build the receptivity data base for future breakdown simulation. The simulation result is in agreement with the LST analysis from previous chapter. In addition, the receptivity in nose region reveals a resonance phenomenon that is sensitive to shock stand-off distance.

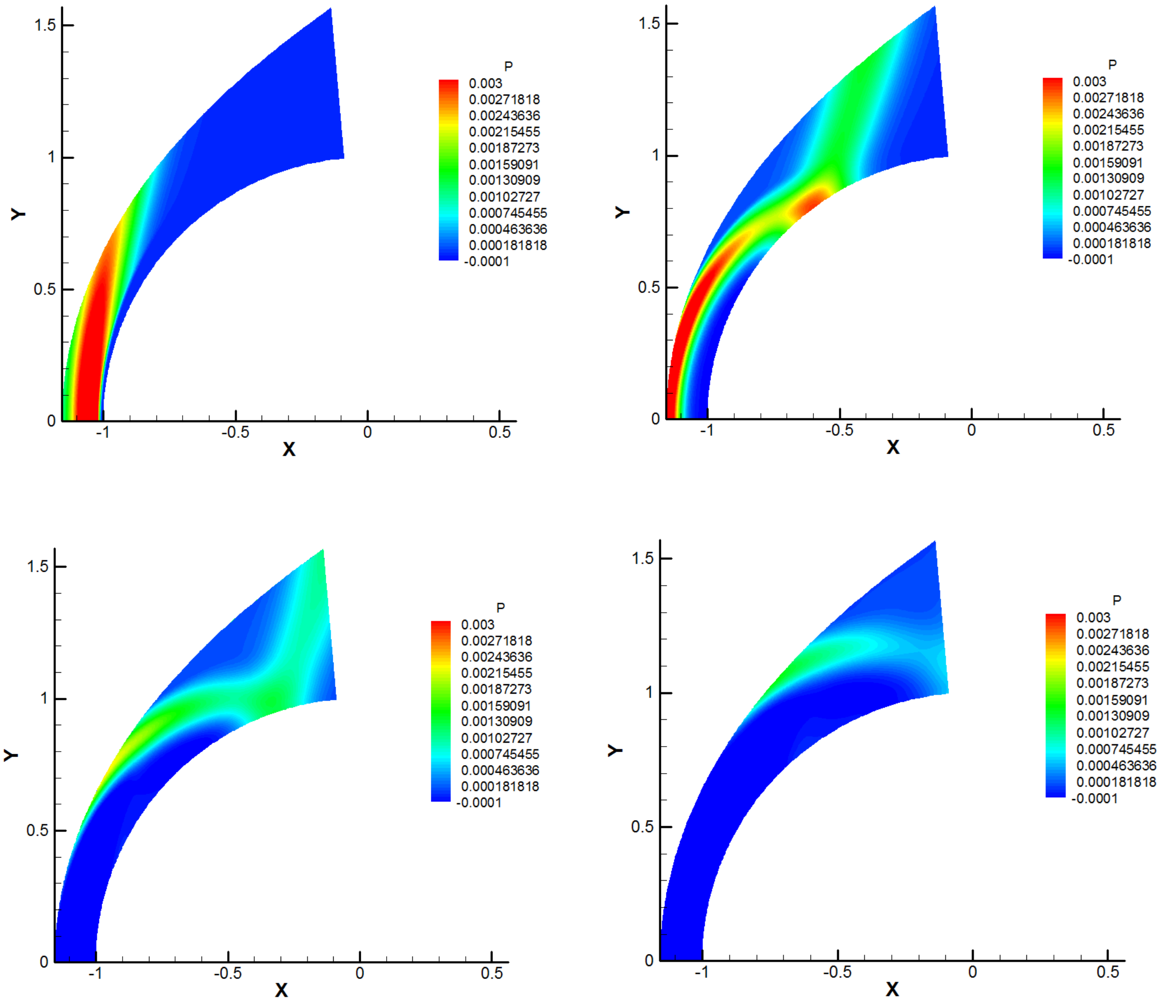

Fig. 30. Snapshots of pressure disturbance contour at the nose region of 0.1mm nose straight cone.

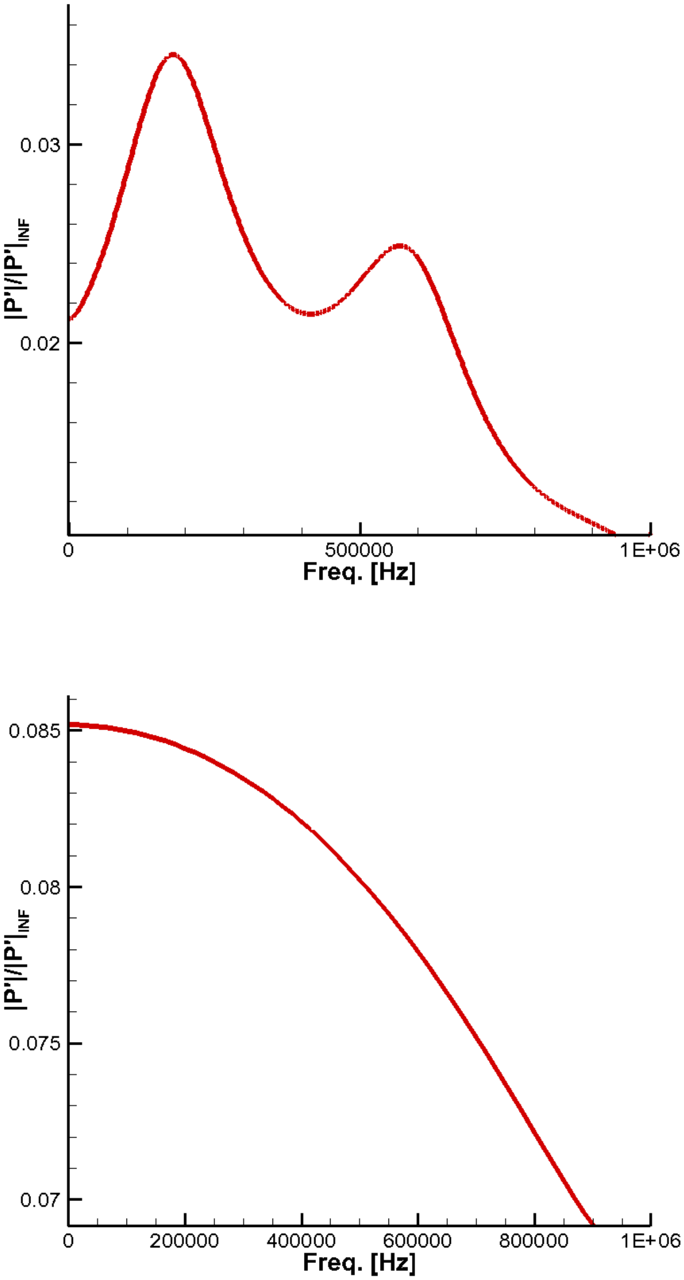

Fig. 31. Pressure disturbance spectrum normalized by the freestream: 0.125 inch nose (top), 0.1 mm nose (bottom).

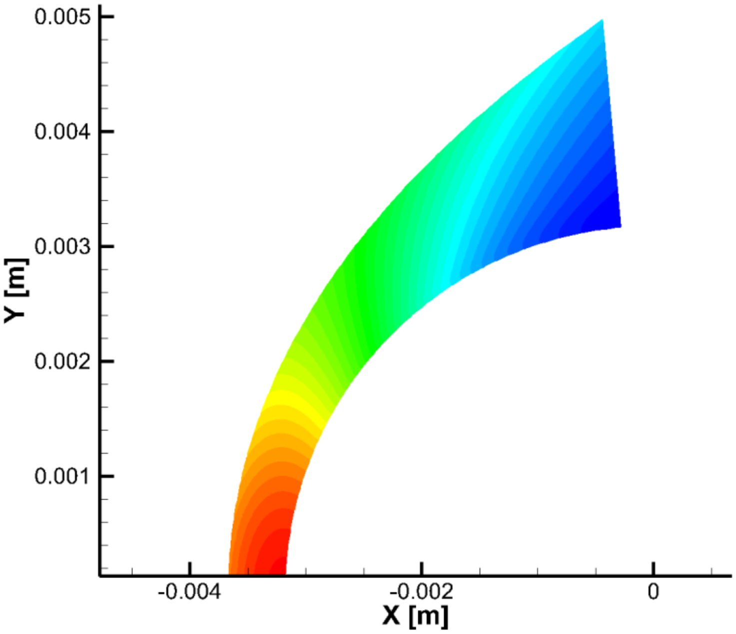

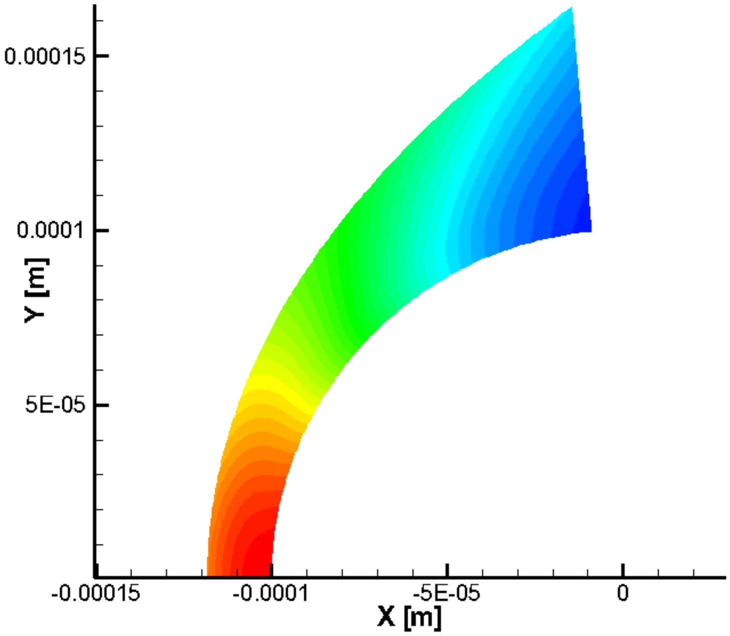

Fig. 32. Pressure contours of nose regions: 0.125 inch nose (top), 0.1mm nose (bottom).

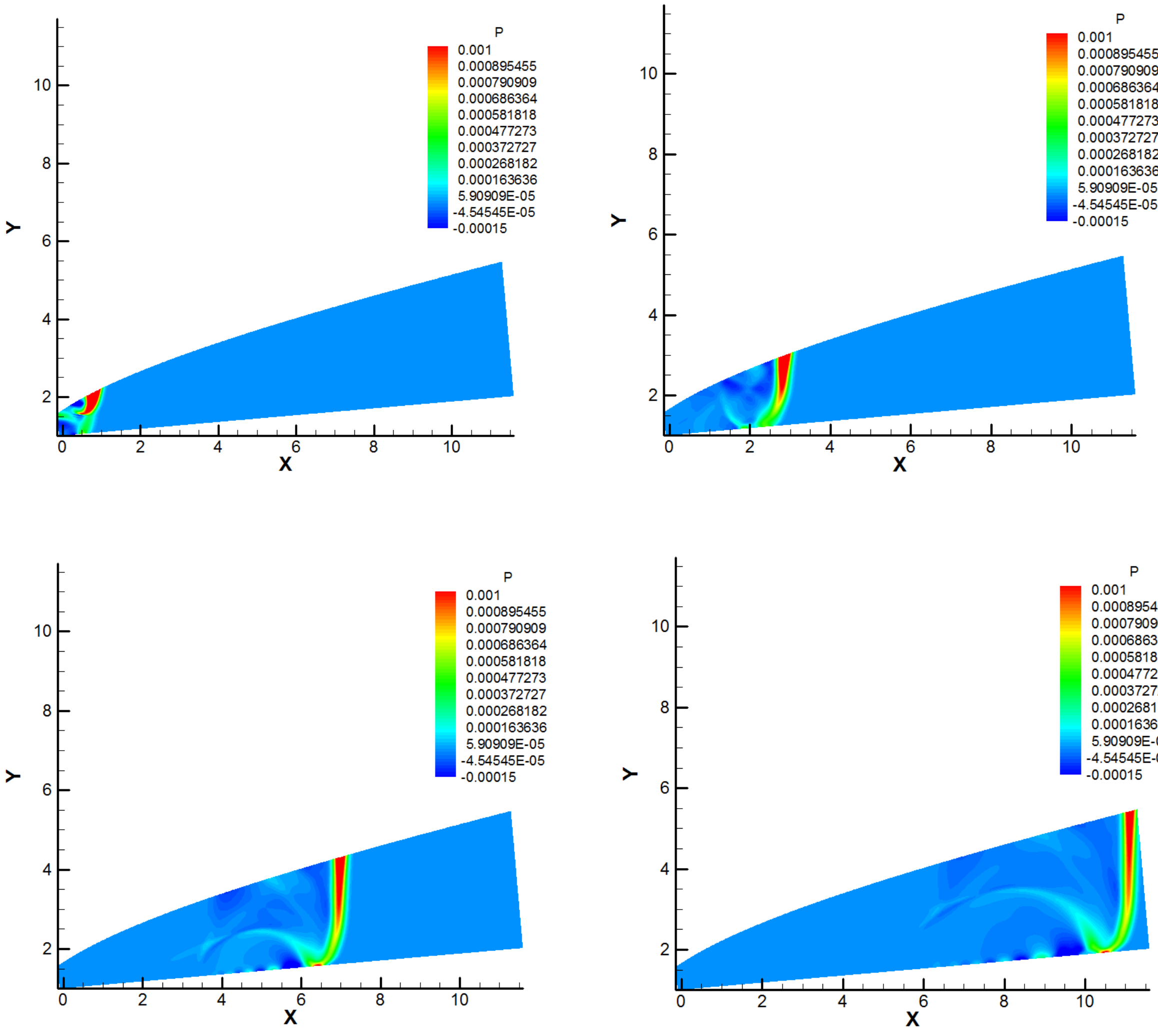

Fig. 33. Snap shot of pressure disturbance contours in the frustum of 0.1mm nose straight cone.

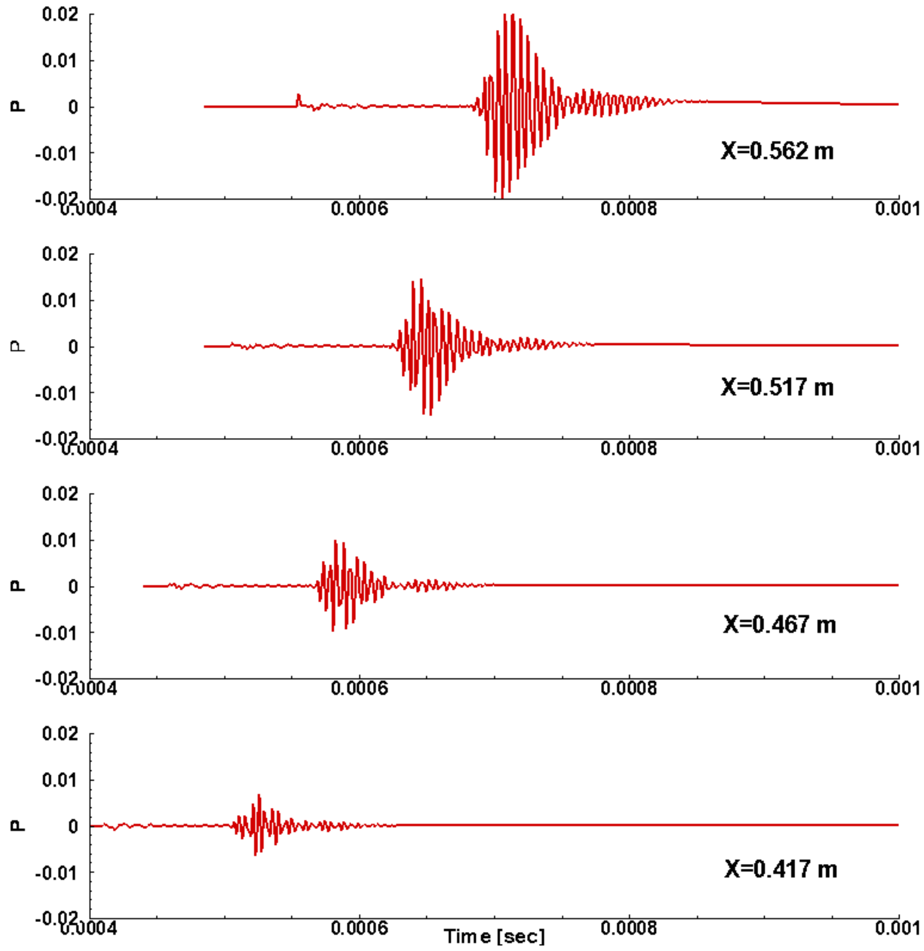

Fig. 34. Pressure disturbances time trace at different surface stations.

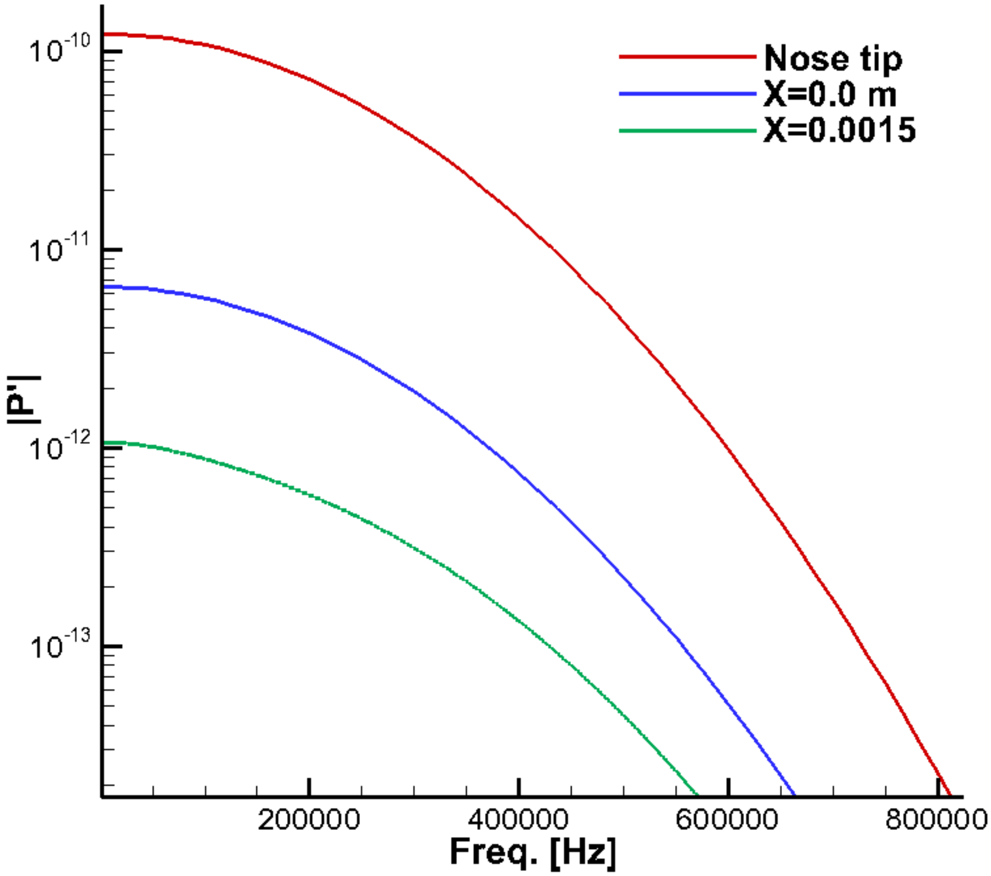
Nose tip
X=0.0 m
X=0.0015
10^{-10}
10^{-11}
10^{-12}
10^{-13}
|P'|
200000
400000
600000
800000
Freq. [Hz]

(a)

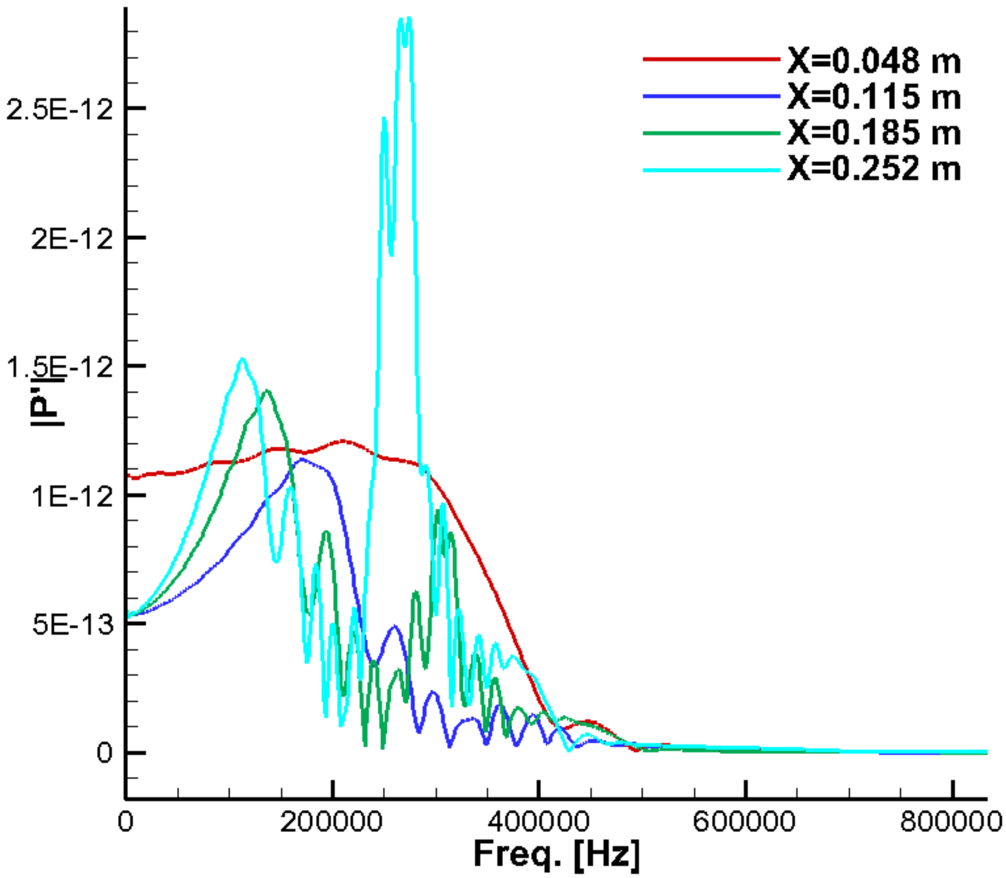

X=0.048 m
X=0.115 m
X=0.185 m
X=0.252 m
|P'|
2.5E-12
2E-12
1.5E-12
1E-12
5E-13
0
0
200000
400000
600000
800000
Freq. [Hz]

(b)

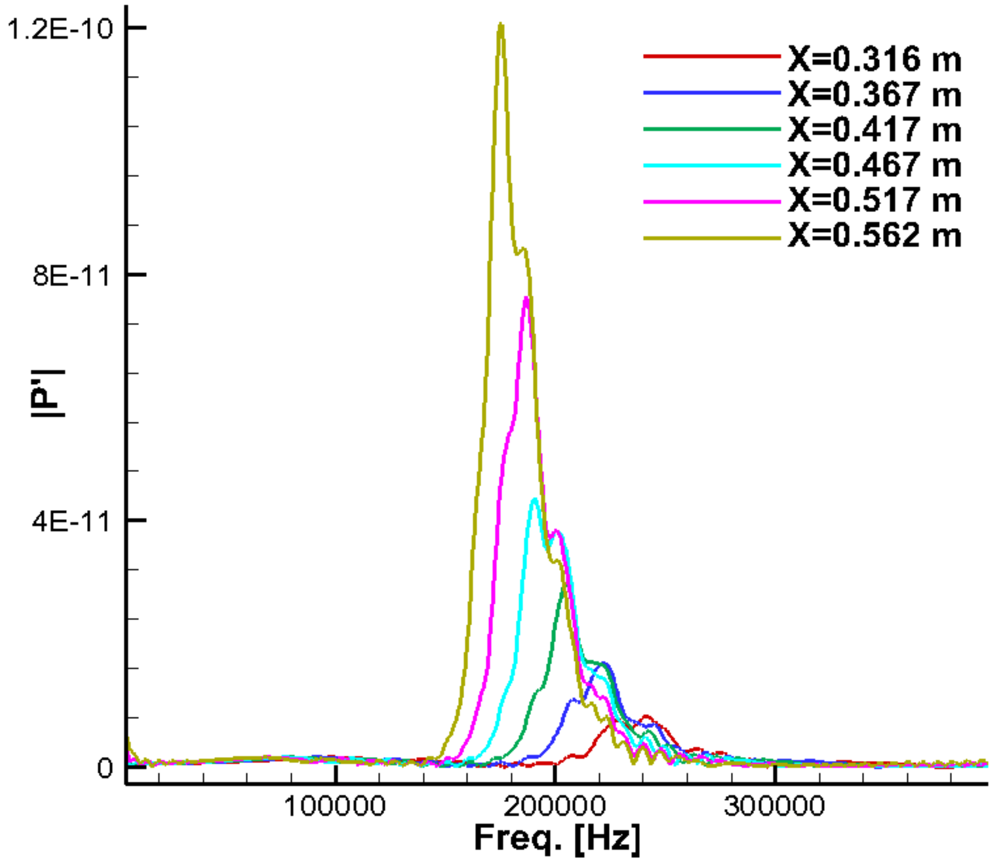

(c)

Fig. 35. Pressure Disturbances spectrum at different stations along the surface.

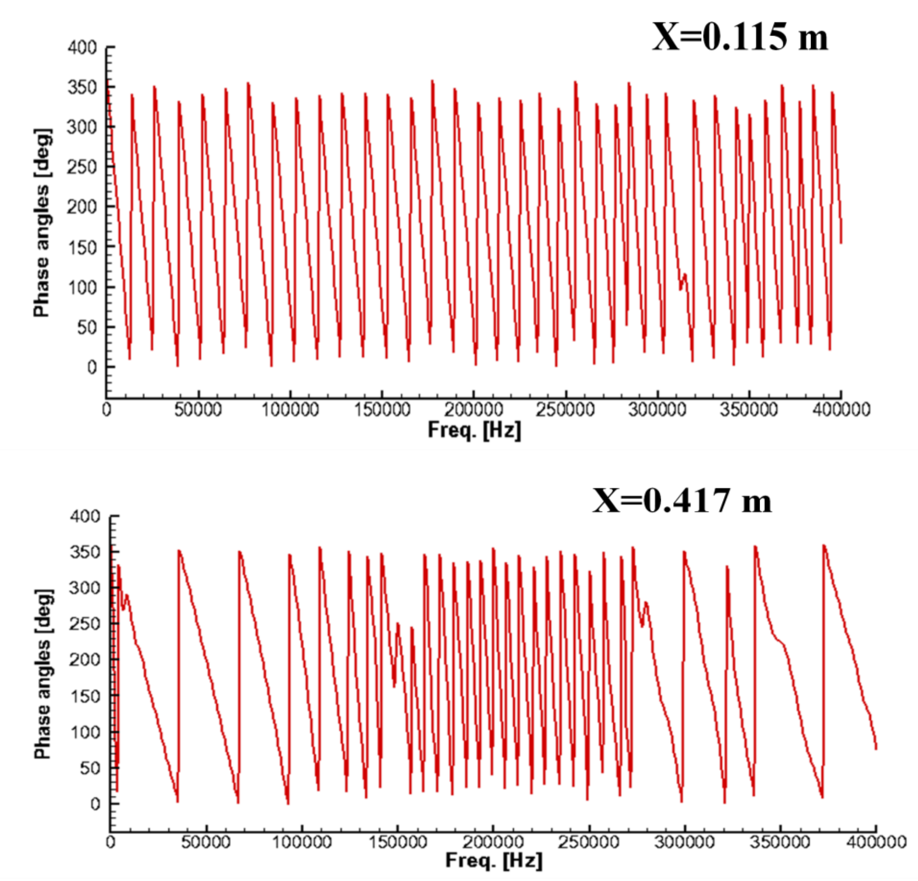

Fig. 36. Phase angles spectra on cone surface before and after the unstable modes become dominant.

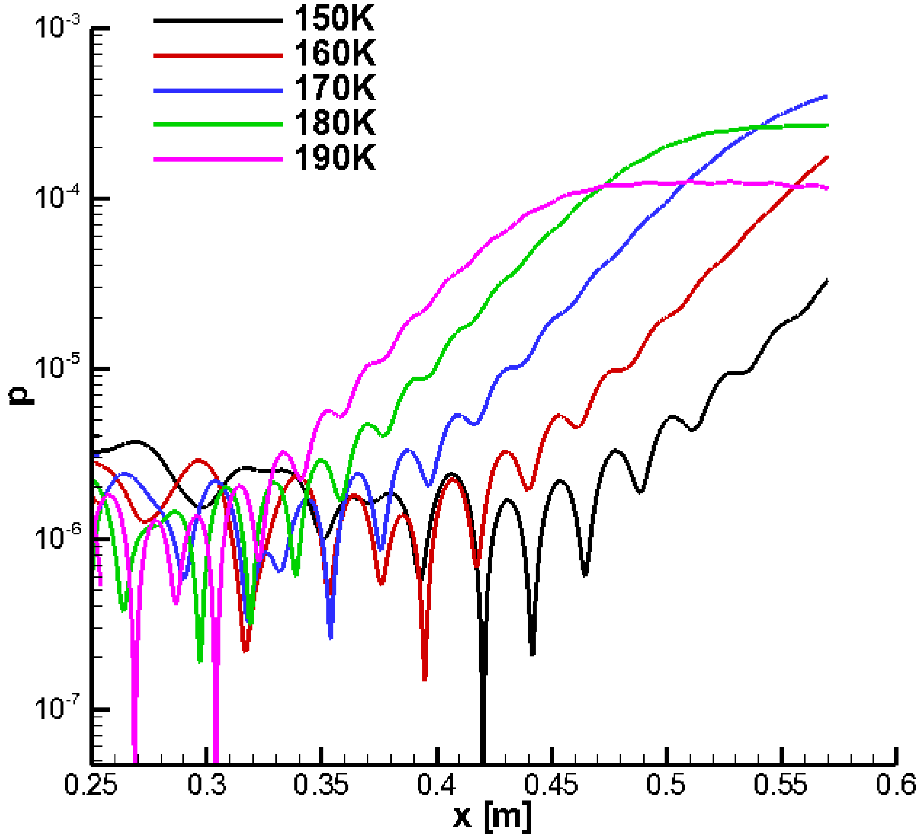

Fig. 37. Pressure disturbance along the surface at selected frequencies.

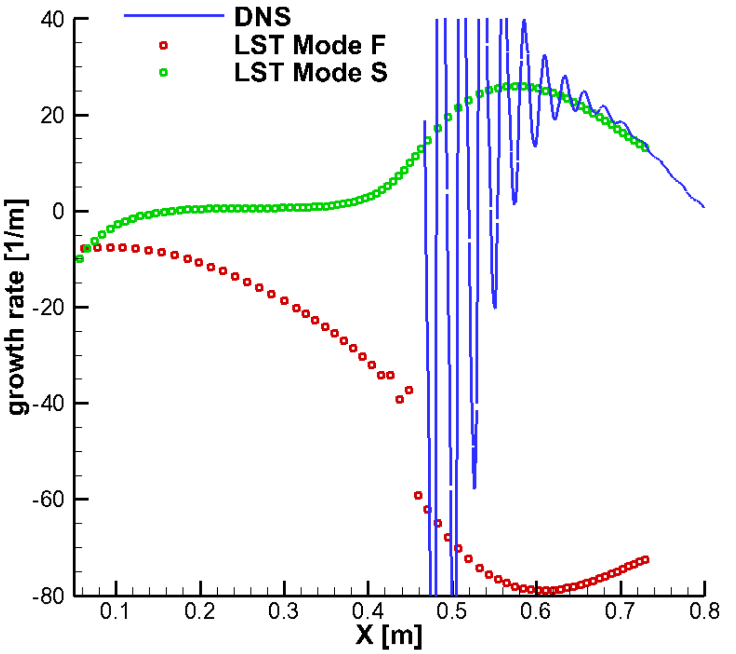

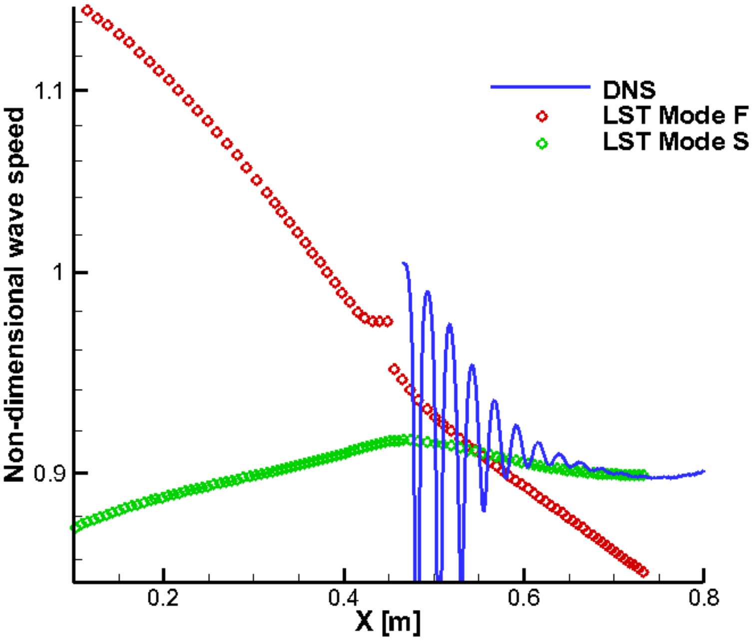

Fig. 38. Comparisons of DNS "—" and LST "o" results at 150 kHz for the 0.1mm nose bluntness case.

6. Nonlinear Breakdown Simulations

Nonlinear breakdown simulations are carried on both Stetson's Mach 5.5 case and TAMU Mach 6 case. Because of the nature of breakdown, the simulation needs to be performed on a three-dimensional computational domain. In order to conserve computational cost, only a small angle of arc in the spanwise direction of cone is simulated with periodic boundary conditions enforced. Since the effect of using only a small section of arc instead of the entire cone in the computation domain is not clear, parametric study is performed to investigate the simulation results with different spanwise arc angles and grid resolutions. The inflow conditions of nonlinear simulation are constructed using the receptivity response library obtained from preceding freestream wave receptivity simulation. Since the receptivity simulation is two-dimensional, it is necessary to enrich the spanwise wave number spectrum. This is achieved by adding low amplitude random noise at the inflow of computation domain. The simulation is carried until the flow reaches the breakdown stage. A buffer zone is used in computational domain to damp out the strong reflection wave near the exit of computational domain. Fig. 39 shows the schematic of the three-dimensional computational domain.

Due the limitation of discrete-frequency freestream wave model, the Stetson's Mach 5.5 case is used primarily for code development and validation purpose. Two study cases were conducted on Stetson's Mach 5.5 case on the cone with 0.156 inch nose radius. The first case used a blowing and suction hole on the surface near inlet to add disturbance into flow field. The second case utilized the freestream fast acoustic wave receptivity simulation result of the 0.156 inch nose case as source to disturbance. Table 2 lists all the study cases with detail parameters for each simulation.

The TAMU Mach 6 case is the primary investigation case used to study the nonlinear breakdown mechanisms. Parametric case studies are carried out to understand how the breakdown occurs and what wave modes is most relevant leading the flow from laminar to turbulent.

Table 2. Summary of study cases for Stetson's cone with 0.156 inch nose radius.

Case	Forcing type	Forcing amp.	Arc angle	Spanwise grid
BS1	Blowing-suction	0.05% of U_∞	6 degree	64
BS2	Blowing-suction	1% of U_∞	12 degree	128
FS1	Freestream + noise	5% of P_∞	6 degree	64

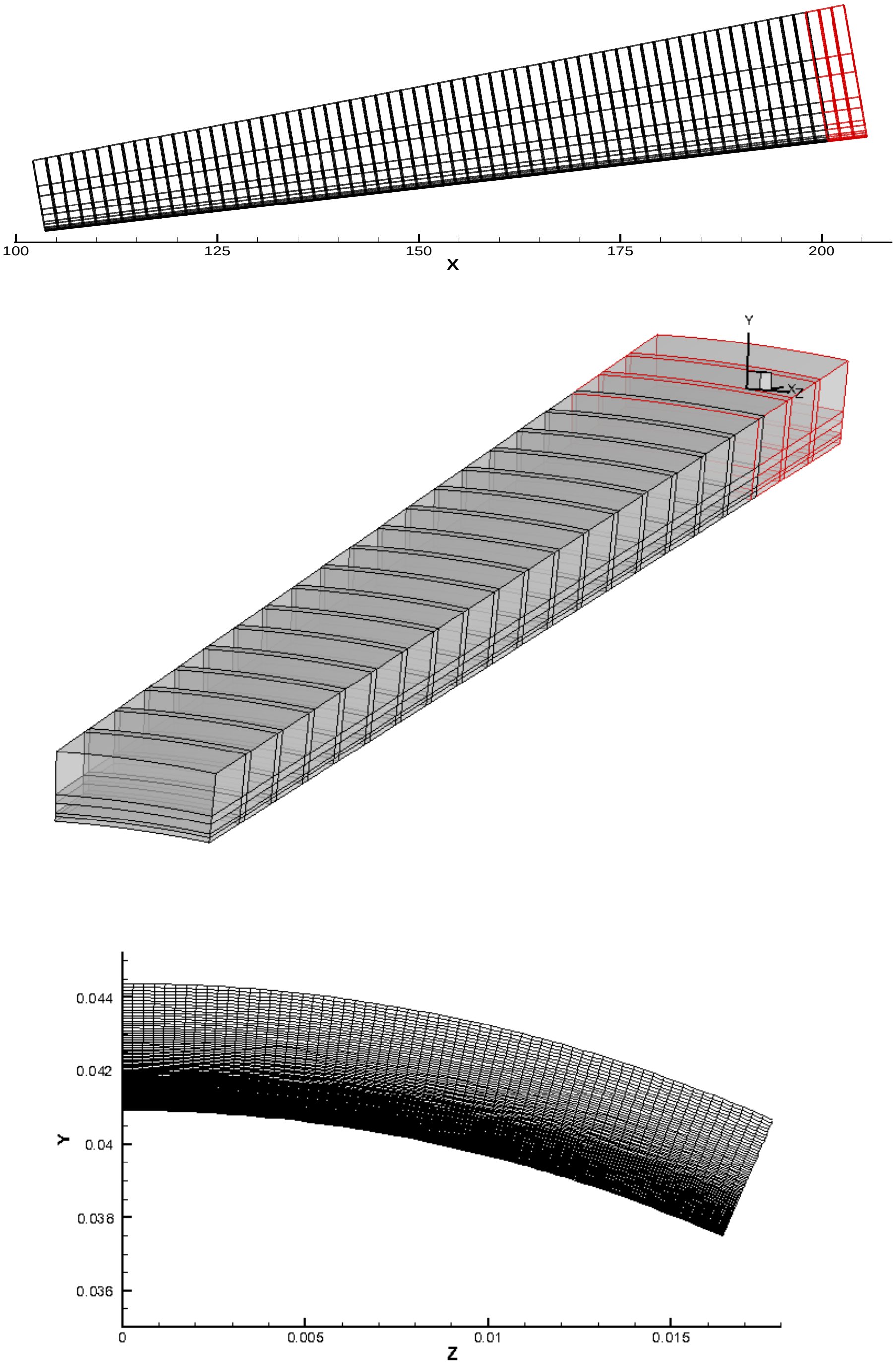

Fig. 39. Sample grid (side, perspective, and front view) of the breakdown simulation with sponge layer indicated in red.

6.1. Blowing and Suction Induced Breakdown

To validate the computation code changed mentioned in section 3.6 to accommodate the current research need, 3-D simulations using blowing and suction as source of disturbance are conducted. The grid sizes of these two cases were 1920x480 in stream-wise and wall-normal direction respectively. A blowing and suction hole is used to introduce the disturbance into flow filed so that the disturbance includes both two-dimensional and oblique angle wave components. The blowing and suction model is slightly modified from the one in previous two dimensional simulations using eq. (63). The blowing-suction hole is placed in the middle of computational domain near the inlet. 15 discrete frequency wave components range from 52.5 kHz to 788.26 kHz are imposed in this simulation.

In a cone configuration, the spanwise wave number is always an integer due to periodicity. For a fixed spanwise wave mode, the spanwise wave length is constantly increased as it travels downstream. For convenience, we define the span wise wave mode number as:

$$K = \frac{\pi d(x)}{\lambda_{\varphi}(x)} \tag{70}$$

K has the unit of [1/rev] instead of [1/m]. For example, K=100 represents a spanwise wave mode that repeats 100 periods in the spanwise direction at a given x location.

The BS1 case is the first three-dimensional test case used for code validation. Hence, we choose to perform a linear blowing-suction simulation to see if the linear wave behavior predicted by linear theory can be observed. The instantaneous pressure disturbance contour along the cone surface is presented in Fig. 40. The contour shows a localized two dimensional and periodic wave pattern until it reaches X=0.8 m, where the localized 2-D wave pattern suddenly fills out the entire computational domain in azimuth direction. This is the indication that the 2-D second modes become globally dominant.

The development of all wave modes can be visualized by the pressure disturbance amplitudes plotted in the spanwise wave mode number vs. frequency plane in Fig. 41. From the wave mode amplitudes plots, we can tell that the disturbance waves remain linear up to X=0.7 m; and the simulation results match the linear theory in that the 2-D second modes grow most rapidly and the growth of 3-D second modes decrease as the spanwise wave number becomes higher. At X=0.75 m, the higher harmonic wave appears which leads to rapidly development of high spanwise wave number modes within second-mode frequency range. Fig. 42 shows the phase angle evolutions of all wave modes from location to location along the downstream direction.

The growth of dominant wave modes within the second-mode frequency range are plotted in Fig. 43 for selected spanwise wave mode numbers. The amplitudes of pressure disturbance along the cone surface are plotted in log scales which clearly demonstrate the exponential growth of second mode instabilities at frequency f = 525.5 and 578.0 kHz. More attention should be paid to the wave modes at 630 kHz and 683 kHz. These two modes, according to LST calculations, should be decaying in the current computational domain. The wave modes follow the LST prediction until X=0.72 m, from where they start to amplify. The growths of wave modes at these two frequencies are an indication of nonlinear effect that essentially leads to secondary wave instability.

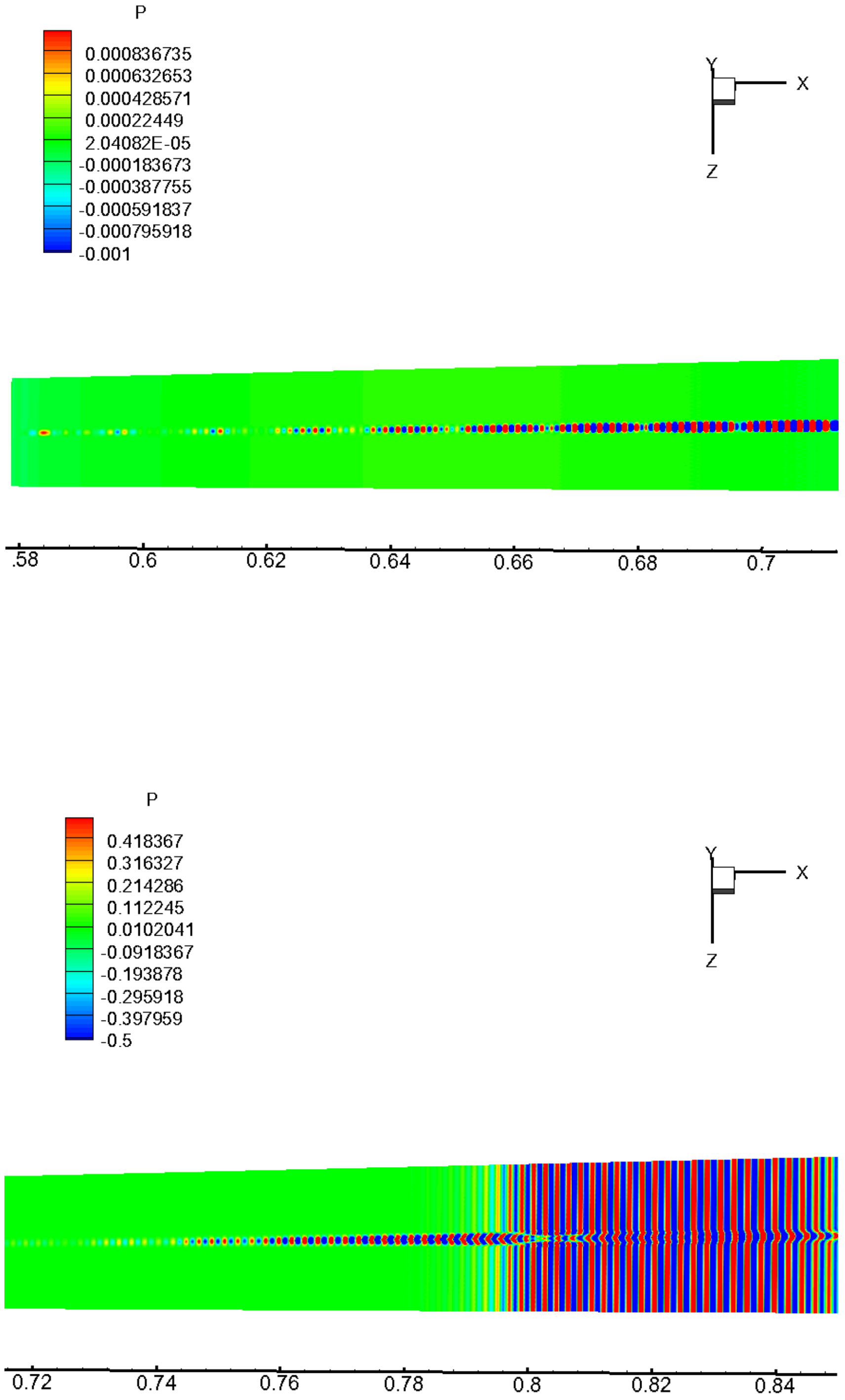

Fig. 40. Pressure disturbance contour along the cone surface.

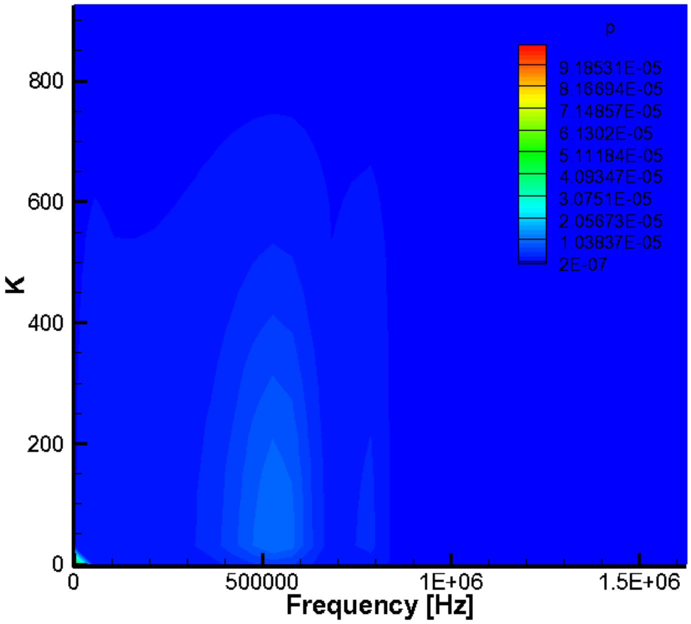
p
9.18531E-05
8.16694E-05
7.14857E-05
6.1302E-05
5.11184E-05
4.09347E-05
3.0751E-05
2.05673E-05
1.03837E-05
2E-07
K
0
200
400
600
800
0
500000
1E+06
1.5E+06
Frequency [Hz]

a)

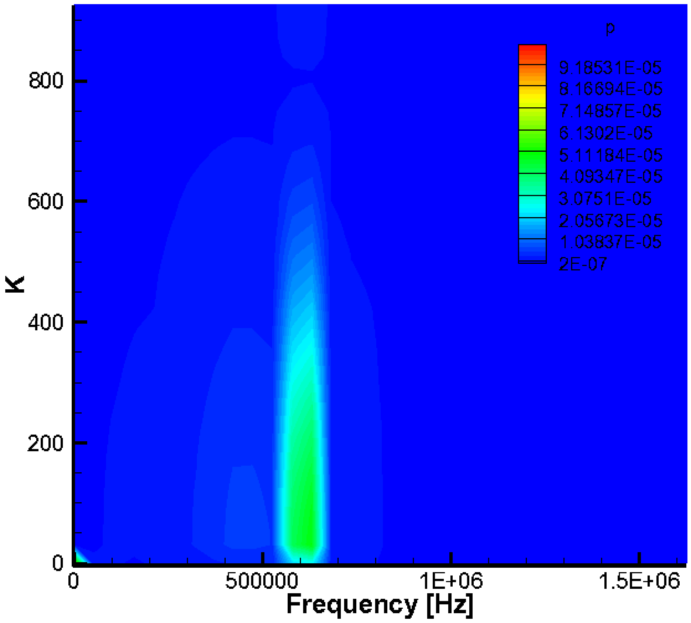
p
9.18531E-05
8.16694E-05
7.14857E-05
6.1302E-05
5.11184E-05
4.09347E-05
3.0751E-05
2.05673E-05
1.03837E-05
2E-07
K
0
200
400
600
800
0
500000
1E+06
1.5E+06
Frequency [Hz]

b)

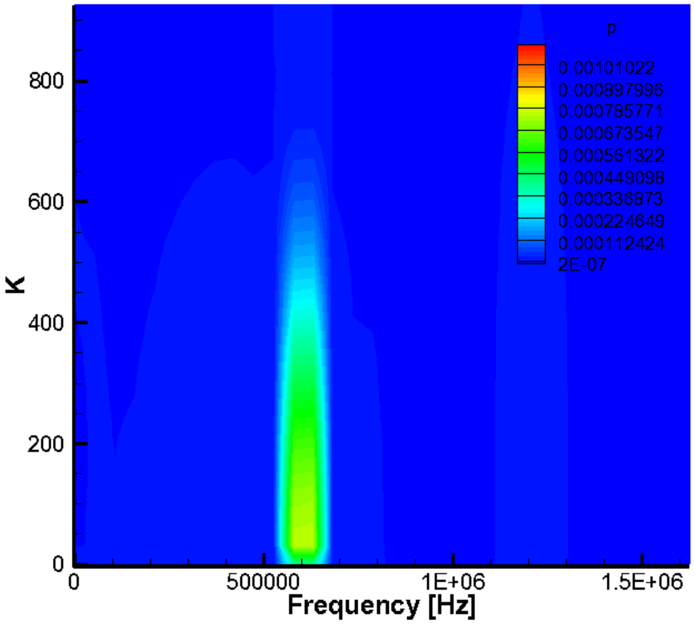
p
0.00101022
0.000897996
0.000785771
0.000673547
0.000561322
0.000449098
0.000336873
0.000224649
0.000112424
2E-07
K
0
200
400
600
800
0
500000
1E+06
1.5E+06
Frequency [Hz]

c)

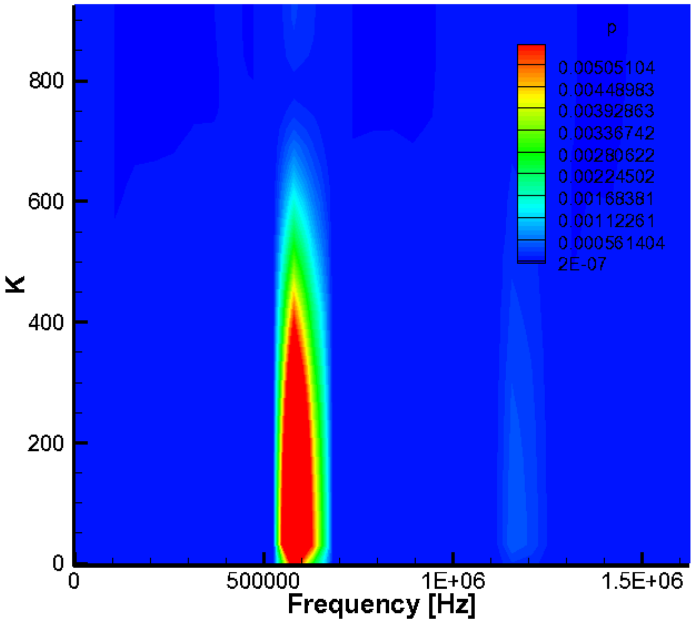
p
0.00505104
0.00448983
0.00392863
0.00336742
0.00280622
0.00224502
0.00168381
0.00112261
0.000561404
2E-07
K
0
200
400
600
800
0
500000
1E+06
1.5E+06
Frequency [Hz]

d)

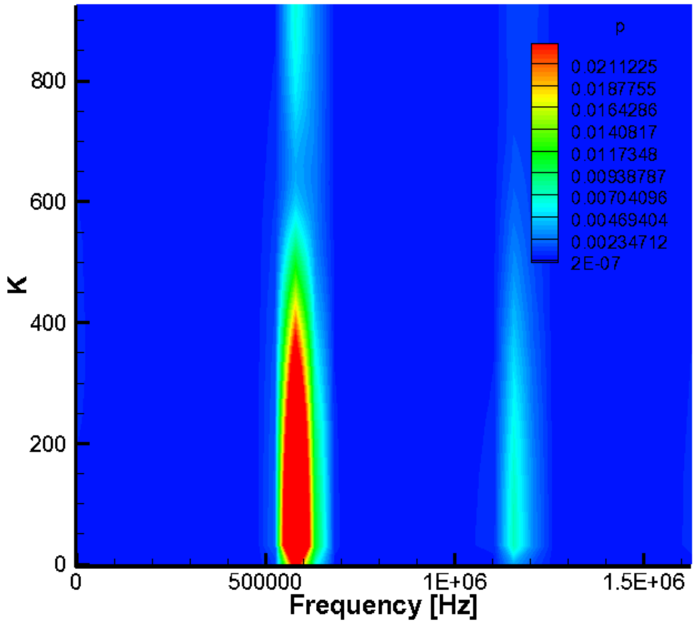

e)

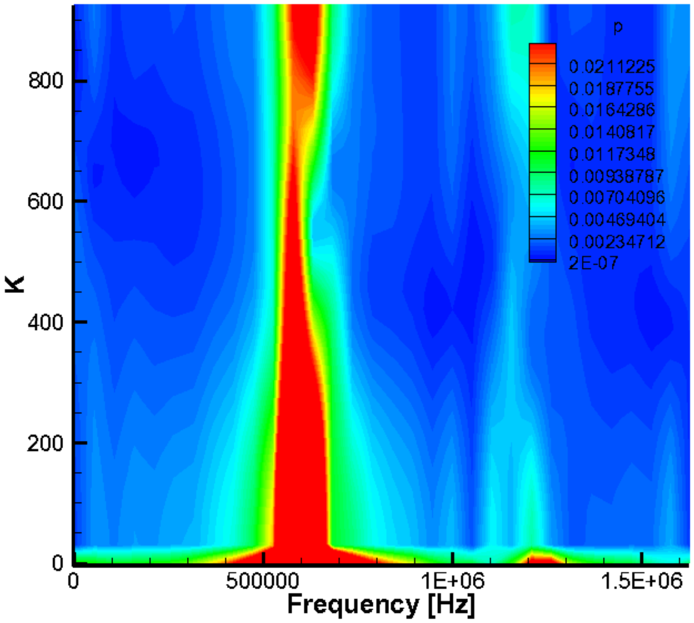

f)

Fig. 41. Frequency vs. azimuth wave number at different surface locations: a) X=0.6m, b) X=0.65m, c) X=0.7m, d) X=0.75m, e) X=0.8m, f) X=0.85m.

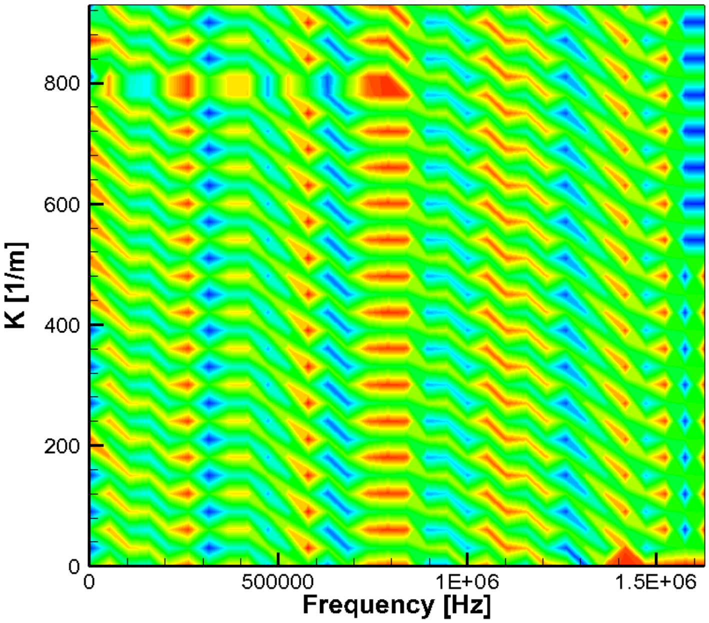
800
600
400
200
0
K [1/m]
0
500000
1E+06
1.5E+06
Frequency [Hz]

a)

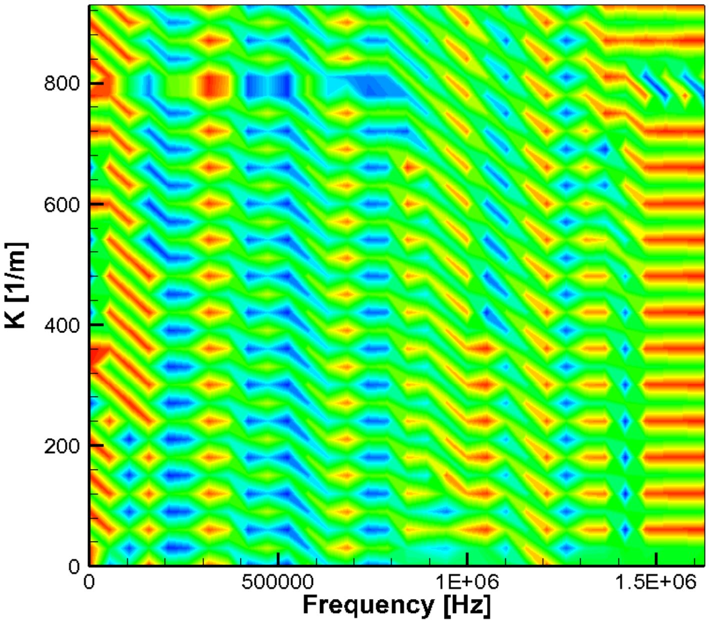
800
600
400
200
0
K [1/m]
0
500000
1E+06
1.5E+06
Frequency [Hz]

b)

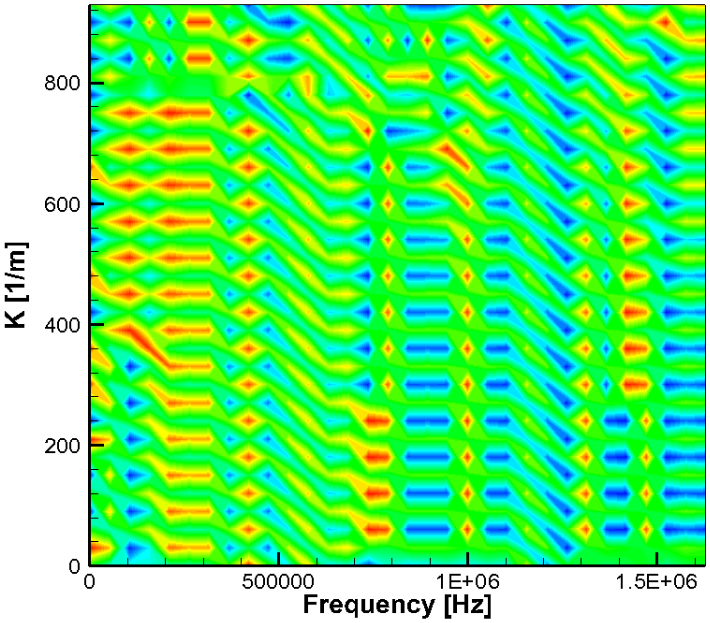
K [1/m]
800
600
400
200
0
0
500000
1E+06
1.5E+06
Frequency [Hz]

c)

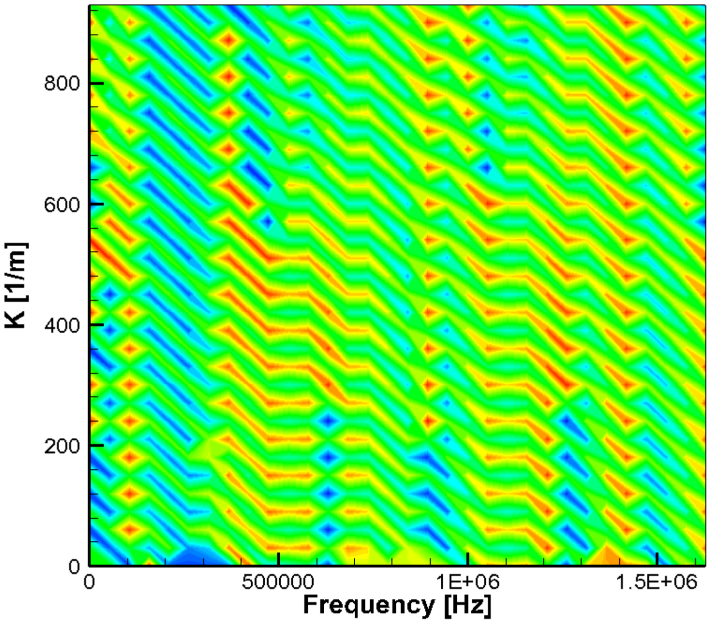
K [1/m]
800
600
400
200
0
0
500000
1E+06
1.5E+06
Frequency [Hz]

d)

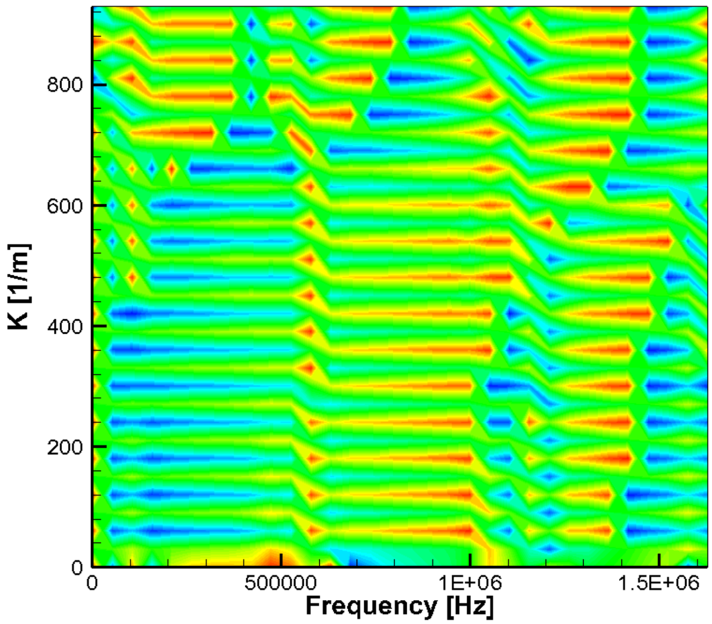

e)

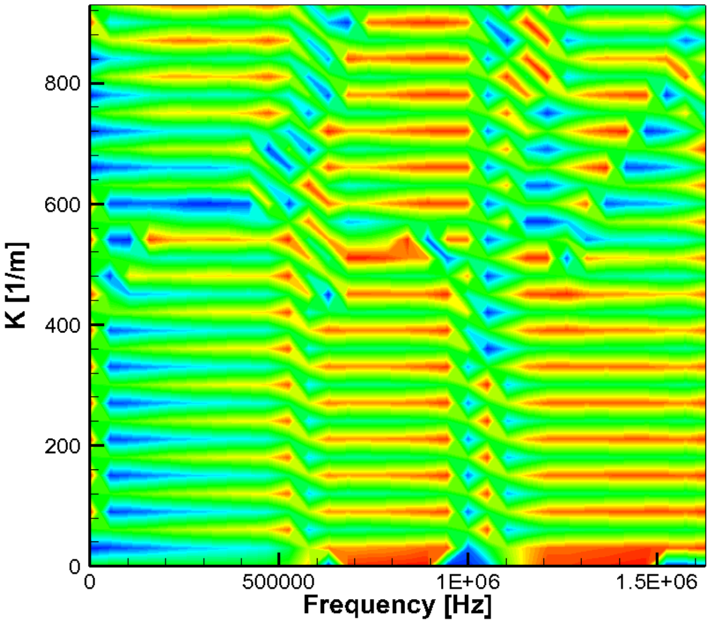

f)

Fig. 42. Spanwise wave number vs. Frequency of phase for all wave modes: a) X=0.6m, b) X=0.65m, c) X=0.7m, d) X=0.75m, e) X=0.8m, f) X=0.85m.

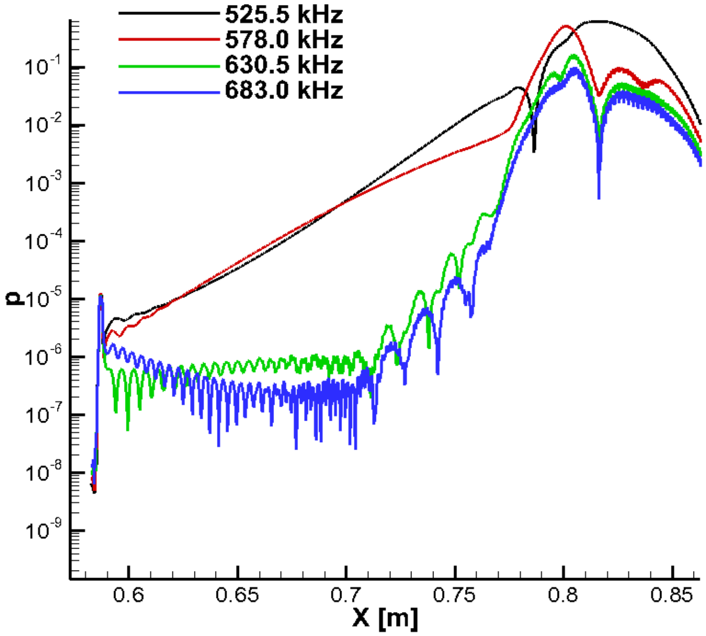
525.5 kHz
578.0 kHz
630.5 kHz
683.0 kHz
p
10^{-1}
10^{-2}
10^{-3}
10^{-4}
10^{-5}
10^{-6}
10^{-7}
10^{-8}
10^{-9}
0.6
0.65
0.7
0.75
0.8
0.85
X [m]

a)

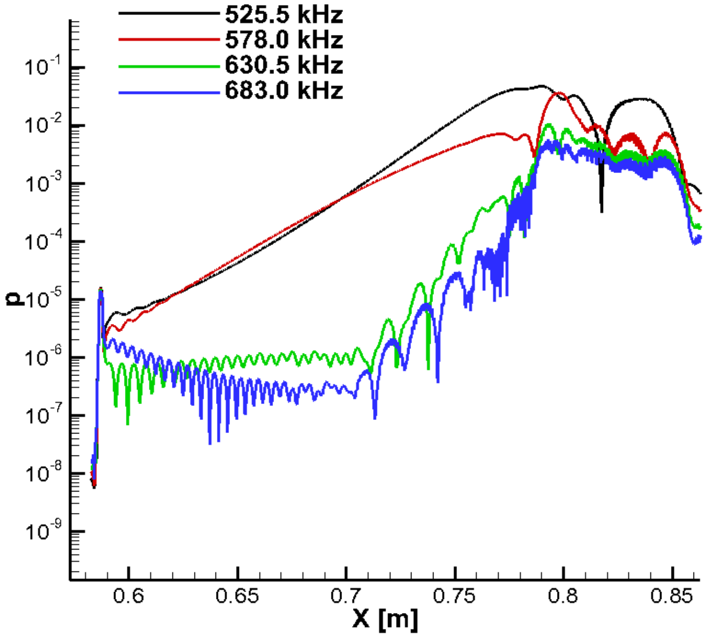
525.5 kHz
578.0 kHz
630.5 kHz
683.0 kHz
p
10^{-1}
10^{-2}
10^{-3}
10^{-4}
10^{-5}
10^{-6}
10^{-7}
10^{-8}
10^{-9}
0.6
0.65
0.7
0.75
0.8
0.85
X [m]

b)

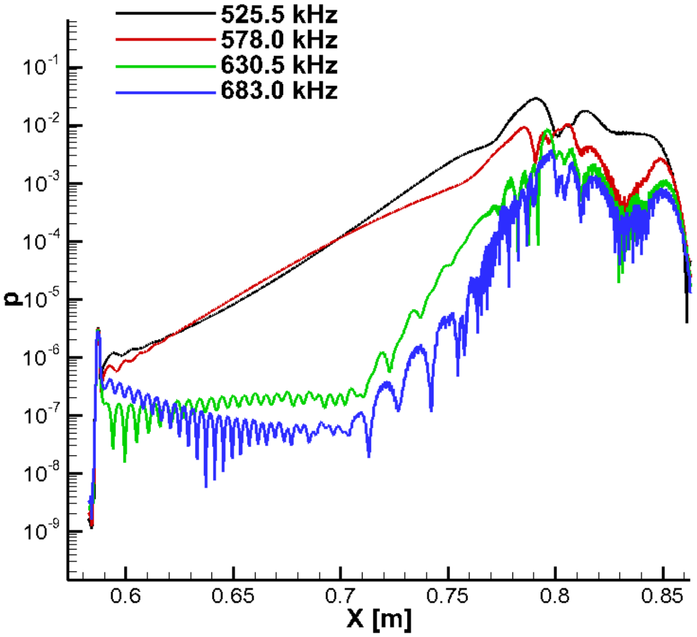

c)

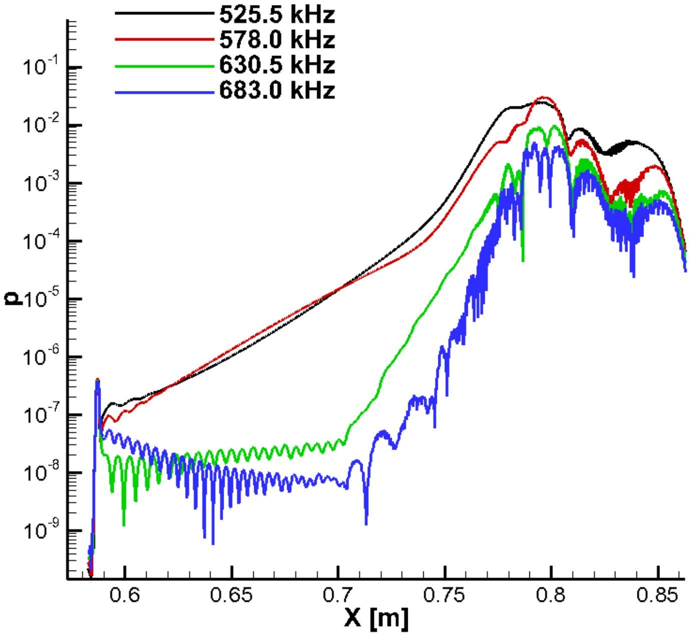

d)

Fig. 43. Selected frequency modes at different spanwise wave numbers: a) K=0, b) K=300, c) K=600, d) K=900

From the BS1 test case, we demonstrate that the modified 3-D simulation program is capable of capturing the linear growth of second-mode instability. BS2 case is the nonlinear version of BS1 case to further test the nonlinear capability of program. In this simulation, the forcing amplitude is increased by 20 times relative to BS1. The pressure disturbance contour along the cone surface as shown in Fig. 44 is significantly different from the linear case (Fig. 40). The localized two-dimensional wave patterns are not observable in this case in the entire computational domain. At the region near exit of computational domain, three dimensional wave patterns develop at the center of flow filed indicating the flow is undergoing breakdown process.

From the pressure disturbance amplitude spectrum plots in Fig. 45, the higher harmonic waves show up as early as at X=0.65 m. This is an indication that the flow is entering nonlinear stage. The strong nonlinear interactions between wave modes lead to energy spreading from high amplitude second modes toward the near-by frequency modes at the same spanwise wave number. The more thorough breakdown occurs at X=0.83m. The phase angle plots are also provided in Fig. 46 to compare with the linear case.

The pressure disturbance amplitudes of dominate wave modes are presented in Fig. 47. There is no clear exponential growth region in the current test case as compared to the linear case. Instead, the growths of dominant wave modes become very oscillatory. This modulation manifests strong nonlinear interactions between wave modes. Another obvious difference between the linear and non-linear case is that in the linear case, waves at 630 kHz and 683 kHz are decaying near the inlet of computation domain. They only start to grow when the disturbance wave reach saturation level which is around X=0.72 m in BS1 case. For the non-linear case, they are growing from the very beginning of the simulation domain due to highly nonlinear forcing wave amplitude.

In summary, the 3-D simulations are conducted successfully using blowing and suction hole as source of disturbance. The simulation results validate the code development and provide some understanding the both linear and nonlinear growth behaviors of hypersonic boundary layer unstable modes.

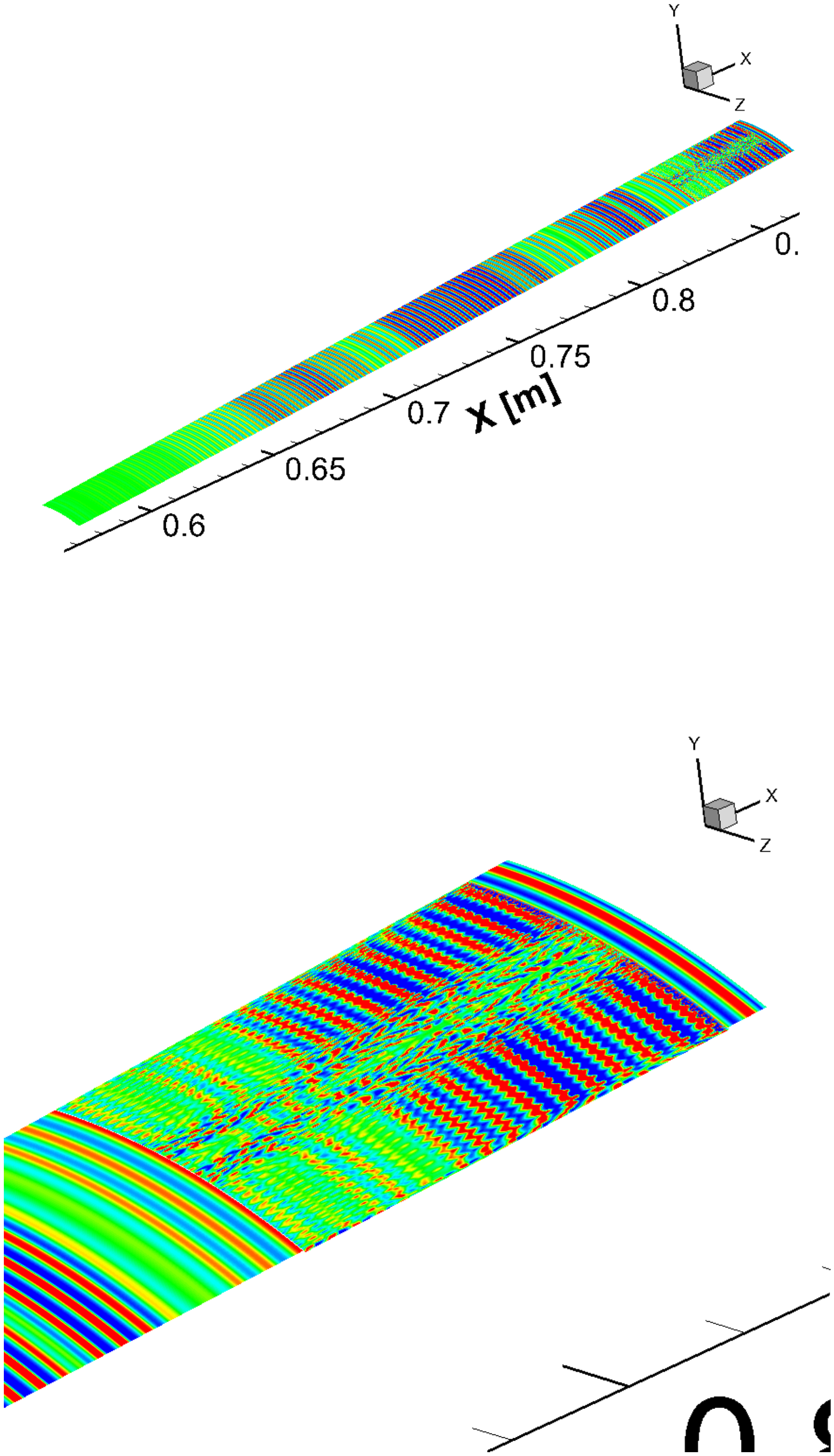

Fig. 44. Pressure disturbance along the surface and the blow-up view of the breakdown region.

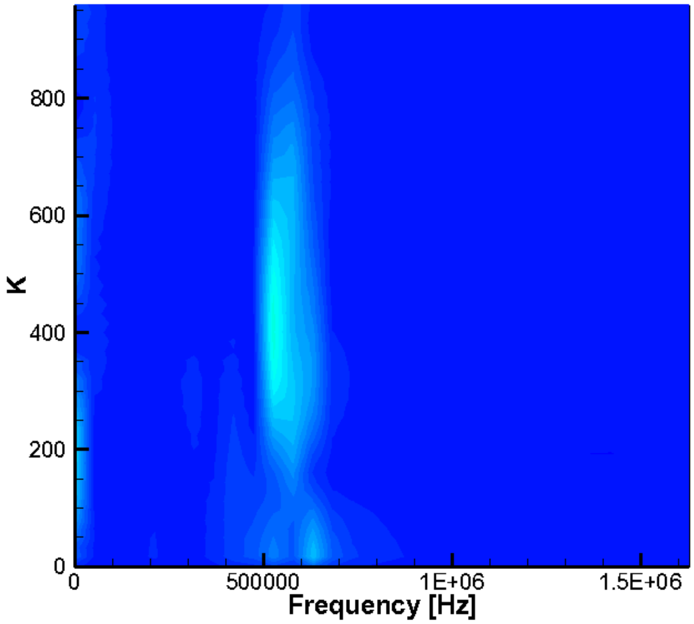
800
600
400
200
0
K
0
500000
1E+06
1.5E+06
Frequency [Hz]

a)

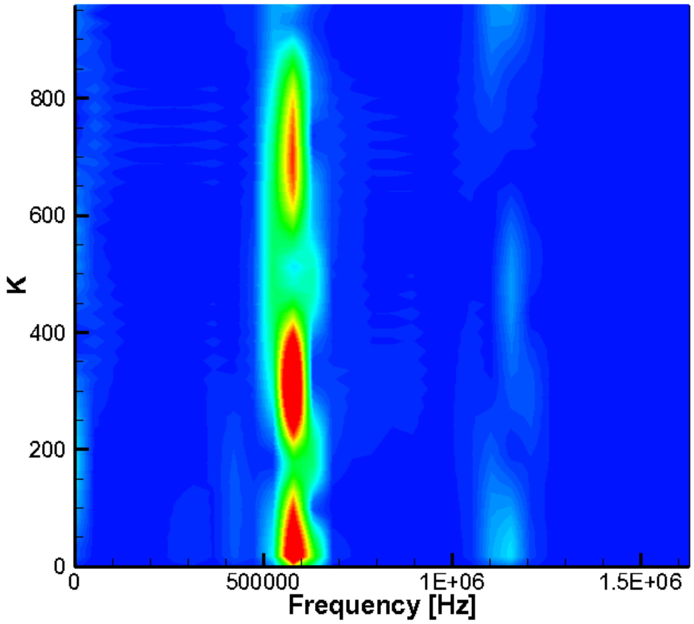
800
600
400
200
0
K
0
500000
1E+06
1.5E+06
Frequency [Hz]

b)

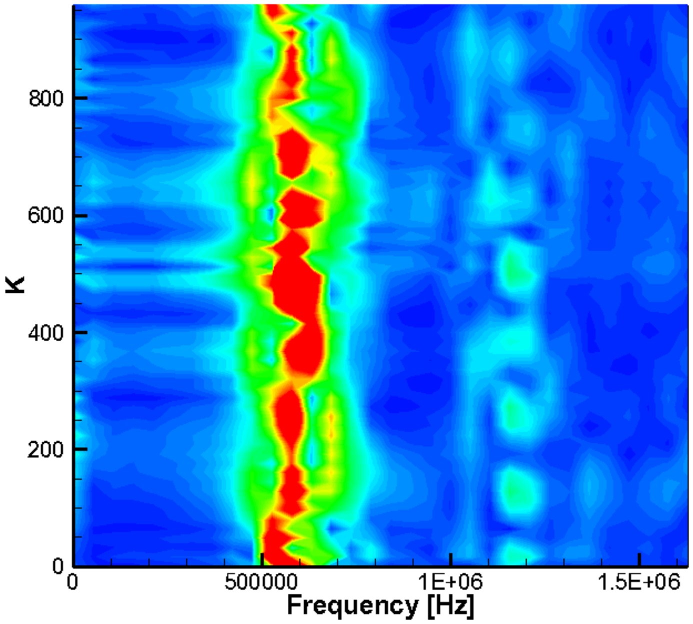
800
600
K
400
200
0
0
500000
1E+06
1.5E+06
Frequency [Hz]

c)

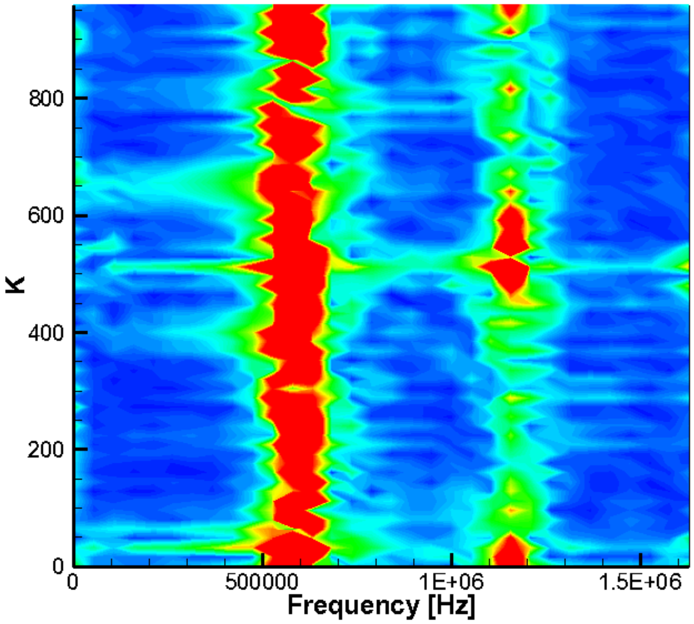
800
600
K
400
200
0
0
500000
1E+06
1.5E+06
Frequency [Hz]

d)

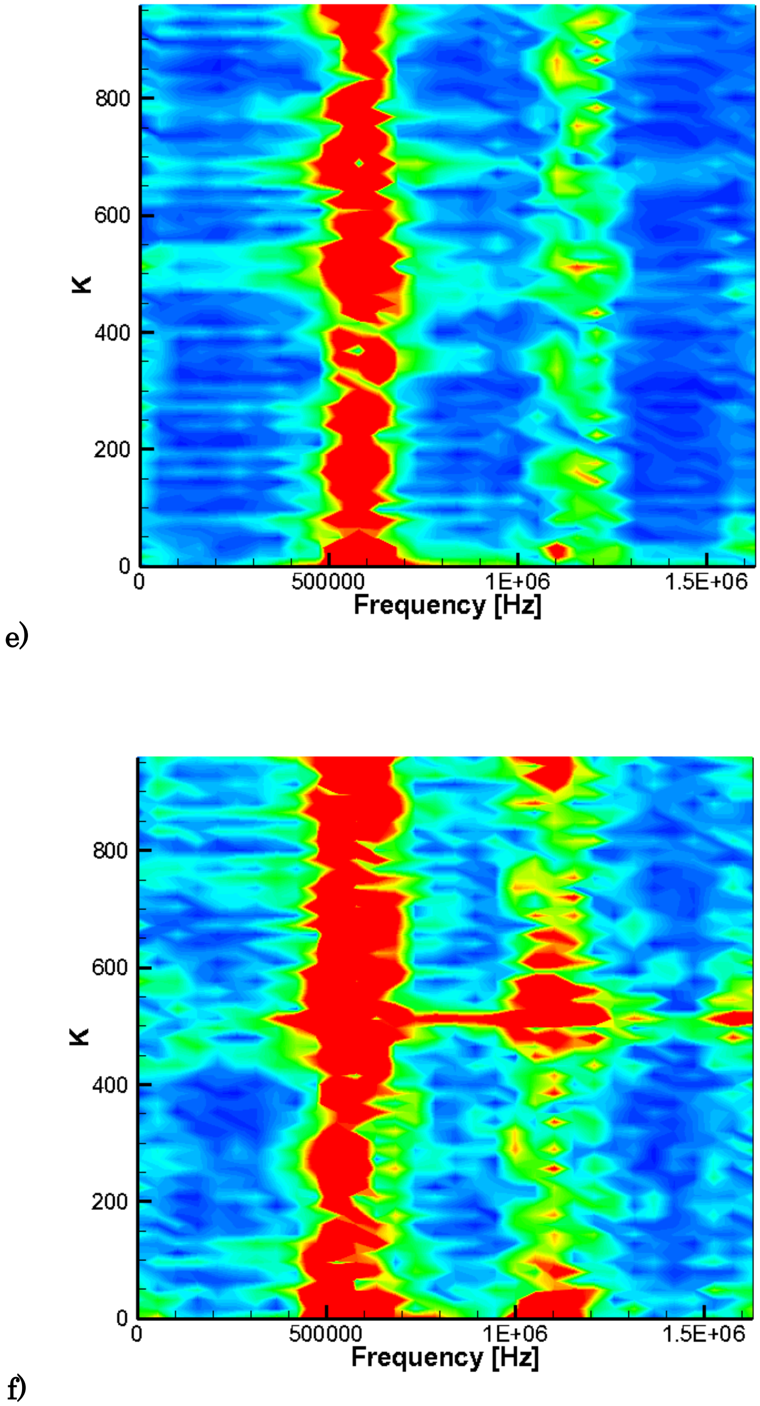

Fig. 45. Frequency vs. azimuth wave number at different surface locations: a) X=0.6m, b) X=0.65m, c) X=0.7m, d) X=0.75m, e) X=0.8m, f) X=0.85m.

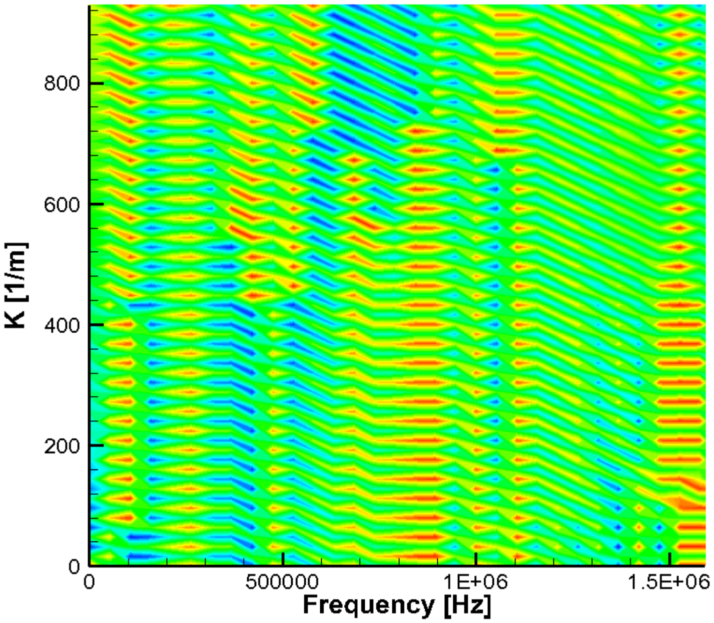
K [1/m]
0
200
400
600
800
0
500000
1E+06
1.5E+06
Frequency [Hz]

a)

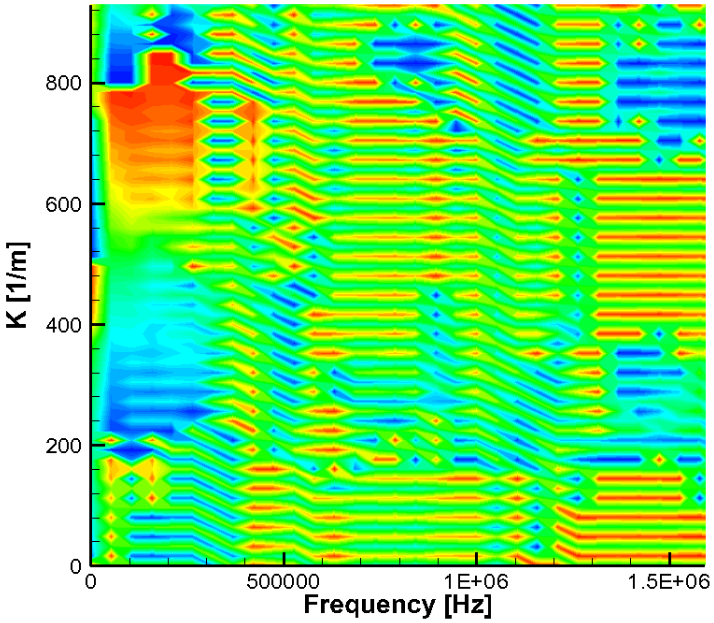
K [1/m]
0
200
400
600
800
0
500000
1E+06
1.5E+06
Frequency [Hz]

b)

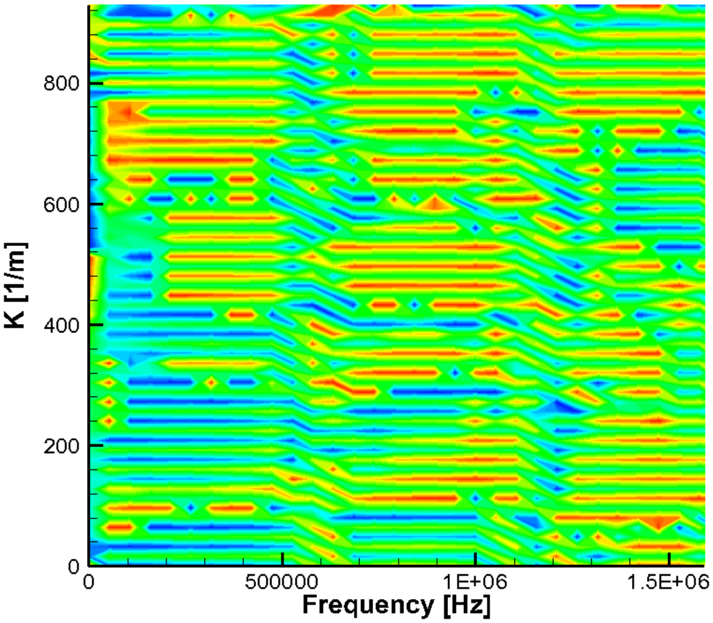
K [1/m]
0
200
400
600
800
0
500000
1E+06
1.5E+06
Frequency [Hz]

c)

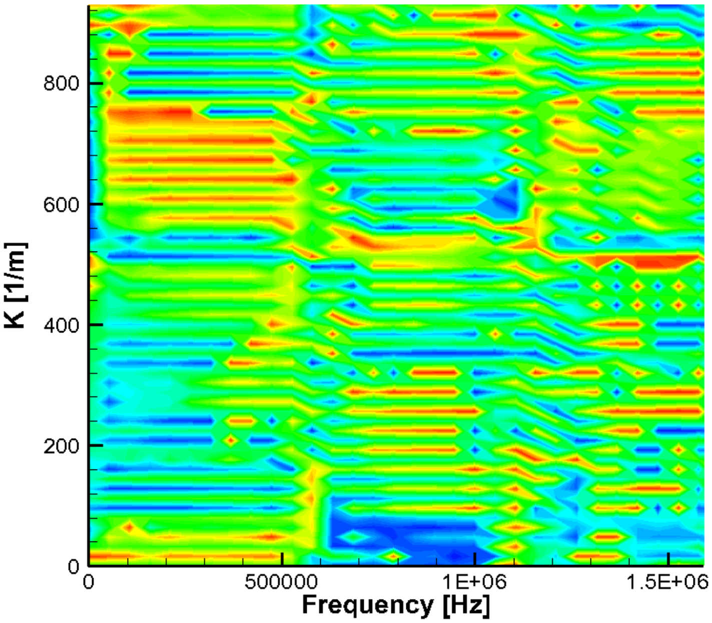
K [1/m]
0
200
400
600
800
0
500000
1E+06
1.5E+06
Frequency [Hz]

d)

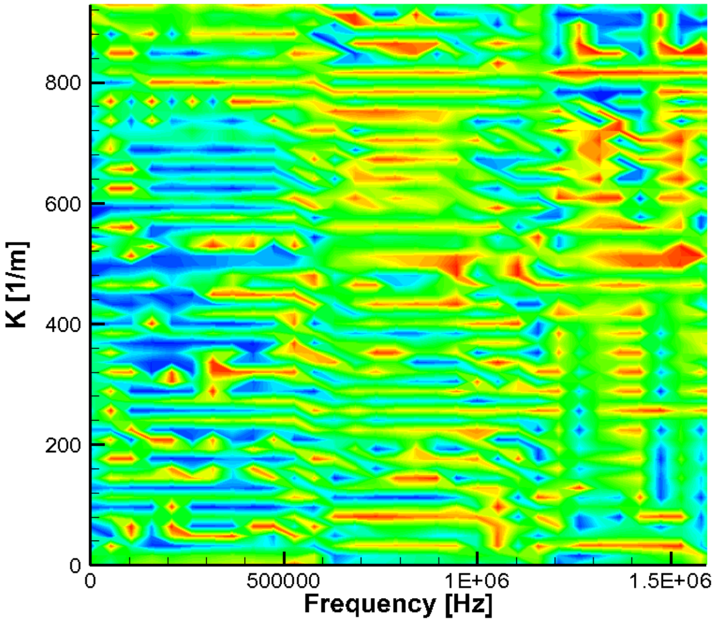

e)

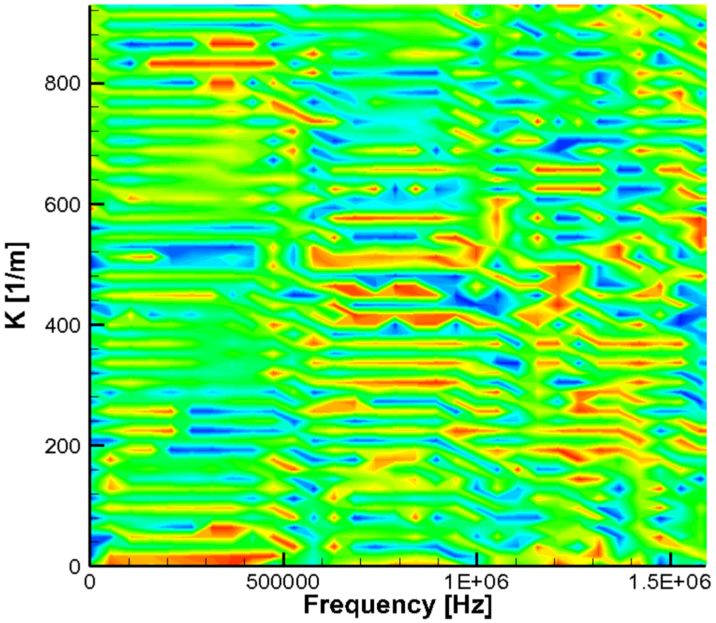

f)

Fig. 46. Spanwise wave number vs. Frequency of phase for all wave modes: a) X=0.6m, b) X=0.65m, c) X=0.7m, d) X=0.75m, e) X=0.8m, f) X=0.85m.

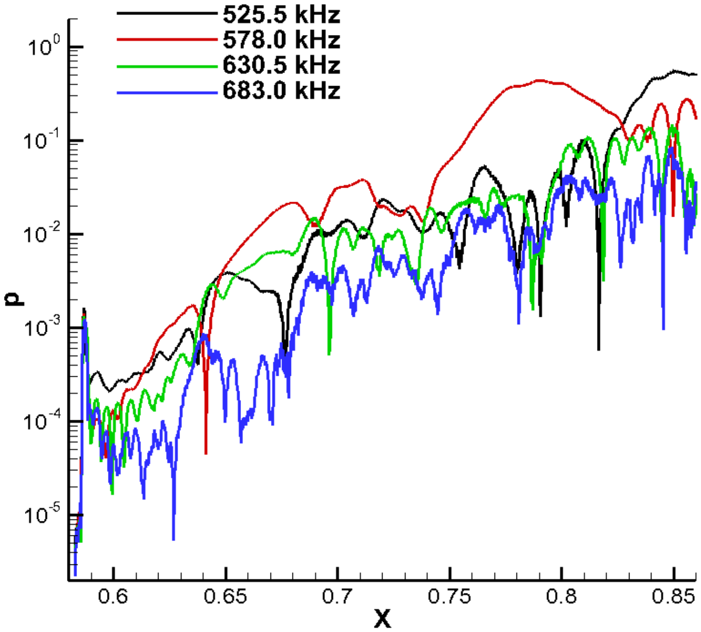
525.5 kHz
578.0 kHz
630.5 kHz
683.0 kHz
10^0
10^{-1}
10^{-2}
10^{-3}
10^{-4}
10^{-5}
p
0.6
0.65
0.7
0.75
0.8
0.85
X

a)

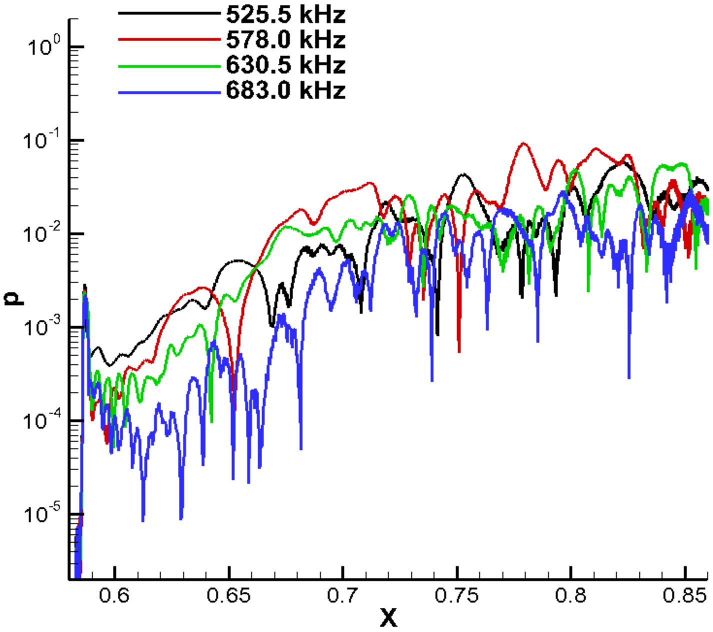
525.5 kHz
578.0 kHz
630.5 kHz
683.0 kHz
10^0
10^{-1}
10^{-2}
10^{-3}
10^{-4}
10^{-5}
p
0.6
0.65
0.7
0.75
0.8
0.85
X

b)

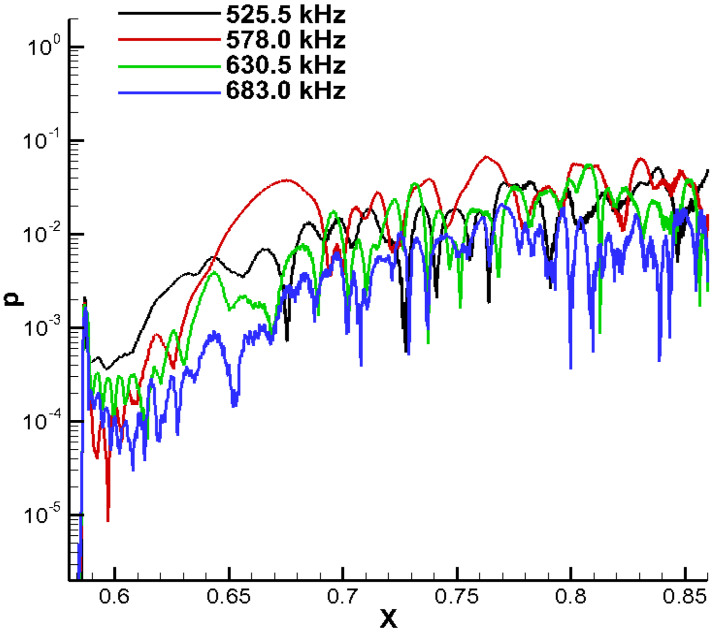

c)

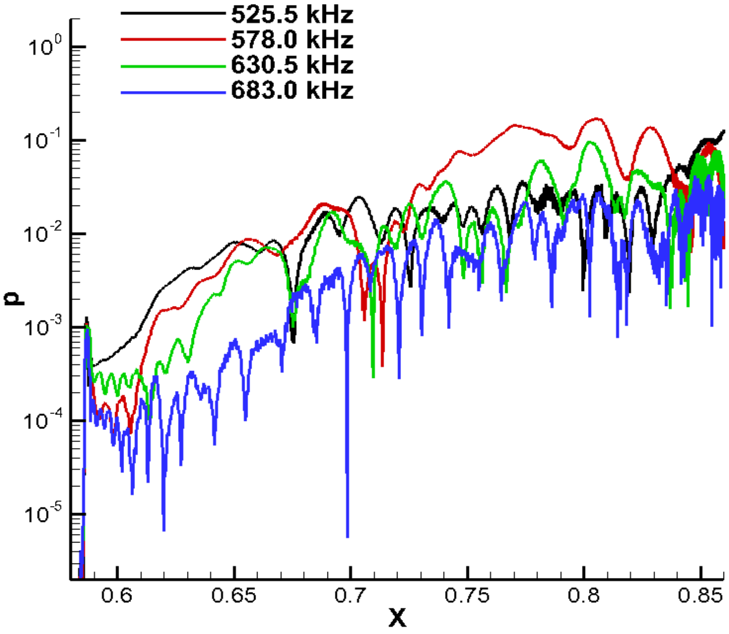

d)

Fig. 47. Selected frequency modes at different spanwise wave numbers: a) K=0, b) K=300, c) K=600, d) K=900.

6.2. Freestream Discrete-frequency Wave Induced Breakdown

Once the 3-D simulation code is validated standing alone with the blowing and suction test cases, the next step is to link the receptivity simulation result to the 3-D breakdown simulation. As the first trial on testing the capability of current computation approach, the fast acoustic wave receptivity results from section 5.1 are used at the inlet of simulation domain. The receptivity results include 15 discrete wave frequencies uniformly distributed between 52.55 kHz and 788.26 kHz. To investigate the non-linear growth in the unsteady simulation, the amplitude level at the inlet of computation domain is scaled up from the original linear receptivity simulation to shorten the linear growth region. The disturbance level at the entrance is scaled up to equivalent to impose the disturbance of 5% of the freestream value from the leading edge. Waves contained 15 discrete frequencies are imposed at the inlet of the computation domain. In addition, to enrich the spanwise wave spectrum to mimic a true three dimensional case, a low magnitude random noise were applied on top of the two dimensional primary waves. The max amplitude of random noise was set to be 5% of instantaneous primary wave amplitude. In Fig. 48, the pressure disturbance contour on the surface of cone body is shown. It can be clearly seen that, the waves are dominantly two dimensional at the area close to the inlet. Immediately, it entered the linear growth region between x=0.6 and 0.7 m. After x=0.75 m, the disturbance reached the saturation level. The breakdown process started at around x=0.82 m.

Fig. 49 shows the evolution of spanwise vorticity near the wall. A clear “rope-like” vorticity wave pattern was observed. Fig. 50 shows the development of streamwise vorticity in the breakdown region. At the early breakdown region, the streamwise vorticity waves are very weak and two dimensional. As they progress further downstream, the three dimensional feature appeared and the vorticity waves tended to break down to smaller and smaller structures.

From the previous LST analysis (Fig. 21), we predict the dominant second-mode unstable frequency in the current simulated region is between 500 and 600 KHz. After the FFT decomposition in both spanwise direction and time domain of current result, we can identify the wave amplitudes for each frequency and spanwise wave number so that we are able to track the evolution of each wave mode. Fig. 51 shows the pressure disturbance amplitudes along the cone surface for all wave modes in the frequency versus spanwise wave mode number plane. The results look very similar to the nonlinear BS2 case. The phase angles of wave modes are provided in Fig. 52 in the same locations as pressure disturbance amplitude plots.

Fig. 53 shows the pressure disturbance along the cone surface in second-mode range at selected spanwise wave numbers. At spanwise wave number k=0, the spectrum represents the two-dimensional disturbance waves which are the primary waves from the freestream receptivity simulation. The 2-D wave at 525 kHz amplifies more than one order of magnitude within the linear growth region which is qualitatively agreed with the LST analysis. However, after its amplitude reaches saturation level. It decays a little bit but sustains at relative high level. On the other hand, the three-dimensional wave behaves quiet differently. They come from the random noise that is introduced at the inlet. They are very weak initially and decay during the linear growth region. Nonetheless, once the 2-D primary wave reaches nonlinear stage, in this case at X=0.75 m, they start to amplify rapidly. Also, the waves at higher spanwise wave number grow slight faster and earlier than the ones at lower spanwise wave number.

In this simulation, we successfully demonstrate the feasibility to simulate the hypersonic boundary layer flow from freestream wave receptivity to breakdown. From the pressure disturbance amplitudes spectra in Fig. 51, the dominant growing waves at all the spanwise wave numbers are essentially in the same frequency range which falls inside the second mode instability frequency range. According to the breakdown theory, this wave mode analysis indicates that the flow was undergoing the so-called fundamental breakdown process, which is commonly observed in incompressible flow transition.

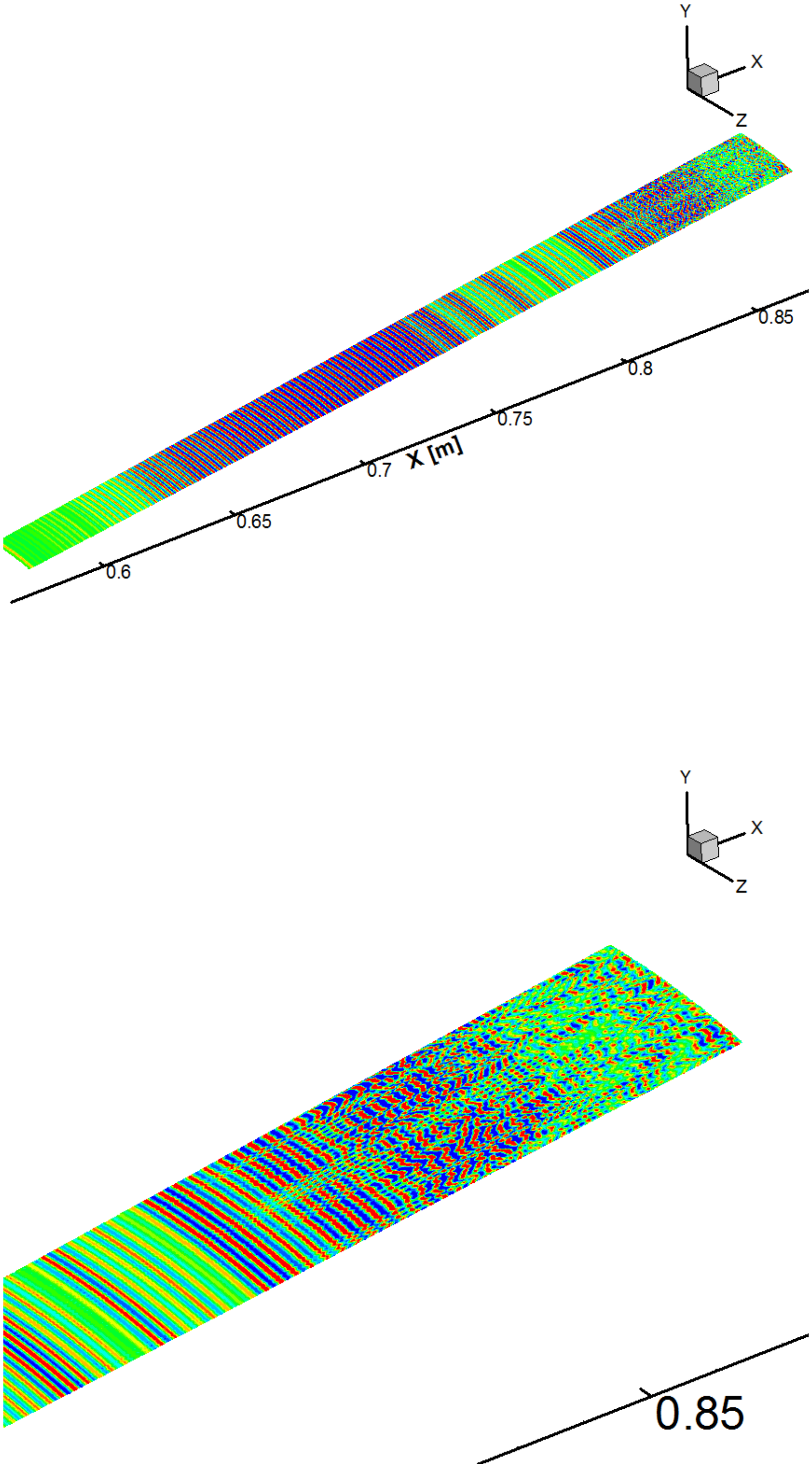

Fig. 48. Pressure disturbance on the cone surface and the blow-up view of the breakdown region.

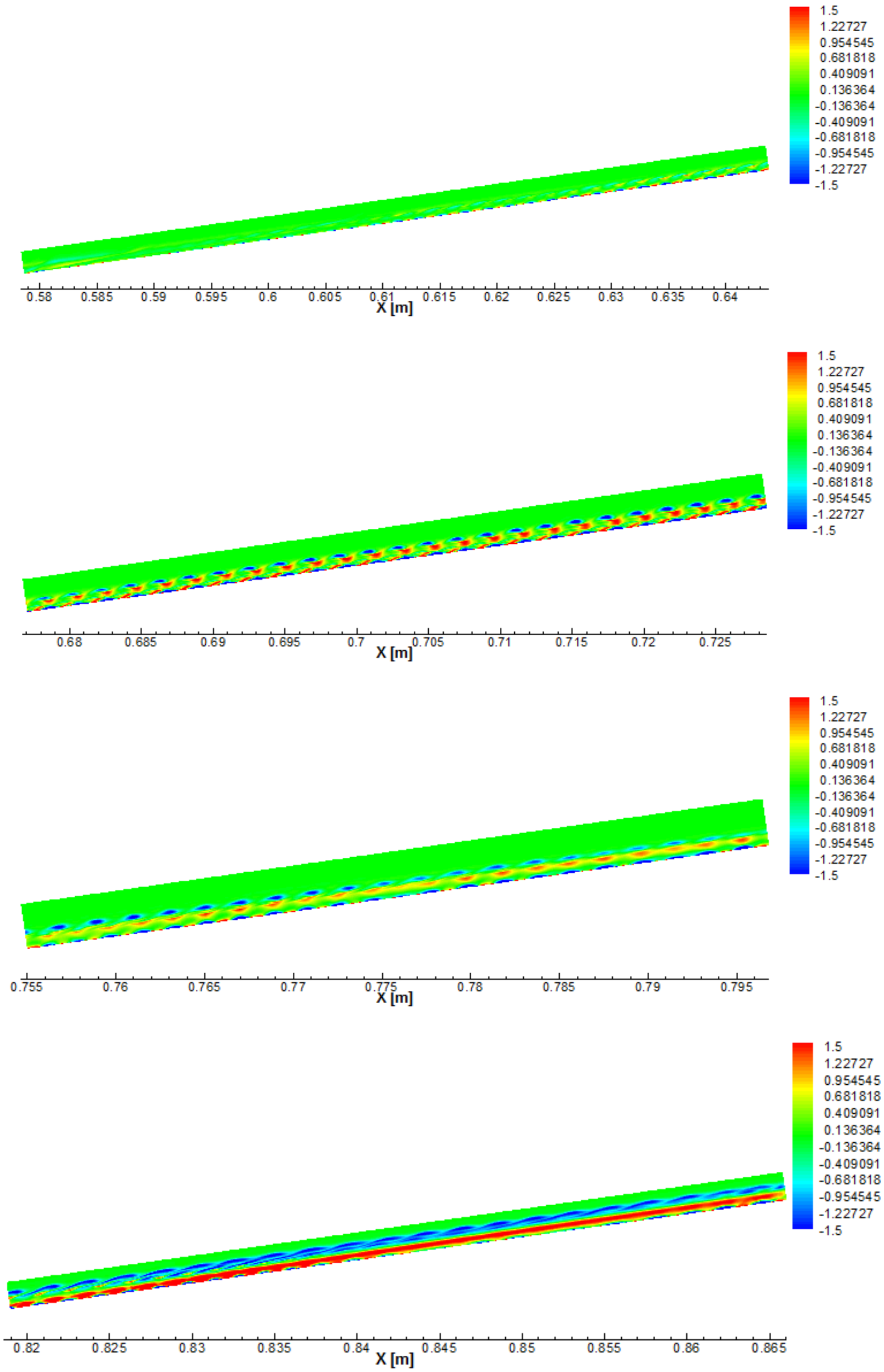

Fig. 49. Spanwise vorticity contours (side view) on the symmetric plane of domain.

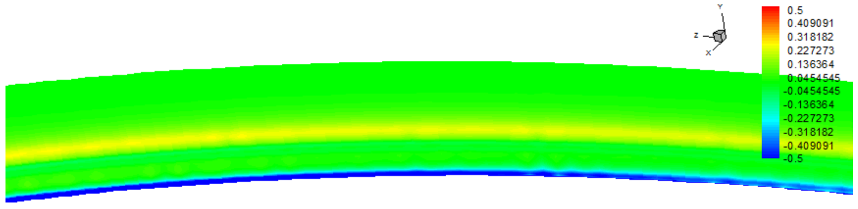

x =0.755 m

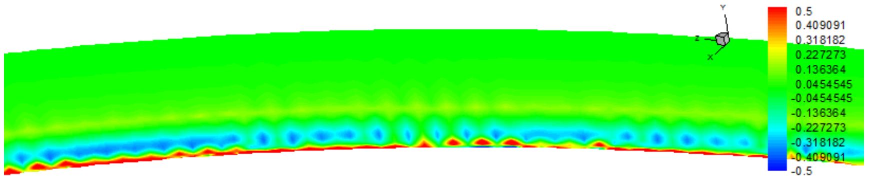

x =0.805 m

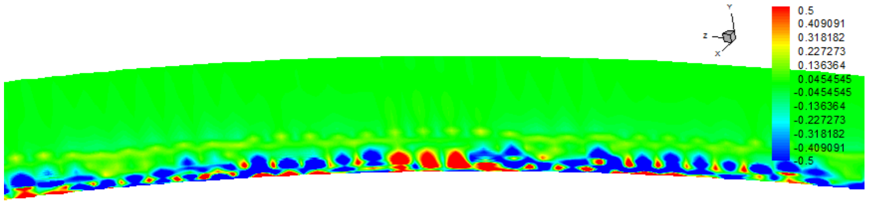

x =0.819 m

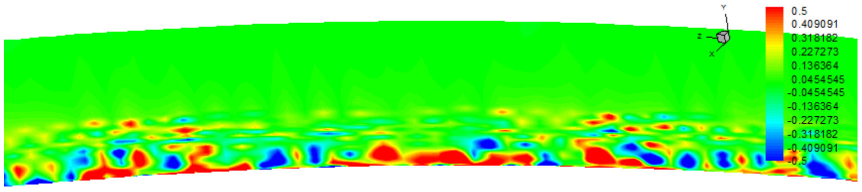

x =0.858 m

Fig. 50. Streamwise vorticity contours (cross-section view) at different streamwise locations.

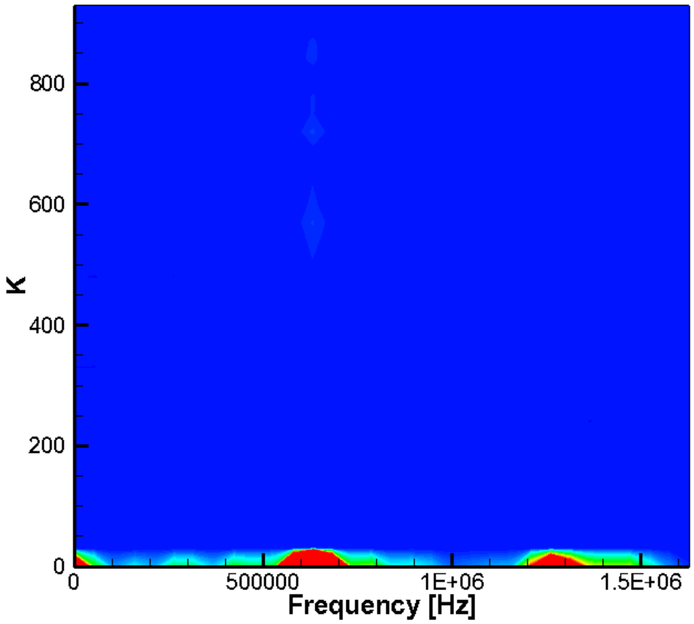
K
800
600
400
200
0
0
500000
1E+06
1.5E+06
Frequency [Hz]

a)

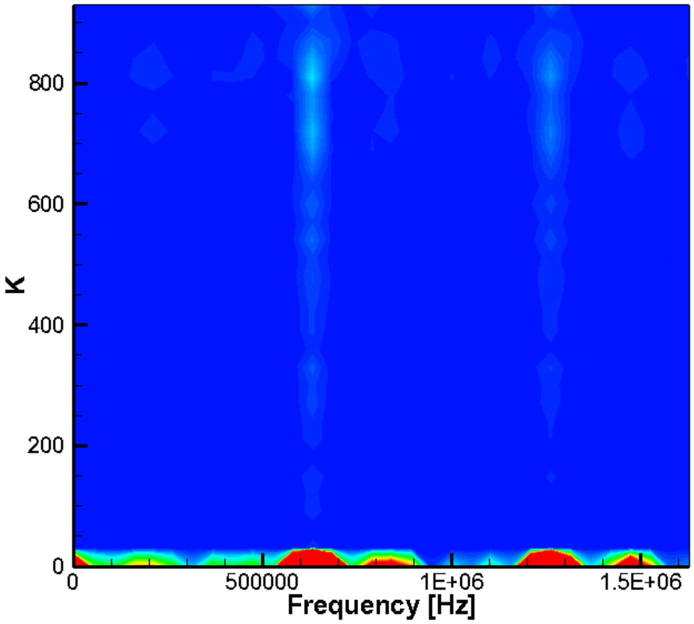
K
800
600
400
200
0
0
500000
1E+06
1.5E+06
Frequency [Hz]

b)

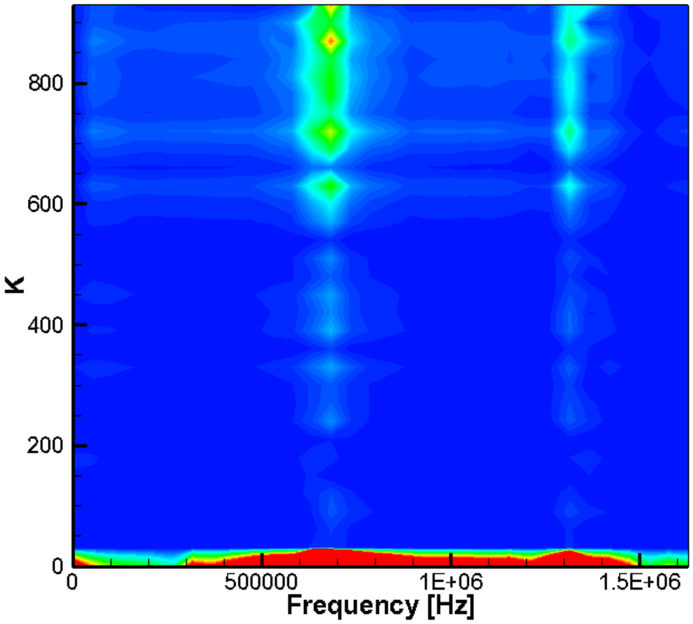
800
600
K
400
200
0
0
500000
1E+06
1.5E+06
Frequency [Hz]

c)

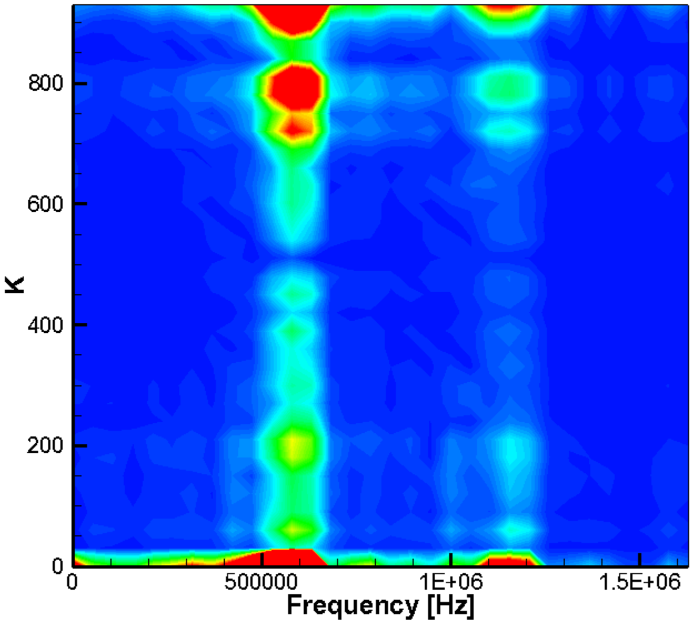
800
600
K
400
200
0
0
500000
1E+06
1.5E+06
Frequency [Hz]

d)

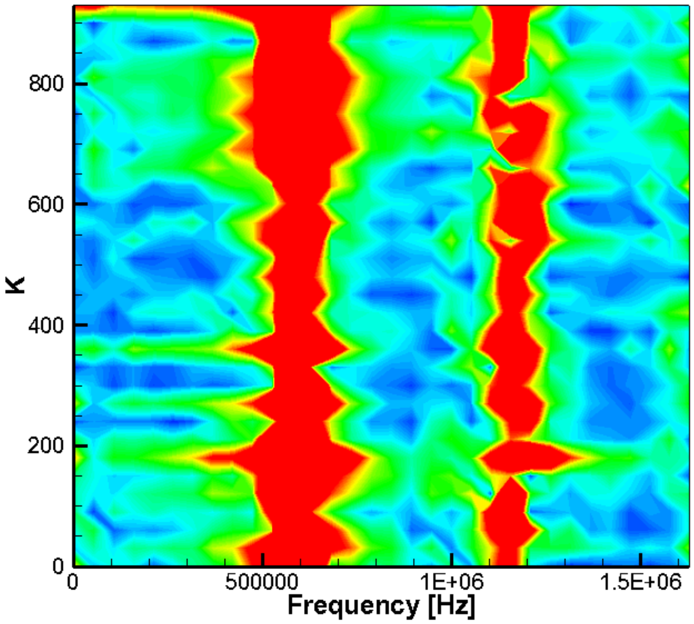

e)

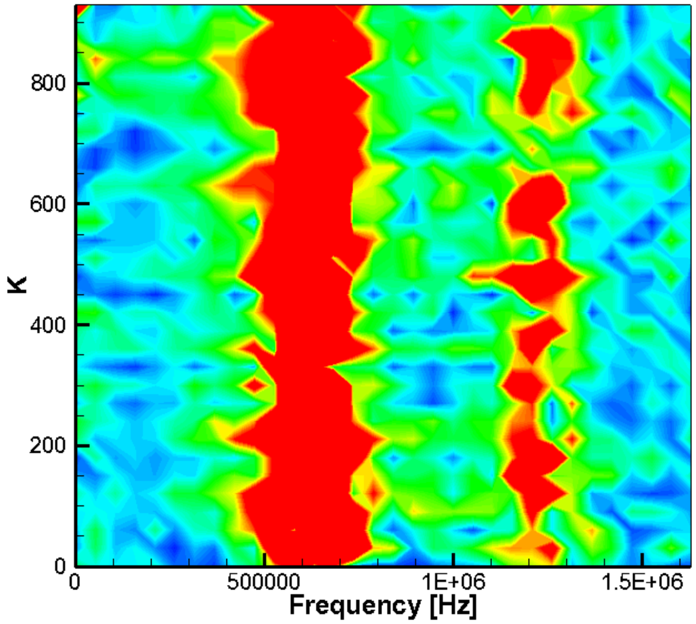

f)

Fig. 51. Frequency vs. azimuth wave number at different surface locations: a) X=0.6m, b) X=0.65m, c) X=0.7m, d) X=0.75m, e) X=0.8m, f) X=0.85m.

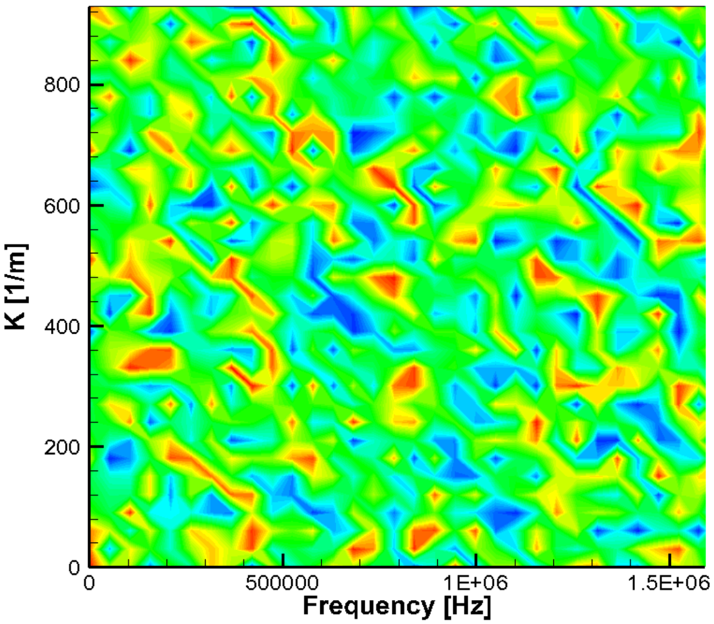
K [1/m]
800
600
400
200
0
0
500000
1E+06
1.5E+06
Frequency [Hz]

a)

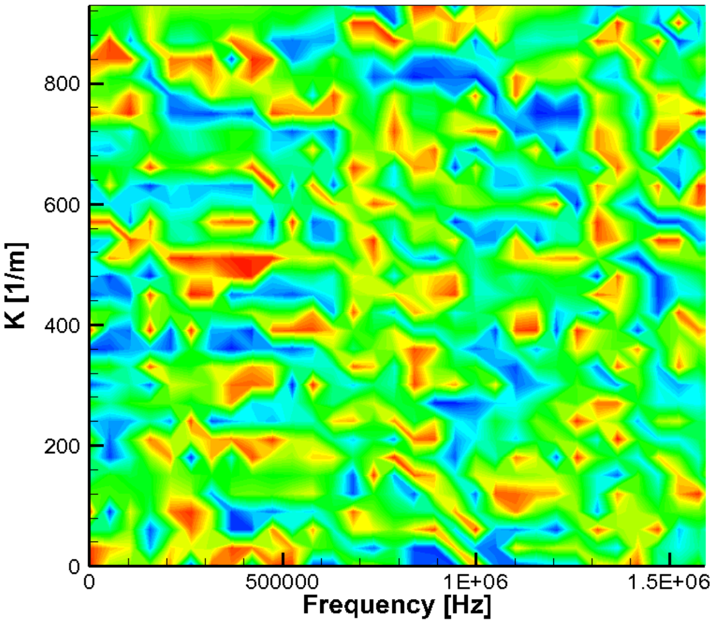
K [1/m]
800
600
400
200
0
0
500000
1E+06
1.5E+06
Frequency [Hz]

b)

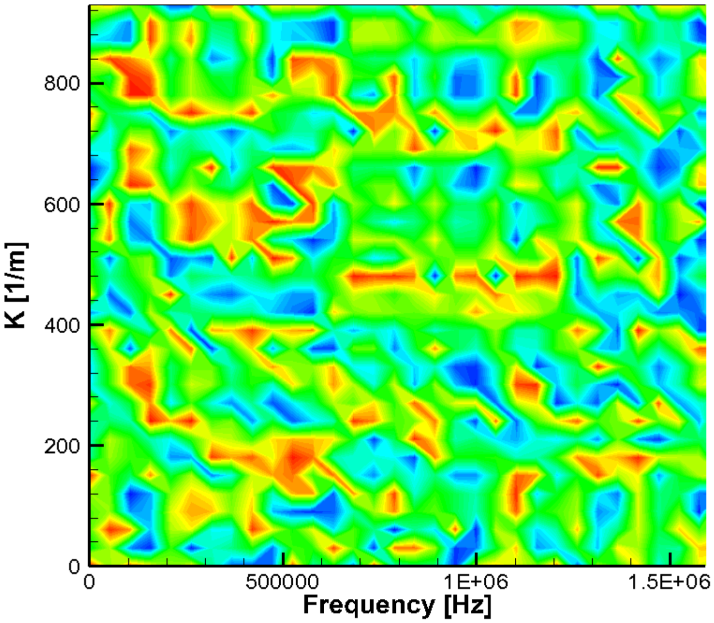
K [1/m]
800
600
400
200
0
0
500000
1E+06
1.5E+06
Frequency [Hz]

c)

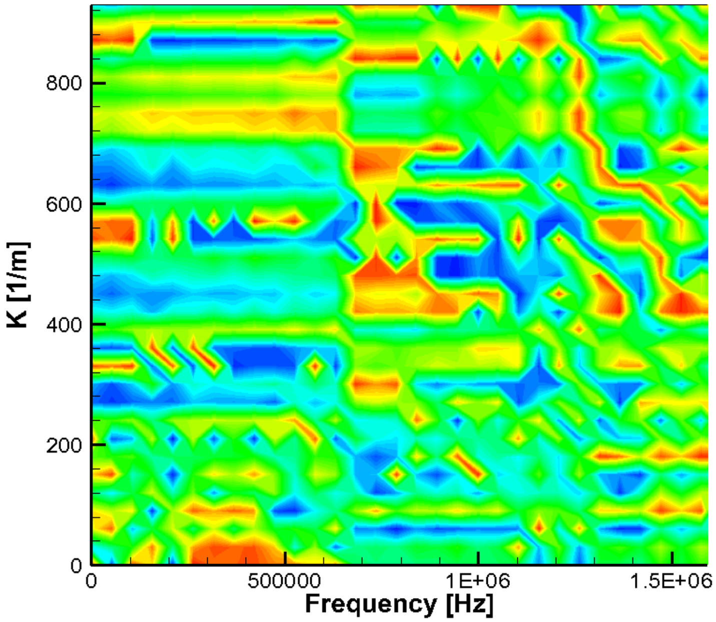
K [1/m]
800
600
400
200
0
0
500000
1E+06
1.5E+06
Frequency [Hz]

d)

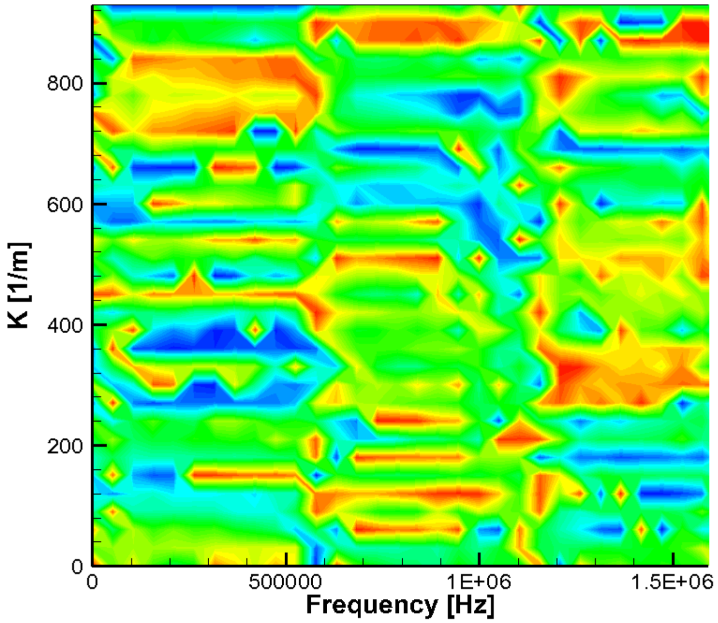

e)

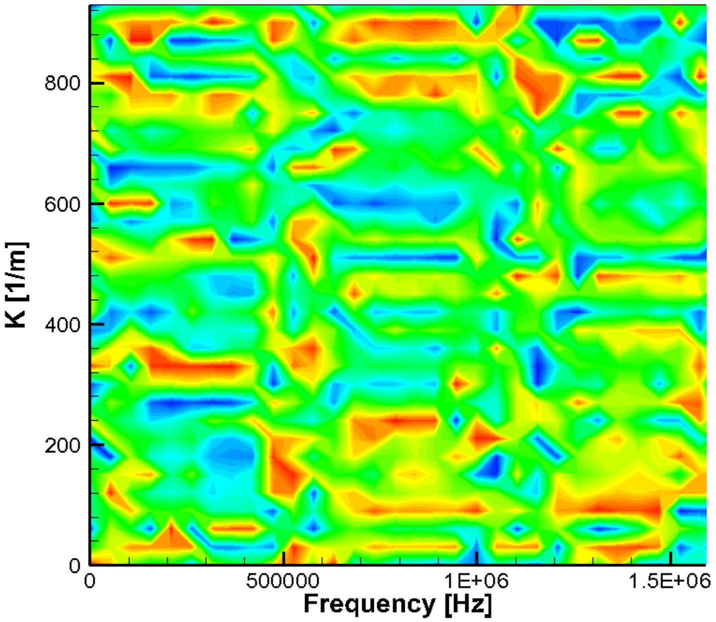

f)

Fig. 52. Spanwise wave number vs. Frequency of phase for all wave modes: a) X=0.6m, b) X=0.65m, c) X=0.7m, d) X=0.75m, e) X=0.8m, f) X=0.85m.

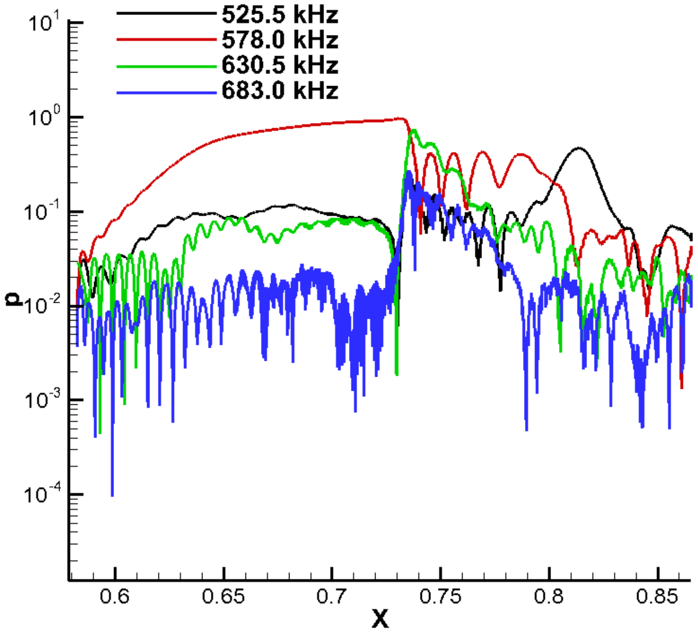
525.5 kHz
578.0 kHz
630.5 kHz
683.0 kHz
10^1
10^0
10^{-1}
10^{-2}
10^{-3}
10^{-4}
p
0.6
0.65
0.7
0.75
0.8
0.85
X

a)

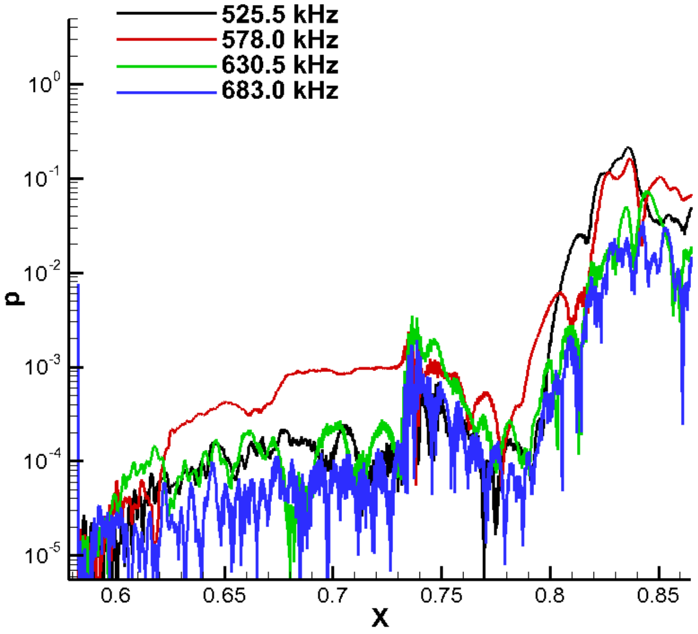
525.5 kHz
578.0 kHz
630.5 kHz
683.0 kHz
10^0
10^{-1}
10^{-2}
10^{-3}
10^{-4}
10^{-5}
p
0.6
0.65
0.7
0.75
0.8
0.85
X

b)

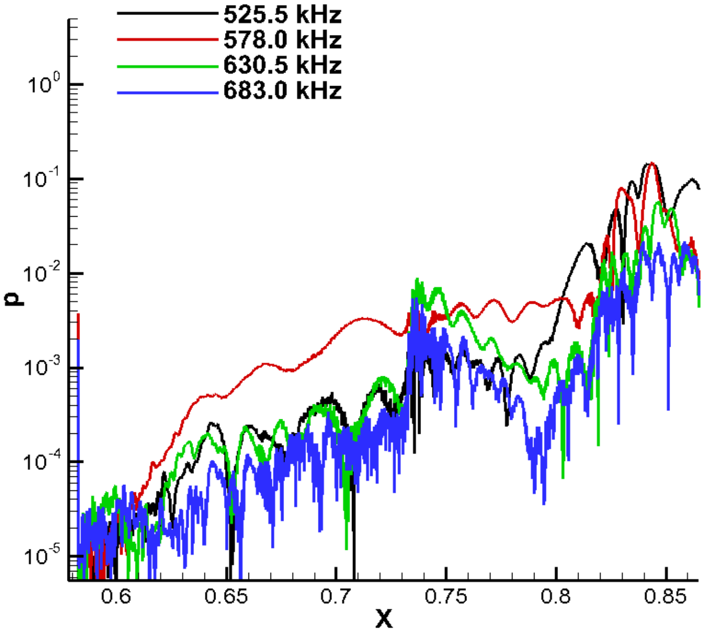

c)

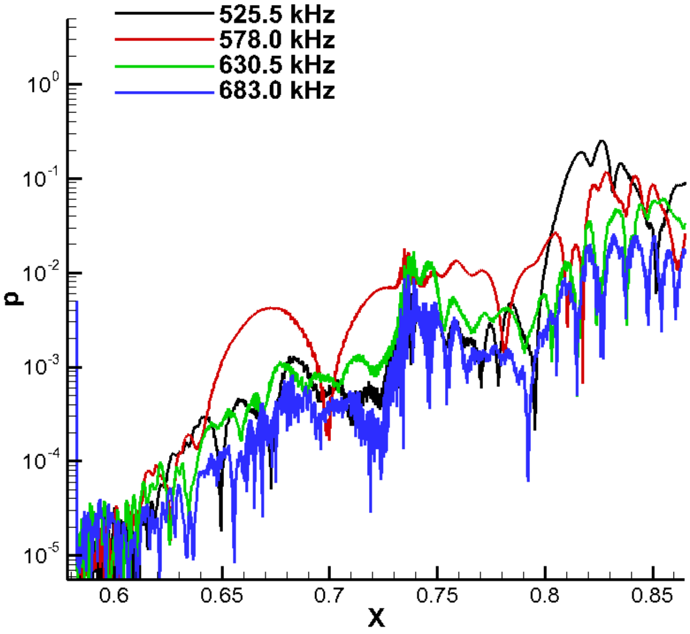

d)

Fig. 53. Selected frequency modes at different spanwise wave number: a) K=0, b) K=300, c) K=600, d) K=900.

6.3. Freestream Wave Pulse Induced Breakdown

In section 5.2.3, we demonstrate that with the newly developed freestream pulse model linear receptivity simulation successfully captures the receptivity response over a continued frequency spectrum. Especially, the unstable second modes are identified and verified with LST calculations. In this section, the receptivity data base from section 5.2.3 is used to construct the inflow conditions for subsequent nonlinear breakdown simulations. But before that, the inflow disturbance profile is re-constructed to match the desired freestream spectrum using the formulations provided in section 2.4. Since we only conduct a two-dimensional receptivity simulation, the receptivity data base is limited to two-dimensional as well. Some three-dimensional wave components need to be introduced at the inflow to enrich the wave spectrum. To achieve that, low amplitude random noise is imposed on top of the primary 2-D wave. In addition, a long computational domain is needed to capture the flow development from weakly nonlinear stage till the occurrence of breakdown. A series of test cases are carried out to perform a extensive parametric study on the breakdown phenomenon.

The nonlinear simulation is carried on TAMU Mach 6 case over the straight cone with 0.1 mm nose radius from x=0.47 m to x=0.95 m using 4680 grid points in streamwise direction and 240 points in wall normal direction. The grid in streamwise direction is slight stretched toward the exit of computational domain so that the breakdown mechanism can be resolved with higher resolution. The grid in wall-normal direction is highly stretched toward the cone surface with at least 100 points within the boundary layer. In order to ensure the grid convergence of simulation results, 2-D simulations with two set of grids are carried out. The standard grid size simulation uses 240 points in the wall-normal direction. The finer grid size uses 480 points in the wall-normal direction with the same stretching coefficient. The grid refinement is only implemented in the wall-normal direction because for boundary layer type of simulation, it is more crucial to ensure the flow field within boundary layer is well resolved. The stream-wise direction grid resolution can be checked by the wave length to grid size ratio. In the current simulation, that ratio remains greater than 10 for the wave frequencies within the unstable second-mode frequency range. In other words, the wave in unstable frequency range has minimum of 10 points per wave period. Fig. 54 shows the comparison of the standard and fine grid results that demonstrates good grid convergence of current simulation results.

After the grid convergence is checked, a series of 3-D breakdown simulations are carried out to study the breakdown mechanisms. Table 3 summarizes all the test cases conducted for the breakdown study.

Table 3. Summary of test cases for TAMU nonlinear breakdown simulation.

Case Name	Pri. Wave Amp.	Noise Amp.	Arc angle	Azimuth Grid Size
TAMU0	0%	0.05	12	64
TAMU1	5%	0.05	2	64
TAMU2	5%	0.05	6	64
TAMU3	5%	0.05	12	64
TAMU4	5%	0.05	12	32

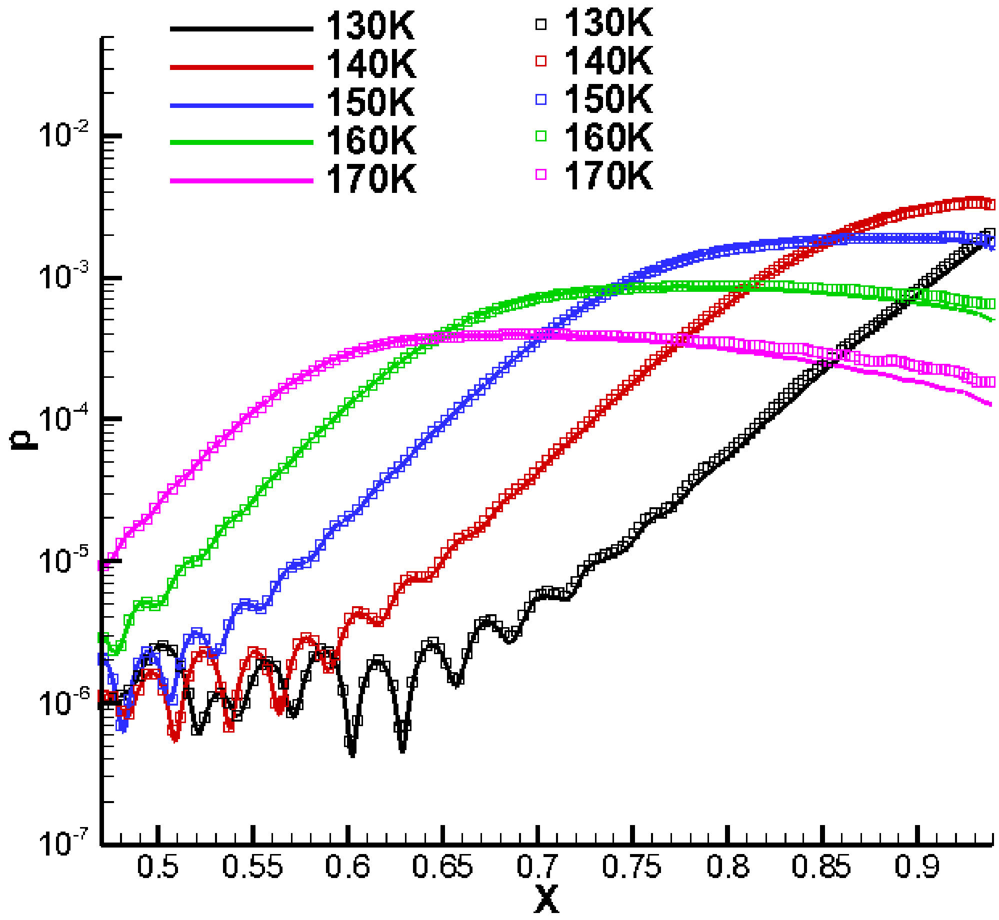

Fig. 54. Comparison of unsteady simulation results of two different grid sizes: '—'original grid, 'o' refined grid.

6.3.1. Reconstruction of Inflow Disturbance Profile

The ultimate goal of current research is to link the freestream disturbance profile to breakdown in transition so that the relevant breakdown mechanisms can be identified. With this in mind, the inlet disturbance profile is reconstructed using the receptivity results from the linear receptivity simulation. The original imposed profile is a Gaussian-shaped function, but the freestream wave spectra from typical experiments will be different. Since no experimental data is available at the time the breakdown simulations are conducted, an analytical function is used as a placeholder. As our first trial, we assume a simple exponential function as the freestream wave spectrum. In the future, the more reliable experimental data can be applied. Furthermore, the limitation on computational grids makes it difficult to resolve high frequency waves in current simulation. Therefore, all the higher frequency waves are truncated.

The original Gaussian pulse in fresstream and the desired freestream spectrum are presented in Fig. 55. With the desired freestream spectrum determined, the receptivity response at the end the linear receptivity computation domain can be rescaled accordingly. Fig. 56 shows the pressure disturbance spectrum of receptivity respond at the end of linear receptivity simulation before and after the rescale. Furthermore, the phase angle relationship between waves is randomized to mimic a realistic freestream conditions. Fig. 57 shows the pressure disturbance time trace at the exit of receptivity simulation before and after the profile reconstruction.

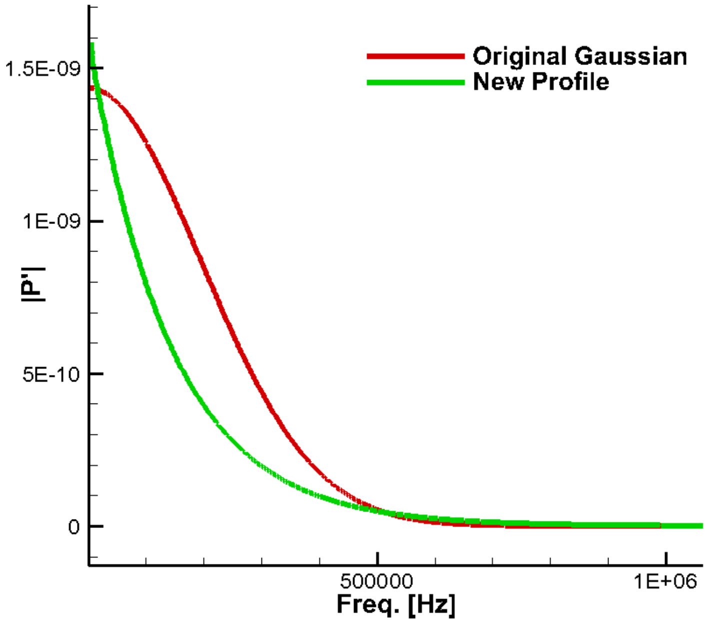

Fig. 55. Original Gaussian spectrum vs. desired freestream spectrum.

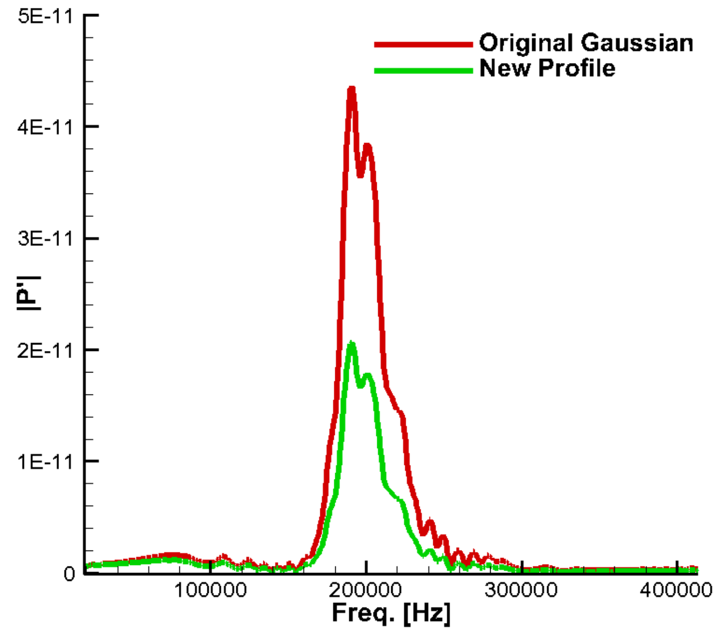

Fig. 56. Receptivity response spectrum before and after reconstruction.

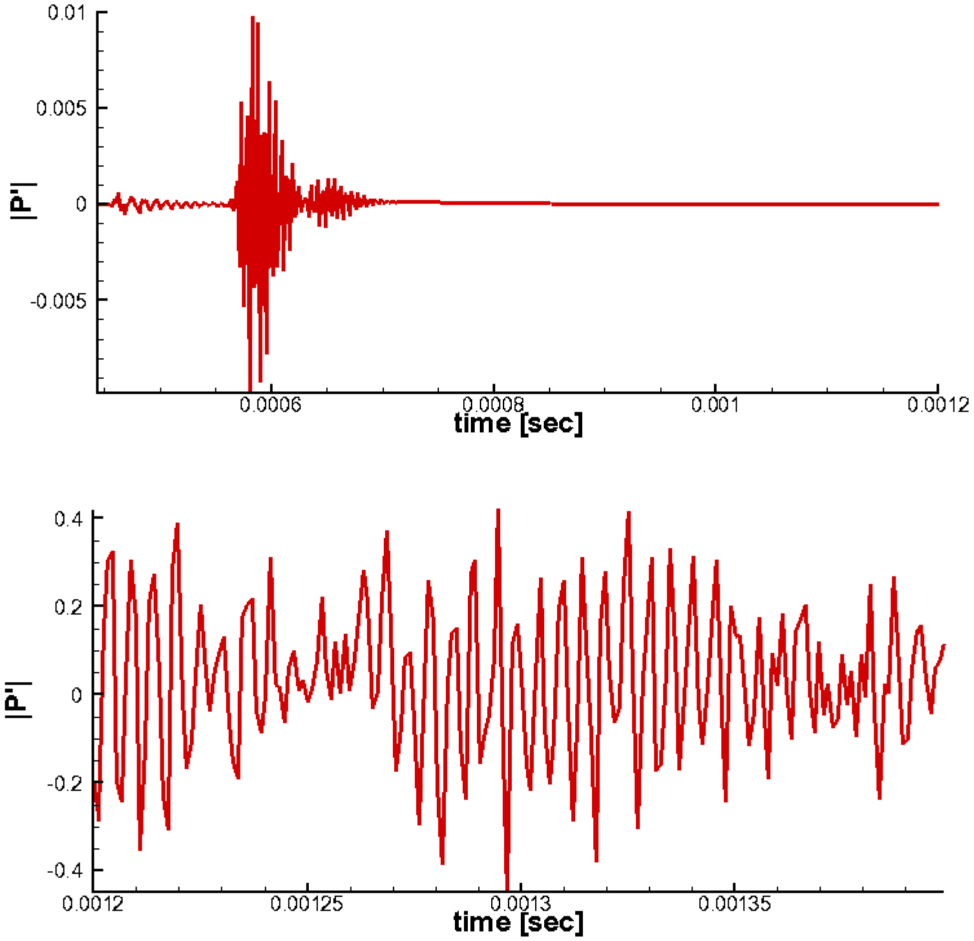

Fig. 57. Inlet pressure time trace before (top) and after (bottom) reconstruction.

6.3.2. TAMU0: Simulation Using Pure Noise at the Inflow

This test case serves the purpose to understand how the imposed noise behaves alone without the influence of strong two-dimensional primary wave. Fig. 58 shows the pressure disturbance development on the cone surface, which clearly indicates that the noise is initially very weak at the inflow of computational domain and gradually grows as it propagates in downstream direction. Some localized two dimensional patterns develop near the exit of computational domain.

The simulation result can be better understood when the inflow noise is decomposed into wave modes in terms of frequency and wave number. Fig. 59 provides the pressure perturbation amplitude in frequency versus spanwise wave number plot at selected surface locations from the beginning to the end of simulation domain. It shows that the imposed noise quickly decay rapidly right after it enters the computation domain. At x=0.7 m, some wave components around 150 kHz start to grow. The wave at lower spanwise wave number grows faster than the one at higher spanwise wave number. This trend remains all the way till the end of simulation domain. The amplitudes of unstable modes remain at relatively low level. The phase angle spectra are also presented at the same locations as amplitude spectrum plots in Fig. 60. Some "phase-locking" feature is observed at the higher end of the frequency spectrum where the wave mode amplitude is very low. Therefore, this feature does not play a significant role in the linear growth region.

To obtain more quantitative looks of simulation results, the pressure perturbation amplitudes at selected frequencies are plotted along the cone surface location for different spanwise wave numbers in Fig. 61. Clear second mode growths on wave modes with frequency higher than 144 kHz are captured in this pure noise case simulation. Both 2-D wave modes and 3-D wave modes at relatively low spanwise wave numbers are significantly amplified. The wave modes at lower frequency are initially decaying until the unstable second modes are excited. The simulation results exactly follow the predication by LST.

Similarly, the pressure perturbation amplitude frequency spectra at different spanwise wave numbers are given in Fig. 62. In this figures, different linear represents spectrum at different surface station equally distributed from the beginning to the end of computation domain. From these figures, we learn that the noise level drop at least two orders of magnitude during its initial adjustment into the flow field. In addition, the random noise provides fairly uniform wave mode amplitudes across both spanwise wave number and frequency spectra, which are what we intent to do to enrich the 3-D wave spectrum.

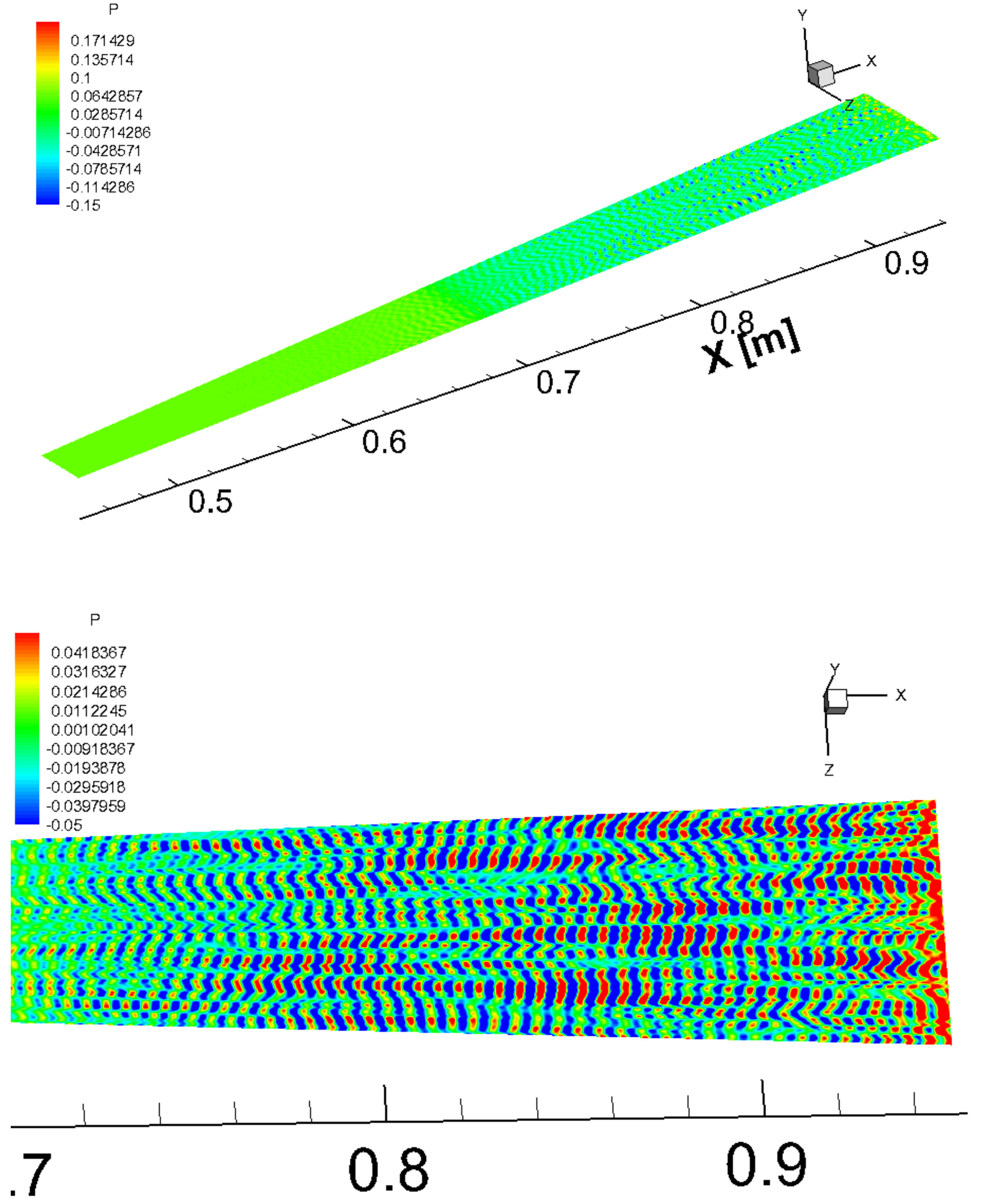

Fig. 58. Pressure disturbance on the cone surface for TAMU0 and the blow-up view near the exit region of the computation domain.

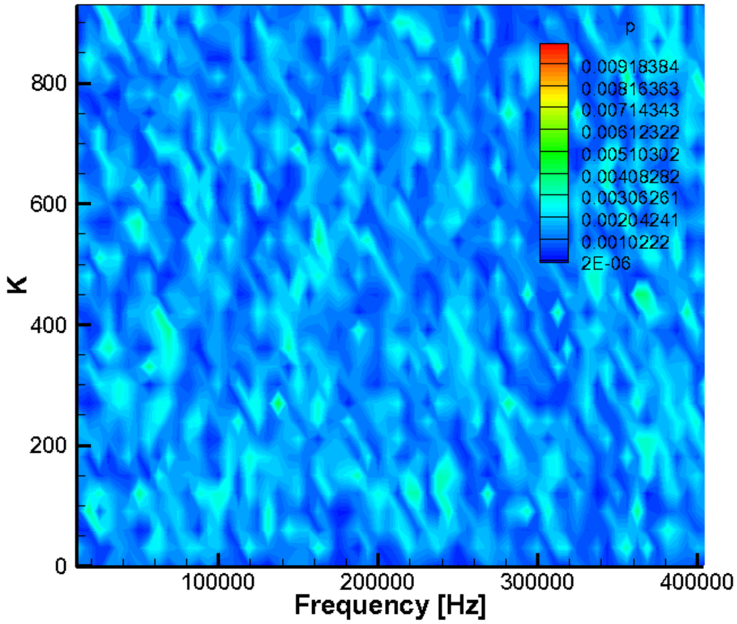
p
0.00918384
0.00816363
0.00714343
0.00612322
0.00510302
0.00408282
0.00306261
0.00204241
0.0010222
2E-06
K
0
200
400
600
800
100000
200000
300000
400000
Frequency [Hz]

a)

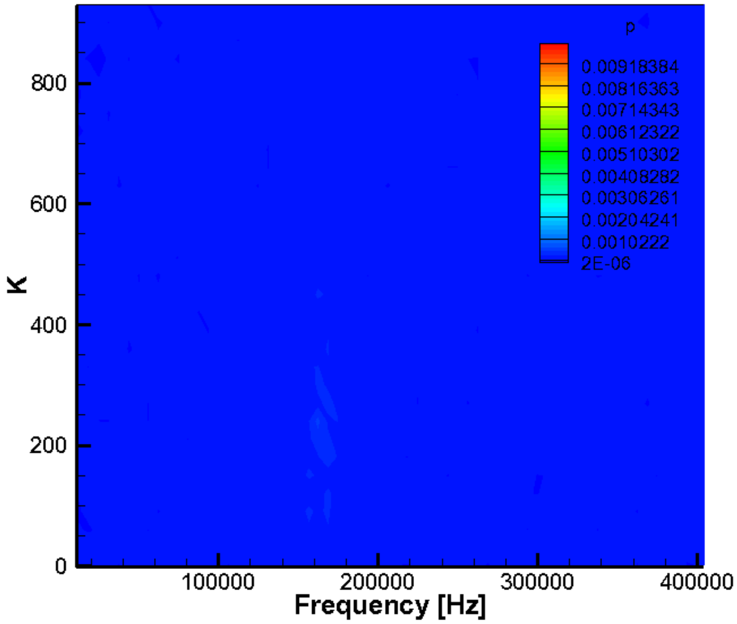
p
0.00918384
0.00816363
0.00714343
0.00612322
0.00510302
0.00408282
0.00306261
0.00204241
0.0010222
2E-06
K
0
200
400
600
800
100000
200000
300000
400000
Frequency [Hz]

b)

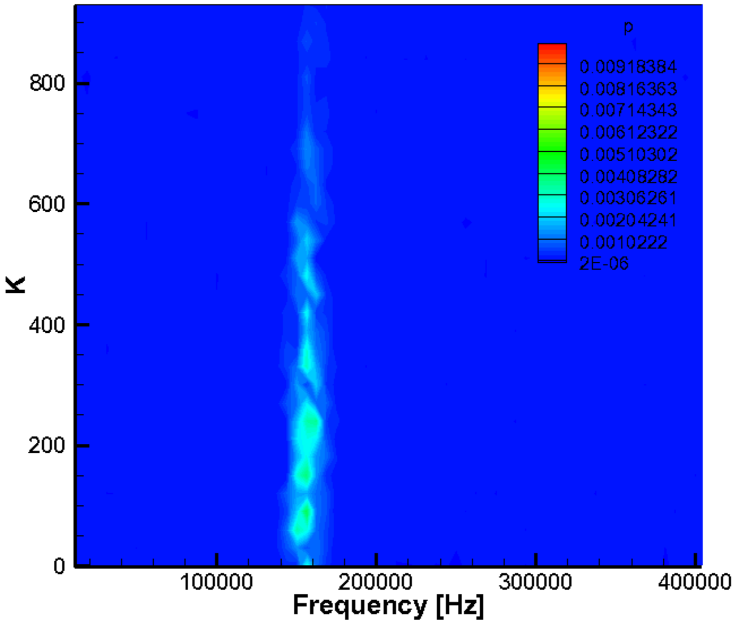
p
0.00918384
0.00816363
0.00714343
0.00612322
0.00510302
0.00408282
0.00306261
0.00204241
0.0010222
2E-06
K
0
200
400
600
800
100000
200000
300000
400000
Frequency [Hz]

c)

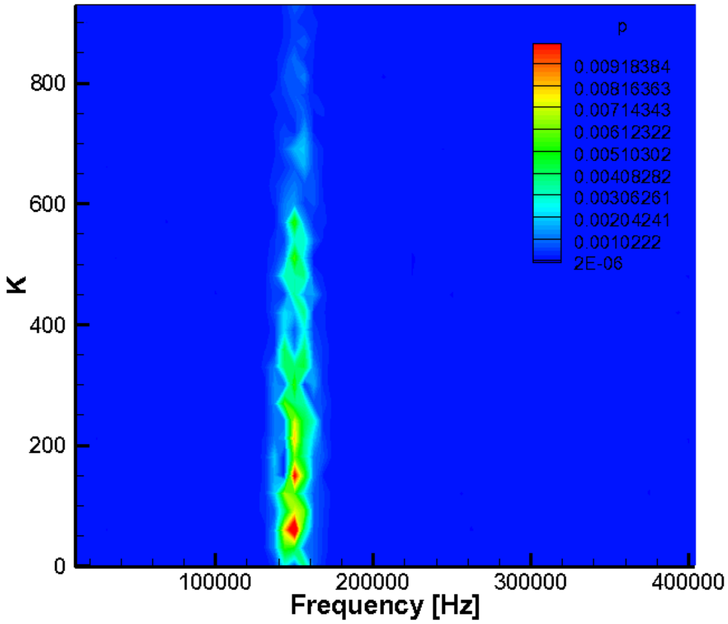
p
0.00918384
0.00816363
0.00714343
0.00612322
0.00510302
0.00408282
0.00306261
0.00204241
0.0010222
2E-06
K
0
200
400
600
800
100000
200000
300000
400000
Frequency [Hz]

d)

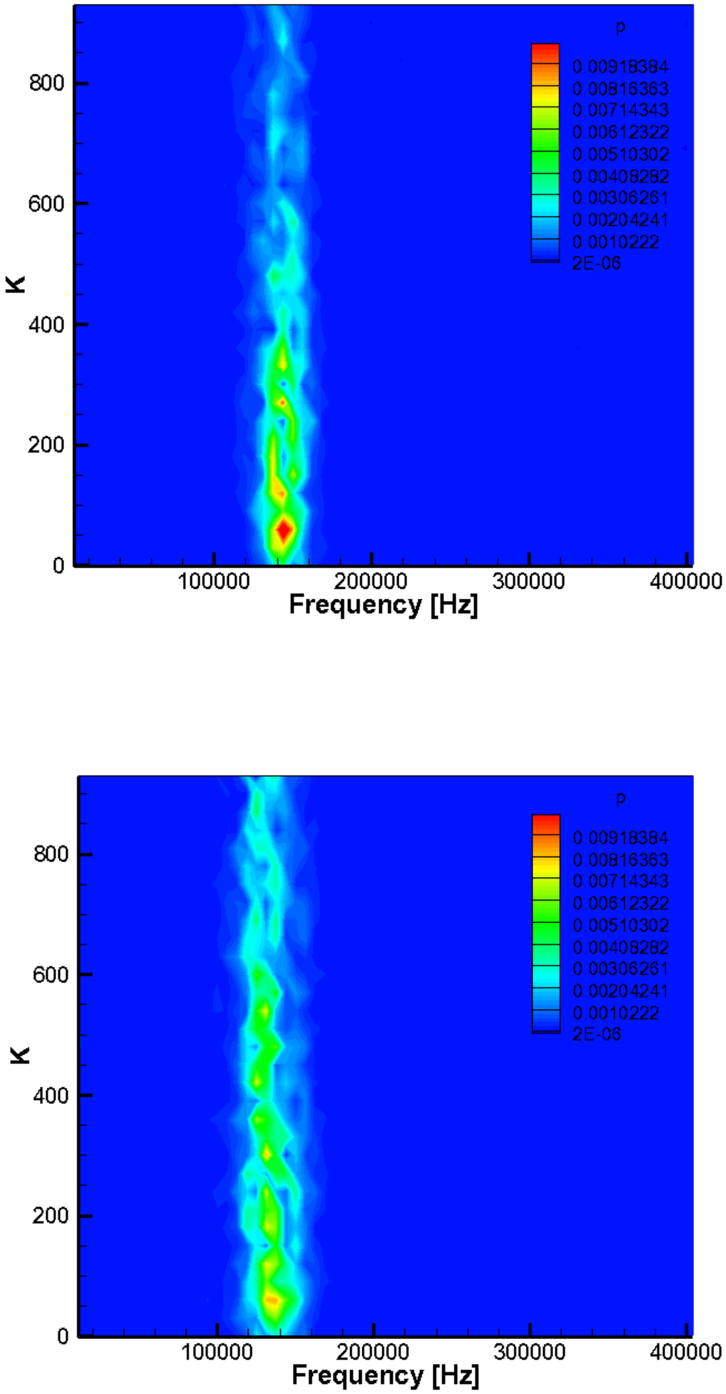

e)

f)

Fig. 59. Frequency vs. azimuth wave number at different surface locations: a) X=0.47m, b) X=0.6m, c) X=0.7m, d) X=0.8m, e) X=0.9m, f) X=0.95m.

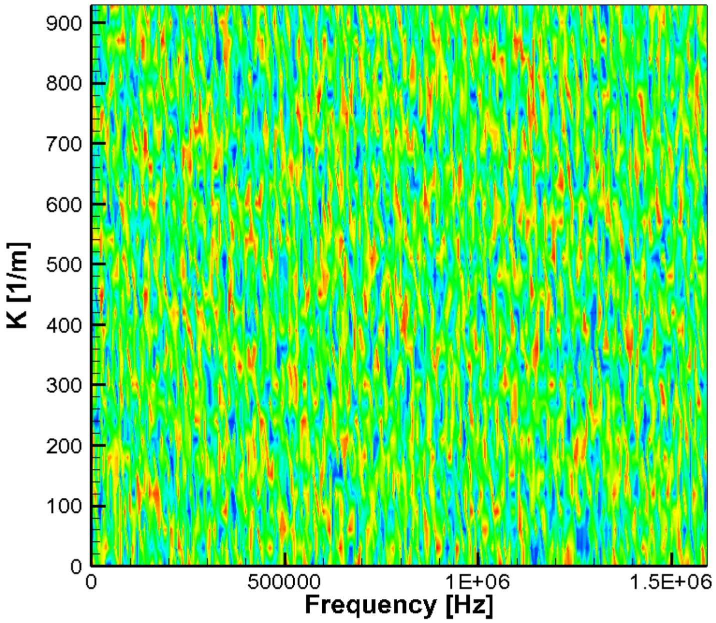
K [1/m]
0
100
200
300
400
500
600
700
800
900
0
500000
1E+06
1.5E+06
Frequency [Hz]

a)

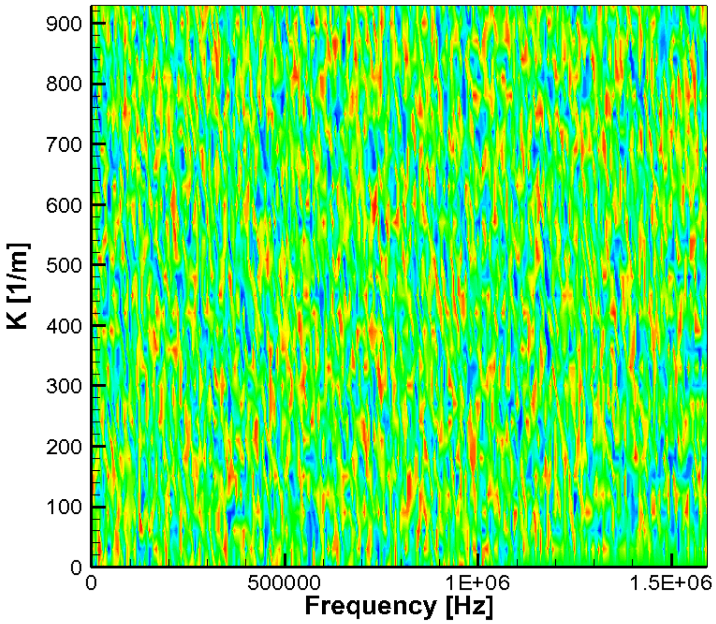
K [1/m]
0
100
200
300
400
500
600
700
800
900
0
500000
1E+06
1.5E+06
Frequency [Hz]

b)

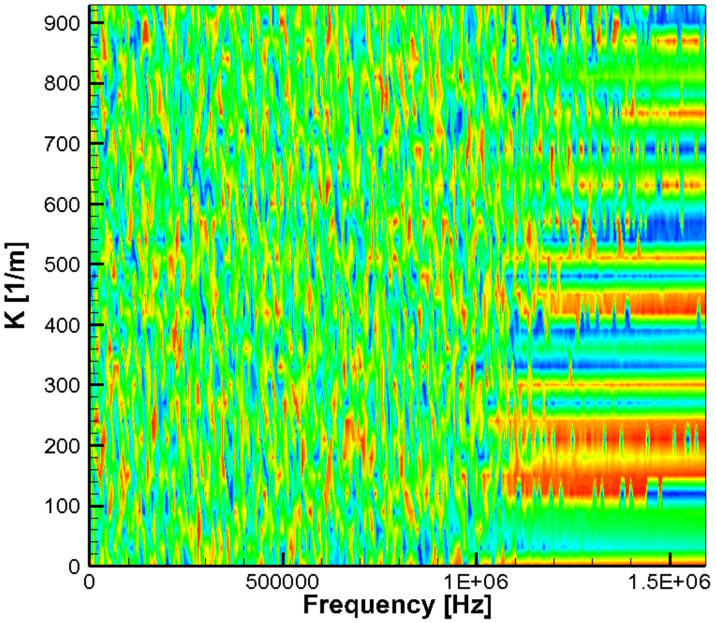

900
800
700
600
500
400
300
200
100
0
K [1/m]
0
500000
1E+06
1.5E+06
Frequency [Hz]

c)

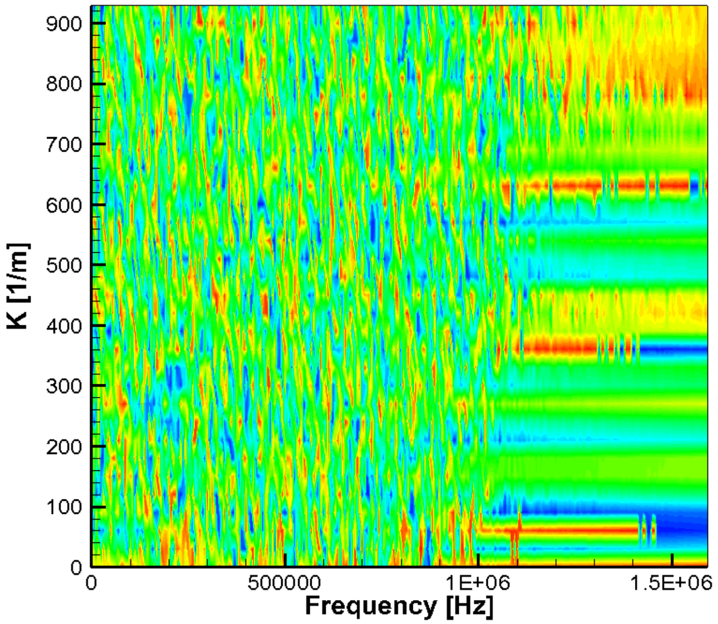

900
800
700
600
500
400
300
200
100
0
K [1/m]
0
500000
1E+06
1.5E+06
Frequency [Hz]

d)

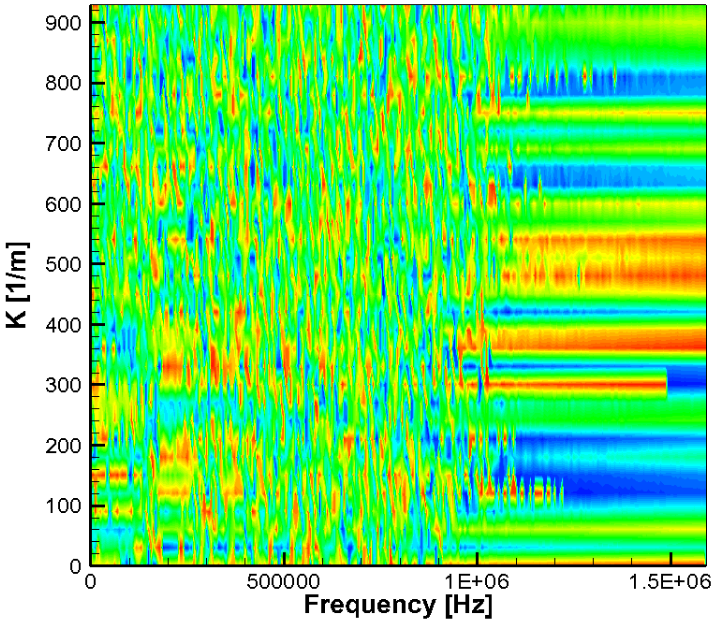

e)

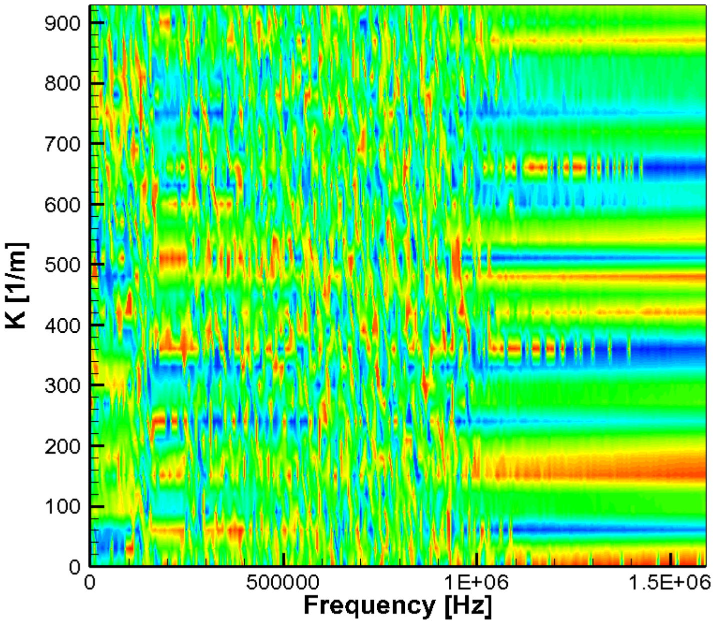

f)

Fig. 60. Spanwise wave number vs. Frequency of phase for all wave modes: a) X=0.47m, b) X=0.6m, c) X=0.7m, d) X=0.8m, e) X=0.9m, f) X=0.95m.

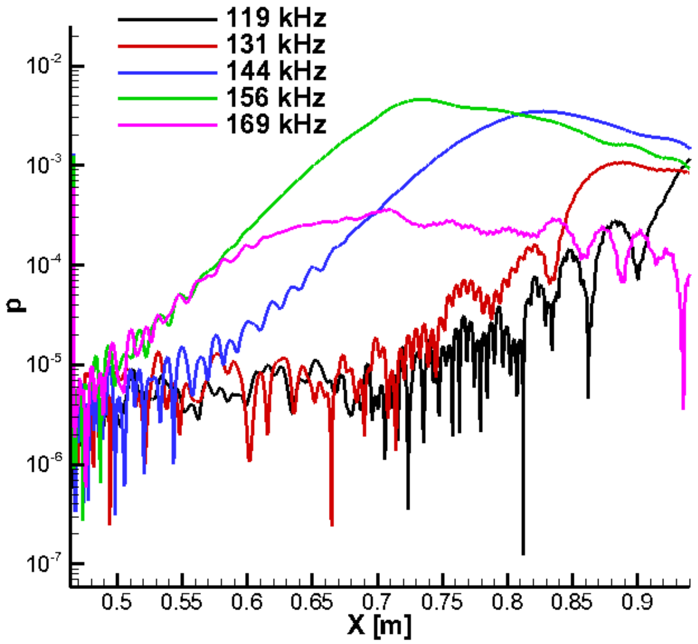

119 kHz
131 kHz
144 kHz
156 kHz
169 kHz
p
10^{-2}
10^{-3}
10^{-4}
10^{-5}
10^{-6}
10^{-7}
0.5
0.55
0.6
0.65
0.7
0.75
0.8
0.85
0.9
X [m]

a)

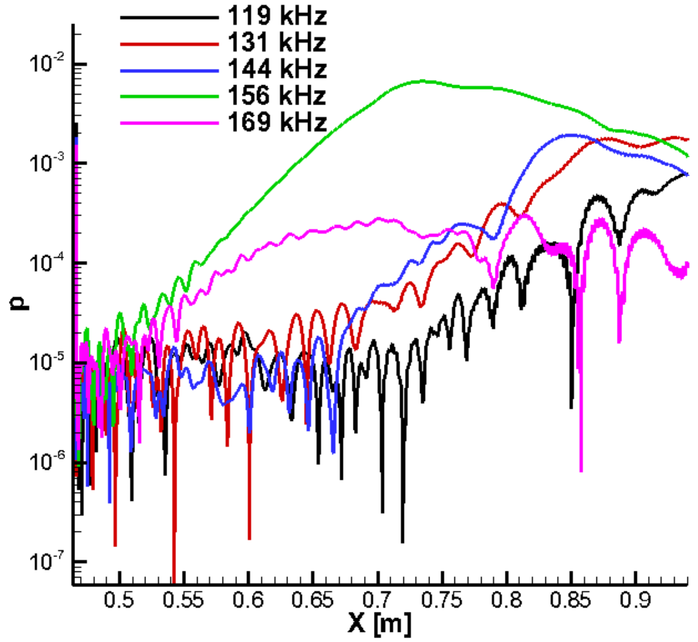

119 kHz
131 kHz
144 kHz
156 kHz
169 kHz
p
10^{-2}
10^{-3}
10^{-4}
10^{-5}
10^{-6}
10^{-7}
0.5
0.55
0.6
0.65
0.7
0.75
0.8
0.85
0.9
X [m]

b)

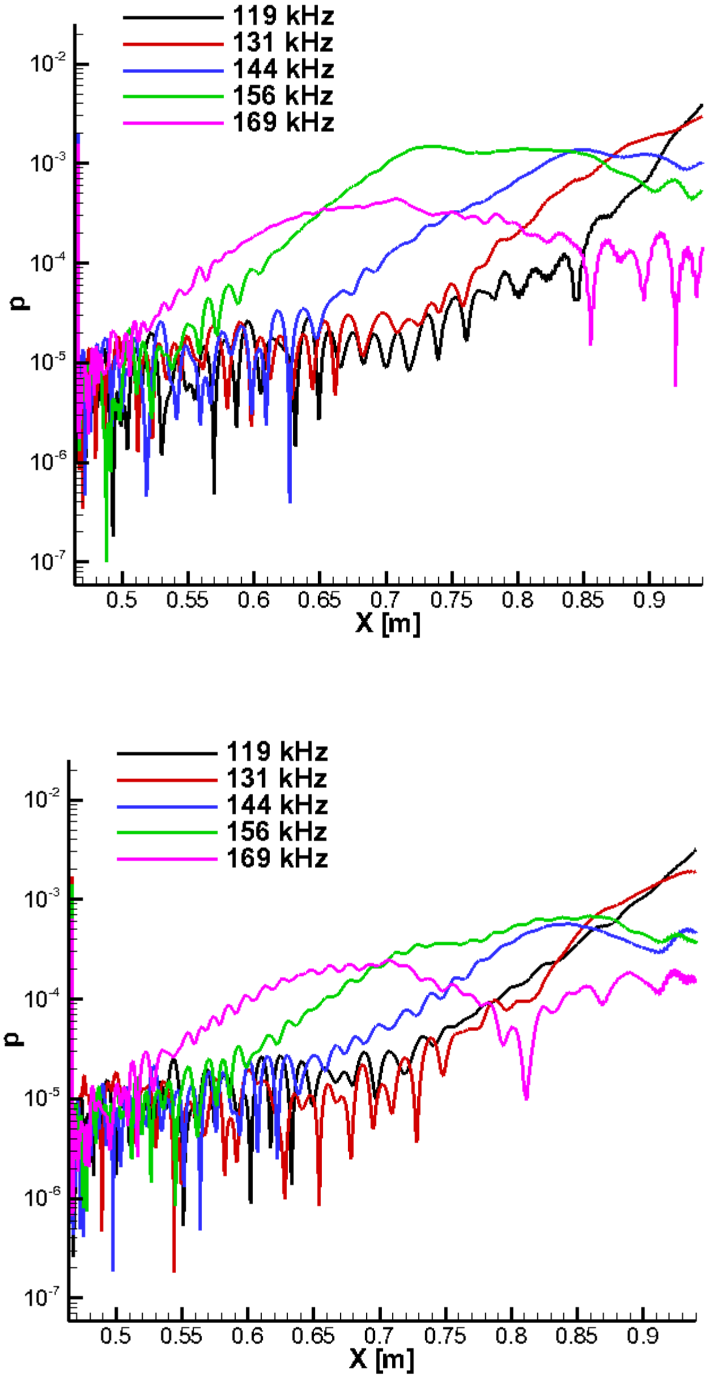

c)

d)

Fig. 61. Selected frequency modes at different spanwise wave numbers: a) K=0, b) K=300, c) K=600, d) K=900.

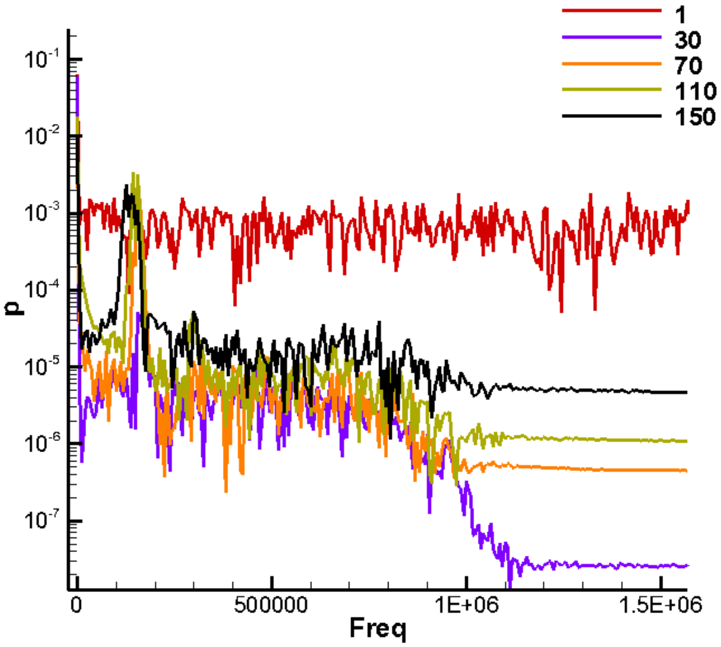
1
30
70
110
150
10^{-1}
10^{-2}
10^{-3}
10^{-4}
10^{-5}
10^{-6}
10^{-7}
p
0
500000
1E+06
1.5E+06
Freq

a)

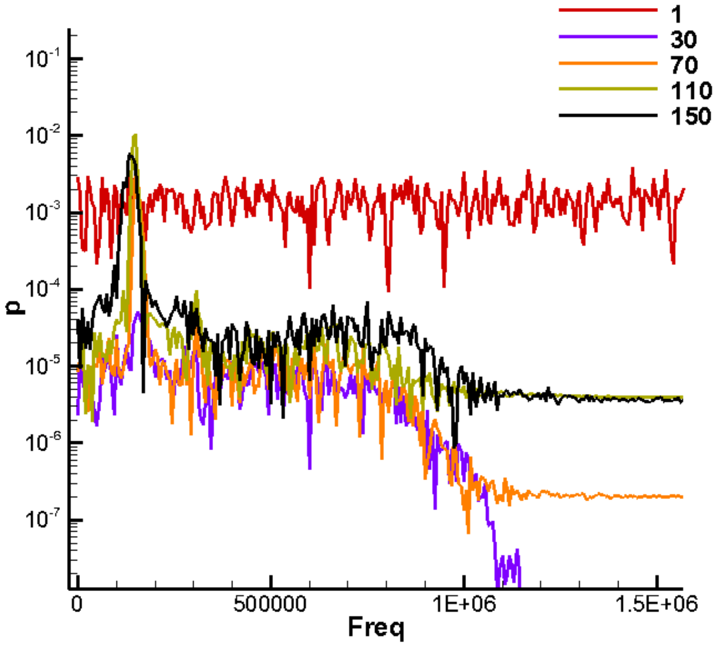
1
30
70
110
150
10^{-1}
10^{-2}
10^{-3}
10^{-4}
10^{-5}
10^{-6}
10^{-7}
p
0
500000
1E+06
1.5E+06
Freq

b)

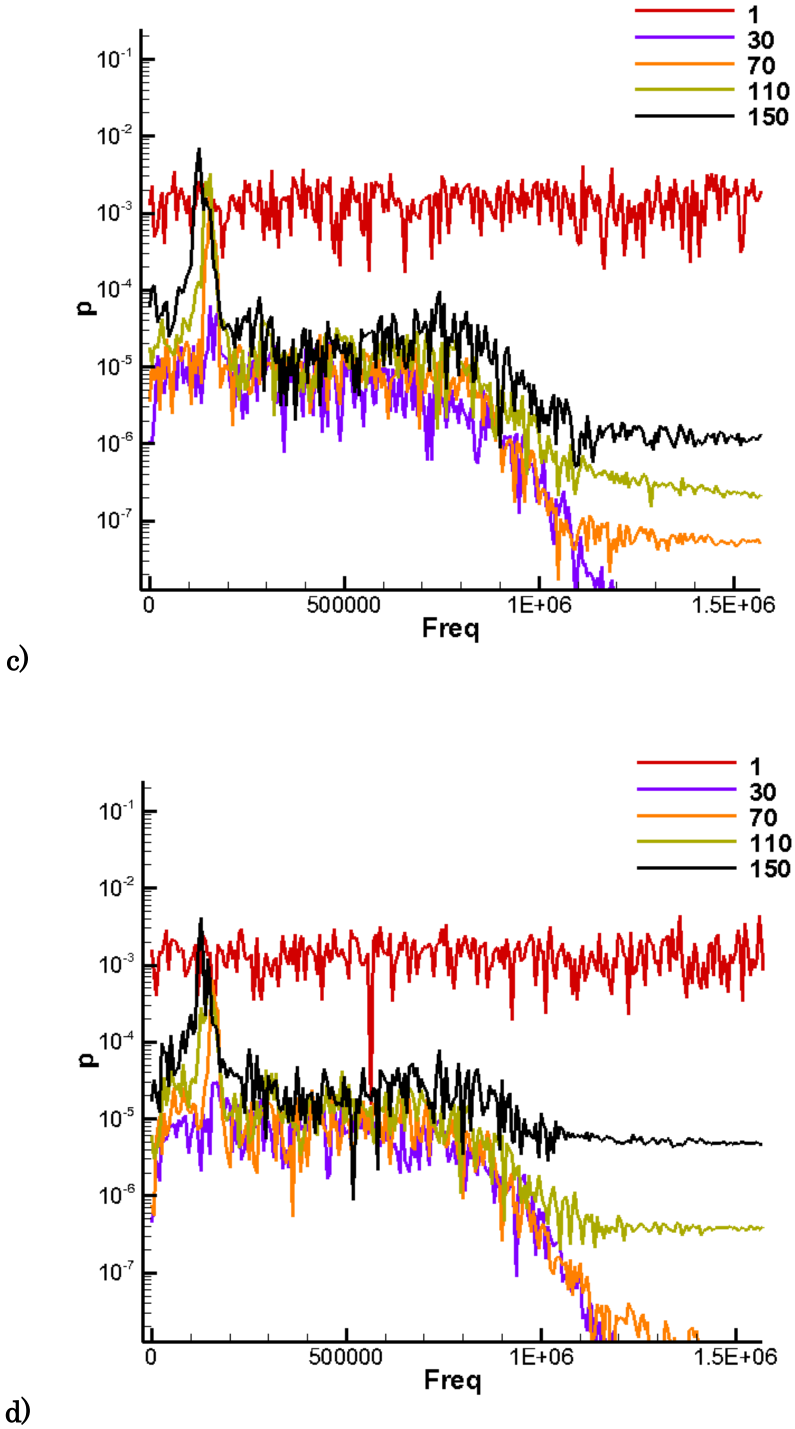

Fig. 62. Pressure perturbation amplitude spectra at different spanwise wave number: a) K=0, b) K=300, c) K=600, d) K=900.

6.3.3. TAMU1: Breakdown Simulation with 2 Degrees Arc in Azimuth Direction

Test cases TAMU1 to 3 are the primary study cases of current research. They are set up to the identical forcing environment and grid resolution with the only exception that the spanwise arc angles in azimuth direction of computational domains are different. For 3-D breakdown simulation, it is very difficult to obtain grid independence result. However, with a parametric study performed to capture different spanwise wave modes, we can better understand how wave modes in different spanwise wave number range play roles in the process of nonlinear breakdown.

The test case TAMU1 presented in this section has a spanwise arc angle of 2 degree resolved by 64 spanwise grid points. With this computation setup, we are able to capture 32 uniformly distributed spanwise wave modes from K=0 to K=5760. Fig. 63 is the instantaneous pressure disturbance contour at the cone surface. It clearly shows that the pressure contour has two dimensional pattern up to x= 0.75 m. The overall disturbance amplitude grows as the disturbance wave moves further in the downstream direction. The pressure disturbance amplitude rapidly drop at X=0.75 m and some three dimensional feature slowly develops. It reaches another peak around X-0.91 m and quickly breaks down to a more chaotic and non-uniformed three dimensional wave pattern.

The evolution of flow structure can be better visualized by looking at the spanwise vorticity development within the boundary layer. Fig. 64 shows the side view of spanwise vorticity contour at different spanwise stations. There are variations from station to station. But it can be observed from the contours that the spanwise vorticity is trapped by the boundary layer and most fluctuated near the edge of boundary layer. The “rope wave” is in well organized pattern at the beginning of the breakdown region but become more and more in-regular as it travels further downstream. This shift of pattern is most obvious at spanwise station φ=0.0 and φ=0.0087.

Fig. 65 shows the contours of wall-normal density gradient. These plots are converted into gray scale to purposely mimic the Schlieren diagrams commonly used in experiment for flow visualization. Again, the highest density gradient locates near the edge of boundary layer. In the plots, we can also see the Mach waves radiating away from boundary layer which is typically found during breakdown process.

Q criterion is commonly used to visualize the flow structure of turbulence flow. It can be computed using the following formula:

$$Q=\frac{1}{2}\left(\Omega_{ij}\Omega_{ij}-S_{ij}S_{ij}\right),\quad \text{where } S_{ij}=\frac{1}{2}\left(\frac{\partial u_i}{\partial x_j}+\frac{\partial u_j}{\partial x_i}\right) \text{ and } \Omega_{ij}=\frac{1}{2}\left(\frac{\partial u_i}{\partial x_j}-\frac{\partial u_j}{\partial x_i}\right) \tag{71}$$

The instantaneous Q criterion iso-surface is presented in Fig. 66 for the flow structure in the breakdown region. From the iso-surface plot, it is observed that the breakdown is not uniformly across the flow field. In the current case, the flow filed near the boundary to the right seems more into the breakdown which shows more in-regular flow structure and more red color than the rest of the flow filed.

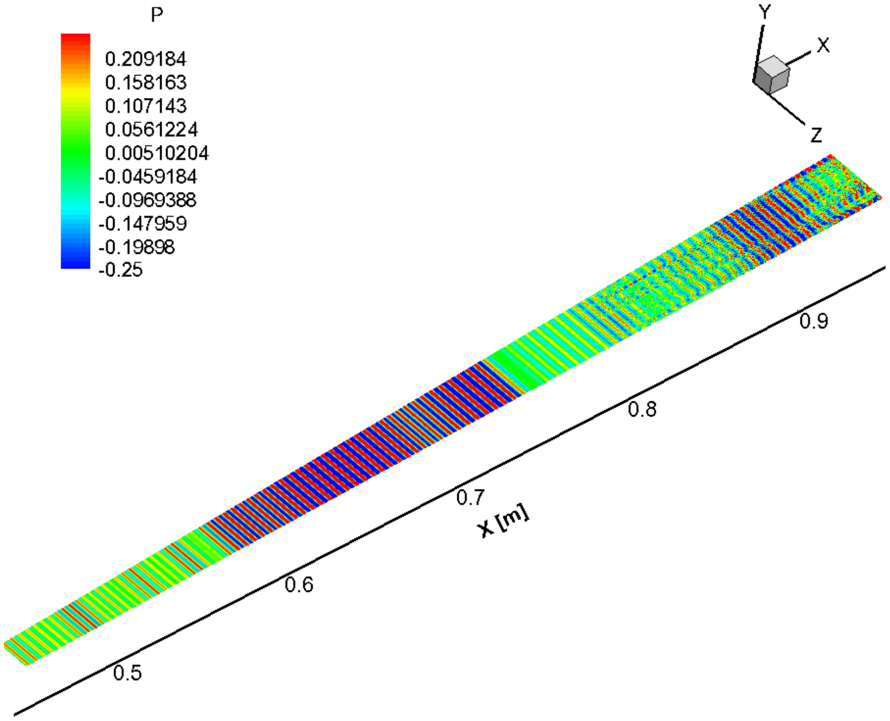

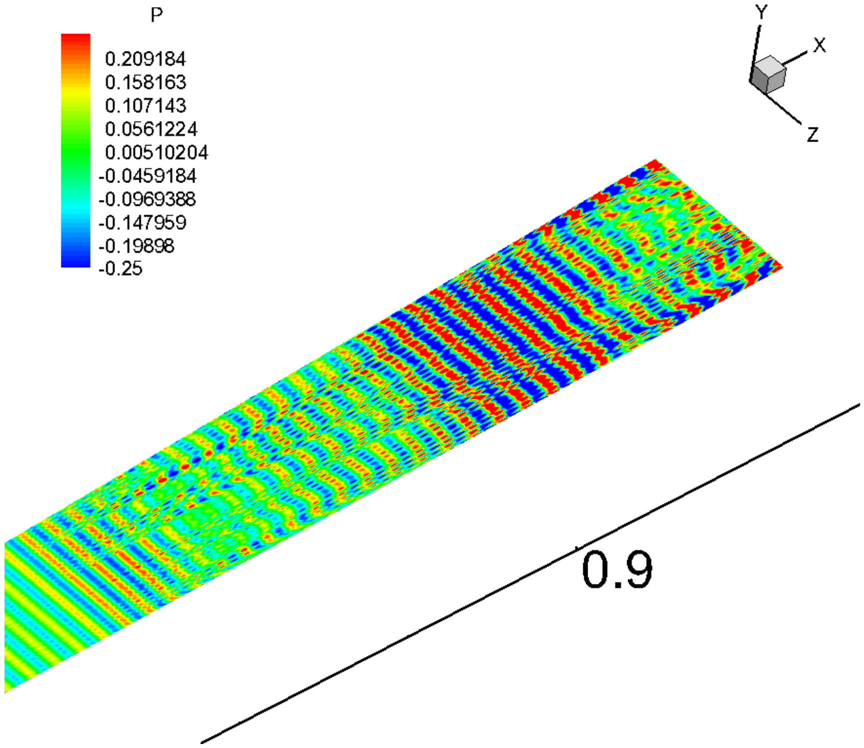

Fig. 63. Pressure disturbance on the cone surface for TAMU1 and the blow-up view of the breakdown region.

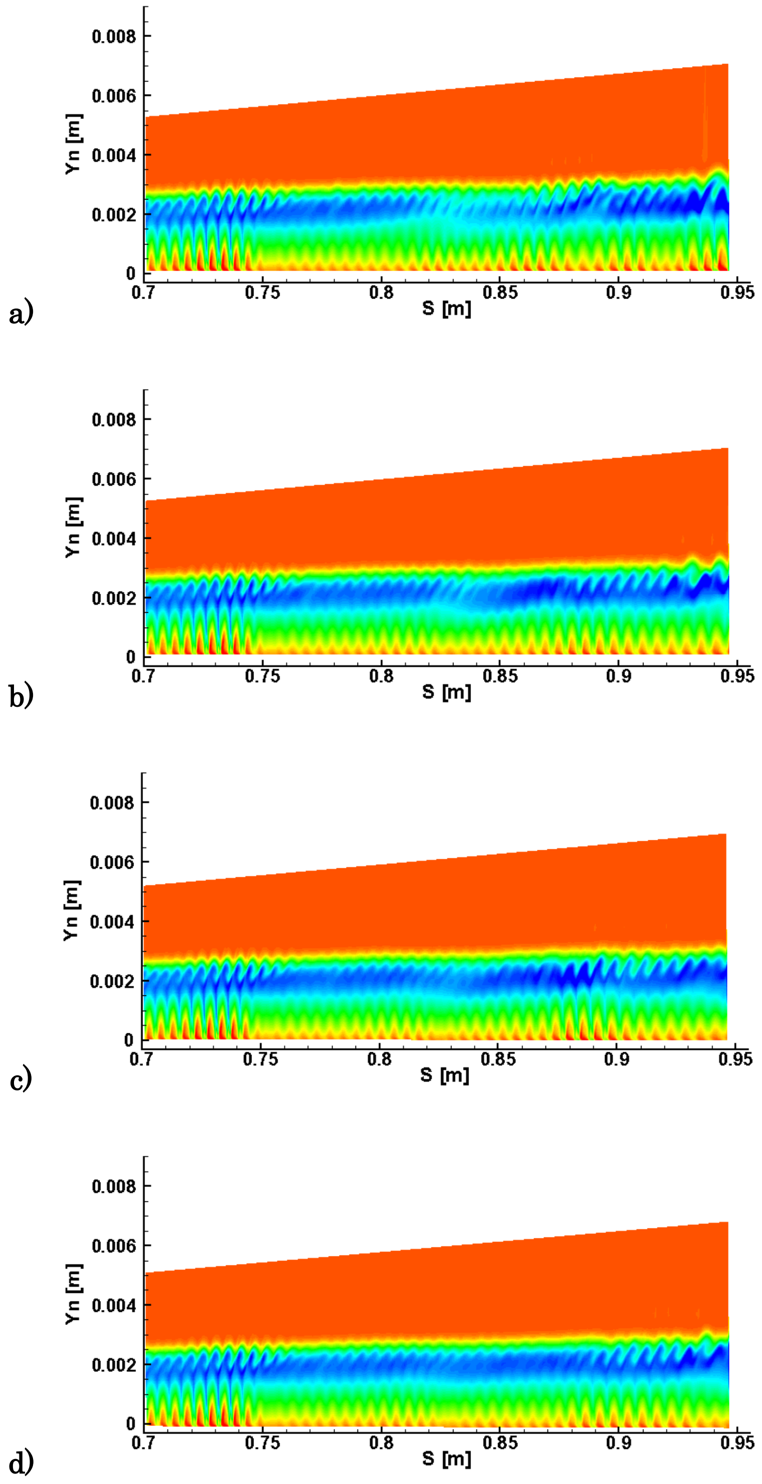

Fig. 64. Spanwise vorticity contour at different azimuth planes: a) φ = 0.0, b) φ = 0.0087 c) φ = 0.0174 d) φ = 0.0261.

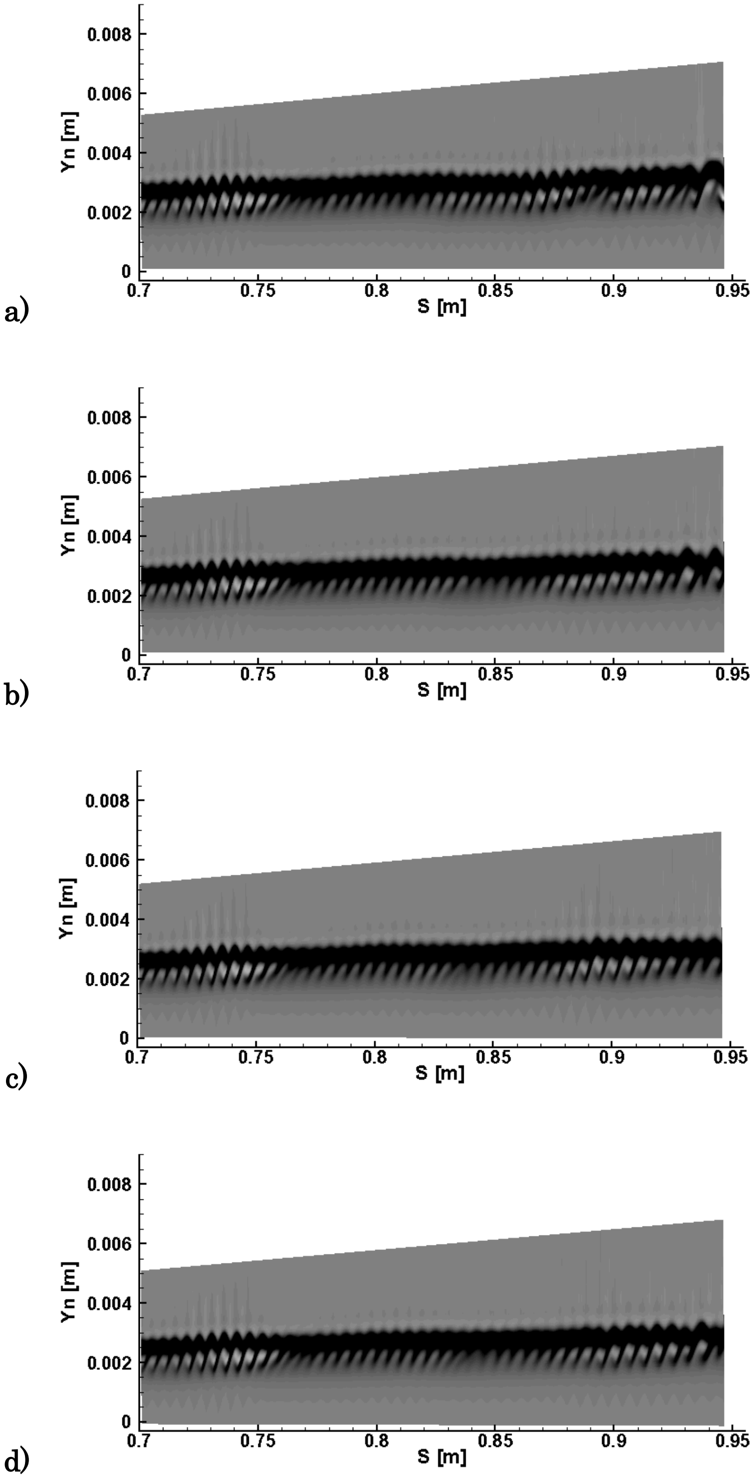

Fig. 65. Density wall-normal gradient contour at different azimuth planes: a) φ = 0.0, b) φ = 0.0087 c) φ = 0.0174 d) φ = 0.0261.

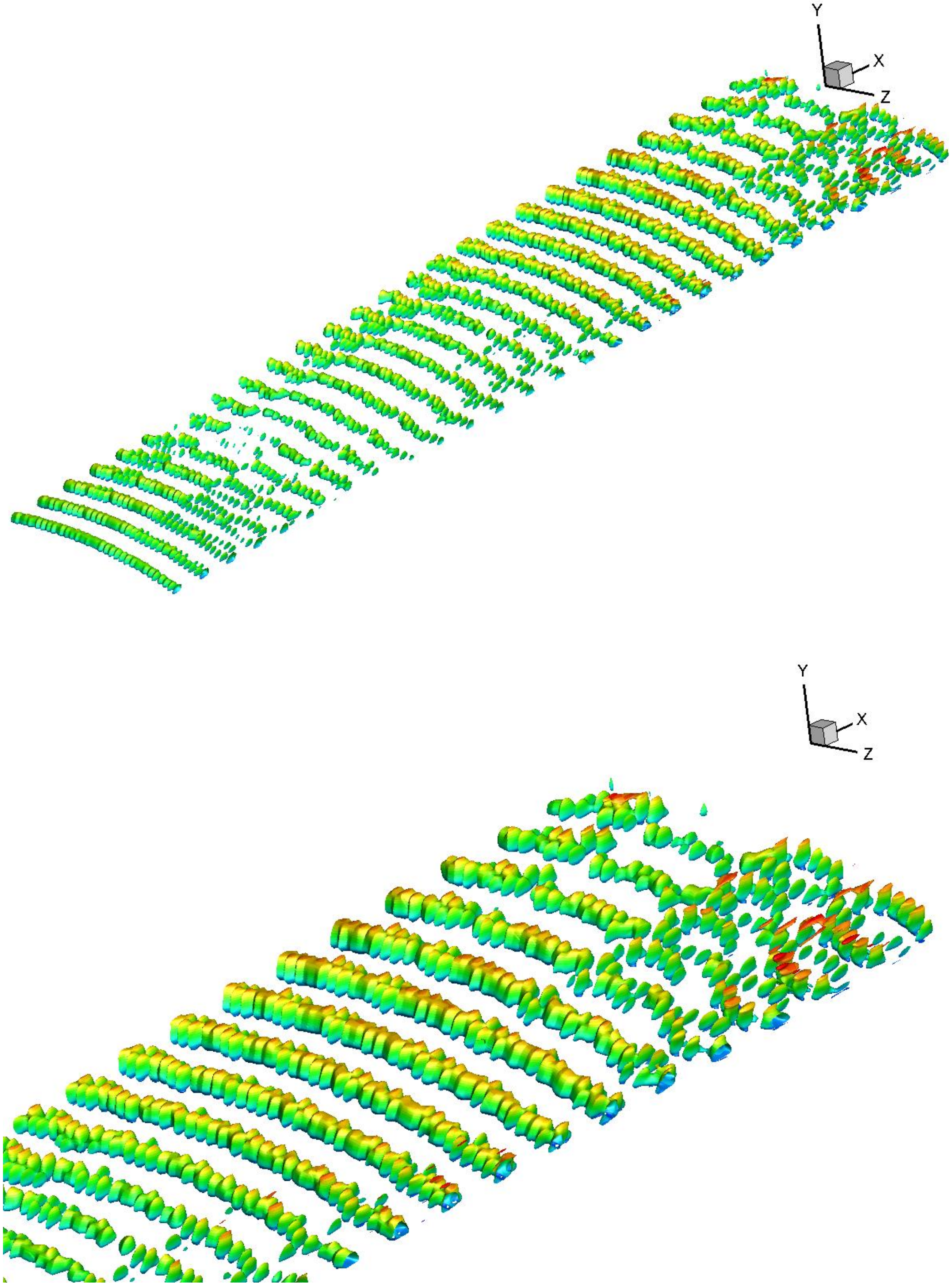

Fig. 66. Iso-surface with vortex detection Q-criterion value set to 5000 colored by streamwise velocity.

To better study the breakdown mechanism of this particular test case, each wave mode's pressure disturbance amplitude is obtained from Fourier decomposition in both time and spanwise spatial direction. The results are plotted in wave mode number versus frequency plane as shown in Fig. 67 for selected location along the downstream direction. At X= 0.47 m, the spectrum shows a strong 2-D second-mode waves between 160 kHz and 200 kHz with the low level noise all over the plane. At x=0.6 m, the noise components are no longer visible but another peak appears around 330 kHz that represents the higher harmonic wave. This is an indication that the disturbance wave amplitudes are large enough that the flow enters the nonlinear stage. Once the waves become strongly nonlinear, some spanwise wave mode that has the same frequency as the second-mode waves start to grow. The growths are stronger at the higher spanwise wave number end. As the disturbance moves further downstream, the peaks at both the lower end and higher end of spanwise wave mode spectrum tend to move toward the middle range. Once the wave modes of entire spanwise wave number spectrum around the second mode frequencies grow to certain threshold level, they further spread the growth to the near-by frequencies at the same spanwise wave number. At X=0.95 m, all the wave modes around the second-mode frequencies and the higher harmonic of second-mode frequencies reach relatively high amplitudes and the energy further spread to near-by wave modes. At X=0.9 m, there is another area outside the second mode region that the wave modes are also growing. The region is at frequencies lower than second mode and at very high spanwise wave numbers. These growing wave modes match the description of sub harmonic resonance. However, the growths of these wave modes are so weak that it cannot play a primary role in breakdown process.

In addition to the disturbance amplitude spectrum, the phase angels are presented in Fig. 68. The phase angle spectra show how the wave modes interact during the secondary nonlinear growth region as well as the breakdown region. There is clearly a shift of pattern from location to location. At the inflow region, the phase angles look completely random. When the nonlinear interaction becomes strong, the phase angles of the wave modes with the same spanwise wave number tend to line up with each others. This kind of lock-up feature seems to help enhancing the growth of wave modes and spreading energy to near-by wave modes.

More quantitative plots to observe wave mode developments are provided in Fig. 69 for the wave modes believed to be most relevant to the breakdown process. All the selected wave modes are within the second-mode frequency range. The plots show that all wave modes are growing but at different rates during the breakdown. And the amplitudes of primary 2-D wave modes are at least one order of magnitudes higher than 3-D modes at their peaks. However, when they reach saturation level, the amplitudes pull down a bit. Meanwhile, the 3-D modes continue their growths trying to catch up to the level of 2-D primary wave modes. Furthermore, the primary modes behave very differently than the linear case. The 2-D wave modes seem to suppress the growth of each other but at the same time relay the growing trend to maintain the overall disturbance amplitude. The growing patterns of higher spanwise wave modes follow the growths of their corresponding 2-D modes closely but the amplitude is much lower.

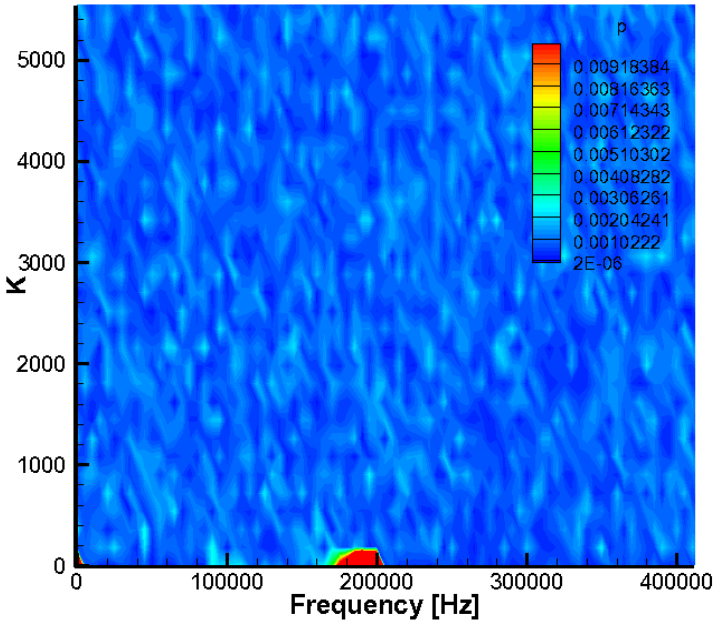
p
0.00918384
0.00816363
0.00714343
0.00612322
0.00510302
0.00408282
0.00306261
0.00204241
0.0010222
2E-06
K
5000
4000
3000
2000
1000
0
0
100000
200000
300000
400000
Frequency [Hz]

a)

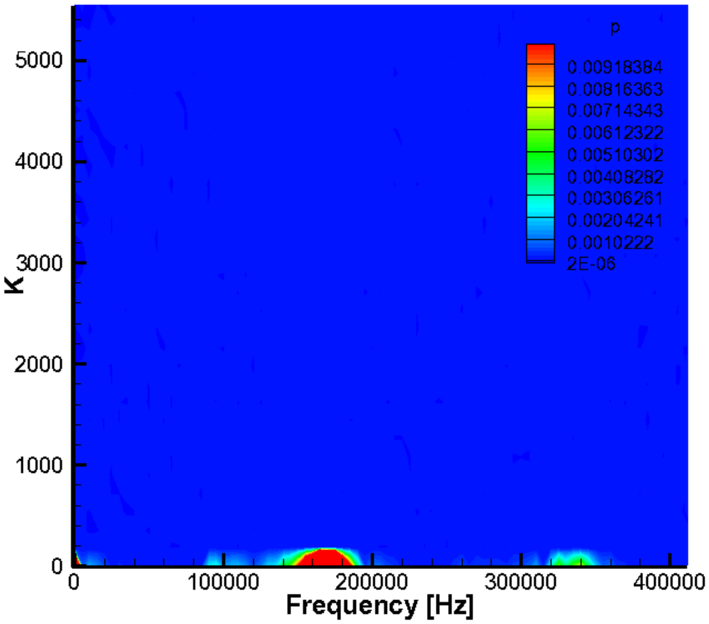
p
0.00918384
0.00816363
0.00714343
0.00612322
0.00510302
0.00408282
0.00306261
0.00204241
0.0010222
2E-06
K
5000
4000
3000
2000
1000
0
0
100000
200000
300000
400000
Frequency [Hz]

b)

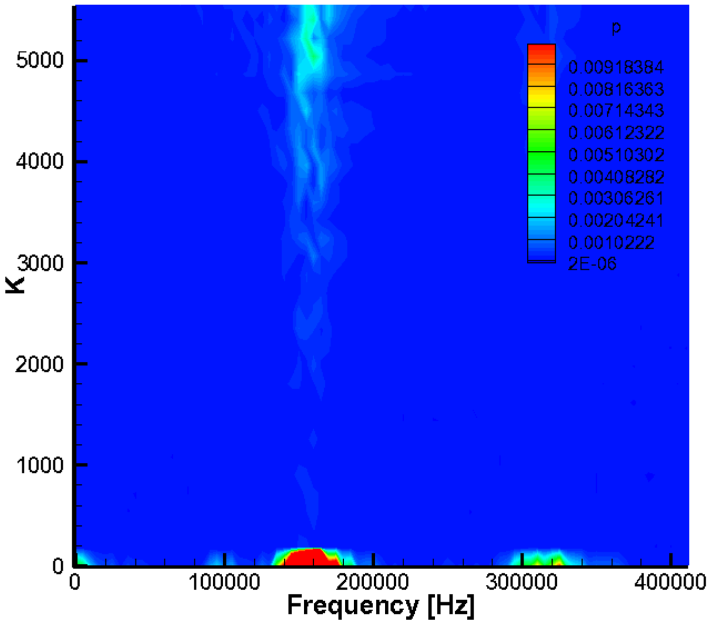
p
0.00918384
0.00816363
0.00714343
0.00612322
0.00510302
0.00408282
0.00306261
0.00204241
0.0010222
2E-06
K
0
1000
2000
3000
4000
5000
0
100000
200000
300000
400000
Frequency [Hz]

c)

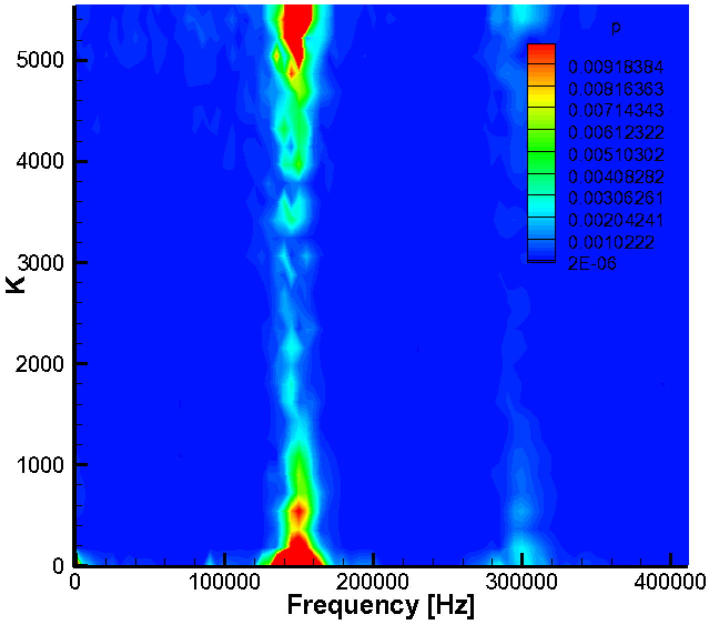
p
0.00918384
0.00816363
0.00714343
0.00612322
0.00510302
0.00408282
0.00306261
0.00204241
0.0010222
2E-06
K
0
1000
2000
3000
4000
5000
0
100000
200000
300000
400000
Frequency [Hz]

d)

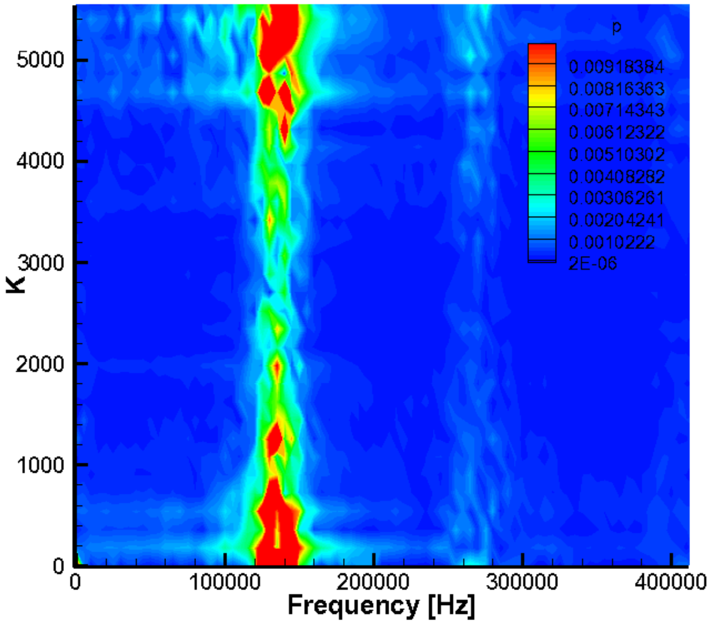

e)

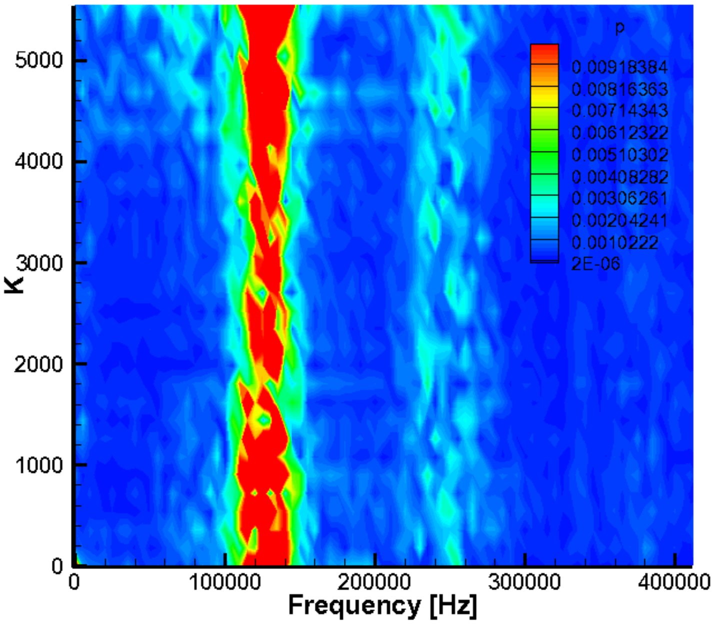

f)

Fig. 67 Frequency vs. azimuth wave number at different surface locations: a) X=0.47m, b) X=0.6m, c) X=0.7m, d) X=0.8m, e) X=0.9m, f) X=0.95m.

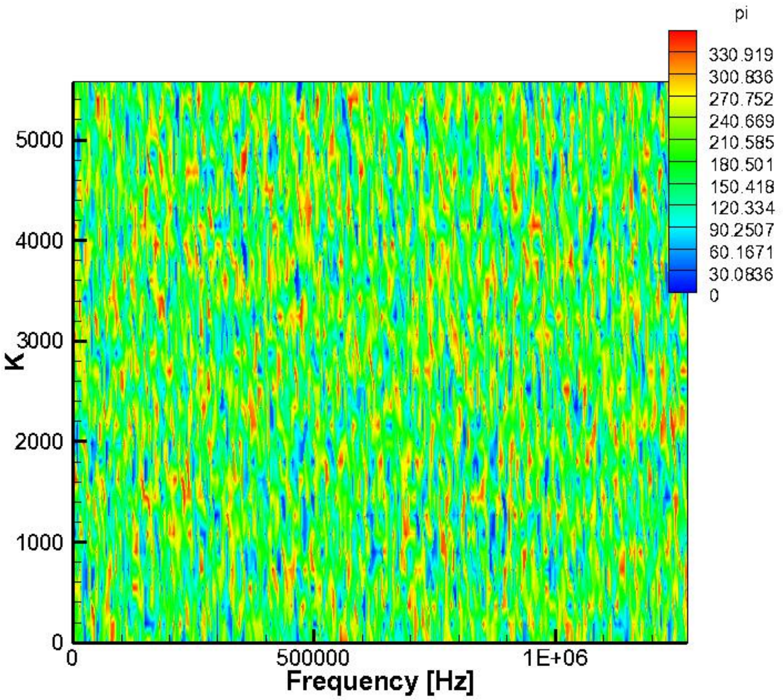
pi
330.919
300.836
270.752
240.669
210.585
180.501
150.418
120.334
90.2507
60.1671
30.0836
0
K
5000
4000
3000
2000
1000
0
0
500000
1E+06
Frequency [Hz]

a)

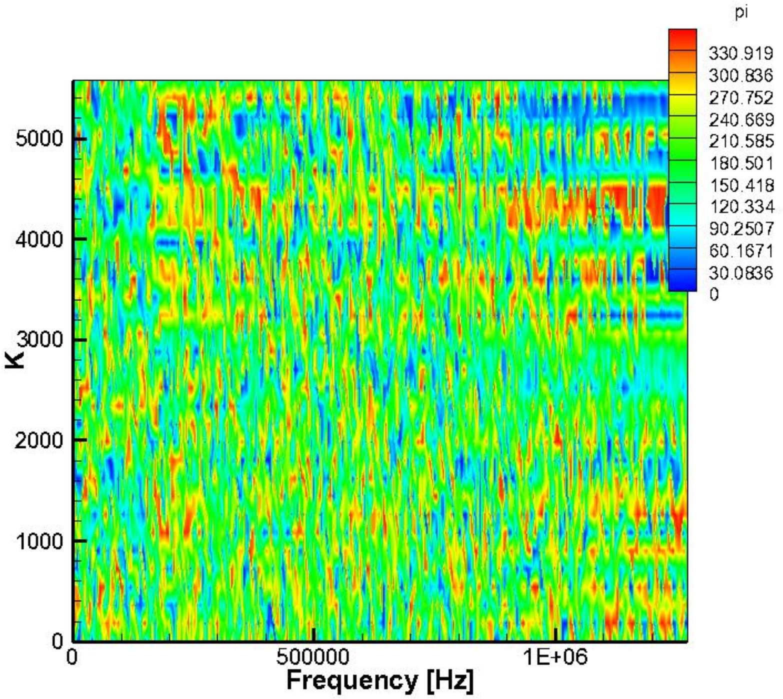
pi
330.919
300.836
270.752
240.669
210.585
180.501
150.418
120.334
90.2507
60.1671
30.0836
0
K
5000
4000
3000
2000
1000
0
0
500000
1E+06
Frequency [Hz]

b)

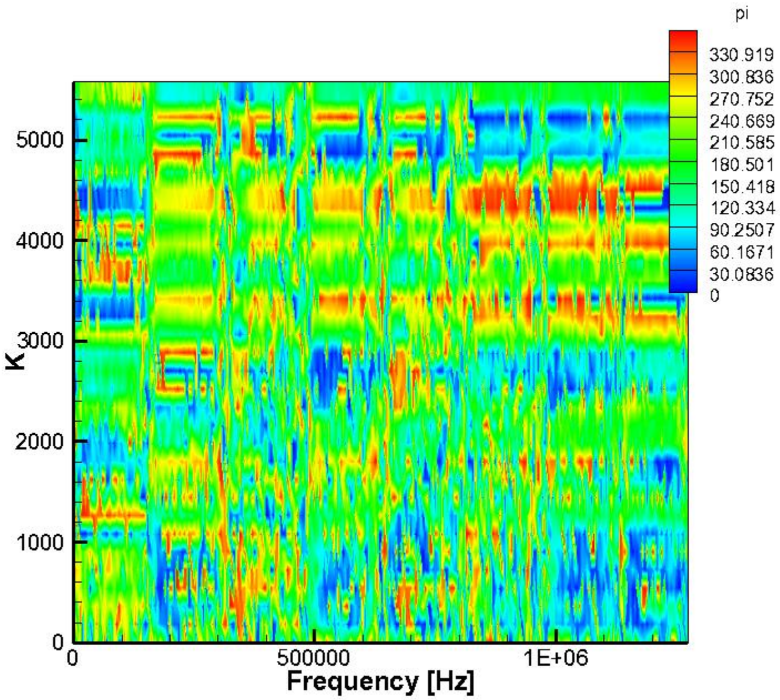
pi
330.919
300.836
270.752
240.669
210.585
180.501
150.418
120.334
90.2507
60.1671
30.0836
0
5000
4000
3000
2000
1000
0
K
0
500000
1E+06
Frequency [Hz]

c)

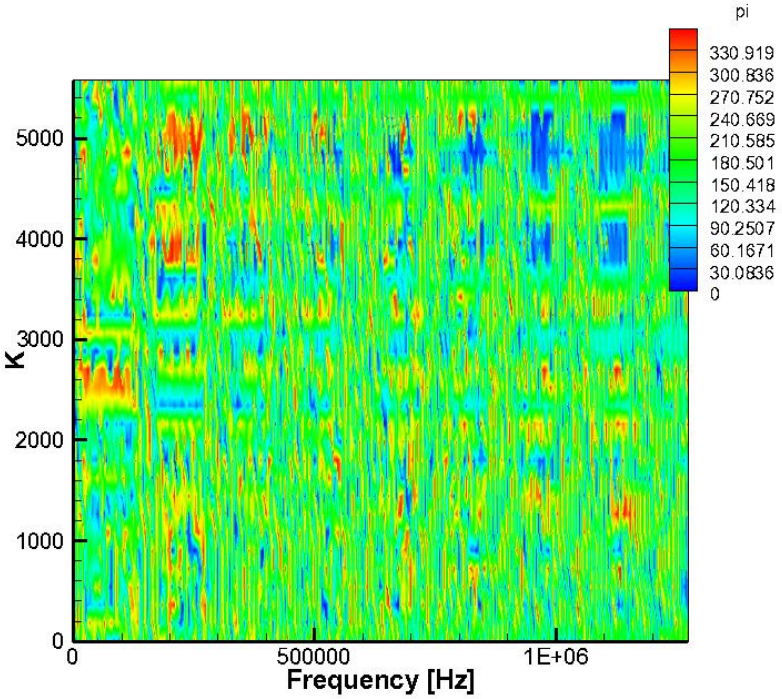
pi
330.919
300.836
270.752
240.669
210.585
180.501
150.418
120.334
90.2507
60.1671
30.0836
0
5000
4000
3000
2000
1000
0
K
0
500000
1E+06
Frequency [Hz]

f)

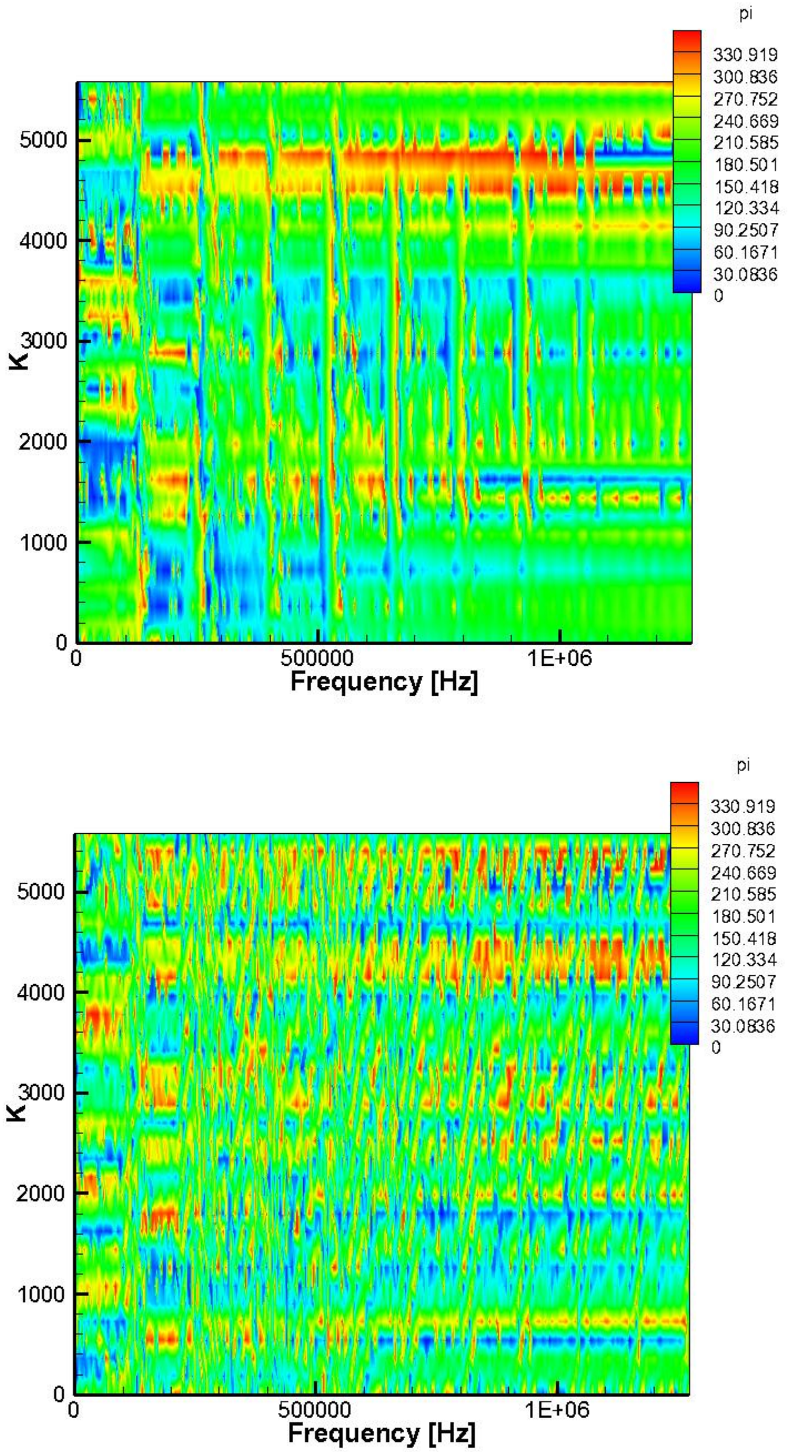

e)

f)

Fig. 68. Spanwise wave number vs. Frequency of phase for all wave modes: a) X=0.47m, b) X=0.6m, c) X=0.7m, d) X=0.8m, e) X=0.9m, f) X=0.95m.

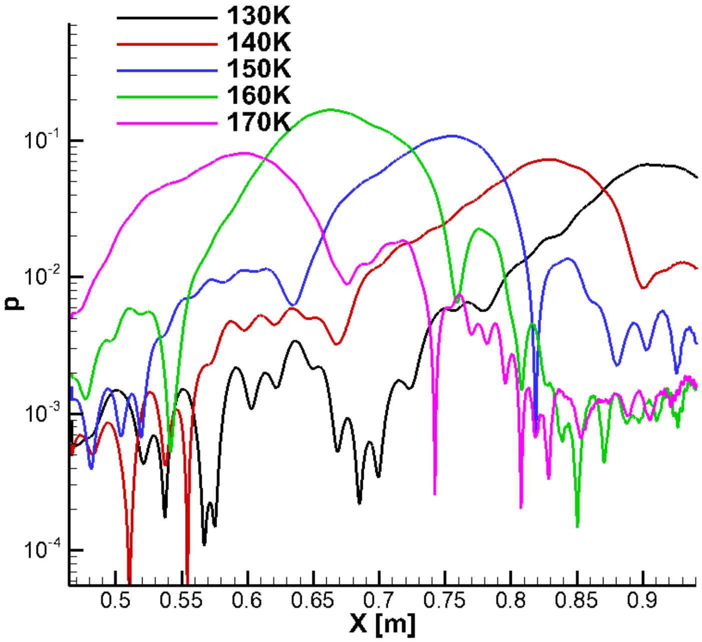
130K
140K
150K
160K
170K
p
10^{-1}
10^{-2}
10^{-3}
10^{-4}
0.5
0.55
0.6
0.65
0.7
0.75
0.8
0.85
0.9
X [m]

a)

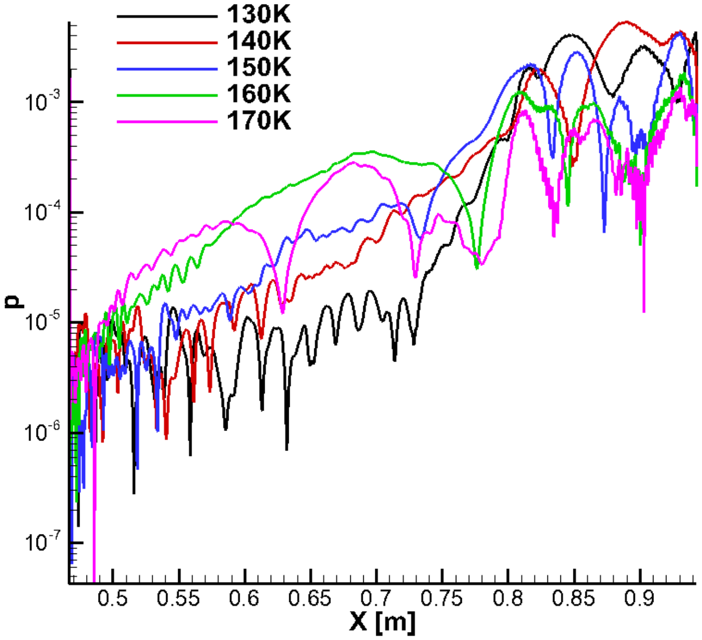
130K
140K
150K
160K
170K
p
10^{-3}
10^{-4}
10^{-5}
10^{-6}
10^{-7}
0.5
0.55
0.6
0.65
0.7
0.75
0.8
0.85
0.9
X [m]

b)

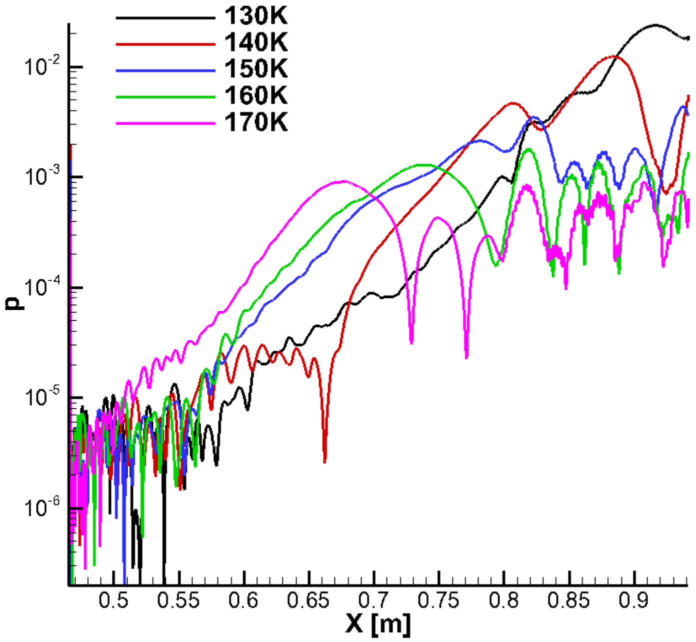

c)

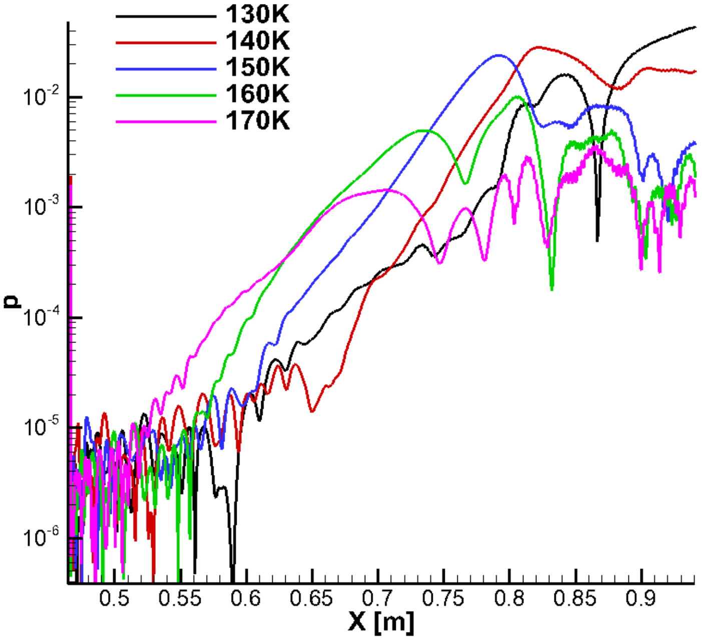

d)

Fig. 69. Selected frequency modes at different spanwise wave numbers: a) K=0, b) K=1800, c) K=3600, d) K=5400.

6.3.4. TAMU2 and TAMU3: Breakdown Simulations with Larger Arc Angles

TAMU2 and TAMU3 case are carried out to investigate how different arc angles in azimuth direction of computational domain affects the simulation result. TAMU2 and TAMU3 cases' computational domains have the spanwise arc angle of 6 degree and 12 degree respectively, which can resolve up to the spanwise wave mode number K=1860 and K=930. The purpose of these two cases is to understand if different spanwise wave number modes will behave differently during the nonlinear interactions within the secondary growth region. Surprisingly, even the arc angles in azimuth direction are greater than the one of TAMU1 case, by keeping the grid resolutions remain the same, the simulation results look very similar to TAMU1 test case.

Fig. 70 and Fig. 71 show the pressure disturbance contours along the cone surface and the blow-up view of the breakdown region. Similar pressure disturbance development patterns are found among all three test cases at the surface. Even the locations where the breakdowns occur are almost the same.

To further compare TAMU2 and TAMU3 cases to TAMU1 case, the pressure disturbance amplitude spectra are presented in Fig. 72 and Fig. 73. Even the spanwise wave number ranges are different; the overall evolutions of wave modes look almost identical. This fact is further manifests by the wave modes development along the streamwise direction for selected dominate modes in Fig. 74 and Fig. 75 for comparison purpose.

General speaking, TAMU2 and TAMU3 simulation results are very similar to TAMU1 case. However, some subtle difference is observed when we inspect the wave mode phase angles spectra development closely from location to location in Fig. 76. The phase locking feature revealed in TAMU1 is not presented in this test case. This can be further confirmed by the amplitude spectra of both TAMU2 and TAMU3 cases, where the energy spreading across wave modes at the same spanwise wave number cannot be seen. Regardless this subtle different, the flows in all these test cases reach the same stage in breakdown, which implies the simulation result is not sensitive to the arc angle of computational domain in general. At this point, it is worth to mention that, when determining what arc angle to use in the break simulation, we calculated that 2 degree arc angle is more than 2 times the boundary layer thickness at the inlet of computational domain.

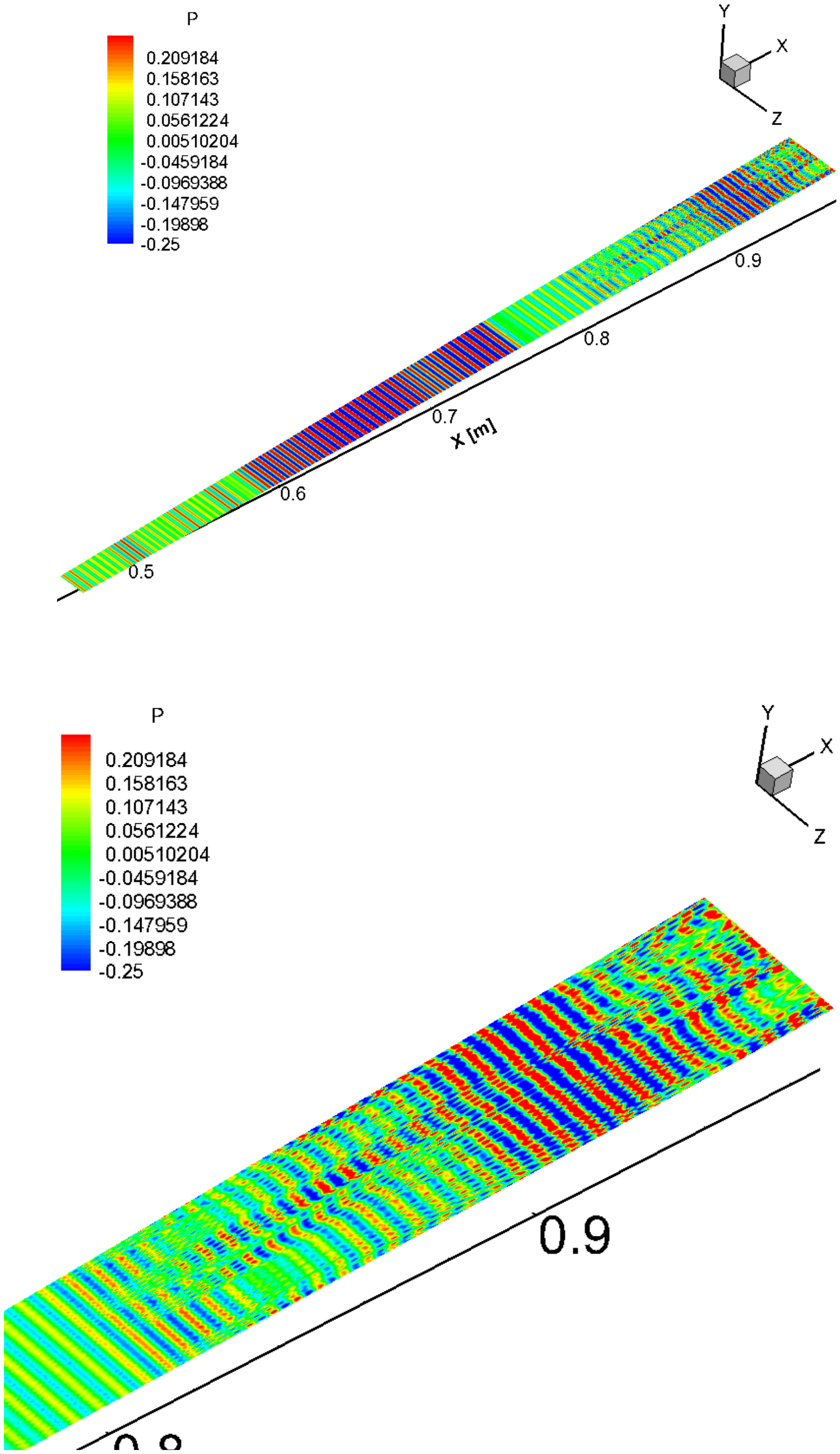

Fig. 70. Pressure disturbance on the cone surface for TAMU2 and the blow-up view of the breakdown region.

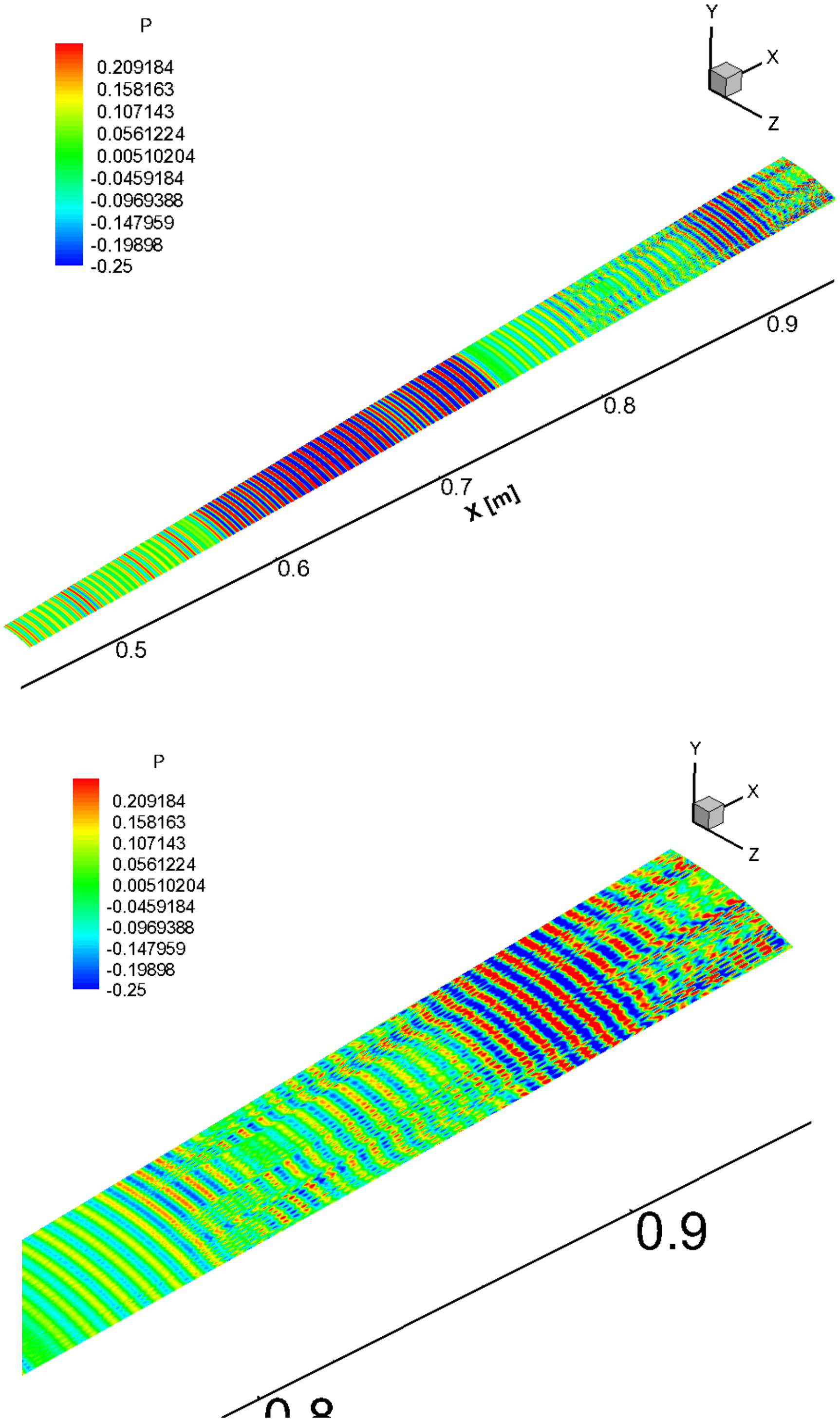

Fig. 71. Pressure disturbance contour at the cone surface for TAMU3 and the blow-up view of the breakdown region.

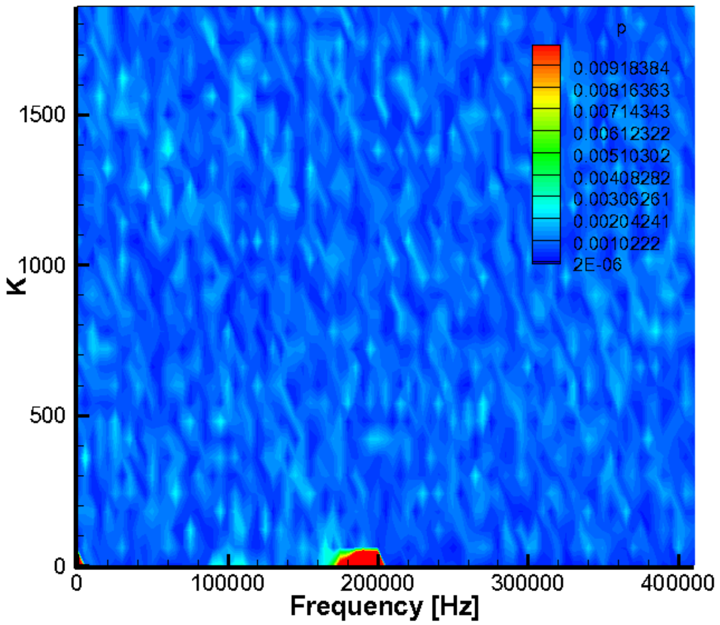
p
0.00918384
0.00816363
0.00714343
0.00612322
0.00510302
0.00408282
0.00306261
0.00204241
0.0010222
2E-06
K
0
500
1000
1500
0
100000
200000
300000
400000
Frequency [Hz]

a)

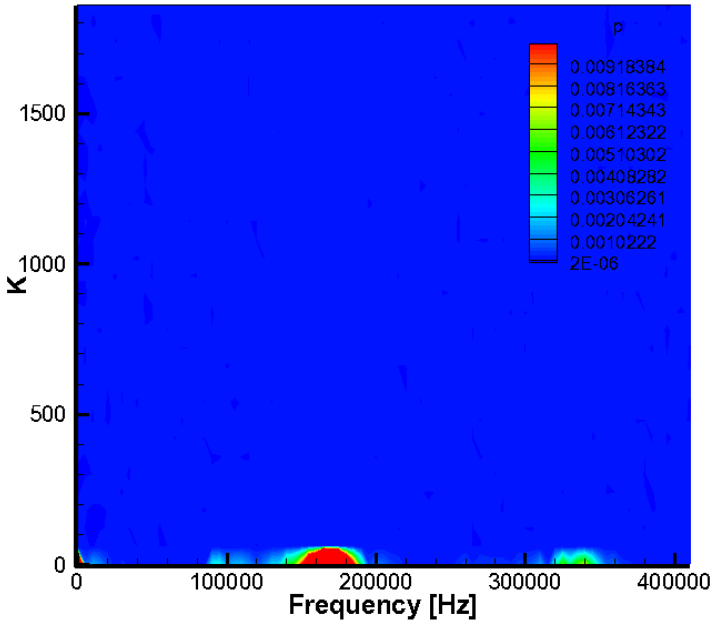
p
0.00918384
0.00816363
0.00714343
0.00612322
0.00510302
0.00408282
0.00306261
0.00204241
0.0010222
2E-06
K
0
500
1000
1500
0
100000
200000
300000
400000
Frequency [Hz]

b)

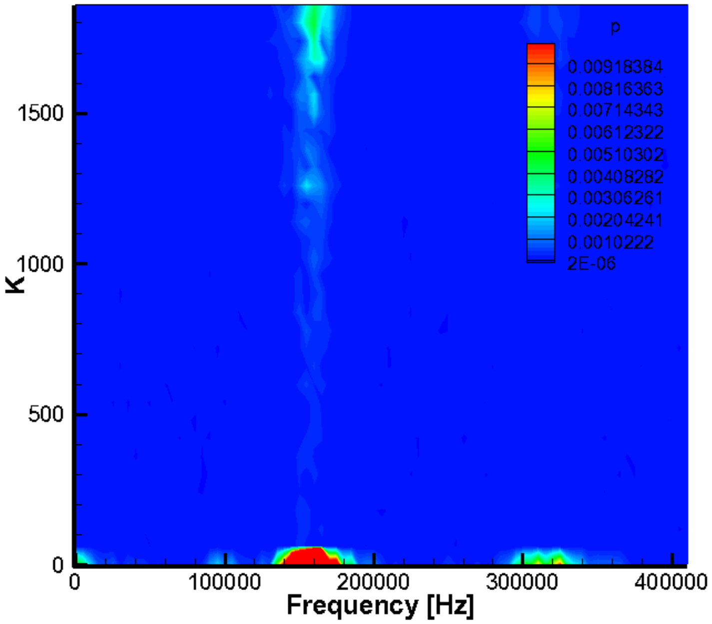
p
0.00918384
0.00816363
0.00714343
0.00612322
0.00510302
0.00408282
0.00306261
0.00204241
0.0010222
2E-06
K
0
500
1000
1500
0
100000
200000
300000
400000
Frequency [Hz]

c)

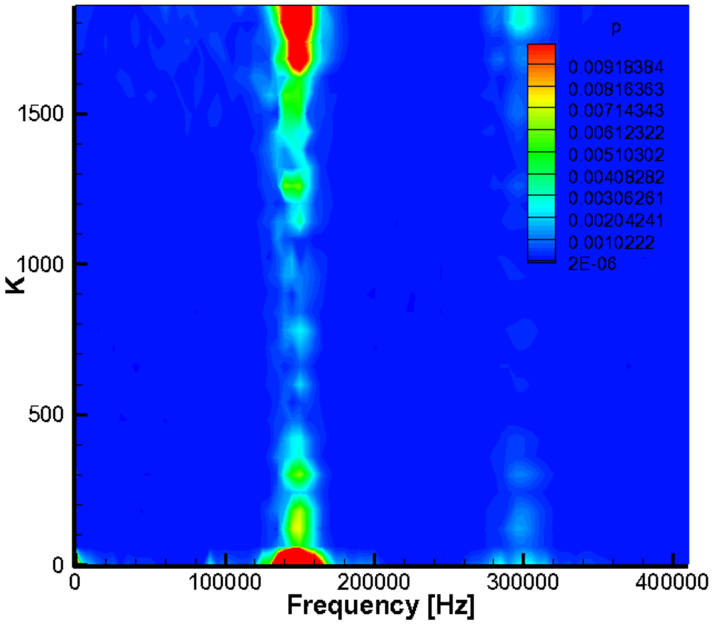
p
0.00918384
0.00816363
0.00714343
0.00612322
0.00510302
0.00408282
0.00306261
0.00204241
0.0010222
2E-06
K
0
500
1000
1500
0
100000
200000
300000
400000
Frequency [Hz]

d)

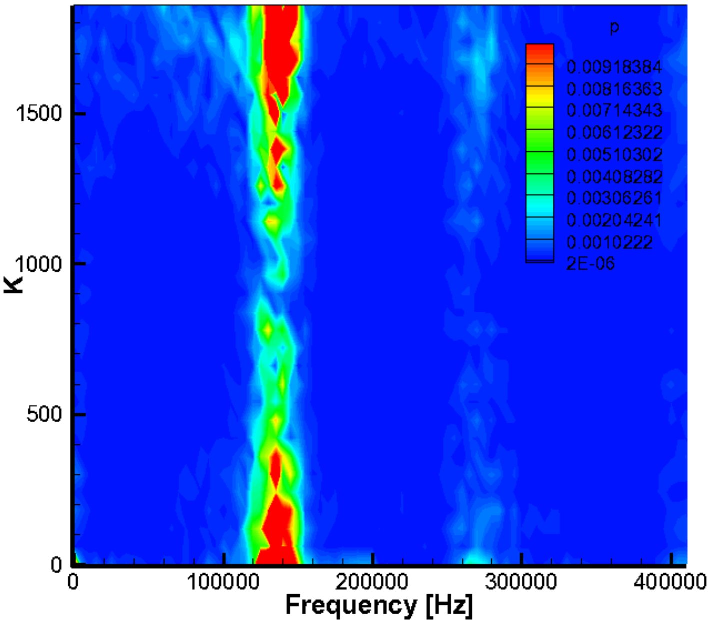

e)

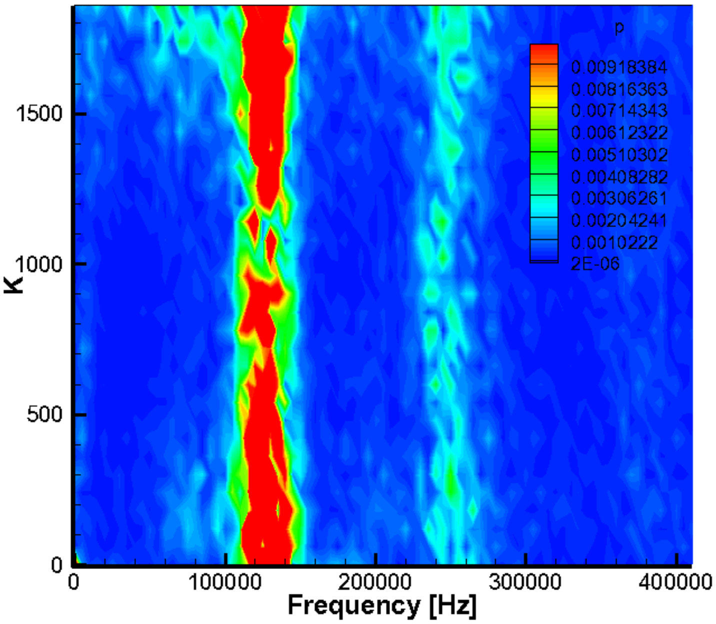

f)

Fig. 72. TAMU2: Frequency vs. azimuth wave number at different surface locations: a) X=0.47m, b) X=0.6m, c) X=0.7m, d) X=0.8m, e) X=0.9m, f) X=0.95m.

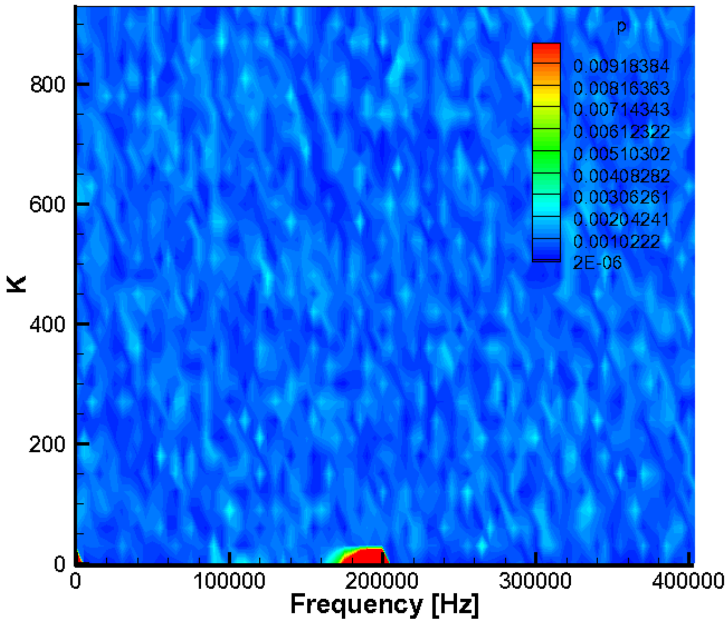
p
0.00918384
0.00816363
0.00714343
0.00612322
0.00510302
0.00408282
0.00306261
0.00204241
0.0010222
2E-06
800
600
K
400
200
0
0
100000
200000
300000
400000
Frequency [Hz]

a)

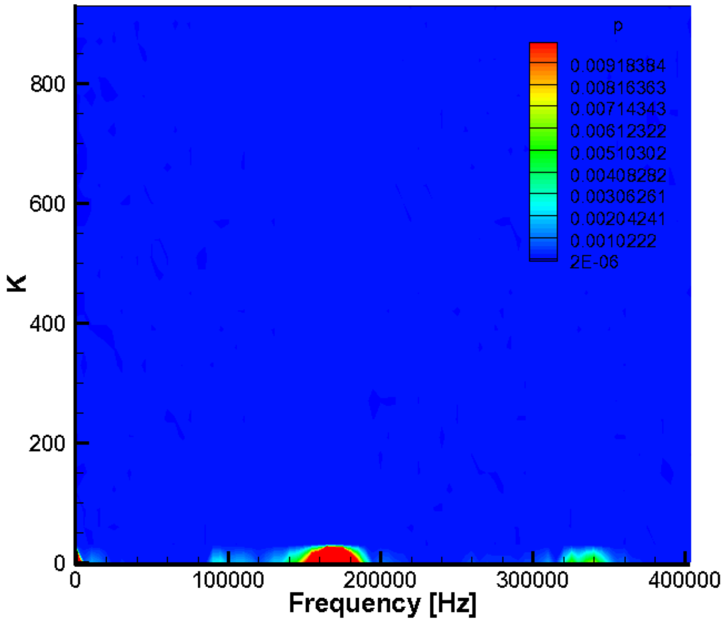
p
0.00918384
0.00816363
0.00714343
0.00612322
0.00510302
0.00408282
0.00306261
0.00204241
0.0010222
2E-06
800
600
K
400
200
0
0
100000
200000
300000
400000
Frequency [Hz]

b)

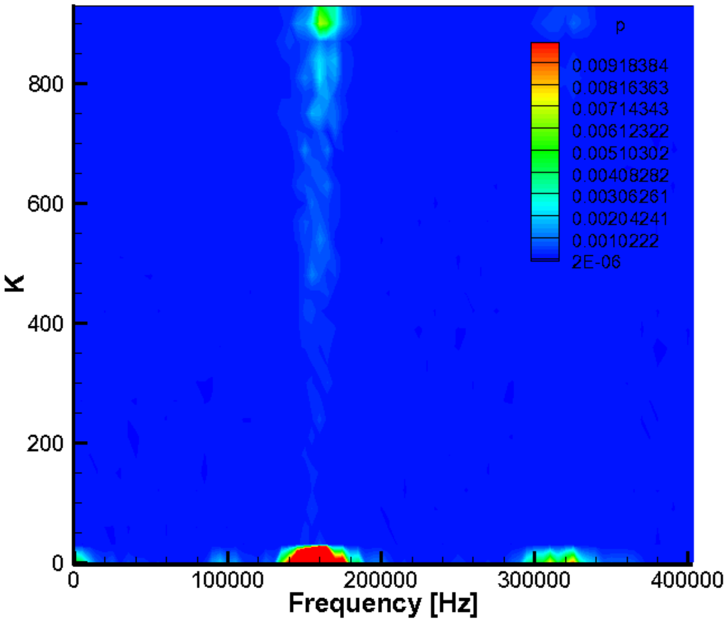

p
0.00918384
0.00816363
0.00714343
0.00612322
0.00510302
0.00408282
0.00306261
0.00204241
0.0010222
2E-06
K
800
600
400
200
0
0
100000
200000
300000
400000
Frequency [Hz]

c)

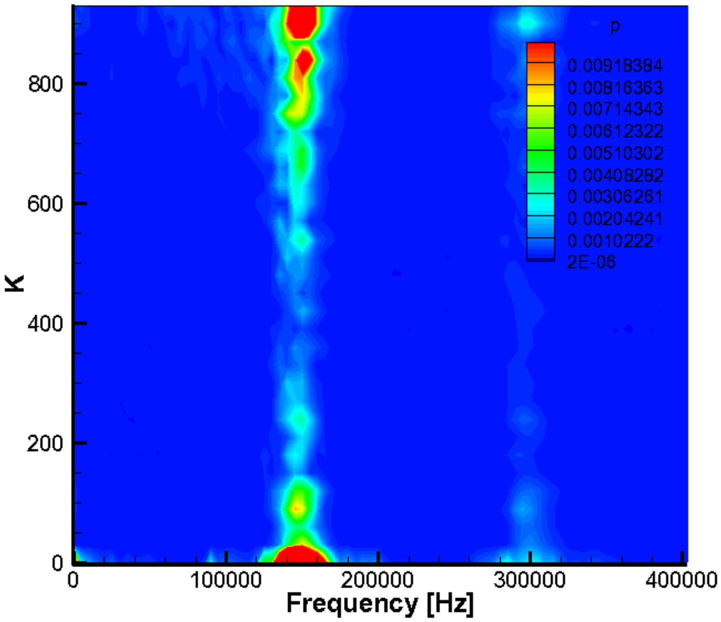

p
0.00918384
0.00816363
0.00714343
0.00612322
0.00510302
0.00408282
0.00306261
0.00204241
0.0010222
2E-06
K
800
600
400
200
0
0
100000
200000
300000
400000
Frequency [Hz]

d)

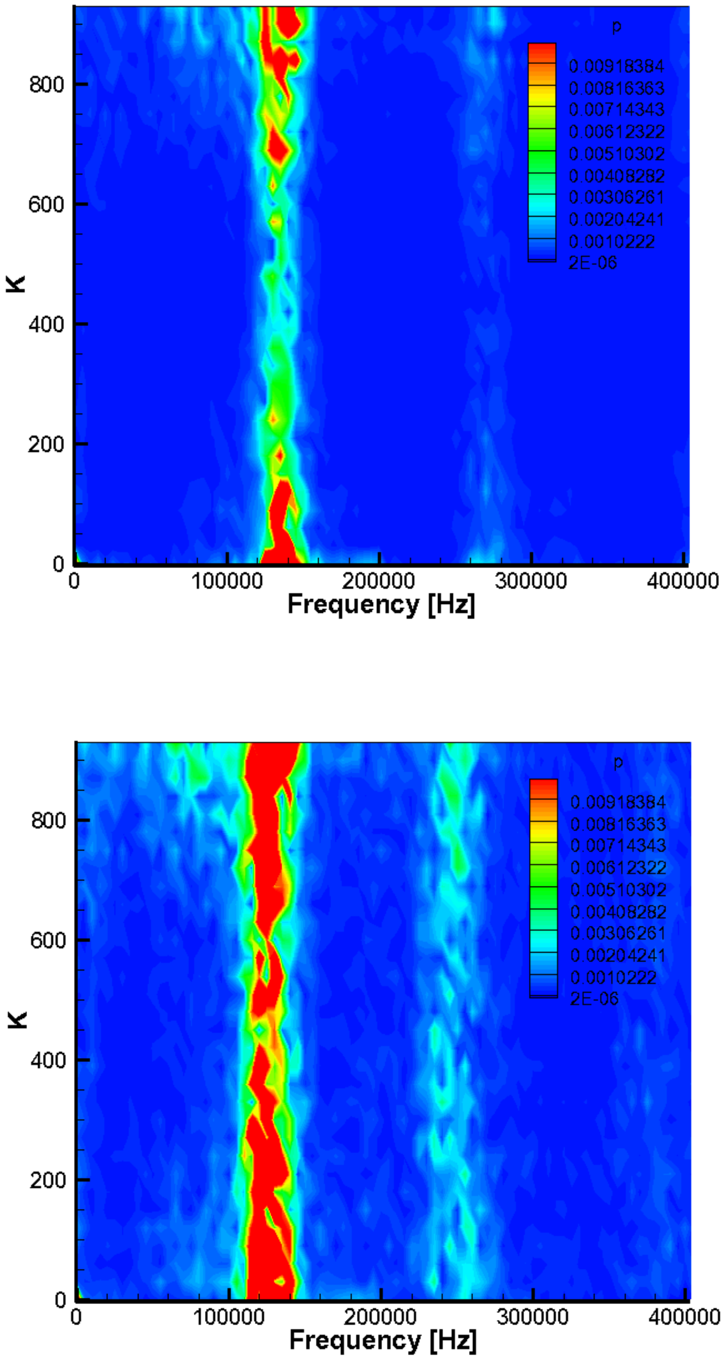

e)

f)

Fig. 73. TAMU3: Frequency vs. azimuth wave number at different surface locations: a) X=0.47m, b) X=0.6m, c) X=0.7m, d) X=0.8m, e) X=0.9m, f) X=0.95m.

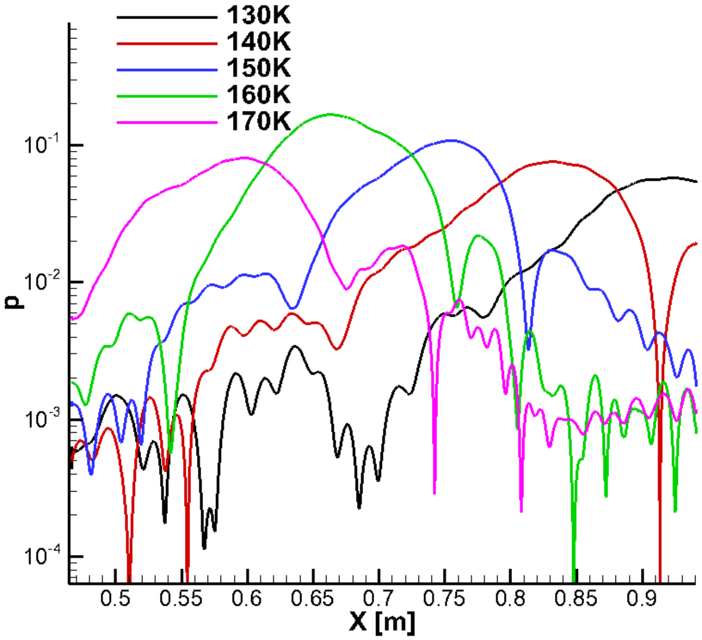
130K
140K
150K
160K
170K
10^{-1}
10^{-2}
10^{-3}
10^{-4}
p
0.5
0.55
0.6
0.65
0.7
0.75
0.8
0.85
0.9
X [m]

a)

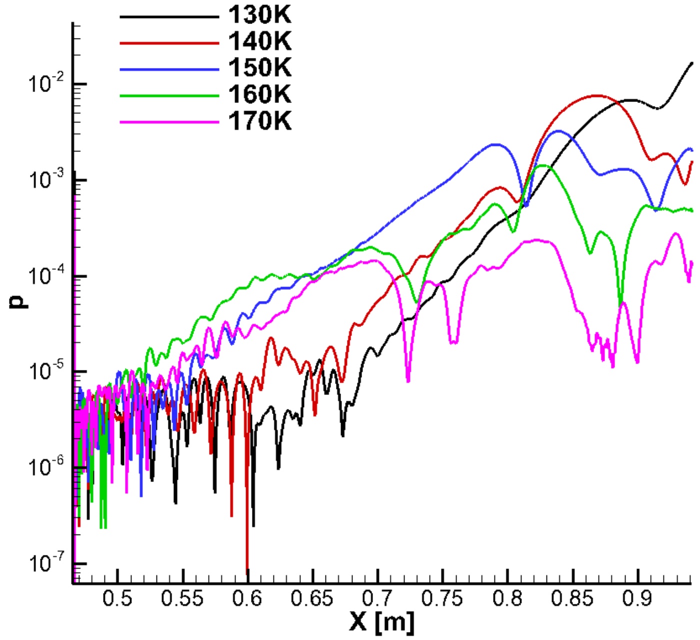
130K
140K
150K
160K
170K
10^{-2}
10^{-3}
10^{-4}
10^{-5}
10^{-6}
10^{-7}
p
0.5
0.55
0.6
0.65
0.7
0.75
0.8
0.85
0.9
X [m]

b)

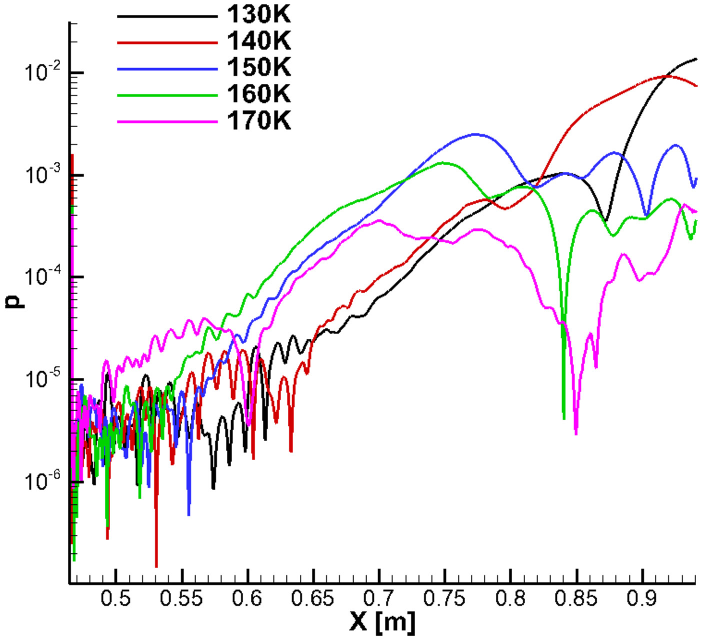

c)

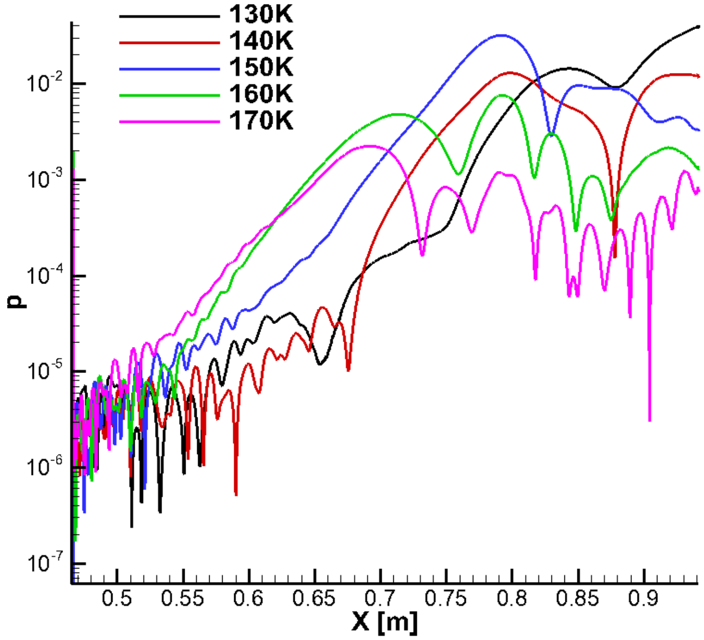

d)

Fig. 74. TAMU2: Selected frequency modes at different spanwise wave numbers: a) K=0, b) K=600, c) K=1200, d) K=1800.

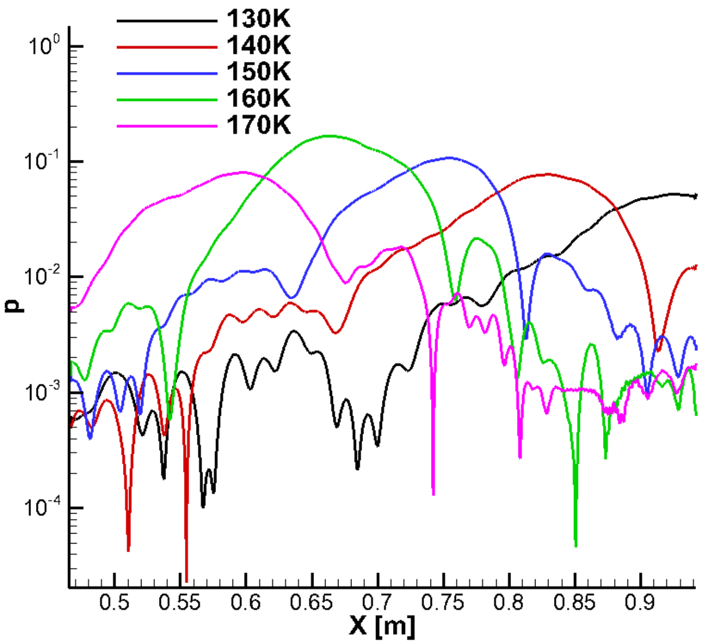
130K
140K
150K
160K
170K
10^{0}
10^{-1}
10^{-2}
10^{-3}
10^{-4}
p
0.5
0.55
0.6
0.65
0.7
0.75
0.8
0.85
0.9
X [m]

a)

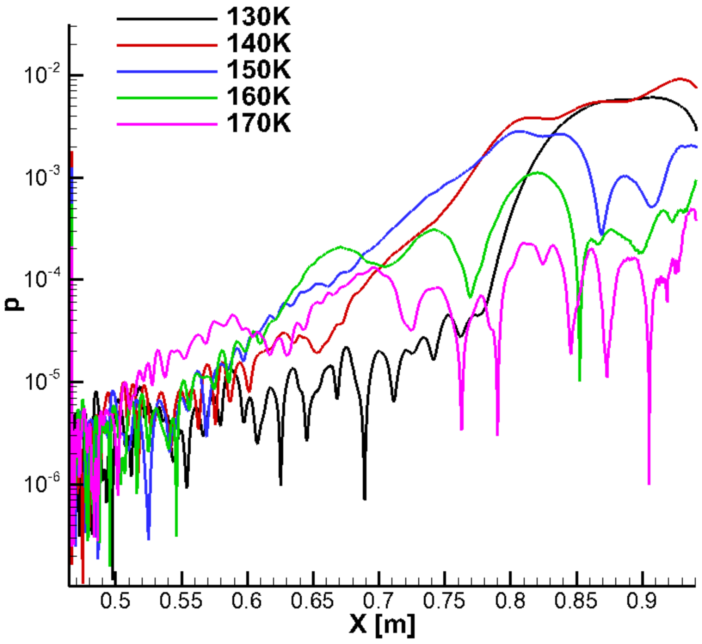
130K
140K
150K
160K
170K
10^{-2}
10^{-3}
10^{-4}
10^{-5}
10^{-6}
p
0.5
0.55
0.6
0.65
0.7
0.75
0.8
0.85
0.9
X [m]

b)

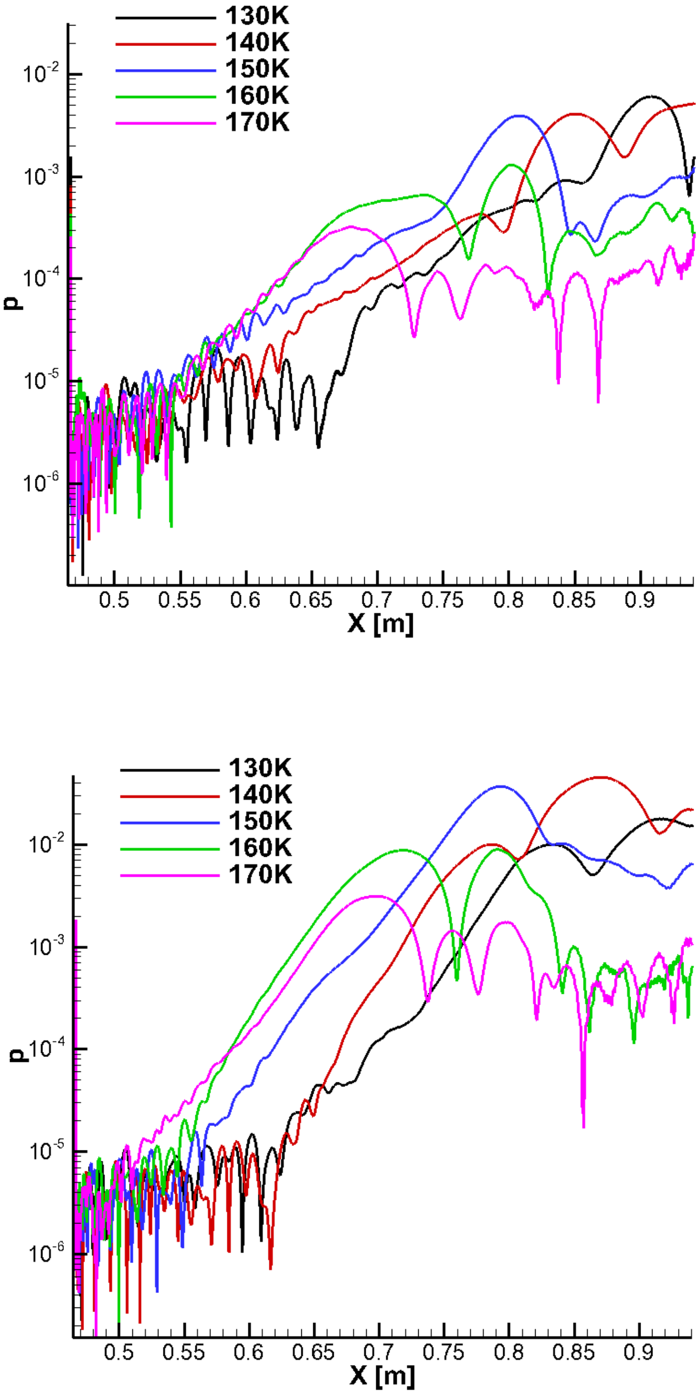

c)

d)

Fig. 75. TAMU3: Selected frequency modes at different spanwise wave numbers: a) K=0, b) K=300, c) K=600, d) K=900.

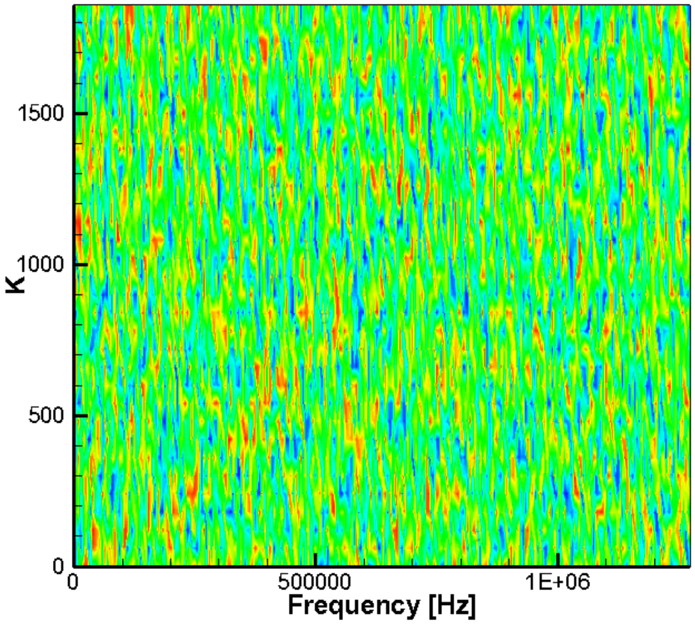

1500
1000
500
0
K
0
500000
1E+06
Frequency [Hz]

a)

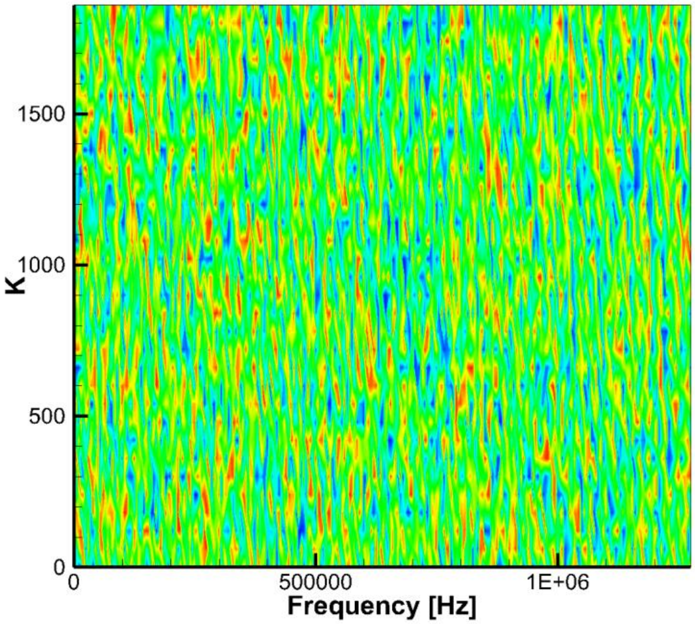

1500
1000
500
0
K
0
500000
1E+06
Frequency [Hz]

b)

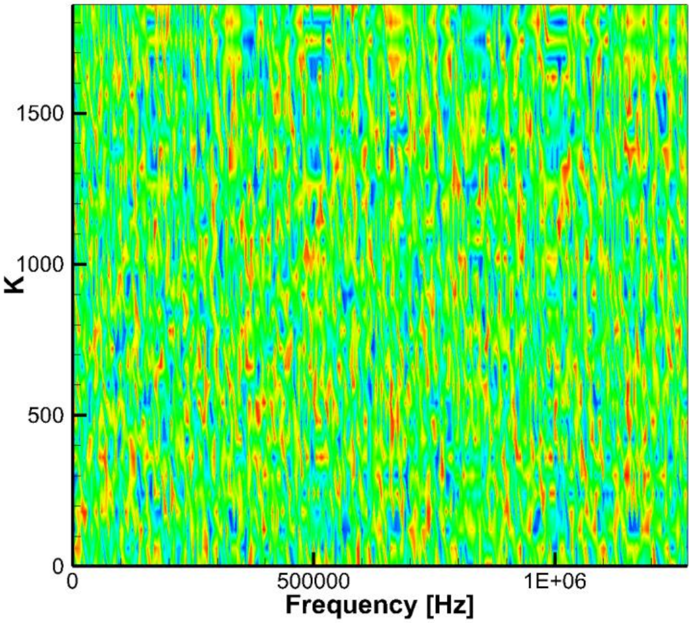
1500
K
1000
500
0
0
500000
1E+06
Frequency [Hz]

c)

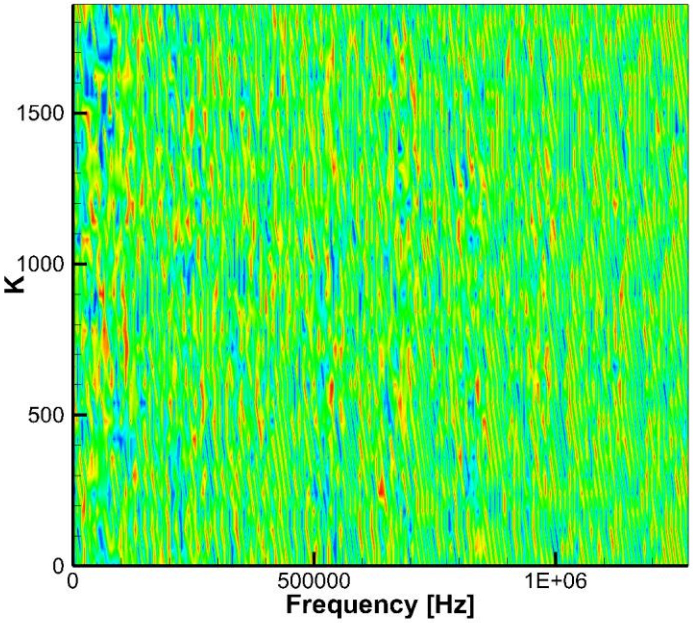
1500
K
1000
500
0
0
500000
1E+06
Frequency [Hz]

d)

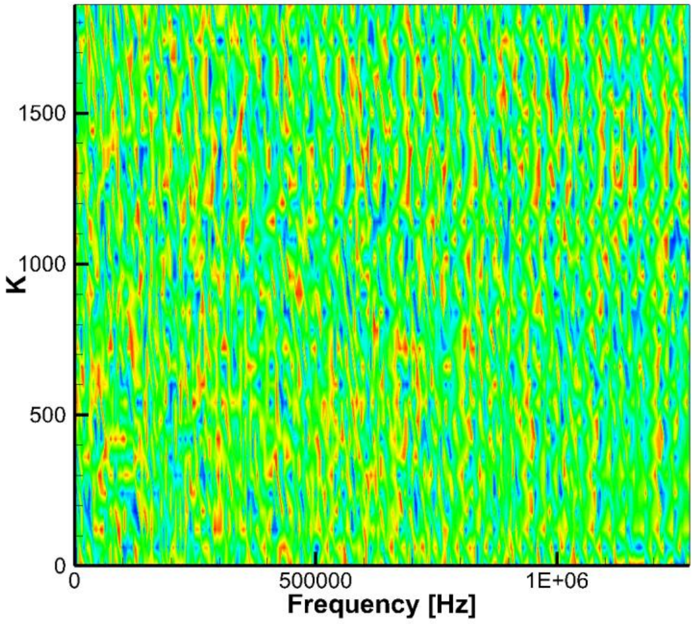

e)

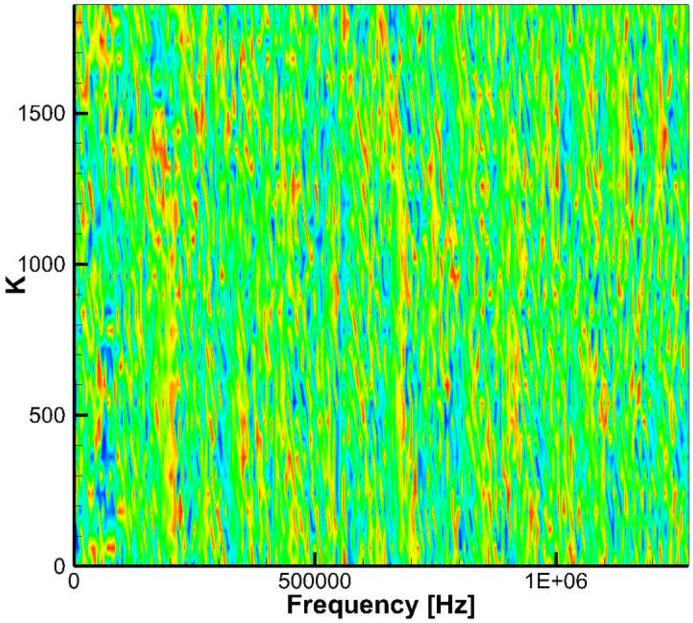

f)

Fig. 76. TAMU2: Spanwise wave number vs. Frequency of phase for all wave modes: a) X=0.47m, b) X=0.6m, c) X=0.7m, d) X=0.8m, e) X=0.9m, f) X=0.95m.

6.3.5. TAMU4: Breakdown Simulation with Reduced Spanwise Grid Resolution

TAMU4 case is used to study grid resolution effect on simulation result. This test case has spanwise are angle of 12 degree resolved by 32 azimuth grid points. The simulation result of this case is very different from other cases with more grid points in azimuth direction. In the current case, no visible breakdown occurs in the entire flow field.

Fig. 77 show the pressure disturbance contours along the cone surface. The disturbance wave remains two-dimensional until the very end of computational domain where some weakly three dimensionalities is observed. From the pressure disturbance amplitude spectra in Fig. 78, the primary 2-D modes are still dominated; however, the growths of 3-D modes within the second-mode frequency range are very moderate even at the highest spanwise wave number. The developments of wave modes believed to be responsible for breakdown shows that the all the 3-D modes fail to attain the amplitude level needed for breakdown to take place. And their amplitudes are at least one order of magnitude lower than the TAMU1, TAMU2 and TAMU3 cases.

Also, in this test case, no phase-locking feature can be seen in second-mode frequency range as shown in Fig. 79. Even some phase-locking feature is observed at frequencies higher than 500 kHz, these wave modes are too weak to interact with each other nonlinearly. Hence, it is believed that these modes cannot lead the flow to breakdown.

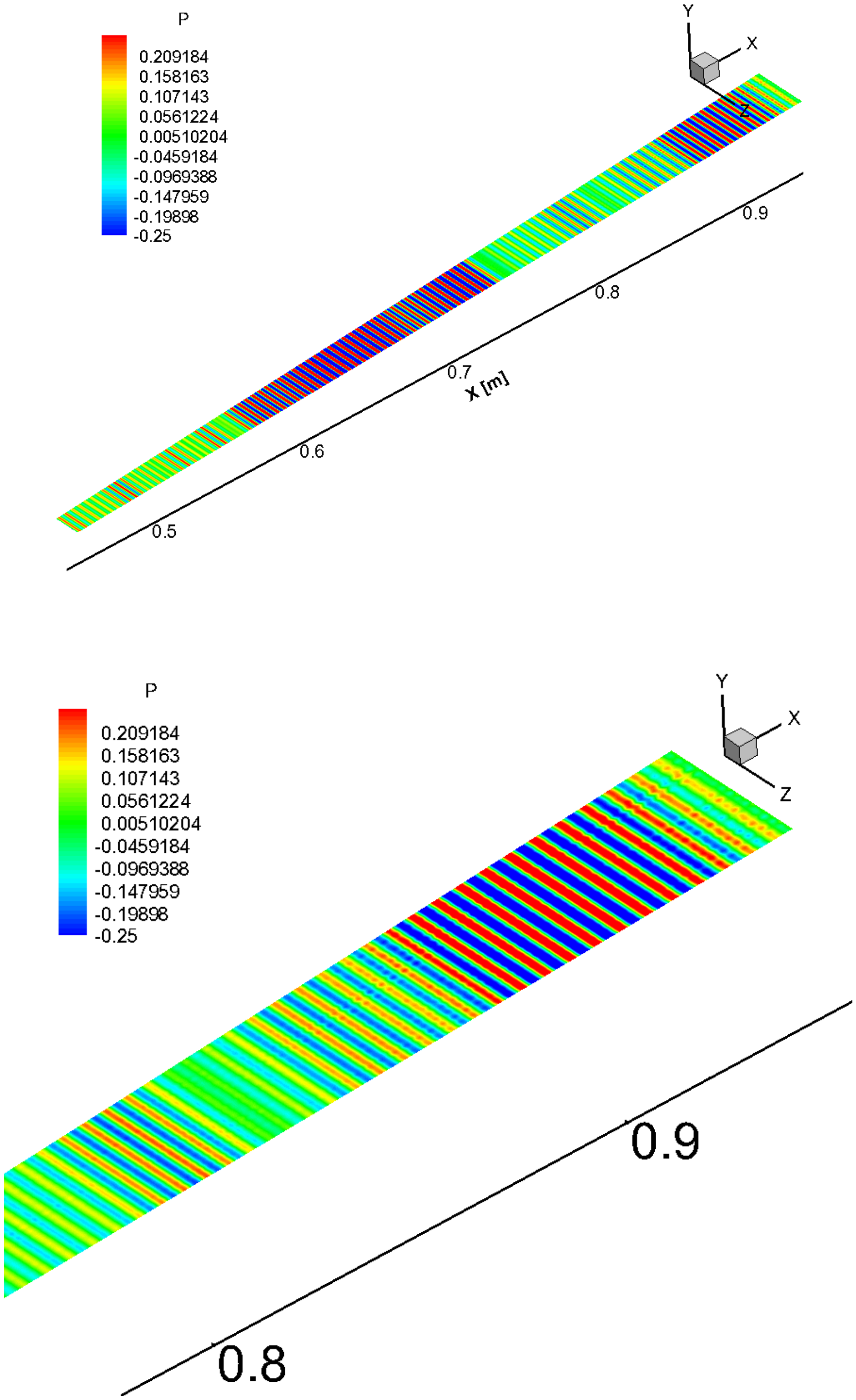

Fig. 77. Pressure disturbance on the cone surface for TAMU4 and the blow-up view of the downstream region.

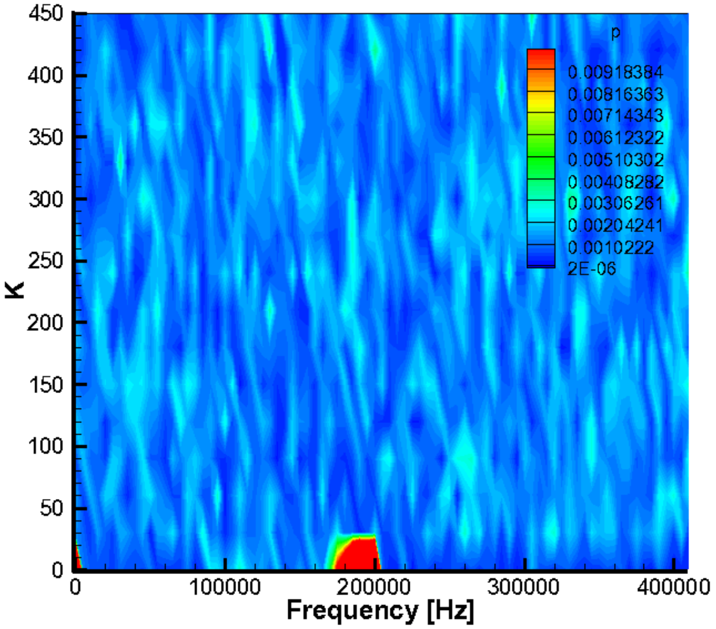
450
400
350
300
250
200
150
100
50
0
K
0
100000
200000
300000
400000
Frequency [Hz]
p
0.00918384
0.00816363
0.00714343
0.00612322
0.00510302
0.00408282
0.00306261
0.00204241
0.0010222
2E-06

a)

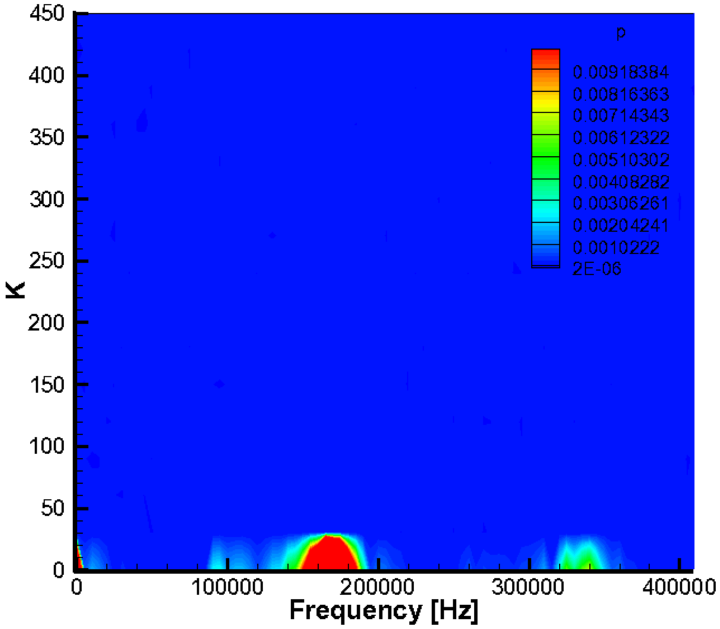
450
400
350
300
250
200
150
100
50
0
K
0
100000
200000
300000
400000
Frequency [Hz]
p
0.00918384
0.00816363
0.00714343
0.00612322
0.00510302
0.00408282
0.00306261
0.00204241
0.0010222
2E-06

b)

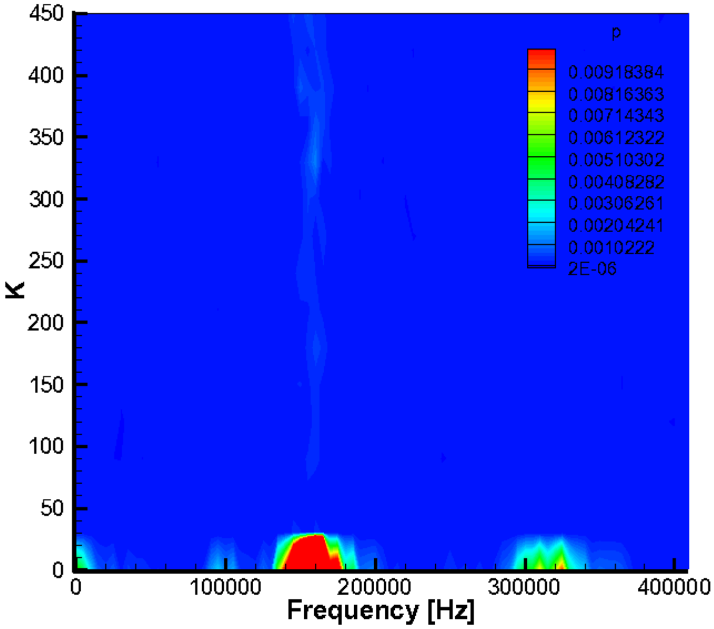
p
0.00918384
0.00816363
0.00714343
0.00612322
0.00510302
0.00408282
0.00306261
0.00204241
0.0010222
2E-06
K
0
50
100
150
200
250
300
350
400
450
0
100000
200000
300000
400000
Frequency [Hz]

c)

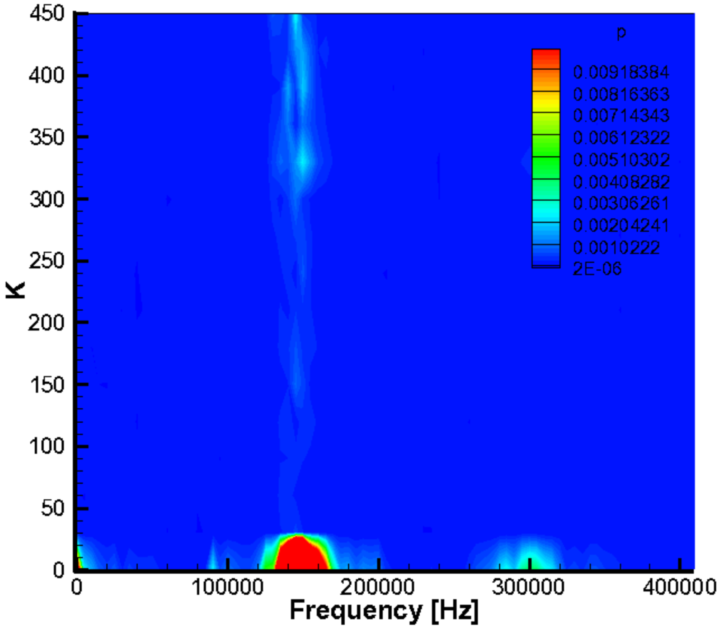
p
0.00918384
0.00816363
0.00714343
0.00612322
0.00510302
0.00408282
0.00306261
0.00204241
0.0010222
2E-06
K
0
50
100
150
200
250
300
350
400
450
0
100000
200000
300000
400000
Frequency [Hz]

d)

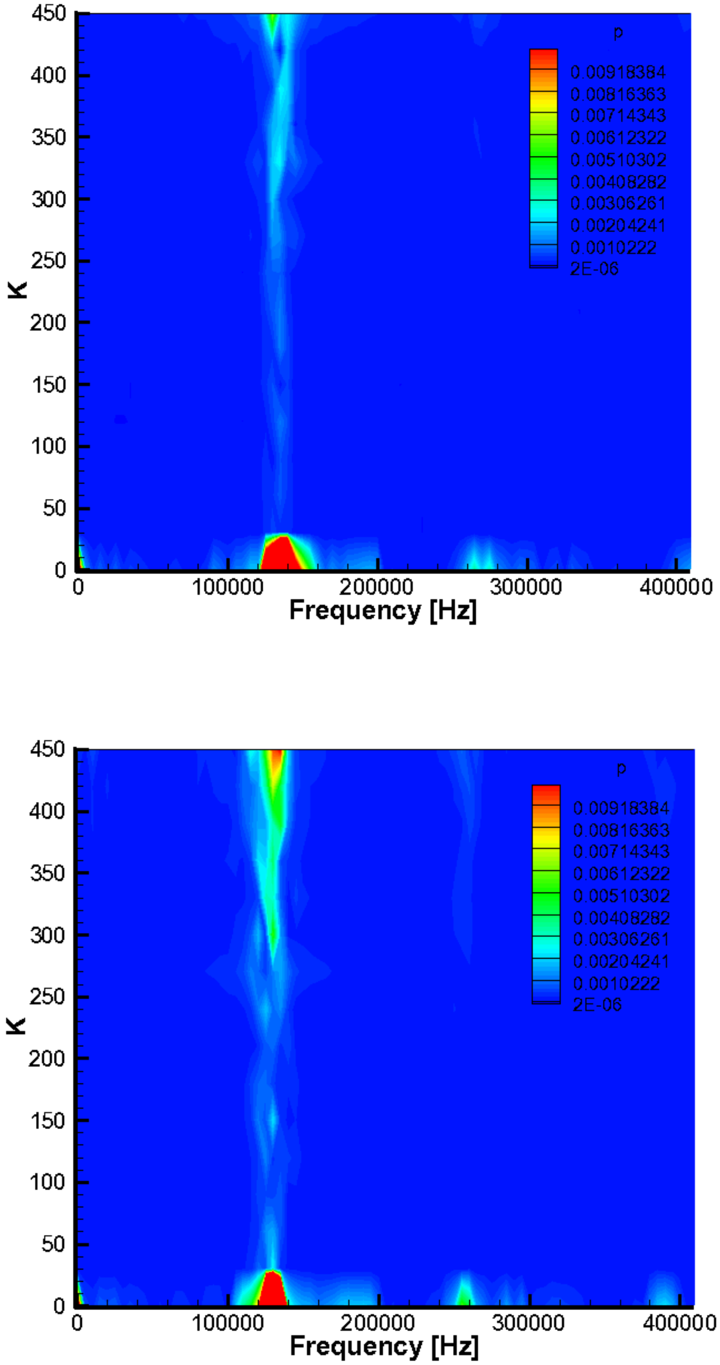

e)

f)

Fig. 78. Frequency vs. spanwise wave number at different surface locations: a) X=0.47m, b) X=0.6m, c) X=0.7m, d) X=0.8m, e) X=0.9m, f) X=0.95m.

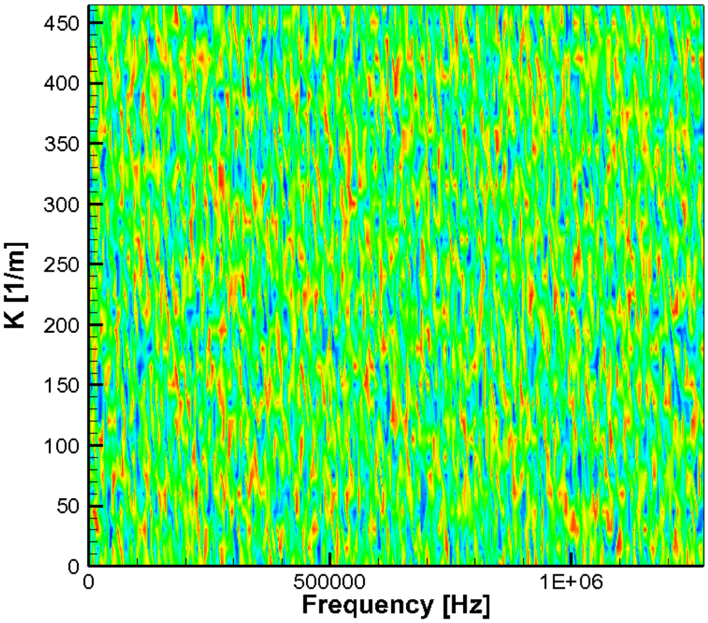
450
400
350
300
250
200
150
100
50
0
K [1/m]
0
500000
1E+06
Frequency [Hz]

a)

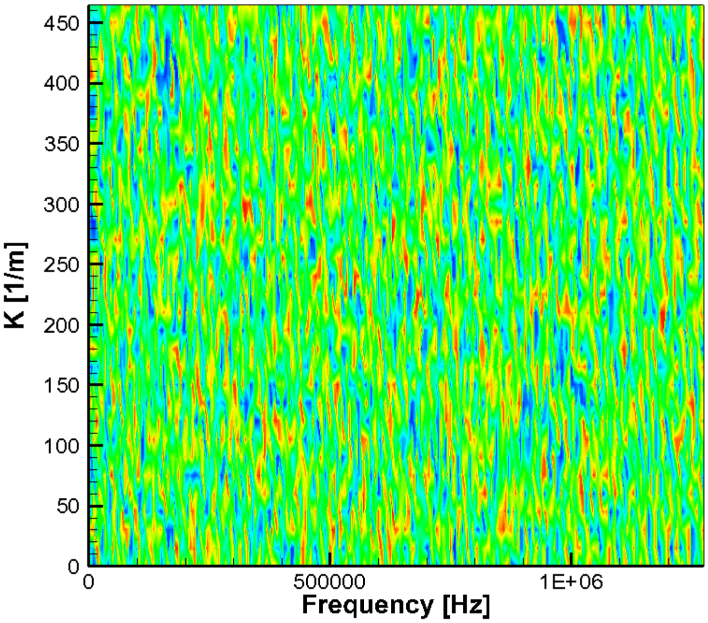
450
400
350
300
250
200
150
100
50
0
K [1/m]
0
500000
1E+06
Frequency [Hz]

b)

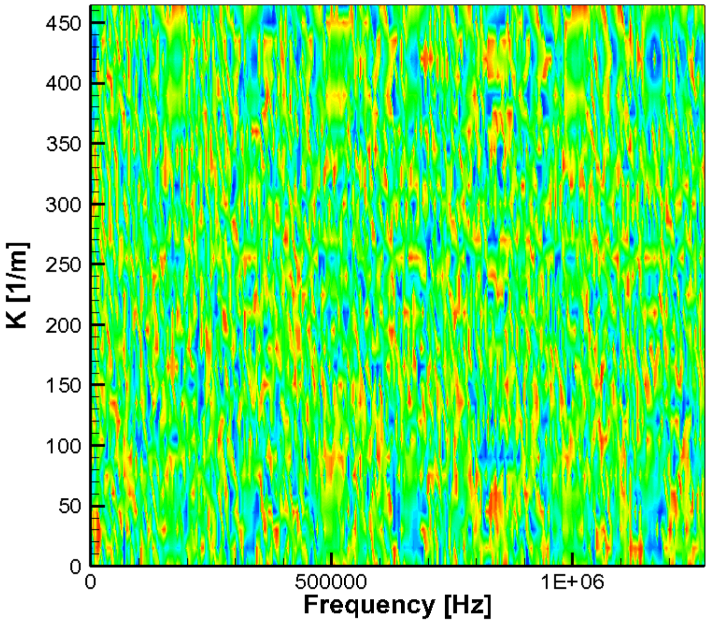
450
400
350
300
250
200
150
100
50
0
K [1/m]
0
500000
1E+06
Frequency [Hz]

c)

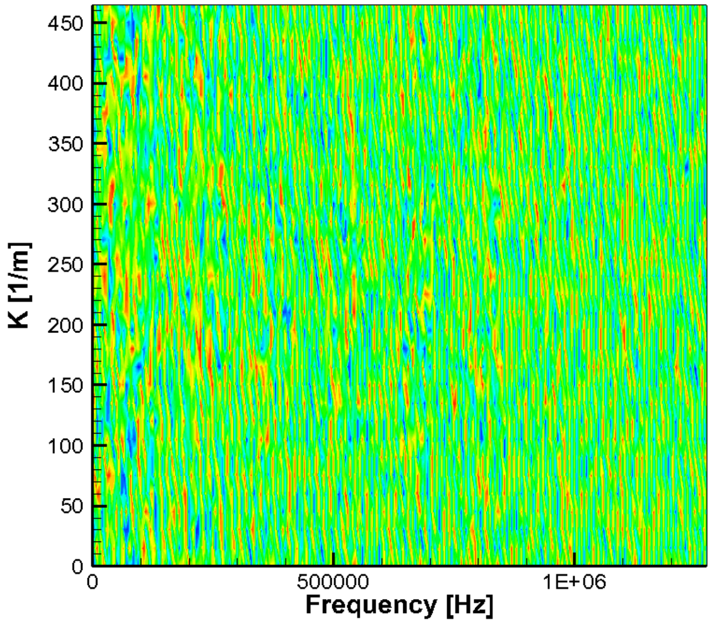
450
400
350
300
250
200
150
100
50
0
K [1/m]
0
500000
1E+06
Frequency [Hz]

d)

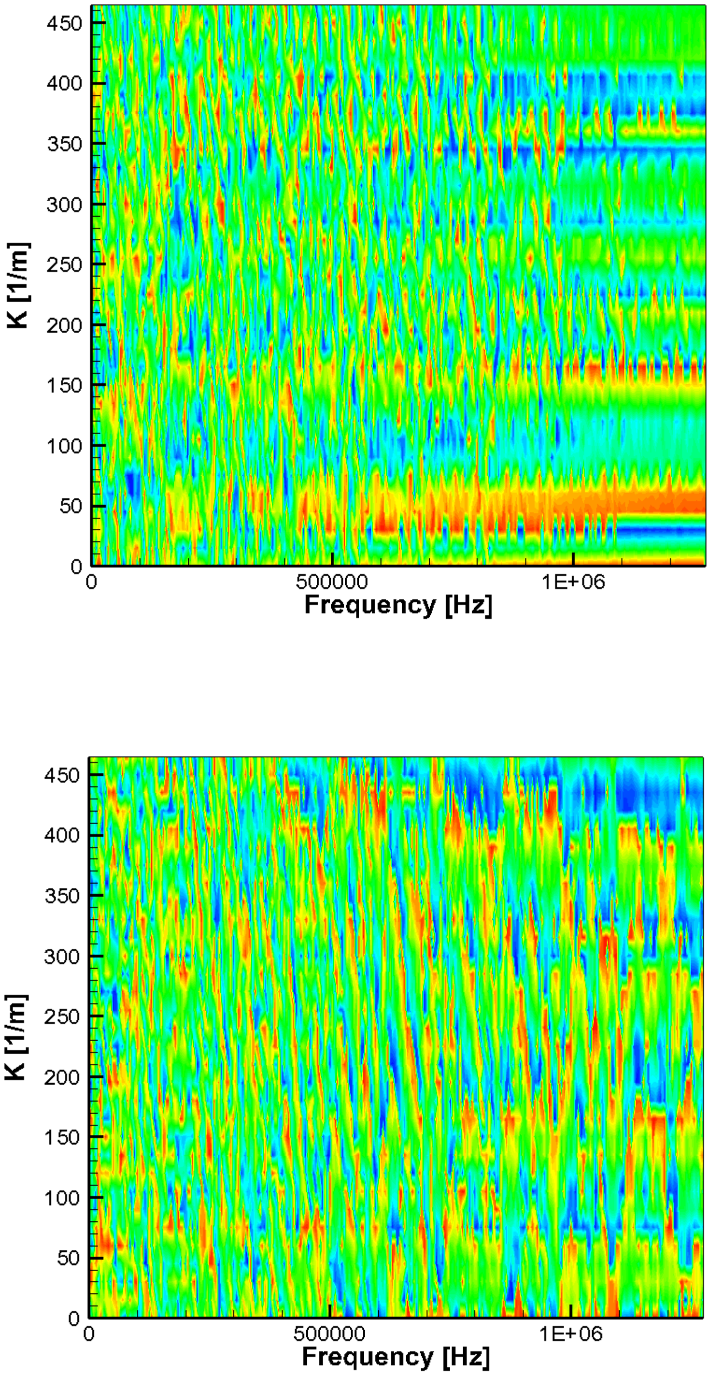

e)

f)

Fig. 79. Spanwise wave number vs. Frequency of phase for all wave modes: a) X=0.47m, b) X=0.6m, c) X=0.7m, d) X=0.8m, e) X=0.9m, f) X=0.95m.

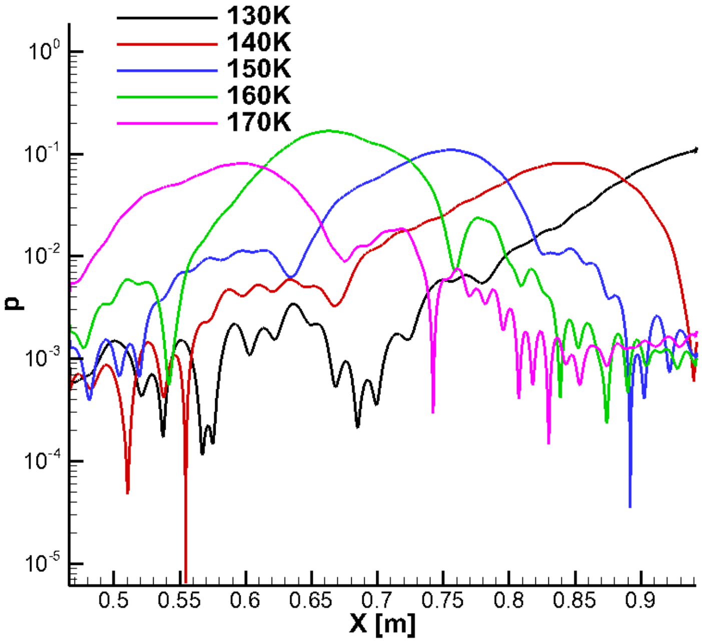
130K
140K
150K
160K
170K
p
10^{0}
10^{-1}
10^{-2}
10^{-3}
10^{-4}
10^{-5}
0.5
0.55
0.6
0.65
0.7
0.75
0.8
0.85
0.9
X [m]

a)

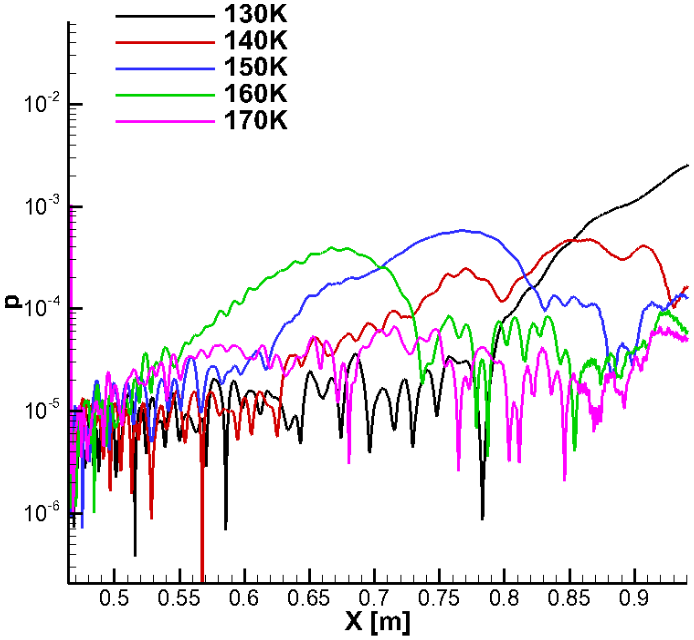
130K
140K
150K
160K
170K
p
10^{-2}
10^{-3}
10^{-4}
10^{-5}
10^{-6}
0.5
0.55
0.6
0.65
0.7
0.75
0.8
0.85
0.9
X [m]

b)

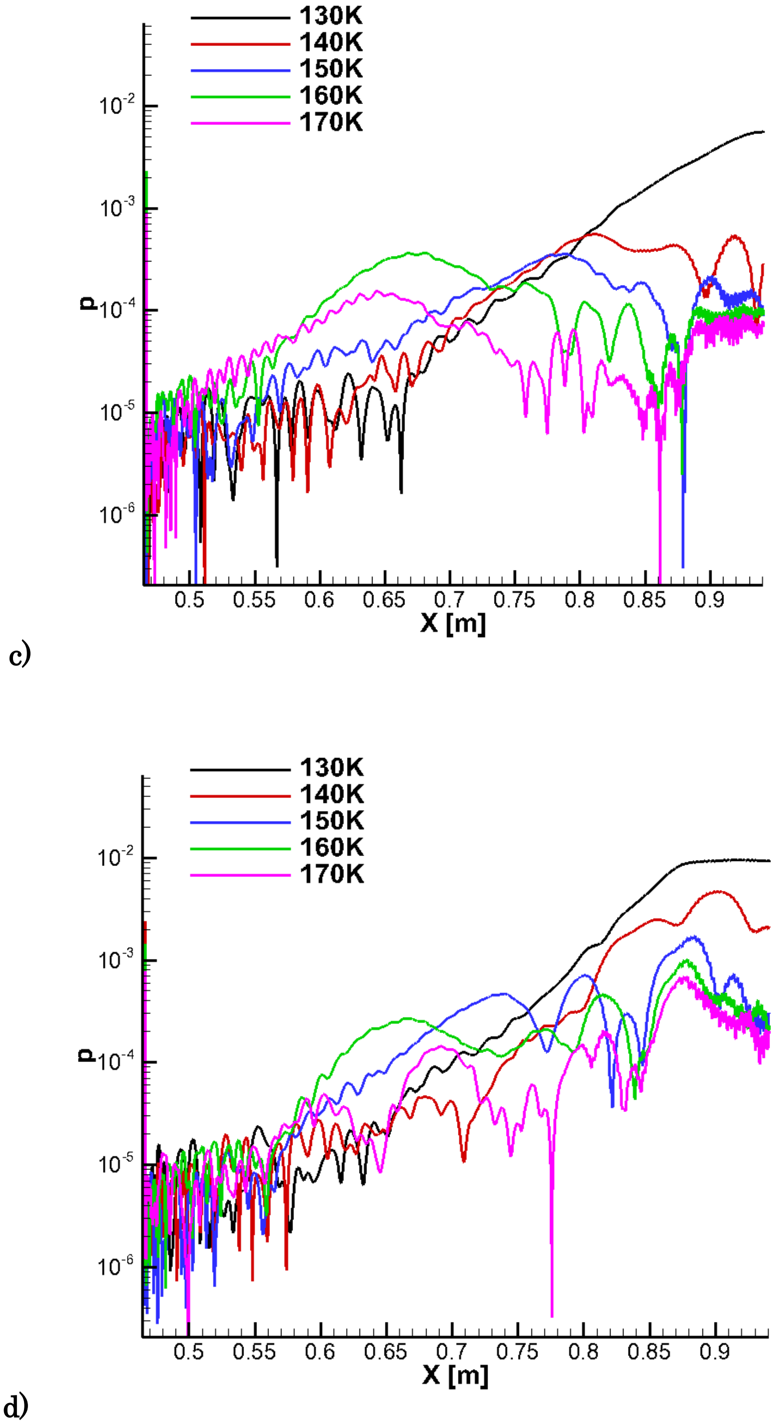

Fig. 80. Selected frequency modes at different spanwise wave numbers: a) K=0, b) K=150, c) K=300, d) K=450.

6.3.6. Summary and Discussion of all Breakdown Simulations

The results from all the test cases are presented in the previous sections. Here are some observations from these results. First, from test cases TAMU1 to TAMU3, the results show that the breakdown mechanism is independent of the spanwise arc angles of computational domains.

From all the breakdown test cases, the 2-D wave mode at 160 kHz attains the highest disturbance amplitude in the simulations. Hence, we use wave modes from this particular frequency to make some comparisons in hope of getting a better understanding of the breakdown mechanism. The primary 2-D wave modes developments at 160 kHz from all TAMU test cases are presented in Fig. 81. We can see from the plot that for all the breakdown simulations, the 2-D wave modes at 160 kHz behave very similarly. They only start to slightly deviate from each other from location X=0.75 m and on. Nevertheless, the growths of higher spanwise wave number modes from these test cases are completely different. As shown in Fig. 82 and Fig. 83, the growths of wave modes at spanwise wave mode numbers K=180 and K=720 respectively are so random that no trend can be observed.

Fig. 84, Fig. 85, and Fig. 86 further confirm the observation that, for all the simulations that the breakdowns take place, the 2-D mode and 3-D modes need to reach the same level in amplitude. And the 3-D modes at higher wave mode numbers grow faster than other 3-D modes. TAMU4 test case as shown in Fig. 87 show that even the higher spanwise wave modes attain the level as 2-D mode, as long as the modes from lower spanwise wave numbers do not reach the same level, breakdown does not occur.

Upon finishing all test cases and being able to simulate the flow to breakdown in some test cases, there are still a few unsolved problems remain. The phase-locking feature revealed in TAMU1 test case is one of them. Even this feature is not observed in TAMU2 and TAMU3 cases, the similar features are found in BS2 and FS1 test cases. And for those two cases, the flows are further into breakdown stage than all TAMU test cases. In the recent paper by Sivasubramanian and Fasel [75], they found that oblique breakdown, which uses a pair of oblique disturbance waves at opposite but equal angles, is more effective in leading hypersonic boundary layer flow to breakdown than conventional fundamental breakdown. This mechanism can possibly be used to explain why the phase-locking can facilitate the breakdown process because a pair of oblique wave is easier to get into phase-locking condition than other scenarios.

Another unanswered question is how realistic to use the current inflow profile setup for transition prediction. From Fig. 88, we see that, in the linear-grow region, even though the two-dimensional wave modes are the fastest growing modes within second-mode frequency range, the 3-D wave modes are also growing substantially. But in the current research effort, only 2-D receptivity data is used. The random noise is used to replace 3-D modes receptivity response in the inflow profile. In reality, the 3-D modes amplitudes will be higher than in our simulations which might lead to quicker breakdown and transition.

Finally, the parametric study shows that the simulation results are insensitive to the arc angels chosen for breakdown simulation. But this should not be used to justify the grid convergence of current results. More thorough case study is needed to better understand what the spanwise resolution should be in order to capture the complete physics during breakdown.

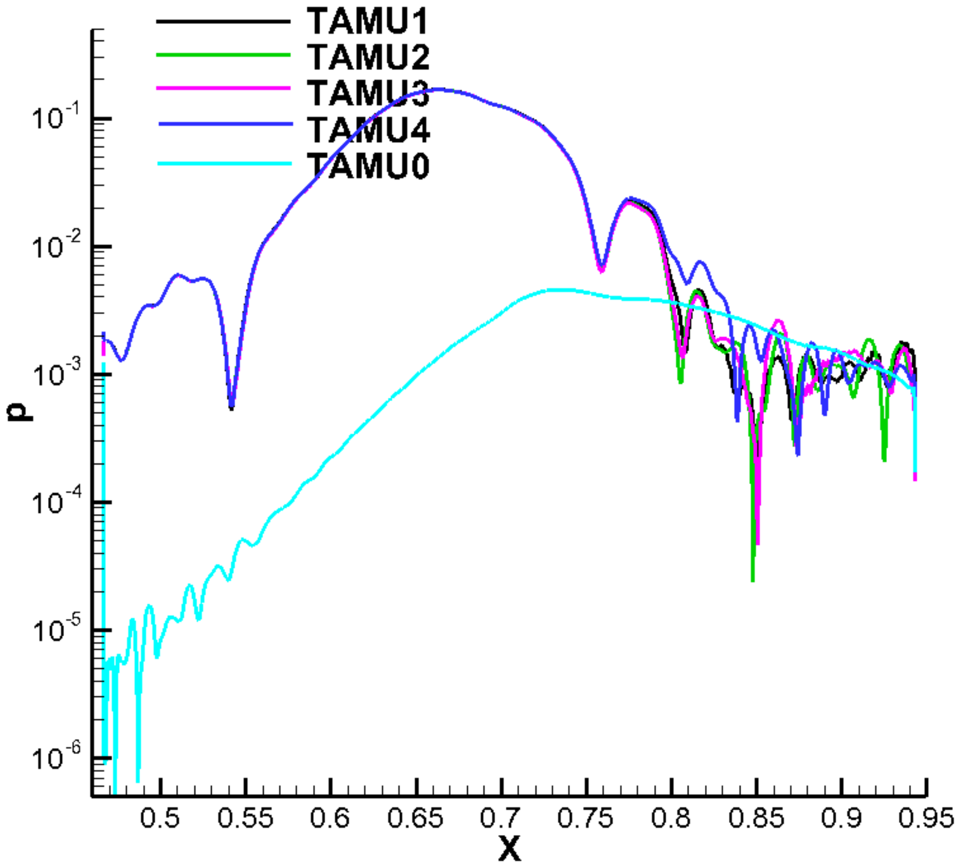

Fig. 81. f=160 kHz, two-dimensional wave modes for different cases.

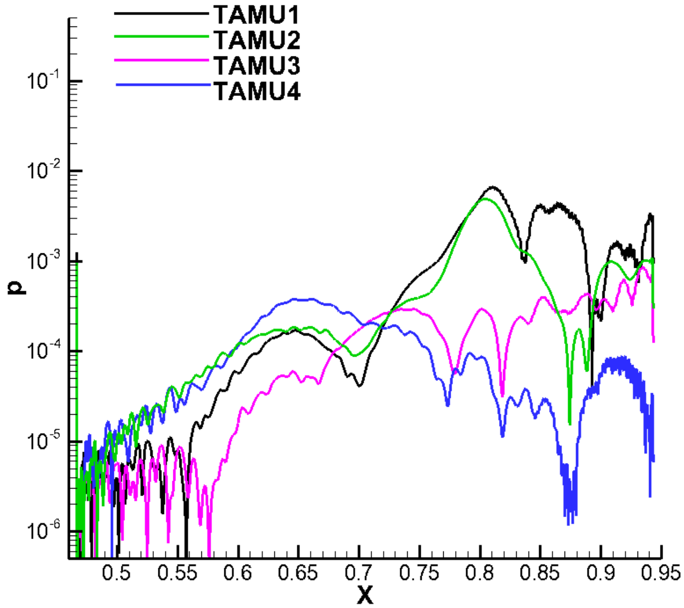

Fig. 82. f=160 kHz, K=180, pressure disturbance amplitude for different test case.

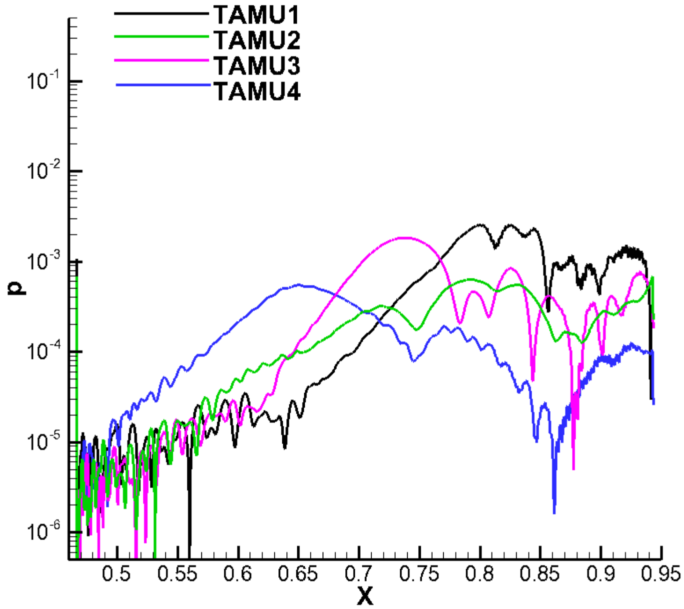

Fig. 83. f=160 kHz, K=720, pressure disturbance amplitude for different test case.

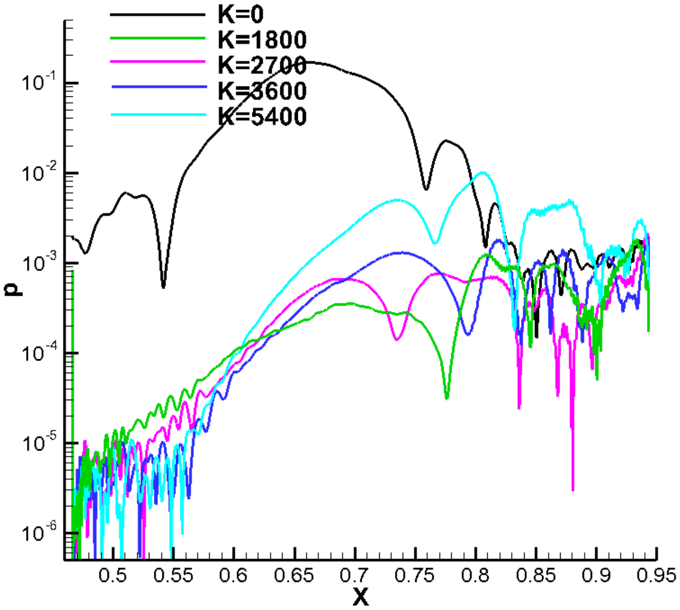

Fig. 84. f=160 kHz, TAMU1 case pressure disturbance for selected spanwise wave numbers.

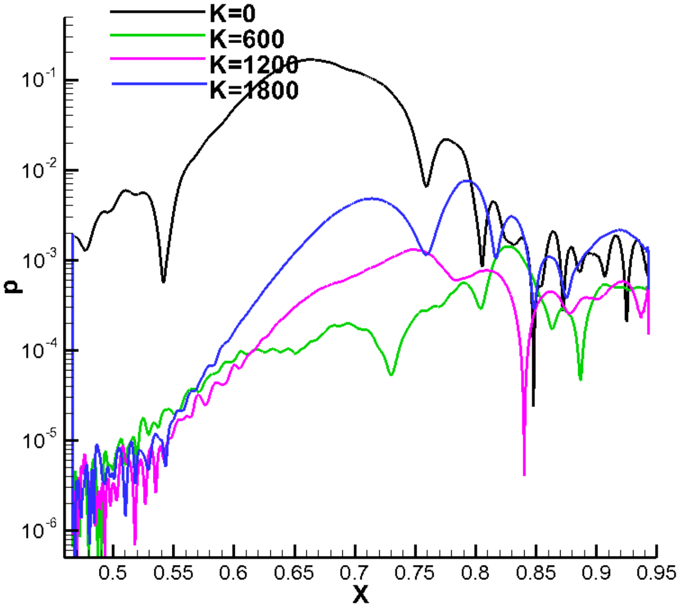

Fig. 85. f=160 kHz, TAMU2 case pressure disturbance for selected spanwise wave numbers.

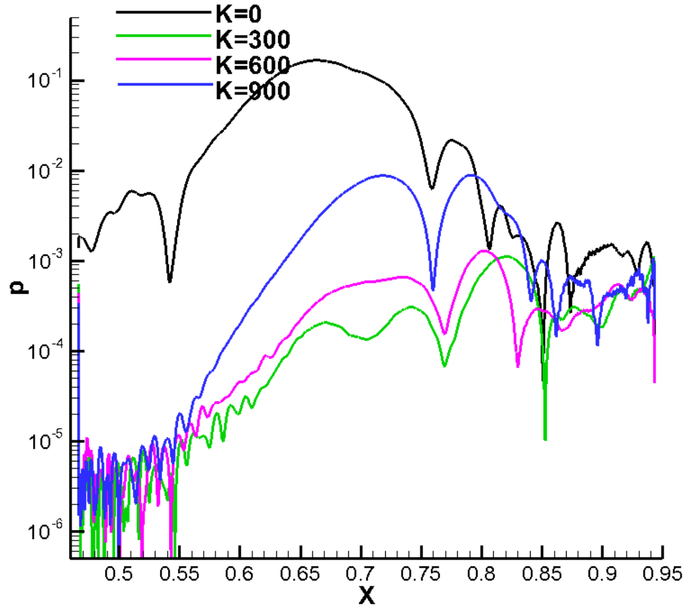

Fig. 86. f=160 kHz, TAMU3 case pressure disturbance for selected spanwise wave numbers.

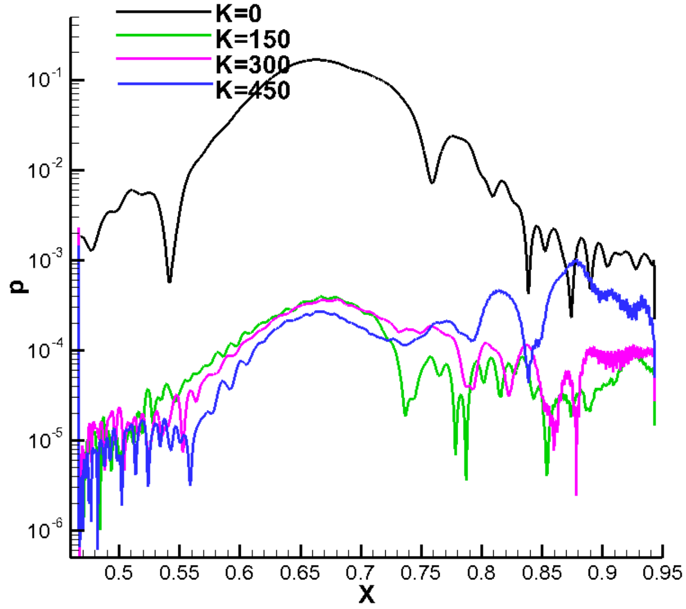

Fig. 87. f=160 kHz, TAMU4 case pressure disturbance for selected spanwise wave numbers.

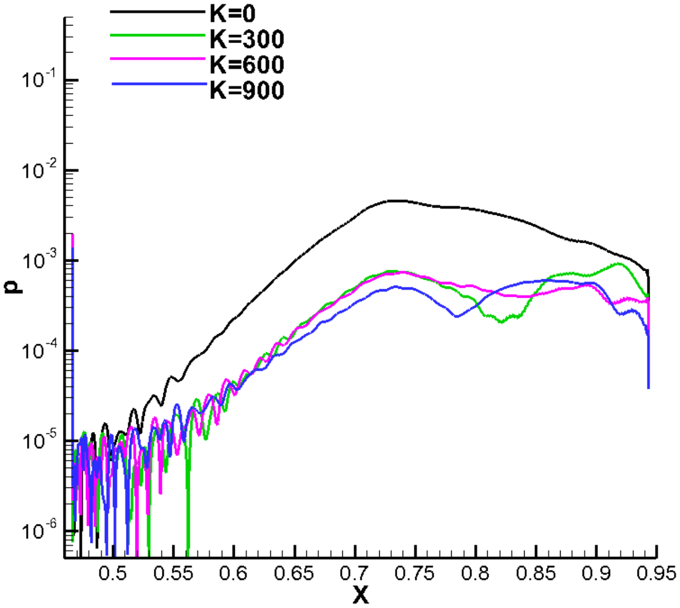

Fig. 88. f=160 kHz, TAMU0 case pressure disturbance for selected spanwise wave numbers.

7. Conclusions

7.1. Accomplishments

The feasibility to simulate the hypersonic boundary layer flow from freestream wave receptivity to the onset of breakdown stage in transition has been successfully demonstrated using the new three-step approach. With this newly developed framework, one complete simulation was performed on the TAMU Mach 6 case over a straight cone with 0.1 mm nose radius. In step I of proposed approach, the meanflow is calculated using a multi-zones technique to reach the flow region where the unstable second-mode instability is dominant. In step II, the 2-D receptivity response induced by freestream fast acoustic pulse containing continued frequency spectrum was captured. Then, this 2-D receptivity data base was used to re-construct the inflow disturbance profile for the nonlinear simulation. In step III, the 3-D nonlinear simulation was carried till the onset of breakdown stage. During the simulation framework development, several research topics were studied in depth. The nose bluntness effects on the hypersonic boundary layer flow stability were investigated on Stetson's Mach 5.5 case using LST analysis. The LST results were validated by comparing with numerical simulations. In the freestream wave receptivity simulation, a new freestream wave pulse model was devised and implemented on TAMU Mach 6 case to study the nose bluntness effect on nose region receptivity as well as the flow stability within the boundary layer. An extensive parametric study was conducted on the breakdown simulations. The simulation results were thoroughly analyzed to understand the breakdown mechanisms during hypersonic boundary layer flow transition.

7.2. Conclusions

In the study of nose bluntness effects on flow stability over circular cones, Stetson's Mach 5.5 experiment conducted in 1967, in which the actual reversals in transition were reported, is investigated using LST analysis and the results are verified by numerical simulations. The second-mode instability for blunt cones with nose radii of 0.156, 0.5 and 1.5 inches are calculated. According to the LST calculations, no reversal in the onset of the second-mode instability is observed. Because the onset locations of instability waves were not measured in the experiment, no comparisons can be made to verify the reversal in experiments were caused by the second-mode instability waves. For the two blunter cases in which the transition reversal were observed experimentally, the N factors based upon the second-mode instability are not large enough to initiate the laminar-turbulent transition at the locations that the actual transitions were observed experimentally. There is likelihood that the reversal is caused by some uncontrollable noises with the amplitude large enough that the growths of disturbances bypass the linear region and force the transition to occur earlier. However, this hypothesis cannot be justified based on the LST analysis.

In the effort to simulate hypersonic boundary layer flow from receptivity to breakdown using freestream wave, the feasibility of three-step approach has been successfully demonstrated in both the Stetson's test cases and TAMU test cases. A two-dimensional linear receptivity simulation utilizing newly developed freestream Gaussian pulse model has been conducted on TAMU straight cone with nose bluntness of 0.1 mm over Mach 6 flow. Upon successfully obtaining the receptivity response at the end of linear receptivity simulation, the inflow disturbance profile is re-constructed using a desired freestream spectrum and used as inflow for breakdown simulations. Subsequently, a series of test cases has been carried out for extensive parametric study. Both the azimuth direction arc angles and grid resolution effects on breakdown simulation results are investigated. For each test case, the developments of all 2-D and 3-D wave modes are obtained using two-dimensional FFT decompositions. From the simulation results, we confirm fundamental breakdown as the key player in the hypersonic boundary layer breakdown process. From the parametric case studies, it is found that breakdown is a localized process. It is not affected by the flow field globally. Also, the breakdown only occurs when all the 3-D wave modes grow to the same amplitude level as 2-D wave modes. During the phase of secondary instability growth, the 3-D modes at higher spanwise wave number tend to grow faster than 3-D modes at lower spanwise wave number.

7.3. Suggestions for Future Studies

Even the framework to simulate the complete process from freestream wave receptivity to breakdown has been successfully demonstrated using our new three-step approach, there are still a few unresolved problems remain for future investigations. First of all, a better inflow disturbance model should be devised so that this new framework can be used for more robust transition prediction. In current research, only 2-D receptivity simulation was carried for feasibility demonstration. Ideally, three-dimensional linear receptivity simulations should be conducted to obtain true 3-D receptivity data base and used to construct the inflow conditions for subsequent breakdown simulations. In addition, more freestream disturbance types should be included in the receptivity data base instead of using fast acoustic wave as the sole source of disturbance. A realistic freestream contains not only fast acoustic wave but also slow acoustic wave, entropy wave, and vorticity wave. Secondly, the effects of freestream disturbance amplitude and spectrum should be investigated to further correlate with the LST analysis so that the freestream disturbance amplitude effects can be incorporated with N factor calculation to provide a more reliable physic based transition prediction. Lastly, more nonlinear breakdown simulations should be conducted to reach further into the breakdown stage or even final transition to turbulent so that the breakdown mechanisms can be better understood. In order to do so, the spanwise grid resolution need to be further investigated. Furthermore, the phase-locking feature observed in some of the test cases needs to be systematically analyzed to reveal the physics beneath it. And the current framework has laid down the corner stone for future studies on all these topics.

REFERENCES

1. Kimmel, R.L., *Aspects of Hypersonic Boundary-Layer Transition Control.* 41st Aerospace Sciences Meeting and Exhibit, 2003. AIAA paper 2003-0772: p. 1-21.
2. Saric, W.S., Reed, H. L., and Kerschen, E. J., *Boundary-Layer Receptivity to Freestream Disturbances.* Annual Review of Fluid Mechanics, 2002. 34: p. 291-319.
3. Fedorov, A.V., and Khokhlov, A. P., *Prehistory of Instability in a Hypersonic Boundary Layer.* Theoretical and Computational Fluid Dynamics, 2001. 14: p. 359-375.
4. Fedorov, A.V. *Receptivity of High Speed Boundary Layer to Acoustic Disturbances.* in *32nd AIAA Fluid Dynamics Conference*. 2002. St. Louis, MO.
5. Fedorov, A.V., and Khokhlov, A. P., *Receptivity of Hypersonic Boundary Layer to Wall Disturbances.* Theoretical and Computational Fluid Dynamics, 2002. 15: p. 231-254.
6. Fedorov, A.V. *Receptivity of Hypersonic Boundary Layer to Acoustic Disturbances Scattered by Surface Roughness*. in *33rd AIAA Fluid Dynamics Conference*. 2003. Orlando, FL.
7. Tumin, A., Wang, X., and Zhong, X. *Direct Numerical Simulation and the Theory of Receptivity in a Hypersonic Boundary Layer* 2006.
8. Tumin, A. *Receptivity of Compressible Boundary Layers to Three-Dimensional Wall Perturbations*. 2006.
9. Reed, H.L., and Saric, W. S., *Linear stability thoery applied to boundary layers.* Annual Review of Fluid Mechanics, 1996. 28: p. 389-428.
10. Schneider, S.P., *Hypersonic Laminar-Turbulent Transition on Circular Cones and Scramjet Forebodies.* Progress in Aerospace Sciences, 2004. 40: p. 1-50.
11. Schneider, S.P., *Laminar-Turbulent Transition on Reentry Capsules and Planetary Probes.* JOURNAL OF SPACECRAFT AND ROCKETS, 2006. 43(6): p. 1153-1173.
12. Schneider, S.P., *Effects of High-Speed Tunnel Noise on Laminar-Turbulent Transition.* journal of Spacecraft and Rockets, 2001. 38(3): p. 323-333.
13. Ma, Y., and Zhong, X., *Receptivity of a Supersonic Boundary Layer over a Flat Plate. Part 1: Wave Structures and Interactions.* Journal of Fluid Mechanics, 2003. 488: p. 31-78.

14. Ma, Y., and Zhong, X., *Receptivity of a Supersonic Boundary Layer over a Flat plate. Part 2: Receptivity to Freestream Sound.* Journal of Fluid Mechanics, 2003. 488: p. 79-121.

15. Ma, Y., and Zhong, X., *Receptivity to Freestream Disturbances of a Mach 10 Nonequilibium Reacting Oxygen Flow over a Flat Plate.* 2004. AIAA 2004-0256.

16. Ma, Y., and Zhong, X., *Receptivity of a Supersonic Boundary Layer over a Flat Plate. Part 3: Effects of Different Types of Free-Stream Disturbances.* Journal of Fluid Mechanics, 2005. 532: p. 63-109.

17. Zhong, X., *Direct Numerical Simulation of Hypersonic Boundary-Layer Transition Over Blunt Leading Edges, Part II: Receptivity to Sound (Invited).* 1997. AIAA Paper 97-0756.

18. Zhong, X., *DNS of Boundary-Layer Receptivity to Freestream Sound for Hypersonic Flows over Blunt Elliptical Cones.* Laminar-Turbulent Transition, editors: H.F. Fasel and W.S. Saric, 1999: p. 445-450.

19. Zhong, X., *Leading-Edge Receptivity to Free Stream Disturbance Waves for Hypersonic Flow over a Parabola.* Journal of Fluid Mechanics, 2001. 441: p. 315-367.

20. Zhong, X., *Receptivity of Mach 6 Flow Over a Flared Cone to Freestream Disturbance.* 2004. AIAA 2004-0253.

21. Zhong, X., and Ma, Y., *Boundary-layer receptivity of Mach 7.99 Flow over a blunt cone to free-stream acoustic waves.* Journal of Fluid Mechanics, 2005. 556: p. 55-103.

22. Egorov, I.V., Fedorov, A. V., and Soudakov, V. G. , *Direct Numerical Simulation of Unstable Disturbances in Supersonic Boundary Layer.* AIAA paper 2004-0588, 2004: p. 1-11.

23. Balakumar, P., and Kegerise, M., *Receptivity of Hypersonic Boundary Layers over Straight and Flared Cones*, in *48th AIAA Aerospace Sciences Meeting and Exhibit.* 2010, AIAA paper 2010-1065.

24. Balakumar, P., and Kegerise, M.A., *Receptivity of Hypersonic Boundary Layers to Acoustic and Vortical Disturbances.* AIAA paper 2011-371, 2011.

25. Fedorov, A., and Tumin, A., *Initial-Value Problem for Hypersonic Boundary Layer* 2001. AIAA Paper 2001-2781.

26. Fedorov, A., *Transition and Stability of High-Speed Boundary Layers.* Annual Review of Fluid Mechanics, 2011. 43: p. 79-95.

27. Reshotko, E., *Transition Issues for Atmospheric Entry.* Journal of Spacecraft and Rockets, 2008. 45(2): p. 161-164.

28. Pruett, C.D., Zang, T. A., Chang, C. L., and Carpenter, M. H., *Spatial Direct Numerical Simulation of High-Speed Boundary-Layer Flows, Part I: Algorithmic Considerations and Validation.* Theoretical and Computational Fluid Dynamics, 1995. 7: p. 49-76.

29. Pruett, C.D.a.C., C. L., *Spatial direct numerical simulation of high-speed boundary-layer flows Part II: Transition on a cone in Mach 8 flow* Theoretical and Computational Fluid Dynamics, 1995. 7: p. 397-424.

30. Erlebacher, G., Hussaini, M. Y., *Numerical Experiments in Supersonic Boundary-Layer Stability.* Physics of Fluids A, 1990. 2(1): p. 94-104.

31. Zhong, X., and Wang, X., *Direct Numerical Simulation on Receptivity, Instability, and Transition of Hypersonic Boundary Layers* The Annual Review of Fluid Mechanics, 2012. 44: p. 527-561.

32. Franko, J.K., Bhaskaran, R., Lele, K. S., *Direct Numerical Simulation of Transition and Heat-transfer Overshoot in a Mach 6 Flat Plate Boundary Layer.* AIAA paper 2011-3874, 2011.

33. Erlebacher, G.a.H., M. Y., *Stability and Transition in Supersonic Boundary Layers.* AIAA Paper 1987-1416, 1987: p. 1-12.

34. Thumm, A., Wolz, W., and Fasel, H. *Numerical simulation of spatially growing three-dimensional disturbance waves in compressible boundary layers.* in *Laminar-Turbulent Transition. IUTAM Symposium.* 1990. Toulouse, France, 1989 Springer-Verlag, Berlin.

35. Fasel, H., Thumm, A., and Bestek, H. *Direct numerical simulation of transition in supersonic boundary layers: oblique breakdown.* in *Fluids Engineering Conference, Transitional and Turbulent Compressible Flows.* 1993. Washington, DC, June 20–24, 1993: ASME, New York.

36. Chang, C.-L.a.M., M. R., *Oblique-mode breakdown and secondary instability in supersonic boundary layers.* Journal of Fluid Mechanics, 1994. 273: p. 323-360.

37. Sandham, N.D., Adams, N. A., Kleiser, L., *Direct simulation of breakdown to turbulence following oblique instability waves in a supersonic boundary layer.* Applied Scientific Research, 1995. 54: p. 223-234.

38. Mayer, C.S.J., von Terzi, D. A., and Fasel, H. F., *DNS of Complete Transition to Turbulence Via Oblique Breakdown at Mach 3.* AIAA paper 2008-4398, 2008: p. 1-21.

39. Laible, A., Mayer, C., and Fasel, H., *Numerical Investigation of Supersonic Transition for a Circular Cone at Mach 3.5.* AIAA paper 2008-4397 2008: p. 1-24.

40. Husmeier, F., Fasel, H. F., *Numerical Investigations of Hypersonic Boundary Layer Transition for Circular Cones.* AIAA paper 2007-3843, 2007: p. 1-17.

41. Stetson, K.F., Thompson, E. R., Donaldson, J. C., and Siler, L. G., *Laminar Boundary Layer Stability Experiments on a Cone at Mach 8, Part 1: Sharp Cone.* 1983. AIAA Paper 83-1761.

42. Stetson, K.F., Thompson, E. R., Donaldson, J. C., and Siler, L. G., *Laminar Boundary Layer Stability Experiments on a Cone at Mach 8, Part 2: Blunt Cone.* 1984. AIAA paper 84-0006.

43. Pruett, C.D.a.C., C. L., *Direct Numerical Simulation of Hypersonic Boundary-Layer Flow on a Flared Cone* Theoretical and Computational Fluid Dynamics, 1998. 11: p. 49-67.

44. Zhong, X., *Additive Semi-Implicit Runge-Kutta Schemes for Computing High-Speed Nonequilibrium Reactive Flows.* Journal of Computational Physics, 1996. 128: p. 19-31.

45. Zhong, X., *High-Order Finite-Difference Schemes for Numerical Simulation of Hypersonic Boundary-Layer Transition.* Journal of Computational Physics, 1998. 144: p. 662-709.

46. Zhong, X., and Tatineni, M., *High-Order Non-Uniform Grid Schemes for Numerical Simulation of Hypersonic Boundary-Layer Stability and Transition.* Journal of Computational Physics, 2003. 190(2): p. 419-458.

47. Zhong, X. *A New High-Order Immersed Interface Method for Multi-Phase Flow Simulation*. in *AIAA paper 2006-1294*. 2006.

48. Rai, M.a.M., P., *Direct numerical simulation of transition and turbulence in a spatially evolving boundary layer.* AIAA Paper 91-1607, 1991: p. 890-912.

49. ADAMS, N.A., KLEISER, L., *Subharmonic transition to turbulence in a flat-plate boundary layer at Mach number 4.5.* Journal of Fluid Mechanics, 1996. 317: p. 301-335.

50. Spalart, P.R., and Yang, K.-S., *Numerical study of ribbon-induced transition in Blasius flow.* Journal of Fluid Mechanics, 1987. 178: p. 345-365.

51. Wang, X., and Zhong, X., *Receptivity of a Mach 8 Flow over a Sharp Wedge to Wall Blowing-Suction.* 2005. AIAA paper 2005-5025.

52. Zhong, X., and Ma, Y., *Boundary-layer receptivity of Mach 7.99 Flow over a blunt cone to free-stream acoustic waves.* Journal of Fluid Mechanics, 2006. 556: p. 55-103.

53. Wang, X.a.Z., X., *Numerical Simulation and Experiment Comparison of Leading-Edge Receptivity of a Mach 5.92 Boundary Layer.* AIAA paper 2006-1107, 2006.

54. Huang, Y., and Zhong, X., *Numerical Study of Laser-Spot Effects on Boundary-Layer Receptivity for Blunt Compression-Cones in Mach-6 Freestream* AIAA 2010-4447, 2010.

55. Zhong, X., and Lei, J., *Numerical Simulation of Nose Bluntness Effects on Hypersonic Boundary Layer Receptivity tp Freestream Disturbances.* 2011. AIAA paper 2011-3079.

56. Dong, H., and Zhong, X., *Numerical Simulations of Transient Growth in a Mach 15 Boundary Layer over a Blunt Leading Edge*, in *41st AIAA Aerospace Sciences Meeting and Exhibit.* 2003, AIAA paper 2003-1266.

57. Rawat, P.S., and Zhong, X., *On high-order shock-fitting and front-tracking schemes for numerical simulation of shock–disturbance interactions.* Journal of Computational Physics, 2010. 229(19): p. 6744-6780.

58. Malik, M.R., *Numerical Methods for Hypersonic Boundary Layer Stability.* Journal of Computational Physics, 1990(86): p. 376-413.

59. Mack, L.M., *Boundary Layer Linear Stability Theory.* AGARD Report, 1984. No. 709.

60. Wheaton, M.B., Juliano, J. T., Berridge, C. D., Chou, A., Gilbert, L. P., Casper, M. K., Steen, E. L., Schneider, P. S., Johnson, B. H., *Instability and Transition Measurement in the Mach 6 Quiet Tunnel.* AIAA 2009-3559, 2009.

61. Malik, M.R., Spall, R. E., and Chang, C. L., *Effect of Nose Bluntness on Boundary Layer Stability and Transition.* 1990. AIAA Paper 90-0112.

62. Stetson, K.F., Rushton, G. H., *Shock Tunnel Investigation of Boundary-Layer Transition at M = 5.5.* AIAA JOURNAL, 1967. 5(5): p. 899-906.

63. Lei, J., Zhong, X., *Linear Stability Analysis of Nose Bluntness Effects on Hypersonic Boundary Layer Transition* Journal of Spacecraft and Rockets 0022-4650, 2011. 49(1): p. 24-37.

64. Bodony, E.D., *Analysis of sponge zones for computational fluid mechanics.* Journal of Computational Physics, 2006. 212: p. 681-702.

65. Stetson, K.F., *Nosetip Bluntness Effects on Cone Frustum Boundary Layer Transition in Hypersonic Flow.* AIAA paper 1983-1763, 1983.

66. Softley, E.J., *Transition of the Hypersonic Boundary Layer on a Cone: Part II - Experiments at Mach 10 and More on Blunt Cone Transition*, in *GE Space Science Lab, R68SD14.* 1968.

67. Herbert, T.a.E., V., *Stability of Hypersonic Flow over a Blunt Body.* AGARD CP, 1993. 514: p. 28.

68. Kufner, E., Dallmann, U., and Stilla, J., *Instability of Hypersonic Flow Past Blunt Cones - Effects of Mean Flow Variations.* 1993. AIAA paper 93-2983.

69. Kufner, E., and Dallmann, U. *Entropy and Boundary Layer Instabilityof Hypersonic Cone Flows - Effects of Mean Flow Variations*. in *IUTAM Symposium on Laminar-Turbulent Transition*. 1994. Sendai/Japan: Springer-Verlag, Berlin.

70. Rosenboom, I., Hein, S., and Dallmann, U., *Influence of Nose Bluntness on Boundary-Layer Instabilities in Hypersonic Cone Flows* AIAA Paper 99-3591, 1999.

71. Dietz, G., Hein, S., *Entropy-layer instabilities over a blunted flat plate in supersonic flow.* Physics of Fluids, 1999. 11(1): p. 7-9.

72. Koevary, C., Laible, A., Mayer, C. and Fasel, H., *Numerical Simulations of Controlled Transition for a Sharp Circular Cone at Mach 8.* 2010. AIAA paper 2010-4598.

73. Tumin, A., *Multimode Decomposition of Spatially Growing Perturbations in a Two-Dimensional Boundary Layer.* Physics of Fluids, 2003. 15(9): p. 2525-2540.

74. Tumin, A., *Nonparallel Flow Effects on Roughness-Induced Perturbations in Boundary Layers.* J. Spacecraft and Rockets, 0022-4650 2008. 45(6): p. 1176-1184.

75. Sivasubramanian, J., and Fasel, F. H., *Direct Numerical Simulation of Controlled Transition In a Boundary Layer on a Sharp Cone at Mach 6.* AIAA paper 2013-0263, 2013.